Title	Nonequilibrium Flow in Classical and Quantum Dynamical Systems
Author(s)	Yukawa, Satoshi
Citation	大阪大学, 1999, 博士論文
Version Type	VoR
URL	https://doi.org/10.11501/3155673
rights	
Note	

Nonequilibrium Flow in Classical and Quantum Dynamical Systems

Satoshi Yukawa
Department of Applied Physics, School of Engineering,
the University of Tokyo

February 24, 1999

①

Nonequilibrium Flow in Classical and Quantum Dynamical Systems

Satoshi Yukawa
Department of Applied Physics, School of Engineering,
the University of Tokyo

February 24, 1999

Preface

In this thesis nonequilibrium steady flows in classical and quantum systems are studied. We deal with two nonequilibrium systems in which a steady flow appears in their far-from-equilibrium states; One is a one-dimensional traffic flow system and the other is a one-dimensional quantum driven dissipative system. For the traffic flow system we focus on properties of the steady flow. For the quantum driven dissipative system, we discuss the generating mechanism of the steady flow. The steady flow appearing in the far-from-equilibrium state, either classical or quantal, is the central issue of this thesis.

A traffic flow system exhibiting steady vehicular flow is an example of macroscopic nonequilibrium systems that have the nonequilibrium steady state. Physically, the system can be identified as a nonequilibrium system of particles with nonlinear interactions. Many interesting phenomena exist, which have significance both in physics and in civil engineering.

In Part I we deal with the one-dimensional traffic flow with computer simulations; Chapter 1 and 2 are devoted to introduction of the one-dimensional traffic flow including its properties and historical review of previous studies.

In Chap. 3, we investigate effects of a bottleneck in an one-dimensional vehicular flow using a cellular automaton (CA) model with a blockage site which transmits cars stochastically. We find three different phases with increasing car concentration. Besides a free flow phase and a jam flow phase, which also exist in the CA model without the blockage, a mixed phase of these two appears at intermediate concentration with clear phase boundaries. This mixed phase, where cars pile up behind the blockage to form a jam region, is characterized by a constant flow. In the thermodynamic limit, we obtain analytical expressions of several characteristic quantities such as an average velocity and an average flow in terms of the car density and the transmission rate at the blockage. These characteristic quantities depend strongly on the system size at the transition points; We analyze these finite size effects based on the computer simulation with the finite-size scaling method.

In Chap. 4, we introduce new concept of traffic flow modeling based on the coupled-map lattice. After the general modeling scheme is discussed, an explicit model is described. By numerical simulations the model is found to reproduce several phenomena which are observed in the real traffic flow. A relationship between flow and concentration of vehicles obtained by the simulation shows clear occurrence of the jamming transition. In addition, in the free flow phase, the power spectrum of temporal density fluctuations at a local section of the road exhibits a power law, $1/f^{1.8}$, where f is the frequency. Such power law is observed in the real traffic flow. The distribution of a headway distance h also follows a power law, $1/h^{3.0}$. The power-law fluctuations are destroyed by the occurrence of a traffic jam above the jamming transition concentration. We find that, near the transition concentration, the traffic jams propagate with a variety of velocities. The informational entropy of the traffic flow becomes a maximum at the transition concentration. Moreover, the relationship between flow and concentration obtained by *local* measurements shows clear double-valued behavior near the critical concentration. From these properties, we can say that the traffic flow is maximally complex near the critical concentration.

Part II is devoted to investigation of the quantum driven dissipative system. We focus on a quantum ratchet system which is a one-dimensional quantum system consisting of an asymmetric periodic potential and particles influenced by the potential. These particles show directional motion and keep steady current in their quantum nonequilibrium steady state, when thermal relaxation and external driving exist. Properties of the system and the current generating mechanism are discussed in this part.

Chapter 5 gives general introduction of classical and quantum ratchet systems. In Chap. 6, we consider treatment of time-dependent quantum dissipative systems based on the projection method. After deriving a fundamental equation describing the dynamics of a density operator, we briefly mention its physical meanings. In Chap. 7 the concept of classical ratchets is extended to the system governed by quantum mechanics. As a specific example of the quantum ratchet, we study a tight-binding model with an asymmetric periodic potential contacting with a heat bath under an external-oscillating field. The dynamics of a density operator of this system is studied numerically using the quantum dissipative Liouville equation. The finite net current is found in the nonequilibrium steady state, which originates from purely quantum mechanical effects. The direction of the current varies with parameters, in contrast with the classical thermal ratchets. We find that the current-generating mechanism essentially depends on dynamical effects; Quantum resonance causes the finite net currents.

Acknowledgments

The author is grateful to Y. Akutsu, M. Kikuchi, S. Miyashita, H. Matsukawa, G. Tatara, N. Ito, M. Bando, K. Hasebe, T. Nagao, H. Ozaki, A. Schadschneider, Y. Sugiyama, S. Tadaki, M. Takayasu, and K. Tokita for valuable discussions. He also thanks the members of the condensed matter theory group of Graduate School of Science, Osaka University for valuable discussions. Numerical calculations were partly done by Fujitsu VPP 500 in the Institute for Solid State Physics, the University of Tokyo and NEC SX-3/14R in the computer center of Osaka University.

Contents

I Classical Nonequilibrium Flow 11

1 Introduction to Traffic Flow 13
1.1 Introduction 13
1.2 Properties of Real Traffic Flow 17
1.2.1 Introduction to Traffic Terminology 17
1.2.2 Fundamental Diagram 19
1.2.3 Density Fluctuations 25
1.2.4 Miscellaneous 28

2 Traffic Flow Models 33
2.1 Macroscopic Modeling 33
2.1.1 Fluid Dynamical Models 33
2.1.2 Stochastic Models 42
2.2 Microscopic Modeling 45
2.2.1 Car-following Models 45
2.2.2 Cellular Automaton Models 50

3 Dynamical Phase Transition Caused by Bottleneck 57
3.1 Introduction 57
3.2 Cellular Automaton Modeling 58
3.3 Results 60
3.3.1 Simulation 60
3.3.2 Thermodynamic Limit 61
3.3.3 Finite-Size Scaling 70
3.4 Summary and Discussion 73

4 Coupled-Map Modeling of Traffic Flow 77
4.1 Introduction 77
4.2 Coupled-Map Traffic Flow Model 78
4.2.1 Concept 78
4.2.2 Model 80
4.2.3 Basic Results 85
4.3 Power-Law Density Fluctuations 90
4.4 Shape of Fundamental Diagram 94
4.5 Entropy of Traffic Flow 100
4.6 Summary 102

II Quantum Nonequilibrium Flow 113

5 Introduction to Dynamics of Ratchet Systems 115
5.1 Introduction 115
5.2 Classical Ratchets 119
5.3 Semi-classical Treatment of Quantum Ratchets 126

6 Numerical Treatment 131
6.1 Projection Method 131
6.1.1 Quantum Driven Dissipative Liouville Equation 131
6.1.2 Physical Interpretation 137
6.2 Steady Periodic States 144
6.3 Heat Bath and Dissipation Kernels 147
6.3.1 Thermal Correlation Function and Model of Heat Bath 147
6.3.2 Dissipation Kernels for Factorized Interaction 151

7 Resonance Current in Quantum Ratchet Systems 155
7.1 Model 155
7.2 Linear Response Theory 158
7.3 Numerical Calculation and Results 159
7.3.1 Dynamics in Steady Periodic State 163
7.3.2 Parameter Dependence 164

7.4 Resonating Behavior: Dependence on Period 174
7.5 Simplified Ratchet Models 179
7.5.1 Ratchet-like Three-Level Model 179
7.5.2 Delta-Kicked Ratchet Model 183
7.6 Summary 192

A Path-Integral Treatment 195

B TC and TCL equations 201

C Numerical Routines 209
C.1 Exponential Integrals 209

Part I

Classical Nonequilibrium Flow

Chapter 1

Introduction to Traffic Flow

1.1 Introduction

Traffic flow is one example of nonequilibrium steady flow appearing in the macroscopic world; In a freeway, vehicles travel from a tollgate to another tollgate, so that flow of vehicle is generated. At the point far from the tollgate, the traffic stream is fully developed and close to steady flow; Traffic streams may become ideal flow there. From the viewpoint of physics, the traffic flow is regarded as the nonequilibrium steady flow of interacting particles in its far-from-equilibrium state. Thus many interesting and universal phenomena will be found in the traffic flow. In the following sections we see some features of traffic flow.

There are features peculiar to the traffic flow: The concept of thermodynamic limits is hardly justifiable, in contrast to the case of other physical system in which nonequilibrium flow is generated; If we stick to "vehicular traffic", the earth restricts maximal length of road as about 40000 km. When an average length of vehicle is about 5 m, the geometrical limit restricts the largest number of vehicles as up to 8 million (about 10^6). This number is much less than the Avogadro number $\sim 10^{23}$. Even though the road connecting between the moon and the earth might be constructed in the future, the limit is up to 10^8. This means that the finite size effects are crucial for real traffic phenomena and relaxation processes play quite important roles in them. The other feature concerns that a vehicle is controlled by human in addition to laws of physics. Thus human responses such as, sudden braking, velocity fluctuation, which may not be periodic but will be chaotic, can affect the behavior of individual motion and the global traffic stream. Moreover each vehicle, or each driver to be precise, has a manner for acceleration and deceleration, preferred velocity, origin and destination that are important in network traffic flow like urban traffic, and so on. These conscious or unconscious controls also influence the traffic phenomena.

In traffic flow, there are a lot of interesting phenomena that attract much attention: Especially a traffic jam is widely recognized [50, 56]; It is sometimes identified as a dense region of traffic stream. Occurrence of traffic jam can be regarded as a dynamical phase transition in nonequilibrium systems. This transition is controlled by concentration of vehicles; As the concentration increases and exceeds some critical concentration, the transition occurs. In addition, the transition is characterized by the values of flow rate of vehicles; We know that the traffic jams suppress the flow rate. Thus the jamming transition point is identified by the concentration corresponding to the maximal flow. The transition and its properties are observed in a real road, for instance, in a highway. Thus the traffic flow is one of good examples which show dynamical phase transitions in the macroscopic world.

A traffic jam itself is also interesting [50]. Traffic jams can be regarded as an extreme case of a density wave in the system. In real traffic flow, it is observed that the traffic jams propagate upstream with clear boundaries, so that we can also consider it as a shock wave in the traffic stream. Moreover such traffic jams have a finite lifetime; Sometimes they are formed spontaneously and sometimes they are destroyed. The reasons of creation and disappearance are still unclear. Other types of density waves are also recognized in the real traffic flow: For example, car bunching is observed, which is sometimes called *a platoon*; A platoon is a single cluster of vehicles and every vehicle consisting of the platoon travels with some definite velocity and headway. The formation of platoon is due to the distribution of driver's preferred velocities; If a slow vehicle runs in front of a group of faster vehicles, the faster vehicles will queue up behind the slow vehicle and a platoon will be formed. The above-mentioned density waves are, in a sense, large-scale density waves. More small-scale and weak density waves [50], which propagate downstream, are also frequency observed inside the freely flowing streams. Such weak density wave causes temporal density fluctuations at spatially fixed points. All types of the density waves can be generated spontaneously without clear causes, so that these properties are essentially embedded in the dynamics of traffic flow.

Weak density waves induce the power-law temporal density fluctuations; In 1976 Musha and Higuchi found that a power spectral density of the real traffic flow obeys power law in low frequency regime [63, 64]. Similar power law phenomena are also found in other nonequilibrium systems such as pipe flow of granular materials experimentally and theoretically [13, 35, 91, 102]. This similarity reminds us of the term *universality*.

So far we have assumed one-dimensional traffic flow. Actual traffic flow may be higher dimensional; Urban traffic flow, which is considered to be two-dimensional traffic flow, is familiar to us. There are lots of interesting phenomena in the urban traffic flow. There, the situation is quite different from the one-dimensional flow: First, crossings of roads must be taken into account; In one-dimensional road it is not necessary. But, in the two-dimensional case, they give large influences to the dynamics of vehicles. Most important and strong influences are effects of queuing; The queue does not appear in homogeneous one-dimensional road. In the traffic network, however, the queue is naturally formed at the crossing. The queuing effects cause bottlenecks, so that the traffic flow is strongly disturbed at the crossing. This effect influences the traffic flow not stationary but dynamically, because the queue is dynamically generated according to volume of traffic flow and capacity of crossing. Second, origin and destination (OD) of each vehicle should be taken into account in the network flow. OD is one of the basic quantities of the vehicle traveling in the network; Once the OD is determined, the drivers will choose a route according to the OD. In one-dimensional traffic flow OD is trivial. But, in the two-dimensional traffic, existence of OD affects the traffic streams; For instance, formation of queues is directly influenced by the routing. The last one is existence of flexibility of selection of routes connecting OD. This flexibility makes a problem of controlling the traffic network difficult; The problem is same as one of finding a set of routes corresponding to the individual ODs and, moreover, these routes must give a minimal travel time of each vehicles or a minimal averaged travel time for all vehicles. This problem resembles the combinatorial optimization problems such as, a ground-state-finding problem of spin glass models [23], and a traveling salesman problem. In the optimized controlling of the traffic network, a travel time of particular vehicle or an averaged travel time of all vehicles is taken as a cost function under the conditions of fixed ODs and topology of networks. The cost function has a lot of local minima as a function of a set of routing; If we chose the best route for our own vehicle, this choice is certainly not the best for others; If everybody selects their best routes and if their ODs are identical, large traffic jams would occur. In such situation finding the routing set corresponding to the global minima is very difficult.

Phenomena in the traffic flow is related with many other systems as was mentioned above; For instance, pipe flow of granular materials [13, 35, 91, 102], asymmetric simple exclusion process of a particle system [38, 39, 57–59], pedestrian dynamics [30], combinatorial optimization problems [23], and so on. In this part we study several properties in the traffic flow, especially one dimensional traffic flow, using computer simulations.

1.2 Properties of Real Traffic Flow

1.2.1 Introduction to Traffic Terminology

In this section, we briefly review properties of real traffic flow. First, terminology used in traffic flow is introduced. Three quantities are fundamental in describing states of traffic streams [56]:

Volume and Flow: They are defined by number of vehicles passing a fixed measuring point x during some time interval ΔT; Let us define the stream function $\Phi_x(t)$ as the accumulated vehicle count at the observed point x during a time interval $(0, t)$; Then the volume Q is define as follows:

$$Q = \frac{\Phi_x(\Delta T)}{\Delta T} . \tag{1.1}$$

Precisely speaking, Q has to be called "ΔT time volume Q". In the above expression we have assumed a steady traffic stream. The statement of traffic volume is not complete without a statement of the time interval over which the vehicles were counted. Thus we usually use the flow q, which is volume per unit time, in stead of Q:

$$q = \lim_{\Delta T \to 0} \frac{\Phi_x(\Delta T)}{\Delta T} . \tag{1.2}$$

In general, the flow is a function of time and position.

Density or Concentration: From the definition of $\Phi_x(t)$, it is clear that

$$N(x, x + \Delta x; t) = \Phi_{x+\Delta x}(t) - \Phi_x(t) \tag{1.3}$$

represents a number of vehicles which are found in a spatial interval $(x, x+\Delta x)$ at time t. This value is called a traffic density. This statement must be accompanied by a statement of the distance Δx, too. Thus the limit

$$\rho = \lim_{\Delta x \to 0} \frac{N(x, x + \Delta x; t)}{\Delta x} , \tag{1.4}$$

which represents the value of density per unit length, is used as the traffic concentration. It also is the function of time and position.

Velocity: There are two types of definition of velocity: space-averaged velocity v_s and time-averaged velocity v_t. The former is defined as follows:

$$v_s = \frac{1}{M} \sum_{i}^{M} v_i , \tag{1.5}$$

where M and v_i are a number of vehicles in some spatial region and a velocity of each vehicle, respectively. If we introduce a *instantaneous* probability distribution function $g_s(v)dv$ of velocity, which represents existence probability of vehicles having the velocity in the range $[v, v + dv]$ in some spatial region at time t, we can write the space-averaged velocity as

$$v_s = \int_0^\infty v g_s(v) dv \ . \tag{1.6}$$

The time-averaged velocity is defined as follows:

$$v_t = \frac{1}{M'} \sum_i^{M'} v_i \ , \tag{1.7}$$

where M' and v_i are a number of vehicles passing some fixed measuring point during some time interval and a velocity of each vehicle, respectively. It is also expressed in an integral form using the *temporal* probability distribution function $g_t(v)dv$ of the velocity at fixed measuring point during some time range:

$$v_t = \int_0^\infty v g_t(v) dv \ . \tag{1.8}$$

Flow and space-averaged velocity are not independent of each other; Consider a single lane circuit of length L with N vehicles. When the vehicles is maneuvered to maintain their velocity near their preferred velocity, the traffic flow becomes almost steady. Using the instantaneous probability distribution function of velocity $g_s(v)dv$, we write the density of vehicles with velocity v as $d\rho(v) = \rho g_s(v)dv$, where ρ is the traffic density defined as $\rho = N/L$. A vehicle traveling with velocity v requires the time interval $\Delta t = L/v$ for going around the circuit once. Thus, at the measuring point, $N d\rho(v)$ vehicles pass in the interval Δt. Then the contribution to Δt volume of the vehicles with velocity v is $N d\rho(v)$. Denoting the contribution of vehicles with velocity v to the flow as $dq(v)$, we obtain

$$dq(v) = \frac{N g_s(v) dv}{\Delta t} = v d\rho(v) \ . \tag{1.9}$$

The flow q is obtained by integrating the above expression:

$$q = \int_0^\infty dq(v) = \rho \int_0^\infty v g_s(v) dv = \rho v_s \tag{1.10}$$

This means that q and ρ are related through the space-averaged velocity v_s.

The space-averaged velocity is related with the time-averaged velocity; Consider the above situation again. At the fixed measuring point, the contribution of the vehicle with velocity v to flow q, which is equivalent to $dq(v)$, can also be expressed as

$$dq(v) = q g_t(v) dv \tag{1.11}$$

with the temporal probability distribution function $g_t(v)dv$. Then we get

$$g_t(v)dv = \frac{dq(v)}{q} = \frac{\rho v g_s(v) dv}{\rho v_s} = \frac{v}{v_s} g_s(v) dv \ , \tag{1.12}$$

and the time-averaged velocity v_t is

$$v_t = \int_0^\infty v g_t(v) dv = \frac{1}{v_s} \int_0^\infty v^2 g_s(v) dv \ . \tag{1.13}$$

Substituting the variance of velocity $\sigma_s^2 = (\int_0^\infty v^2 g_s(v) dv) - v_s^2$, we obtain

$$v_t = v_s + \frac{\sigma_s^2}{v_s} \ . \tag{1.14}$$

If the vehicles are ideal, that is, characteristic properties such as the preferred velocity are identical, and the traffic stream is steady, then the variance σ_s^2 is zero. In this case time-averaged velocity and space-averaged velocity are equivalent. In general, however, these two averaged velocities are not identical.

1.2.2 Fundamental Diagram

A diagram representing relationship between the flow and the concentration is called "fundamental diagram" or "q-k diagram" in traffic engineering. The fundamental diagram shows characteristic feature of the road on which data are taken; Typical fundamental diagrams are shown in Figs. 1.1 and 1.2 [28, 50], both of which were actually observed in roads in Japan and Canada. We can recognize that the essential behavior of the traffic stream does not depend on details of the system like properties of vehicles, condition of roads, and drivers' skills. The behavior of fundamental diagram may be *universal* for the traffic stream.

As shown in Figs. 1.1 and 1.2, typical fundamental diagram has a single peak. This peak separates into two phases, the free flow phase and the congested flow phase. The

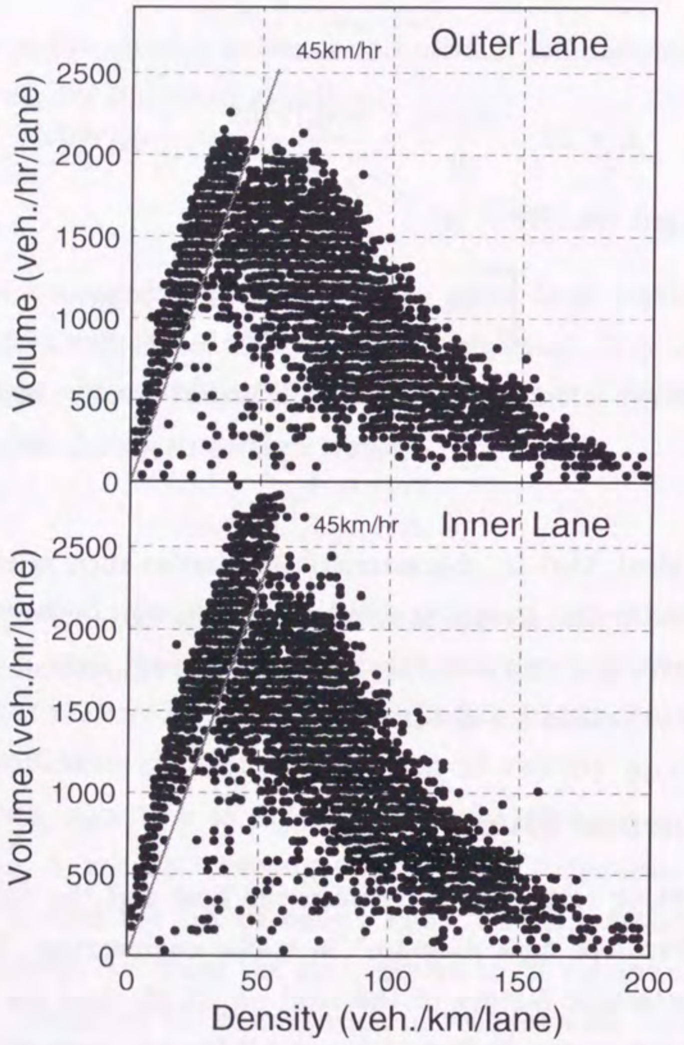

Figure 1.1: Observational result of fundamental diagram taken from Ref. [50] (Japan).

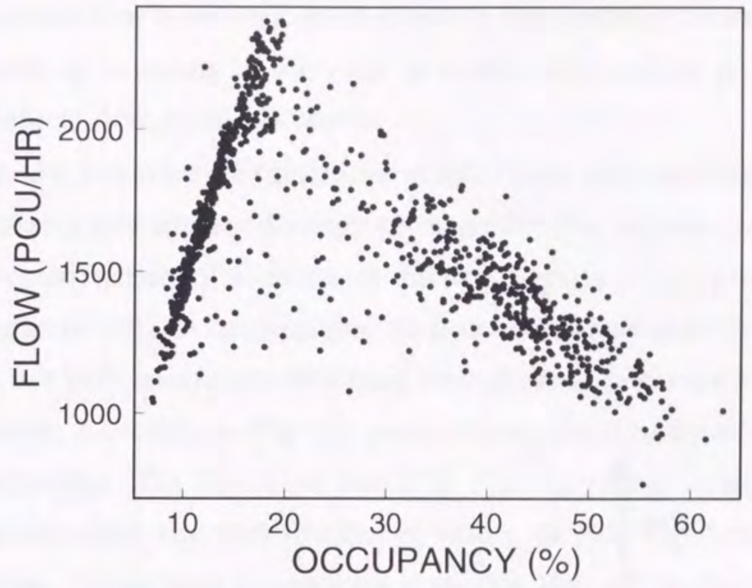

Figure 1.2: Observational result of fundamental diagram taken from Ref. [28] (Canada).

concentration corresponding to the peak can be regarded as the transition point or the critical concentration. In the concentration lower than the critical concentration, the flow increases linearly with concentrations and, in the higher concentration. On the other hand, above the critical concentration, the flow decreases as the concentration increases, and, finally it seems to vanish. The reason why it behaves like that is clear; In the lower concentration regime, traffic stream moves smoothly. Then vehicles are free from influence of other vehicles and the vehicles can travel at their own preferred velocity. Thus the average velocity is independent of the concentration, so that the flow, which is defined as the average velocity times the concentration, is proportional to the concentration. In the higher concentration regime, the average velocity is not independent of the concentration; It decreases as increasing concentration. In the case of traffic stream, velocity decreases faster than the increase of the concentration. Therefore the flow decreases as increasing the concentration. This situation is owing to the time delay in the response of vehicles or drivers to the action of the preceding vehicles. Schematically a fundamental diagram behaves like Fig. 1.3.

As was mentioned above, the fundamental diagram represents characteristic features of the road on which data are taken; For example, as shown in Fig. 1.1, vehicles travel at velocity $\sim 45\mathrm{km/h}$ in the free flow phase. This speed is close to the legal velocity of

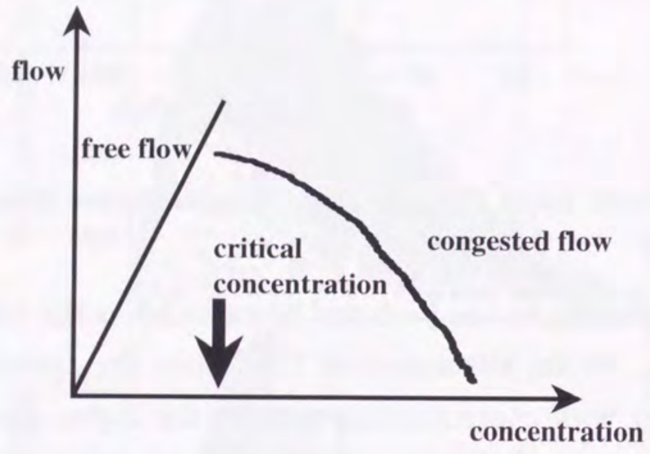

Figure 1.3: Schematic Fundamental Diagram. It has single peak. Corresponding concentration is a critical concentration and corresponding value of flow is called a capacity. At concentration lower than the critical concentration, traffic stream is in a free flow phase and, at higher concentration, it is in a congested flow phase. Behavior of flow near the critical concentration has not been clearly understood.

the road. The maximal flow is an important quantity representing characteristic features of roads. It is called as *capacity* of the road in traffic engineering; A road with higher capacity can let vehicle flow more efficiently.

Understanding the behavior of the traffic stream near the capacity is important in both traffic engineering and nonequilibrium physics; For the engineering it is crucial for construction or reconstruction of a road and, for the physics, it is important for understanding the features of critical nonequilibrium flow. But the behavior near the critical concentration has not been clearly understood; Complicated behavior has been observed in real traffic streams; Actually, in Fig. 1.1 (outer lane), flow changes continuously near the critical concentration. On the other hand, in Fig. 1.1 (inner lane), overhanging of flow is seen; It means that the distribution of values of flow has two peaks near the critical concentration. Other type of behavior is seen in Fig. 1.2; In this case, flow shows discontinuity near the critical concentration. Canadian traffic engineers, Hall *et al.*, classified feasible shapes of flow near the critical concentration into four types (see Fig. 1.4) according to shapes of functions fitting data well [28]:

- **Reversed λ:** The flow takes two values in a finite range of concentration (Fig. 1.1 (inner lane)). Then the distribution of flow has two peaks in the same range.

- **Gap:** The flow has a discontinuity (gap) at the critical concentration (Fig. 1.2). For explaining traffic data, this type of discontinuous functions are sometimes preferred [9, 21, 80].

- **Smooth:** The flow is continuous and continuously differentiable function of the concentration (Fig. 1.1(outer lane)); No clear phase transition is expected in this case.

- **Inverted V:** The flow is continuous, but not continuously differentiable function at the critical concentration.

Among these possibilities, they concluded that the inverted V shape is suitable for representing the fundamental diagram; Appearance of other types are just due to lack of observational data. Their argument is based on assumption that the traffic current is a one-valued function of the concentration, which is intuitive view accepted among traffic

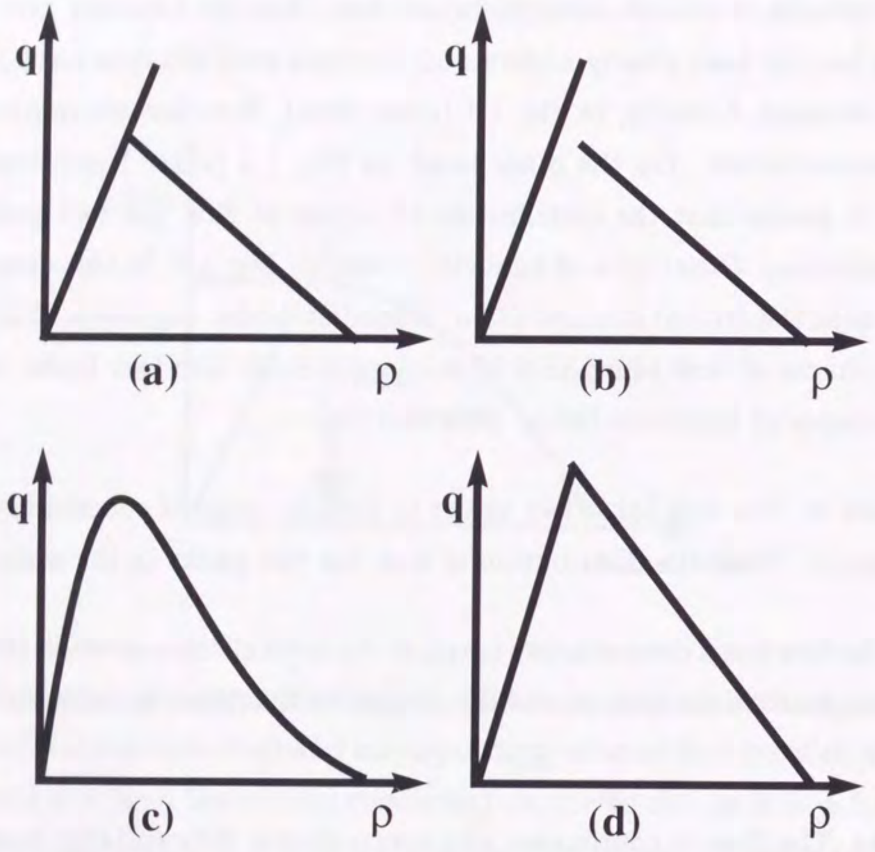

Figure 1.4: Feasible four shapes of fundamental diagram: (a) reversed λ shape; (b) discontinuous type; (c) continuous and continuously differentiable type; (d) continuous but not continuously differentiable type.

engineers. Moreover they empirically explained why the inverted V shape was suitable, using the catastrophe theory [100].

Their argument is as follows [27, 74, 75]: They assume that the traffic data, flow, concentration, and velocity are on a catastrophe manifold, exactly speaking, a cusp catastrophe manifold. Cusp catastrophe theory offers a way to explain systems in which one of the variables exhibits discontinuous behavior, while others are showing only smooth and continuous change. Figure 1.5 shows schematic picture how the discontinuous behavior appears in traffic data based on the catastrophe theory; If traffic data are on the cusp catastrophe manifold, which is folded in some region, the discontinuity appears in the flow-concentration curve. This theory clearly gives the origin of discontinuity. The real data seem to be on the cups catastrophe manifold (see Fig. 1.6). But this explanation is empirical; The reason why the data are on the cusp catastrophe manifold is not explained.

From physicist's point of view, if a jamming transition is actually a dynamical phase transition, fluctuation grows near the critical concentration, and causes such behavior. However, the detail is still unclear.

1.2.3 Density Fluctuations

In 1976 Musha and Higuchi observed temporal density fluctuations of a traffic stream on the Tomei Expressway in Japan. They found that power spectral density of the density fluctuations obeyed a power law [63, 64]; To avoid disturbance from various extrinsic sources such as traffic signals, or traffic jams, the observations were made at the expressway. They recorded transit times of vehicles at a three-lane part of the expressway, from the bridge over them. They calculated the power spectral density from observed data and found a white power spectrum in high frequency regime and power-law power spectrum $1/f^{\alpha}$ (f is frequency) in low frequency regime. Their result is shown in Fig. 1.7. In addition, they estimated the exponent α as $\alpha = 1$ by fitting the data, while a phenomenological analysis on the same data using Burgers equation gave $\alpha = 1.4$.

Recently another observation was made by P. Wagner and J. Peinke [101]. They collected the traffic data by a loop detector over more than one week and analyzed them based on the multi-scaling concept (e.g. [62]), which is used in the analysis of

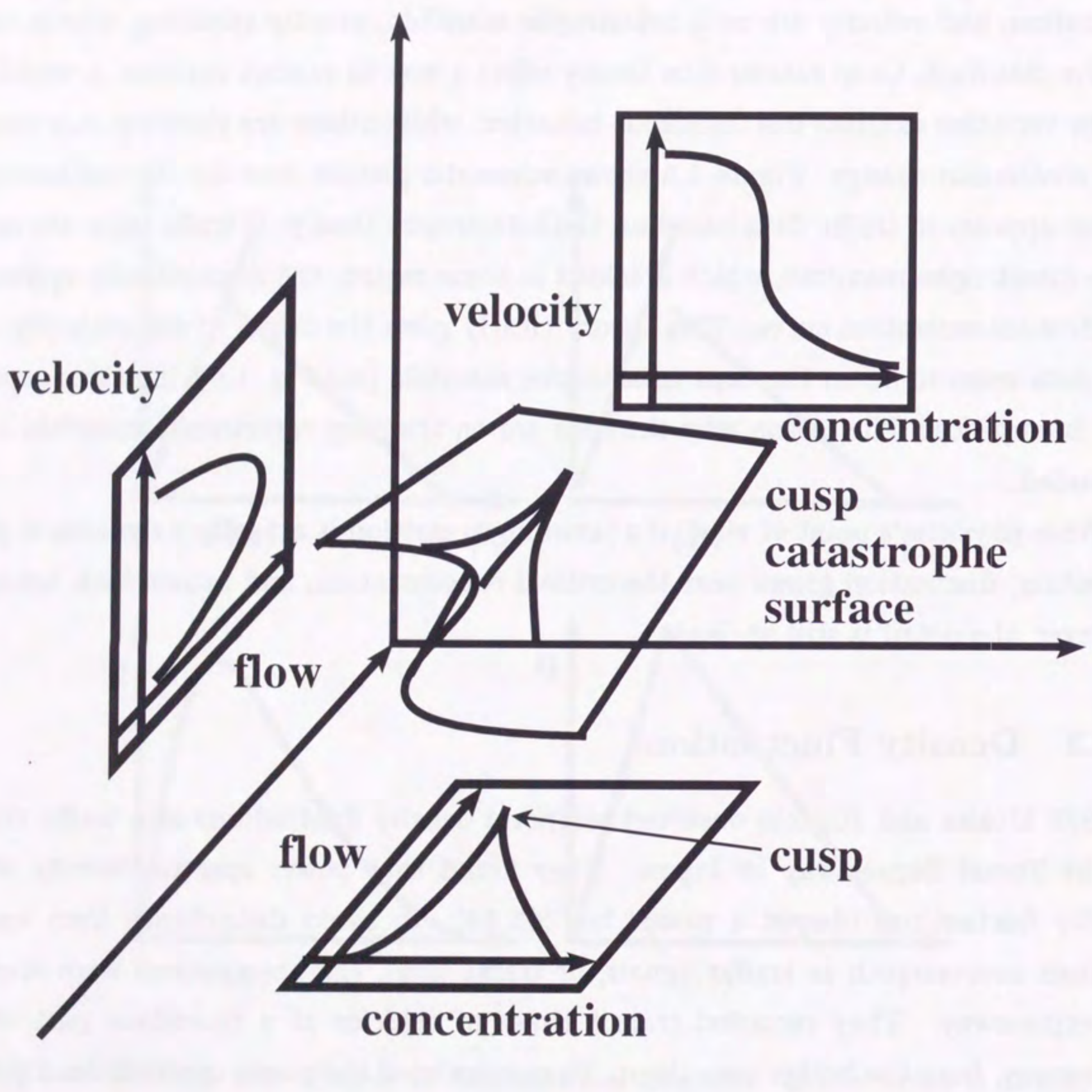

Figure 1.5: Schematic picture of some relationship of traffic flow data based on the catastrophe theory. Folded surface embedded into three-dimensional Euclidean space shown in center is a cusp catastrophe manifold. Assuming that traffic data are on the catastrophe manifold, we can explain three different behavior: discontinuous, continuous, and continuous of curves.

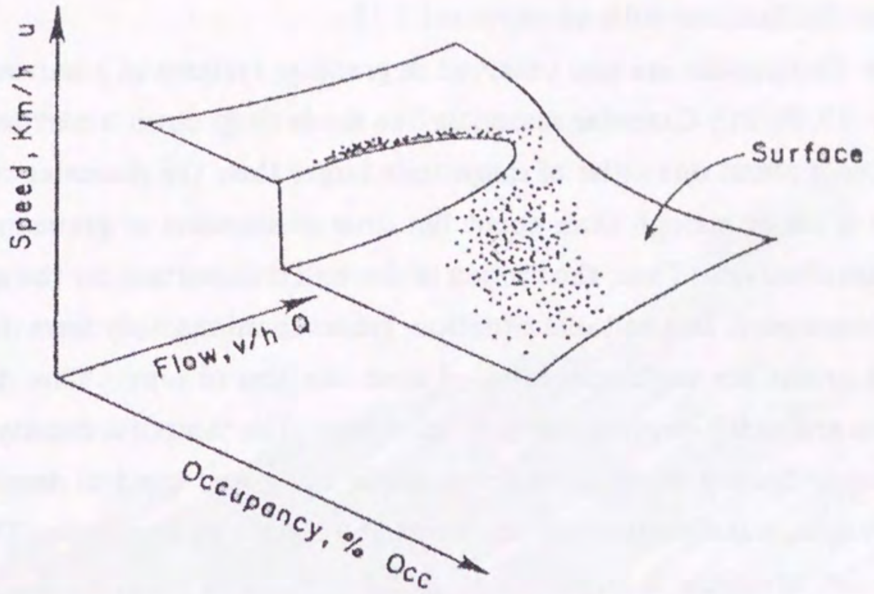

Figure 1.6: Three dimensional plot of real traffic data taken from Ref. [75]. Data are same data plotted in Fig. 1.2.

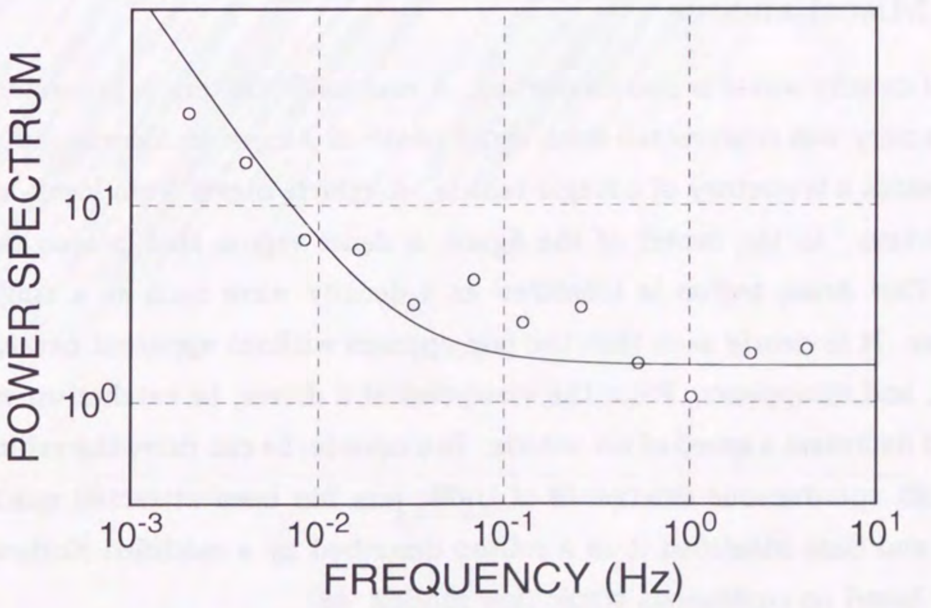

Figure 1.7: Power spectral density of real traffic flow taken from Ref. [64]. Solid line is a analytic result based on Burgers equations and fitting: $S(f) = 0.0084/f^{1.4} + 1.572$.

turbulent flow. They concluded that the traffic stream has multi-scaling properties and the power-law fluctuations with an exponent 1.14.

Power-law fluctuations are also observed in granular systems in a narrow channel experimentally [13, 35, 91]; Granular materials like sands drop down a narrow pipe, whose inner diameter is about one order of magnitude larger than the diameter of granules. If the diameter is larger enough than about ten time of diameter of grains, no power-law phenomena are observed. Thus, the friction of the wall is important for the appearance of power-law phenomena. In a suitable situation, grains spontaneously form density waves, although the grains are uniformly injected from the top of pipe. This density waves develop as the grains fall down to the bottom of pipe. The temporal density fluctuations of well-developed density waves show power-law in the power spectral density, when the local concentration is instantaneously measured at a certain point of pipe. The exponents of the power-law spectrum is estimated as about $\alpha = 1 \sim 1.5$ experimentally [35]. Some theoretical results and numerical simulations support $\alpha = 4/3$ [29, 82, 83]. These phenomena seems to provide evidence for existence of universality class of nonequilibrium one-dimensional flow of interacting "particles".

1.2.4 Miscellaneous

Pattern of density waves is also interesting. A real traffic pattern is presented in Fig. 1.8; This trajectory was constructed from aerial photo at American freeway [56]. Each black line represents a trajectory of a single vehicle. A vehicle moves from lower-left to upper-right direction. In the center of the figure, a dense region that propagates upstream is seen. This dense region is identified as a density wave such as a traffic jam or a shock wave. It is clearly seen that the jam appears without apparent cause, propagates upstream, and disappears. From the viewpoint of a driver, he catches up with the jam region and decreases a speed of his vehicle. In a minute, he can drive the vehicle smoothly again. Such spontaneous emergence of traffic jam has been attracted much attention; Komatsu and Sasa identified it as a soliton described by a modified Korteweg-de Vries equations based on continuous traffic flow models [48].

There are other interesting problems, although we did not mention in detail; One is the problem whether the traffic stream is chaotic. Experimentally time series analysis of urban road in traffic network shows a slight evidence of chaotic behavior [16]. But

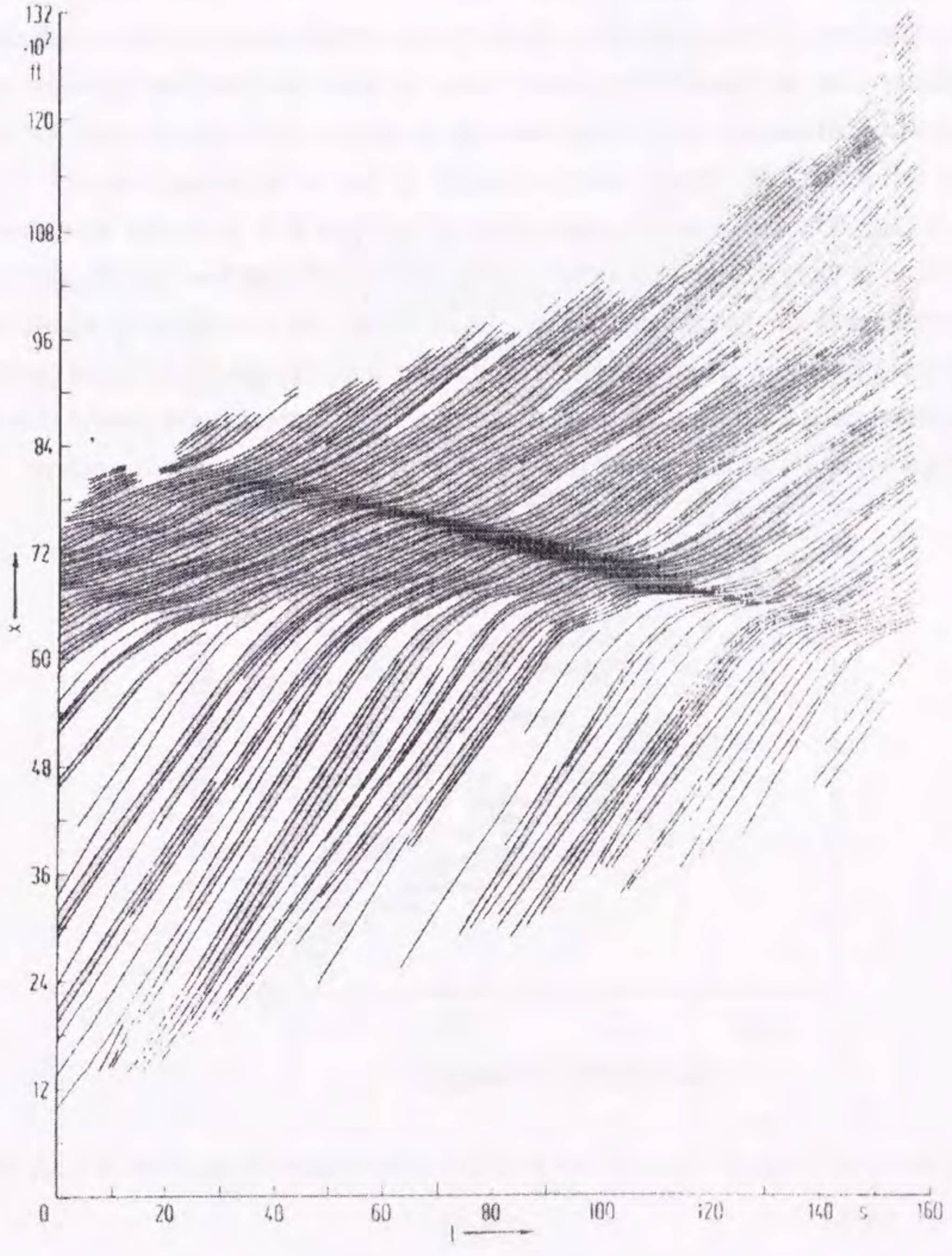

Figure 1.8: Actual traffic pattern taken form Ref. [56]. This was constructed from aerial photo at American freeway.

we cannot conclude that the traffic stream is chaotic at present. Other way of studying the chaotic behavior is to observe a trajectory of a tracer vehicle in a headway-velocity plane, so called car-following behavior. If the tracer vehicle is in a uniform traffic stream, the trajectory may be bounded in a small area, because the headway distance and the velocity are almost steady. If the traffic stream is chaotic, the trajectory will behave like a strange attractor. One experimental example of the car-following behavior is shown in Fig. 1.9 [50]; The behavior of congested flow and free flow is clearly separated; The bunch of dots in the right side of figure corresponds to the free flow branch and another bunch corresponds to the congested flow. In addition, the car-following behavior does not draw a simple loop. Therefore, the results may support the evidence of chaos. But the experiment does not reflect the pure dynamics of traffic stream, because it is observed in a strongly noisy situation. Thus, the chaos in a traffic stream is still unclear.

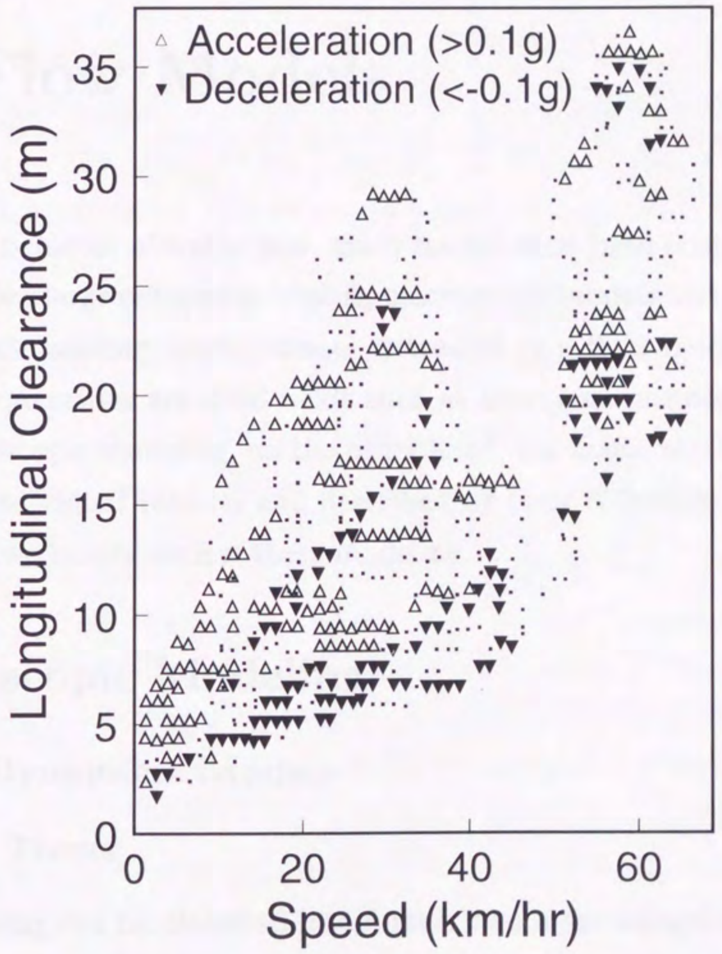

Figure 1.9: Results of experiments of following behavior taken from Ref. [50].

Chapter 2

Traffic Flow Models

To understand the behavior of traffic flow, many models have been proposed so far. They are classified into two large categories, that is, macroscopic models and microscopic ones; In the macroscopic modeling, traffic stream is treated as a fluid mechanical object, so that fundamental quantities are local fields such as local concentration, local flow and so on. In the microscopic modeling, on the other hand, the traffic stream is decomposed into dynamics of individual vehicles and described by their collective dynamics. In the following sections, we briefly review these modeling.

2.1 Macroscopic Modeling

2.1.1 Fluid Dynamical Models

Kinematic Wave Theory

Macroscopic modeling can be classified into further two more categories: Fluid dynamical models and stochastic models. One of the simplest approaches to fluid dynamical models is a kinematic wave treatment [55, 60, 61]. Kinematic wave theory can be applied to any one-dimensional flow as well as one-dimensional traffic flow whenever the local relationship between the concentration and the flow is given. The model is "kinematic", because it is only described by a continuity equation, in contrast to the case of "dynamical" waves that require the additional equation determining the motion.

In 1955, Lighthill and Whitham have given theoretical framework of the kinematic wave [60, 61]. They applied the kinematic wave theory to the different types of one-dimensional flow, flood motion in long rivers and a traffic stream on long crowded roads. Richards have also developed the kinematic wave theory for a traffic stream independently, although he did not call it "kinematic wave" explicitly [89].

In a kinematic wave approach two fundamental equations appear; The one is the continuity equation as follows:

$$\frac{\partial \rho}{\partial t} + \frac{\partial q}{\partial x} = 0 \ , \tag{2.1}$$

where $\rho(x,t), q(x,t)$ are local fields of the concentration and the flow both of which are functions of position x and time t, respectively. Another one is a relationship between the flow and the concentration, that is, a fundamental diagram, $q(x) = f(\rho(x))$. Introducing a quantity $c(x,\rho) = (\partial q/\partial \rho)_{x:\mathrm{fixed}}$, we can rewrite the continuity equation as

$$\frac{\partial \rho}{\partial t} + c(x,\rho)\frac{\partial \rho}{\partial x} = 0 \ . \tag{2.2}$$

The flow q is also represented as $q(x) = v(x)\rho(x)$ with a velocity $v(x)$. Then

$$c(x,\rho) = v(x) + \rho(x)\frac{dv}{d\rho} \ . \tag{2.3}$$

Equation (2.2) describes a motion of waves with velocity $c(x,\rho)$. Waves which obey the above equation are called "kinematic waves" , and $c(x,\rho)$ is called a velocity of the kinematic wave. Equation (2.3) gives us a relation between the velocity of kinematic waves and the fundamental diagram; Graphically $c(x,\rho)$ represents a slope of a tangent line of the fundamental diagram at concentration ρ (see Fig. 2.1). Therefore the kinematic wave theory allows the density waves which propagate upstream in the congested flow phase. It agrees with the observed results.

Kinematic wave theory can also describe the velocity of a shock front which separates a traffic stream into two regions with different concentrations; Consider a shock front between the region I and the region II. The concentration and the flow in the region I (II) are defined as ρ_{I} and q_{I} (ρ_{II} and q_{II}), respectively. Conservation of number of vehicles going through the shock front with velocity u gives

$$q_{\mathrm{I}} = q_{\mathrm{II}} - (\rho_{\mathrm{II}} - \rho_{\mathrm{I}})u \ . \tag{2.4}$$

Then the velocity of the shock front u is

$$u = \frac{q_{\mathrm{I}} - q_{\mathrm{II}}}{\rho_{\mathrm{I}} - \rho_{\mathrm{II}}} \ ; \tag{2.5}$$

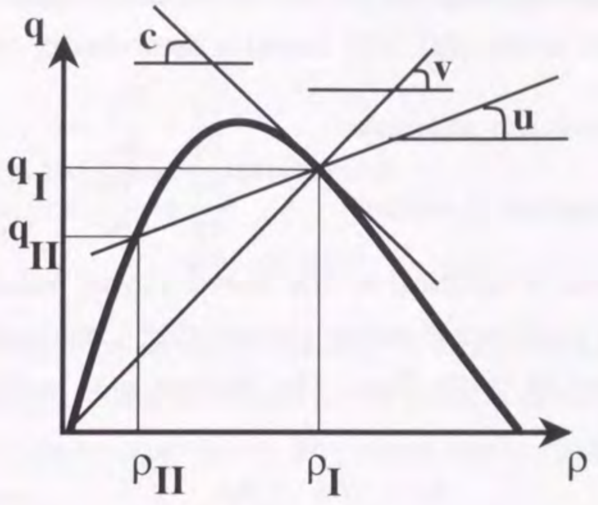

Figure 2.1: Relationship among flow q , velocity of density waves c, average velocity of vehicles v, velocity of shock waves u and concentration ρ in kinematic wave theory.

Graphically the velocity of the shock front is a slope of line connecting $(\rho_{\mathrm{I}}, q_{\mathrm{I}})$ and $(\rho_{\mathrm{II}}, q_{\mathrm{II}})$ (see Fig. 2.1). Recently the system with many interacting shock fronts have been simulated numerically based on the kinematic wave theory [55].

General Fluid Dynamical Models

Kinematic wave models are very simple and easily treated. But they can not predict macroscopic features of traffic stream such as the form of fundamental diagram, because it requires the fundamental diagram as an initial assumption. A few years later, the fluid dynamical models accompanying the equation of motion have been proposed. To distinguish the models from the kinematic wave model, which is a kind of fluid dynamical model, we call them general fluid dynamical models. A typical equation of motion of the models are based on the one-dimensional Navier-Stokes' equation:

$$\frac{\partial v}{\partial t} + v\frac{\partial v}{\partial x} = \frac{\mu}{\rho}\frac{\partial^2 v}{\partial x^2} - \frac{1}{\rho}\frac{\partial p}{\partial x} + \frac{1}{\rho}X \ , \tag{2.6}$$

where v and ρ are the locally averaged velocity and the concentration of the vehicles, respectively, μ is viscosity, p is local pressure, and X represents the sum of interactions between vehicles. In the general fluid dynamical models, the traffic stream is described as a one-dimensional compressible flow.

In 1959, Greenberg have proposed an exactly solvable[1] model as a special case of the general fluid dynamical model [26]. The model is described by the following equations:

$$\text{a continuity equation} \qquad \frac{\partial \rho}{\partial t} + \frac{\partial q}{\partial x} = 0 \ , \tag{2.7}$$

$$\text{a equation of motion} \qquad \frac{\partial v}{\partial t} + v\frac{\partial v}{\partial x} = -\frac{c^2}{\rho}\frac{\partial \rho}{\partial x} \ . \tag{2.8}$$

The equation of motion is identical to the Navier-Stokes' equation with $\mu = X = 0$ and $p = -c^2\rho$. c is a positive parameter representing a width of velocity distribution, so called "temperature" of traffic flow. The relation $q = \rho v$ allows us to rewrite the continuity equation as

$$\frac{\partial \rho}{\partial t} + \rho\frac{\partial v}{\partial x} + v\frac{\partial \rho}{\partial x} = 0 \ . \tag{2.9}$$

Let the velocity be a function of concentration only $v = v(\rho)$. Then

$$\frac{\partial v}{\partial t} = \frac{dv}{d\rho}\frac{\partial \rho}{\partial t} \ , \tag{2.10}$$

$$\frac{\partial v}{\partial x} = \frac{dv}{d\rho}\frac{\partial \rho}{\partial x} \ . \tag{2.11}$$

After substituting the above identities into the continuity equation and the equation of motion, we obtain

$$\frac{\partial \rho}{\partial t} + \left(\rho\frac{dv}{d\rho} + v\right)\frac{\partial \rho}{\partial x} = 0 \ , \tag{2.12}$$

$$\frac{\partial \rho}{\partial t} + \left\{ v + \frac{c^2}{\rho}\left(\frac{dv}{d\rho}\right)^{-1} \right\}\frac{\partial \rho}{\partial x} = 0 \ . \tag{2.13}$$

To have a nontrivial solution for the above simultaneous equations, the determinant of the coefficients of the partial derivatives must vanish. Thus

$$\left(\frac{dv}{d\rho}\right)^2 = \frac{c^2}{\rho^2} \ . \tag{2.14}$$

Since the velocity is a monotonically decreasing function of concentration, we take negative sign of square root;

$$\frac{dv}{d\rho} = -\frac{c}{\rho} \ . \tag{2.15}$$

---

[1] In the present case "solvable" means that we can calculate a functional form of the fundamental diagram.

Integrating above equation, we get the functional form of the average velocity:

$$v(\rho) = c\ln\frac{\rho_s}{\rho} \ , \tag{2.16}$$

or the functional form of the fundamental diagram:

$$q(\rho) = c\rho\ln\frac{\rho_s}{\rho} \ , \tag{2.17}$$

where ρ_s gives maximally allowed concentration. A critical concentration is easily obtained as $\rho_s e^{-1} \sim 0.3679\rho_s$. This fundamental diagram is continuous near the critical concentration and thus has no singularity. For actual application the parameters c and ρ_s are fitting parameters.

There are more complicated general fluid dynamical models than the Greenberg model. Payne model is described by the following equation of motion [80, 81]:

$$\frac{\partial v}{\partial t} + v\frac{\partial v}{\partial x} = \frac{\tilde{v} - v}{\tau} + \frac{1}{2\tau\rho}\frac{\partial \tilde{v}}{\partial \rho}\frac{\partial \rho}{\partial x} \ , \tag{2.18}$$

where $\tilde{v}$ is an equilibrium average velocity dependent on the concentration. The first term of right hand side represents the relaxation effects of velocity. The second term of right hand side expresses the pressure term. $(\partial\tilde{v}/\partial\rho)$ is a negative function of ρ, because $\tilde{v}$ is a monotonically decreasing function of the concentration. Thus this term is similar to the pressure term of the Greenberg model, although c is independent of ρ in the Greenberg model. The parameter τ is relaxation time of velocity and typically is taken to be order of 30 sec. If the relaxation term is ignored, the model becomes similar to the Greenberg model. The Pyne model has been widely used as a good tool for describing the traffic stream; The network traffic flow has been simulated based on it for a long time [80, 81]. It has, however, difficulties in describing transients and high concentration traffic, especially when a queuing or bottleneck is simulated. Mathematically the reason of these difficulties is the lack of a second order spatial derivative in the equation of motion.

These difficulties are avoided by addition of the viscosity term. The model with the viscosity term is described by the following equation of motion:

$$\frac{\partial v}{\partial t} + v\frac{\partial v}{\partial x} = \frac{\tilde{v} - v}{\tau} - \frac{c^2}{\rho}\frac{\partial \rho}{\partial x} + \frac{\mu}{\rho}\frac{\partial^2 v}{\partial x^2} \ , \tag{2.19}$$

where τ is again relaxation time, c represents "temperature" of traffic stream, and μ is the viscosity. Note that the coefficient c is positive constant again in contrast to the Payne model.

For the above general fluid dynamical model, Kerner and Konhäuser showed that a region of high concentration and low average velocity of vehicles spontaneously appears from an initially homogeneous traffic flow [46, 47]; Consider a linear stability analysis according to them. We impose periodic boundary condition and system length is taken to be L. The boundary condition can be written as

$$q(0,t) = q(L,t) \ , \quad v(0,t) = v(L,t) \ , \quad \left.\frac{\partial v}{\partial x}\right|_{x=0} = \left.\frac{\partial v}{\partial x}\right|_{x=L} \ ,$$

where $q(x,t)$ is the local flow of vehicles defined by $q(x,t) = v(x,t)\rho(x,t)$. Integration of local concentration $\rho(x,t)$ for whole system gives a total number of vehicles N:

$$N = \int_0^L dx\rho(x,t) \ . \tag{2.20}$$

A concentration of homogeneous traffic stream ρ_h is defined by $\rho_h = N/L$. The corresponding value of an equilibrium velocity v_h, follows from the relationship:

$$v_h = \tilde{v}(\rho_h) \ . \tag{2.21}$$

If N and L are given, there is a unique homogeneous flow characterized by $\rho = \rho_h$ and $v = v_h$.

Let us consider linear fluctuations from the homogeneous flow $(\rho = \rho_h, v = v_h)$. Defining fluctuations as

$$\delta\rho(x,t) = \delta\rho_0 \exp(-\gamma t + ikx) \ , \tag{2.22}$$

$$\delta v(x,t) = \delta v_0 \exp(-\gamma t + ikx) \ , \tag{2.23}$$

and substituting $\rho = \rho_h + \delta\rho(x,t)$ and $v = v_h + \delta v(x,t)$ into the equations, we get

$$\int_0^L dx\delta\rho(x,t) = 0 \qquad \text{from the definition of } \rho_h, \tag{2.24}$$

$$\exp(ikL) = 1 \qquad \text{from the periodic boundary condition,} \tag{2.25}$$

$$\begin{aligned}&\left(-\gamma + ikv_h + \frac{1}{\tau} + \mu k^2 \rho_h^{-1}\right)\delta v(x,t)\\ &\quad + \left(ikc^2\rho_h^{-1} - \frac{1}{\tau}\xi(\rho_h)\right)\delta\rho(x,t) = 0 \qquad \text{from the equation of motion,}\end{aligned} \tag{2.26}$$

$$ik\rho_h\delta v(x,t) + (-\gamma + ikv_h)\,\delta\rho(x,t) = 0 \qquad \text{from the continuity equation,} \tag{2.27}$$

by linearizing the equations, where $\xi(\rho)$ is a slope equilibrium velocity, that is, $\xi(\rho) = d\tilde{v}/d\rho$. The last two equations give the dispersion relation, which determines the nature of the perturbations; The determinant of the coefficients makes the dispersion relation as follows:

$$\gamma^2 - \gamma\left(2ikv_h + \mu k^2\rho_h^{-1} + \frac{1}{\tau}\right) + k^2(c^2 - v_h^2) + ik\left(\frac{v_h}{\tau} + \mu k^2 v_h \rho_h^{-1} + \frac{\rho_h}{\tau}\xi(\rho_h)\right) = 0 \ . \tag{2.28}$$

Introducing dimensionless variables,

$$\tilde{\gamma} = \tau\gamma, \qquad \tilde{k} = lk, \qquad \tilde{v_h} = v_h\frac{\tau}{l},$$

$$\tilde{\rho_h} = \frac{\rho_h}{\hat{\rho}}, \qquad \tilde{c} = c\frac{\tau}{l}, \qquad \tilde{\xi} = \xi\frac{\tau\hat{\rho}}{l},$$

where $\hat{\rho}$ is maximally allowed concentration defined by $\tilde{v}(\hat{\rho}) = 0$, and l is a unit of length defined by $l = \sqrt{\mu\tau\hat{\rho}^{-1}}$. Omitting $\tilde{}$, we get the dispersion relation as

$$\gamma^2 - \gamma\left(2ikv_h + k^2\rho_h^{-1} + 1\right) + k^2(c^2 - v_h^2) + ik\left(v_h + k^2 v_h\rho_h^{-1} + \rho_h\xi(\rho_h)\right) = 0 \ . \tag{2.29}$$

The boundary condition gives

$$k = \frac{2\pi m}{L} \qquad \text{for } m = 1, 2, \ldots, L-1 \ . \tag{2.30}$$

We remove the perturbation with $k = 0$ because it changes the number of vehicles N.

By separating γ into real part and imaginary one, $\gamma = \lambda + i\omega$, the dispersion relation Eq. (2.29) is decomposed into two equations:

$$\lambda^2 - \omega^2 - \lambda(1 + k^2\rho_h^{-1}) + 2\omega k v_h + k^2(c^2 - v_h^2) = 0 \ , \tag{2.31}$$

$$(2\omega - 2kv_h)\lambda - \omega(1 + k^2\rho_h^{-1}) + k(v_h + k^2 v_h \rho_h^{-1} + \rho_h \xi(\rho_h)) = 0 \ . \tag{2.32}$$

We are interested in the point where the homogeneous flow becomes unstable, that is, near $\lambda = 0$. By substituting $\lambda = 0$, the first equation gives two ω:

$$\omega_1 = k(v_h - c), \quad \omega_2 = k(v_h + c) \ .$$

For each ω, unstable condition $\mathrm{Re}\,\gamma < 0$ gives

$$\rho_h \left(-1 - \frac{\rho_h \xi(\rho_h)}{c} \right) > k^2 \qquad \text{for } \omega_1, \tag{2.33}$$

$$\rho_h \left(-1 + \frac{\rho_h \xi(\rho_h)}{c} \right) > k^2 \qquad \text{for } \omega_2 \ . \tag{2.34}$$

The second inequality can not be fulfilled due to the negativity of ξ, because $\tilde{v}$ is the monotonically decreasing function of ρ. Therefore the first inequality determines the linear stability condition:

$$\rho_h \left(-1 - \frac{\rho_h \xi(\rho_h)}{c} \right) > \left(\frac{2\pi}{L} \right)^2 , \tag{2.35}$$

where we use minimal value of k^2. For example, consider the Greenshields model $\tilde{v}(\rho) = 2c(1 - \rho)$. When the system is large enough, the unstable condition is

$$2\rho_h^2 - \rho_h > 0 \ . \tag{2.36}$$

Thus, for $\rho_h > 1/2$, the homogeneous stream is unstable.

The velocity of spontaneously generated density waves can be found by the form of fluctuation as

$$v_p = \frac{\omega_c}{k_c} = v_h - c \ , \tag{2.37}$$

where k_c and ω_c are the critical values of k and w, respectively, defined by $k_c = 2\pi/L$ and $\omega_c = k_c(v_h - c)$. Thus the spontaneously generated density waves can propagate both upstream and downstream according to the parameter c.

As was mentioned above, the general fluid dynamical model shows spontaneous generation of density waves by small perturbations, when the concentration of vehicle in the flow exceeds some critical values, although the traffic stream is initially homogeneous. This instability condition depends on the model of equilibrium velocity function and the system length. From the above result the models show the discontinuous type fundamental diagrams. In general, however, the critical concentration of instabilities is different from the concentration at the capacity. What corresponds to this difference in the real traffic flow is not clear yet.

The discontinuous fundamental diagram is reproduced by the present model. But, like the case of kinematic wave theory, the present model is not appropriate to explain, for example, the form of the fundamental diagram, because the theory contains the phenomenological functions of the equilibrium velocity. To understand the shape of the fundamental diagrams, we require the microscopic modeling.

Burgers Equation

Burgers equation, which was used by Musha and Higuchi to explain the power-law density fluctuations [63, 64], contains the equation of kinematic wave as the special case. It also is one-dimensional version of Navier-Stokes' equation with $p = X = 0$ [7]; Consider the continuity equation:

$$\frac{\partial \rho}{\partial t} + \frac{\partial q}{\partial x} = 0 \ . \tag{2.38}$$

Assuming that a flow is decomposed into two parts, drift term and diffusion term, that is, $q = \rho v - D(\partial\rho/\partial x)$, where D is a diffusion constant, we obtain

$$\frac{\partial \rho}{\partial t} + v\frac{\partial \rho}{\partial x} + \rho\frac{\partial v}{\partial x} = D\frac{\partial^2 \rho}{\partial x^2} \ . \tag{2.39}$$

The phenomenological assumption of the form of equilibrium velocity $v = v_0(1 - \rho/\rho_s)$, which gives the Greenshields[2] model of a fundamental diagram, leads us to the final expression

$$\left(\frac{\partial}{\partial t} + v_0\frac{\partial}{\partial x} \right)\rho - 2\left(\frac{\rho}{\rho_s} \right) v_0 \frac{\partial \rho}{\partial x} = D\frac{\partial^2 \rho}{\partial x^2} \ . \tag{2.40}$$

---

[2] In Ref. [63], the linear form $v = v_0(1 - \rho/\rho_s)$ of a fundamental diagram is called as Greenberg model. But it is incorrect; Greenberg model is logarithmic form $v = v_0 \log(\rho_s/\rho)$. Correctly, the linear model is called Greenshields model.

Taking a moving frame of $x' = -x + v_0 t, t' = t$, we get

$$\frac{\partial \rho}{\partial t'} + 2\frac{\rho}{\rho_s}k\frac{\partial \rho}{\partial x'} = D\frac{\partial^2 \rho}{\partial x'^2} \ . \tag{2.41}$$

This is the Burgers equation. If we choose $D = 0$, then the above treatment is identical to the kinematic wave treatment with Greenshields' model of fundamental diagram.

2.1.2 Stochastic Models

In addition to the fluid dynamical models, stochastic approach also is a macroscopic treatment of traffic flow. In 1960, Prigogine developed stochastic treatment of traffic flow based on the Maxwell-Boltzmann equation [85]. This treatment has both features of macroscopic modeling and microscopic one. In this approach the velocity distribution function is a fundamental quantity. We denote the distribution function of velocity as $f(x, v, t)$, which is a function of position x and time t; For example, $f(v, x, t)dxdv$ represents the number of vehicles existing in spatial region $[x, x + dx]$ with velocity in the range $[v, v + dv]$ at time t. Local concentration $\rho(x, t)$, local flow $q(x, t)$ and local average velocity $\bar{v}(x, t)$ can be expressed by an integral form with f:

$$\rho(x,t) = \int_0^\infty f(x,v,t)dv \ , q(x,t) = \int_0^\infty vf(x,v,t)dv \ , \text{and} \quad \bar{v}(x,t) = \frac{\int_0^\infty vf(x,v,t)dv}{\int_0^\infty f(x,v,t)dv} \ .$$

Let us start with the following equation:

$$\frac{df}{dt} = \left(\frac{\partial f}{\partial t}\right)_{\text{rel.}} + \left(\frac{\partial f}{\partial t}\right)_{\text{coll.}} \ ; \tag{2.42}$$

That is, the temporal change of f can be described as a result of only two processes: the relaxation process $(\partial f/\partial t)_{\text{rel.}}$ and the collision process $(\partial f/\partial t)_{\text{coll.}}$. Expanding the total derivative of f, we obtain

$$\frac{\partial f}{\partial t} + v\frac{\partial f}{\partial x} = \left(\frac{\partial f}{\partial t}\right)_{\text{rel.}} + \left(\frac{\partial f}{\partial t}\right)_{\text{coll.}} \ . \tag{2.43}$$

The relaxation process expresses the relaxation of velocity distribution function; We assume the existence of an ideal distribution function or a zero-concentration distribution function $f^0(x, v)$, which is the distribution that would be realized if there was no

disturbance of other vehicles or if the system was infinitely dilute. f^0 also is the distribution of preferred velocities. The information such as the legal speed, bottleneck, and characteristics of vehicles are included in the ideal distribution function. Whenever f deviates from the ideal distribution for same position and time, a force acts for returning the distribution to the ideal one. We assume the form of relaxation term as

$$\left(\frac{\partial f}{\partial t}\right)_{\text{rel.}} = -\frac{f - f^0}{T} \ , \tag{2.44}$$

where T expresses a relaxation time. There are many mechanisms contributing to T; For example, the movement of vehicles from one position where f^0 takes one value to another where f^0 has different value causes some relaxation process in a time T_1. Another relaxation process is caused by passing. We denote a corresponding relaxation time as T_2; If the vehicle does not pass another vehicle, then $T_2 = \infty$; If the vehicle passes another vehicle instantaneously, then $T_2 = 0$. Therefore, introducing the probability of passing p, we may expect the relaxation time T_2 has the form

$$T_2 = \tau\frac{1 - p}{p} \ , \tag{2.45}$$

where τ is the relaxation time at $p = 1/2$. The total relaxation time T will be achieved by the largest relaxation time. If the road is smooth, T_1 may be smaller than T_2. When we want to deal with effects like bottleneck, we take the largest relaxation time as T_1. Here we consider the situation in which the passing relaxation effects become dominant, so that the form of the relaxation term is as follows:

$$\left(\frac{\partial f}{\partial t}\right)_{\text{rel.}} = -\frac{(f - f^0)p}{\tau(1 - p)} \ . \tag{2.46}$$

Note that this relaxation term contains only the effects of relaxation caused by passing; Effects of interaction due to the passing is included in the collision term.

For the collision term, we assume the following form by an analogy to gas kinematics:

$$\left(\frac{\partial f(x, v_i, t)}{\partial t}\right)_{\text{coll.}} = \sum_j (\Gamma_{ij}^{(+)} - \Gamma_{ij}^{(-)})(1 - p) \ ; \tag{2.47}$$

This term is described as the summation of influence to type i vehicles, which travel with velocity v_i, from other vehicles before passing. The coefficient $\Gamma_{ij}^{(-)}dvdxdt$ equals the number of vehicles subtracted from volume $dvdx$ by collisions with vehicles with velocity v_j during an interval dt. And $\Gamma_{ij}^{(+)} dv dx dt$ equals the number of vehicles added to the same volume by collisions with vehicles with velocity v_j during the same interval. The no-passing probability $1-p$ is multiplied to these coefficients, because the influence is kept for the intervals in which vehicles does not pass.

Consider the coefficient $\Gamma_{ij}^{(-)} dv dx dt$. The vehicles with velocity $v_j (< v_i)$ in front of the vehicles with velocity v_i contributes to the coefficient. During time interval dt the number of such vehicles is $f(x, v_j, t)(v_i - v_j)dt$, because only vehicles in the front range $(v_i - v_j)dt$ are struck by the vehicles with velocity v_i during dt. Therefore the number of vehicles which are struck by the vehicles with velocity v_i is

$$\int_0^{v_i} f(x, v_j, t)(v_i - v_j) dt dv_j \ . \tag{2.48}$$

The number of target vehicles with velocity v_i is $f(x, v_i, t) dx dv_i$. Thus

$$\Gamma_{ij}^{(-)} dx dv_i dt = f(x, v_i, t) dx dv_i \int_0^{v_i} f(x, v_j, t)(v_i - v_j) dt dv_j \ . \tag{2.49}$$

Similarly we can obtain the coefficient $\Gamma_{ij}^{(+)} dv dx dt$ as

$$\Gamma_{ij}^{(+)} dx dv_i dt = f(x, v_i, t) dx dv_i \int_{v_i}^{\infty} f(x, v_j, t)(v_j - v_i) dt dv_j \ , \tag{2.50}$$

counting the number of vehicles behind the target vehicles.

Summing two coefficients, we obtain the collision term as

$$\left(\frac{\partial f(x, v_i, t)}{\partial t} \right)_{\text{coll.}} = \sum_j (\Gamma_{ij}^{(+)} - \Gamma_{ij}^{(-)})(1-p) \tag{2.51}$$

$$= \sum_j f(x, v_i, t) \int_0^{\infty} dv_j f(x, v_j, t)(v_j - v_i)(1-p) \tag{2.52}$$

$$= f(x, v_i, t)(q(x, t) - v_i \rho(x, t))(1-p) \ . \tag{2.53}$$

Omitting the index i we get

$$\left(\frac{\partial f}{\partial t} \right)_{\text{coll.}} = f\rho(\bar{v} - v)(1-p) \ . \tag{2.54}$$

Therefore over-all Boltzmann equation for the evolution of one-vehicle distribution function is

$$\frac{\partial f}{\partial t} + v \frac{\partial f}{\partial x} = -\frac{(f - f^0)p}{\tau(1-p)} + f\rho(\bar{v} - v)(1-p) \ . \tag{2.55}$$

This is the fundamental equation derived by Prigogine for uniform road traffic. Steady solution is given as the solution of the integral equation of

$$0 = -(f(x, v, t) - f^0(x, v, t))p + f(x, v, t)\rho \left(\int_0^{\infty} v f(x, v, t) dv - v \right) \tau(1-p)^2 \ . \tag{2.56}$$

In the limit $\rho \to 0$ for finite p, f surely becomes f^0, which have been our requirement. If p equals to unity, the actual distribution is equivalent to the ideal one.

In the approach with Maxwell-Boltzmann equation, the ideal distribution is required. This is a macroscopic quantity and is empirically determined by the experience. Therefore this approach is not suitable for microscopic understanding of the traffic stream and is used for phenomenological studies of traffic flow.

2.2 Microscopic Modeling

2.2.1 Car-following Models

In this section, we consider another class of traffic flow model, that is, microscopic modeling. In contrast to the macroscopic modeling like fluid dynamical models or stochastic models, microscopic modeling deals with individual vehicles, so that the motion of the traffic stream is described by the collective motion of individual movement of vehicles; Motion of each vehicle is governed by the locally described equations or "rules", that is, the reaction of vehicles is determined by the local environment such as relative velocity, relative position, road condition, and so on.

There are two large categories of microscopic modeling; One is car-following model and another is cellular automaton model. Here we start with car-following models. They are described by simultaneous differential equations. In 1952, Pipes presented a simple car-following model [84]; Consider a single lane road and the situations that vehicles travel on the road along one direction and passing is forbidden. Then each driver may keep the individual headway distance $x_{k-1} - x_k$ as

$$x_{k-1} - x_k = b + Tv_k + L_k \ , \tag{2.57}$$

where x_k, v_k, L_k are the position of k-th vehicle, its velocity, and its length, respectively. b is the natural headway distance taken at the vehicle coming to a stop. The term Tv_k

represents the length in which the vehicle can stop suddenly, when the vehicle travels with the velocity v_k, so that T is a response time due to both human and vehicle. This regulation of the headway distance is ideal one, which was written in the driving manual [84], so that the model describes the only ideal traffic flow. Pipes derived the equation of motion based on above regulation: Taking time derivative of the regulation, we get

$$\dot{v}_k = \frac{1}{T}(v_{k-1} - v_k) \ . \tag{2.58}$$

Physically this equation is identical to the following one:

$$m\frac{d^2x_k}{dt^2} = \lambda\left(\frac{dx_{k-1}}{dt} - \frac{dx_k}{dt}\right) \tag{2.59}$$

with $\lambda/m = 1/T$; The acceleration of vehicle is proportional to the relative velocity between the foregoing vehicle. By considering the equations for $k = 1, \ldots, N$ simultaneously, a traffic stream constructed by N vehicles can be studied. For convenience we take $L_k = 1$ and renormalize $b \to b - 1$. The essential of traffic stream is not affected by this change. The uniform stream with the velocity v and the interval $b + Tv$,

$$x_k^0(t) = vt - k(b + Tv), \tag{2.60}$$

is the solution of the simultaneous equations.

Next consider a linear stability of the uniform traffic stream; Substituting $x_k(t) = x_k^0(t) + f_k \exp(i\omega t)$ into the integrated equation (2.59), we get

$$i\omega T f_k = f_{k-1} - f_k \ . \tag{2.61}$$

If we take $f_0 = 1$, then $f_k = (1 + i\omega T)^{-k}$. The fluctuation amplitude of k-th vehicle

$$|f_k| = (1 + \omega^2 T^2)^{-k/2} \tag{2.62}$$

is always less than one. Therefore the system is stable for any T. But this is unrealistic situation. According to Eq. (2.62), the traffic stream is stable, even in the limit $T \to 0$, which allows the traffic stream with no headway distance and with very high speed; Such flow, of course, is unstable in the real world. The reason why such unrealistic situation is allowed is that the sensitivity λ is not bounded; It can become arbitrary large. In the realistic situation, the sensitivity is limited by the reaction of human or vehicle.

To improve the Pipes model, time delay of reaction has been introduced by Chandler *et al* [10]. The fundamental equations are

$$m\frac{d^2x_k(t)}{dt^2} = \lambda\left(\frac{dx_{k-1}(t-\Delta)}{dt} - \frac{dx_k(t-\Delta)}{dt}\right) \ , \tag{2.63}$$

where Δ represents the time delay. This model also has a uniform solution of traffic stream. Consider a linear stability of traffic flow: Substituting $x_k(t) = x_k^0(t) + f_k \exp(i\omega t)$, where $x_k^0(t)$ is the uniform traffic stream mentioned above, we obtain

$$f_k = (1 + i\omega T \exp(i\Delta\omega))^{-k} f_0, \tag{2.64}$$

and thus the magnitude of f_k becomes

$$|f_k| = \left(1 + \omega^2 T^2 - 2\omega T \sin(\Delta\omega)\right)^{-k/2} \ . \tag{2.65}$$

Here we take f_0 to be 1. Clearly the traffic stream becomes unstable, if $\omega T < 2\sin\Delta\omega$. This condition restricts the value of T to a realistic value.

In both Pipes and Chandler models the acceleration is proportional to the relative velocity; Thus the vehicle is influenced by the foregoing vehicle which is at, say, 10 km ahead. Such behavior is owing to the constant sensitivity. In addition, a leading vehicle must exist in the theory, because the reaction is basically determined by the relative velocities in both models. Therefore these models are suitable for dense traffic streams; They are useful for study of the stability analysis of a platoon or shock wave propagation in the platoon and not suitable for study of the macroscopic feature of traffic stream such as the shape of fundamental diagram.

Many improvement have been developed; For example, Kometani and Sasaki added the term dependent on the velocity of the foregoing vehicle [49]. Gazis *et al.* have introduced the sensitivity that depends on the relative position and the velocity of the vehicle [25]. Then the equation of motion becomes

$$\frac{d^2x_k(t)}{dt^2} = \lambda(x_k, x_{k-1})\left(\frac{dx_{k-1}(t-\Delta)}{dt} - \frac{dx_k(t-\Delta)}{dt}\right) \ , \tag{2.66}$$

where Δ is time delay. $\lambda(x_k, x_{k-1})$ is the sensitivity depending on the relative position and the velocity of the vehicle, described as

$$\lambda(x_k, x_{k-1}) = \frac{a\dot{x_k}^m(t)}{(x_k(t-\Delta) - x_{k-1}(t-\Delta))^l} \ , \tag{2.67}$$

where l and m are positive parameters. This model overcomes the large headway problems, because the sensitivity decays with power law for the large headway distance. The uniform stream is the solution of the above model. Using the function $f_p(x)$:

$$f_p(x) = \begin{cases} x^{1-p} & \text{for } p \neq 1, \\ \ln x & \text{for } p = 1, \end{cases} \tag{2.68}$$

we write the uniform solution as

$$f_m(u) = cf_l(s) + c' \ , \tag{2.69}$$

where, u, s are the velocity and the headway distance, respectively, c is constant dependent on m, l, a and c' is another constant. If $l = 1, m = 0$, the solution is equivalent to the Greenberg model [26]. Nonlinearity of the model enables us to describe the steady-state macroscopic feature of traffic flow.

Newell has also proposed a better car-following model than Pipes or Chandler models by modifying the sensitivity [76]. The sensitivity of his model is as follows:

$$\lambda_k(x_k, x_{k-1}) = \lambda_k \exp\left\{-\lambda_k V_k^{-1}(x_{k-1}(t-\Delta) + x_k(t-\Delta) - L_k)\right\} \ , \tag{2.70}$$

where V_k is a preferred velocity, with which the vehicle travel in a free run, L_k is a parameter related with the length of the vehicle and the natural headway distance. The equation of motion is as follows:

$$\frac{d^2x_k(t)}{dt^2} = \lambda_k(x_k, x_{k-1})\left(\frac{dx_{k-1}(t-\Delta)}{dt} - \frac{dx_k(t-\Delta)}{dt}\right) \tag{2.71}$$

with nonlinear sensitivity $\lambda_k(x_k, x_{k-1})$. Integrating above equation, we obtain original model by Newell:

$$\frac{dx_k(t)}{dt} = V_k - V_k \exp\left\{-\lambda_k V_k^{-1}(x_{k-1}(t-\Delta) + x_k(t-\Delta) - L_k)\right\} \ . \tag{2.72}$$

Owing to the introduction of the preferred velocity, the model can describe the steady flow with large headway, as well as treatment of stability of platoons or propagation of density waves.

Above mentioned car-following models are essentially described by first order differential equations, so that the artificial time delay must be introduced to make models realistic. In addition, the last two nonlinear car-following models give only the continuous fundamental diagram, which does not agree with the actual observation, although these models can treat the steady dynamics. But there is no crucial modification of model in last forty years. Recently theoretical breakthrough of the car-following models has been achieved by Bando *et al* [3,4]. Their model is called the optimal velocity (OV) model. The OV model is described by second order simultaneous differential equations in contrast with the previous ones. The equation of motion is as follows:

$$\frac{d^2x_k(t)}{dt^2} = a\left(V(x_{k-1}(t) - \nu_k(t)) - \frac{dx_k(t)}{dt}\right) \ , \tag{2.73}$$

where a is the sensitivity. $V(\Delta x)$ is an optimal velocity function which is function only of the headway distance. Typically $V(\Delta x)$ is taken to be $\tanh(\Delta x) + \tanh 2$, that is, monotonically increasing function. When the headway distance is large enough, the function becomes asymptotically constant, which corresponds to the preferred velocity introduced by Newell. Remarkable feature is that the time delay is not required; Effects of time delay is naturally introduced by the feature of second order differential equation. In addition, the model exhibits instability of a homogeneous traffic flow as the increase of the concentration.

Consider a linear stability analysis. First, we construct the solution of uniform traffic stream: N vehicles having the same velocity are uniformly distributed on the circular road with length L, then the solution is

$$x^0_{k-1}(t) - x^0_k(t) = \frac{L}{N} \tag{2.74}$$

$$x^0_k(t) = aV\left(\frac{L}{N}\right) - \frac{L}{N}k \ . \tag{2.75}$$

Next consider a fluctuation from the uniform stream; We denote $x_k(t) = x^0_k(t) + y_k(t)$ and linearize the equation for the fluctuation $y_k(t)$. We obtain

$$\frac{d^2y_k(t)}{dt^2} = aV'\left(\frac{L}{N}\right)(y_{k-1}(t) - y_k(t)) - a\frac{dy_k(t)}{dt} \ . \tag{2.76}$$

Substituting $y_k(t) = f_k \exp i\omega t$ into the above equation, we get

$$f_k = \left(\frac{aV'(L/N)}{aV'(L/N) - \omega^2 + i\omega a}\right) f_{k-1} \ . \tag{2.77}$$

If the amplitude of f_k is less than unity, the uniform stream is stable. Therefore the stability condition is

$$\frac{\omega^2}{a^2} - 2\frac{V'(L/N)}{a} + 1 > 0 \ . \tag{2.78}$$

In the static limit $\omega \to 0$ the condition becomes

$$\frac{V'(L/N)}{a} < \frac{1}{2} \ . \tag{2.79}$$

This is an important result; The stability of the uniform traffic stream depends on the concentration, because L/N is an inverse of the concentration. For the optimal velocity function such as $V(\Delta x) = \tanh(\Delta x) + \tanh 2$, it is easily checked that the uniform stream becomes unstable as increase the concentration. In the unstable regime inhomogeneous traffic stream spontaneously appears, even though the stream is initially homogeneous. Inhomogeneous traffic stream consists of regions of tow distinct types; One has high average velocity and low concentration and the other has low average velocity and high concentration. Similar to the general fluid dynamical models, the critical concentration of instability slightly differs from the concentration corresponding to the capacity.

The OV model is simple and has beautiful mathematical structure, so that many analytical studies have been done, in order to understand the mathematical properties behind the equations, as well as the features of traffic stream including universality with the granular systems [29]. For the application to real situations with intention of controlling traffic, however, it is not appropriate; Mathematical simplicity makes introducing the other elements such as randomness of preferred velocity, or inhomogeneous condition of road difficult.

2.2.2 Cellular Automaton Models

Recently another type of microscopic models, based on the concept of cellular automata (CA) (e.g. [103, 104]), has been developed. Cellular automata are mathematical idealizations of physical systems with space and time being discrete. Physical quantities are described by finite discrete values. Properties of simple cellular automata have been investigated extensively by Wolfram [103, 104]; These cellular automata consists of a one-dimensional lattice and a discrete internal state on every site, so called a "cell". The state of the cellular automaton is completely determined by the state of each cell. Temporal evolution of a cellular automaton obeys discrete-time dynamics. Here we consider a elementary cellular automata; The local internal state is described by only binary states $\{0, 1\}$ and its temporal evolution is affected by the state of nearest neighboring sites and the state itself. The states of cells are simultaneously updated based on a definite set of rules.

Consider an example of the elementary cellular automata. Let s_n^{t+1} be a state of the center cell of the neighborhood at the $t+1$ time step and $s_{n-1}^t, s_n^t, s_{n+1}^t$ are states of the neighborhood at the t time step. Three neighbors $\{s_{n-1}^t, s_n^t, s_{n+1}^t\}$ can take 2^3 possible states, because the state of each cell is 0 or 1. s_n^{t+1} is determined by $\{s_{n-1}^t, s_n^t, s_{n+1}^t\}$ according to the set of rules. Thus there are $2^{2^3} = 256$ possible distinct sets of rules in the elementary cellular automaton. Let us see the following the set of rules, for example:

$$\frac{s_{n-1}^t s_n^t s_{n+1}^t}{s_n^{t+1}} = \left\{ \frac{111}{1}, \frac{110}{0}, \frac{101}{1}, \frac{100}{1}, \frac{011}{1}, \frac{010}{0}, \frac{001}{0}, \frac{000}{0} \right\} \ . \tag{2.80}$$

The eight possible states of three adjacent sites are given above the line and the lower digits present the state s_n^{t+1}; For instance, if the three neighbors take 101, the state of center cell becomes 1 at the next time step. This rule is called rule 184 according to Wolfram's classification, because the binary number 10111000 in (2.80) represents 184 in decimal number. The rule 184 is called "illegal" in the terminology of Wolfram, because the spatial reflection symmetry is broken. For the elementary cellular automata, temporal evolution rules can also be considered as a Boolean function f_a of the states. For example, the rule 184 can be represents as follows:

$$s_n^{t+1} = f_{184}(s_{n-1}^t, s_n^t, s_{n+1}^t) \equiv (s_{n-1}^t \wedge \neg s_n^t) \vee (s_n^t \wedge s_{n+1}^t) \ . \tag{2.81}$$

The rule-184 cellular automaton can be regarded as a simplest traffic flow model; If the states $0, 1$ are identified as an empty site and the occupied site by a vehicle, respectively, the rule expresses that a vehicle moves one step rightward, when the right-neighboring site is empty. This model is quite simple, so that it is not only the model of traffic flow, but also of other systems; For example, it is regarded as the surface growth model by identifying the movement of a vehicle to single step growth of surface [52]; Mathematically the model is also related with totally asymmetric simple exclusion processes (TASEP) [57–59], and ultra-discretized Burgers equation [78].

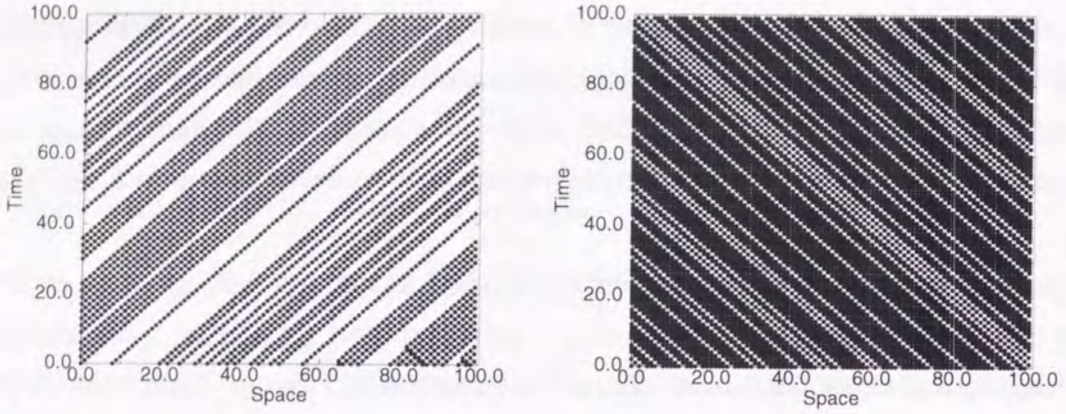

(a) low concentration

(b) high concentration

Figure 2.2: Typical space-time trajectories of the rule-184 cellular automaton model. (a) in low concentration $\rho = 0.3$, (b) in high concentration $\rho = 0.8$. Black circle represents a vehicle. Periodic boundary condition is imposed.

For latter convenience, we describe features of the rule-184 cellular automaton model using traffic terminology. Consider one-dimensional periodic array of cells, which represents a periodic road. Concentration ρ is defined as a ratio of a number of vehicles N and a number of cells L: $\rho = N/L$. The averaged velocity is defined by a number of moved vehicles per one time step; If the number of such vehicle at an i-th time step is n_i, the average velocity $\langle v\rangle$ is

$$\langle v\rangle = \frac{1}{T}\sum_{i=1}^{T}\frac{n_i}{N} \tag{2.82}$$

with a duration of observation T. Therefore the maximal allowed average velocity is 1. Typical space-time trajectories of the rule-184 cellular automaton model are shown in Fig. 2.2: (a) in low concentration $\rho = 0.3$, all the vehicles travel with maximal velocity and $\langle v\rangle = 1$. (b) in high concentration $\rho = 0.8$, the average velocity is less than 1. But because of the particle-hole symmetry inherent in the model, empty site travels with maximal velocity 1 to the opposite direction.

The dependence of the average velocity on the concentration is presented in Fig. 2.3. The average velocity is calculated for 100 steps after discarding 100 steps for relaxation.

The number of cells is taken to be 100. Clearly we can see that the average velocity is 1 in low concentration, while for concentration larger than $\rho = 0.5$ it decreases as increasing the concentration. The fundamental diagram is obtained by multiplying the concentration to the average velocity shown in Fig. 2.4. It is clearly seen that a flow takes a peak at the concentration $\rho = 0.5$ and thus the capacity is 0.5. The concentration $\rho = 0.5$ corresponds to the transition point. But in this case, there is no critical behavior at the transition point. This fundamental diagram is classified into the inverted V shape. The behavior of the fundamental diagram is understood by the following arguments; If the number of cells is even, then the space-time trajectory at the transition point draws a checkerboard pattern. It means that the traffic stream is spontaneously organized into the state in which the vehicles align alternately in the cell. Such self-organized state is a consequence of the particle-hole symmetry of the model. In the concentration lower than the transition point, the traffic stream is made by replacing the appropriate number of vehicles with the empty sites in the self-organized state. Therefore the average velocity still takes maximal value 1. In higher concentration, on the other hand, vehicles are added to the self-organized state, that is, the empty site is occupied by the vehicle. Therefore the average velocity of vehicle is less than 1; Empty sites travel with velocity 1.

In the rule-184 cellular automaton model, analytic forms of the average velocity and flow can be obtained; In the limit $T \to \infty$ in the lower concentration, the number of movable vehicles equals the total number of vehicles, because of the local property of the self-organized state; Thus

$$\langle v\rangle = \lim_{T\to\infty}\sum_{i}^{T}\frac{N}{N} = 1 \qquad \text{for } \rho < 1/2 \ . \tag{2.83}$$

In high concentration the number of movable vehicles is the number of holes due to the particle-hole symmetry. Thus

$$\langle v\rangle = \lim_{T\to\infty}\sum_{i}^{T}\frac{L-N}{N} = \frac{1-\rho}{\rho} \qquad \text{for } \rho > 1/2 \ . \tag{2.84}$$

Using them, we obtain the flow as follows:

$$q = \begin{cases} \rho & (0 < \rho \le 1/2) \\ 1-\rho & (1/2 < \rho \le 1) \end{cases} \ . \tag{2.85}$$

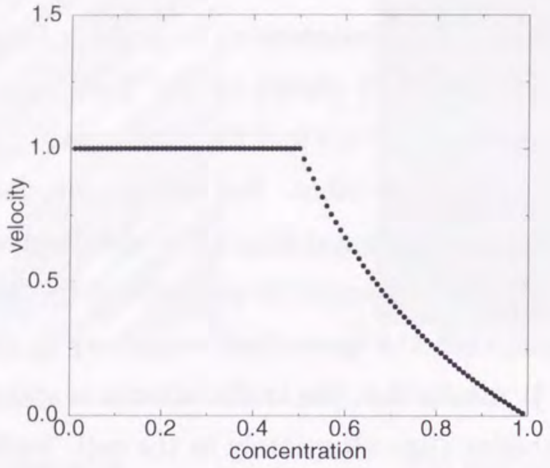

Figure 2.3: The average velocity against the concentration of the rule-184 cellular automaton model. The number of cells is 100. We calculate the average velocity for 100 steps after discarding 100 steps for relaxation.

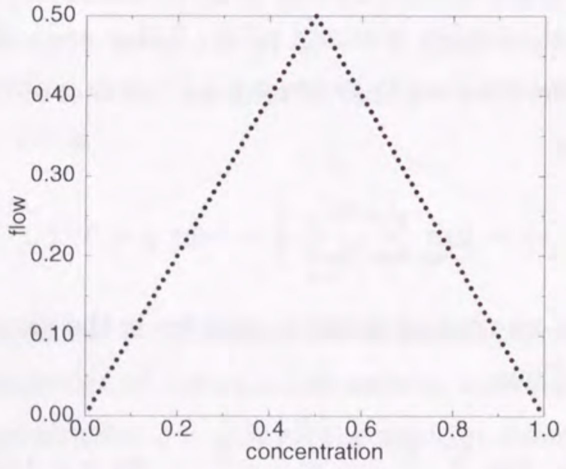

Figure 2.4: The fundamental diagram of the rule-184 cellular automaton model. The flow is obtained by multiplying the concentration to the velocity.

The rule-184 cellular automaton model has the essentials of traffic flow, although the model is very simple; For instance, the time delay of reaction of vehicles is contained in the rules and the model can reproduce the discontinuous change between free flow and congested flow. But it is not suitable for studying the problems such as density fluctuations.

Recently more realistic extensions of the rule-184 CA model have been proposed. Takayasu and Takayasu have introduced time-delay in acceleration and random noises and studied density fluctuations [99]. As a consequence, their model shows the $1/f$ type power-law density fluctuation. Nagel and Schreckenberg have proposed more generic cellular automaton model, so called NS model [70, 73]. This model has many internal states of cell and update rule includes more than three neighbors. The NS model is described as follows: The system consists of one-dimensional array and vehicles on it. Each vehicle has a integer valued velocity $v = 0, 1, 2, \ldots, v_{max}$. At single updating process, positions and velocities are updated by the following rules:

- **Acceleration:** If the velocity v of a vehicle is lower than v_{max} and the distance d to the next vehicle ahead is larger than v, the velocity is added by one: $v \to v + 1$.
- **Slowing down (due to other vehicles):** If the distance d to the next vehicle ahead is not larger than v, that is, $v > d$, the velocity is reduced to $d-1$: $v \to d-1$.
- **Randomization:** With probability p, the velocity of a vehicle (if grater than zero) is subtracted by one; $v \to v - 1$
- **Car motion:** Each vehicle is advanced v sites.

Above rule is applied to all vehicles simultaneously. The randomization process makes the NS model nondeterministic. This randomization is quite important for reproduce several phenomena like power-law density fluctuations, power-law jam lifetime distribution [92]. Actual time evolution is presented in Figs. 2.5: (a) in low concentration $\rho = 0.1$ and (b) in high concentration $\rho = 0.3$. The time evolution from regular initial condition is plotted. Density waves propagating upstream are seen. Sometimes they emerge and vanish as a result of the randomization processes. A fundamental diagram calculated from the NS model becomes nearly inverted V shape; Randomness smoothes out a singularity of fundamental diagram. They also studied some power-law phenomena and discussed them

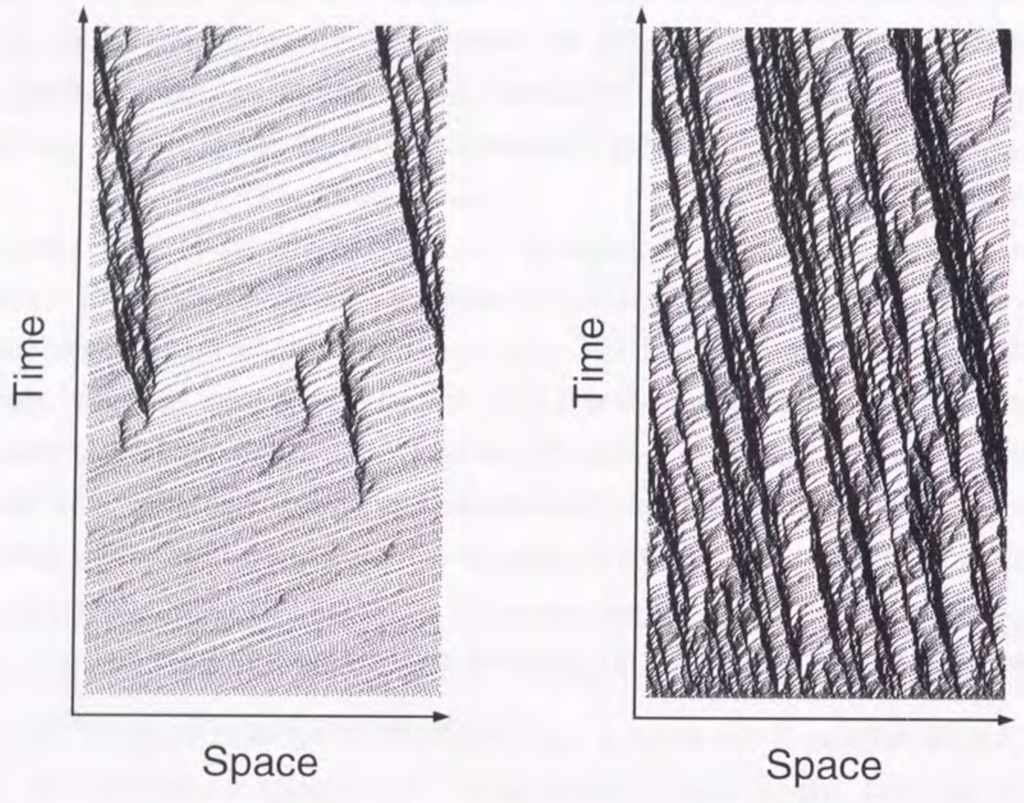

(a) Low concentration (b) High concentration

Figure 2.5: Space-time trajectories of the Nagel-Schreckenberg model taken from Ref. [92]. (a) in low concentration $\rho = 0.1$. (b) in high concentration $\rho = 0.3$. v_{max} is taken to be 5.

as concerning with "self-organized criticality" or "edge of chaos" [71, 72]. Simplicity of the model allowed some analytical treatments like mean field approximation [92].

There also are many other extensions that we did not mention above; Two dimensional cellular automaton traffic flow model have been proposed by Biham *et al* [6, 12, 96]. Their model is constructed on regular two-dimensional lattice and vehicles travels along individually definite directions, upward or rightward, according to rule-184 CA. As a consequence of computer simulations, their model shows sharp jamming transition. For the one-dimensional or pseudo-one-dimensional traffic flow, models of two lane, single lane with crossing, single lane with bottleneck have also been investigated based on the rule-184 CA model [65–68, 108].

Chapter 3

Dynamical Phase Transition Caused by Bottleneck

3.1 Introduction

In this chapter, we study effects of a bottleneck on the traffic flow in a road. The bottleneck is defined as a part of the road whose capacity is lower than that of the rest of the road. As has already been discussed in Ref. [61], it is expected that if the concentration is high to some extent the cars pile up behind the bottleneck and form a "shock front". We introduce a blockage site in the rule-184 CA to consider the bottleneck. The blockage site transmits the cars with some transmission probability. This blockage mimics the effect of the bottleneck caused by the road construction, the tunnel, and so on in the real world. As will be shown in later sections, the introduction of the blockage site causes nontrivial behavior. Nagatani has investigated the effects of a bottleneck in two-lane road by a CA model in which cars can move back and forth stochastically between the two lanes [68]. The model we treat, on the other hand, has only a single lane, and the movements of the cars are deterministic except for a single site, that is, blockage.

The CA model of traffic flow is closely related to the one-dimensional totally asymmetric simple-exclusion process (TASEP) [57] as was mentioned in the previous chapter. The TASEP is not a deterministic process; Rather, a randomly chosen particle is moved to its neighboring site at each time step. While the rule-184 is regarded as a model for the traffic flow, the TASEP may be regarded as a model for charged particles adsorbed on a solid surface with the electric field gradient imposed. Janowsky and Lebowitz have reported the simulation of TASEP with a blockage similar to one in our model [38]. They found a formation of the shock front, and analyzed its properties. Our model can also be regarded as a deterministic version of their model. Apart from the difference in the dynamics of two models, we focus mainly our attention on the behavior near the transition point between the free phase and the phase where the shock front exists.

The present chapter is organized as follows: In Sec. 3.2, we describe the model and define quantities we observe. The results of simulations are given in Sec. 3.3. We perform a mean-field-like approach for thermodynamic limit, and make analysis based on the finite-size scaling idea. The last section is devoted to summary and discussions.

3.2 Cellular Automaton Modeling

We start from describing the pure rule-184 CA without a blockage again. Suppose we have a one-dimensional lattice where each site can take either of the two states, 0 and 1. The CA evolves in discrete time step; The state of each site at the next time step is determined from the state of the site itself and those of the two nearest-neighbor sites. The evolution rule for the rule-184 CA is expressed symbolically by the following set of fractions:

$$\left\{\frac{111}{1},\frac{110}{0},\frac{101}{1},\frac{100}{1},\frac{011}{1},\frac{010}{0},\frac{001}{0},\frac{000}{0}\right\}. \tag{3.1}$$

The three binary numbers in the numerators express the states of the three sites, the site in concern and the two neighboring sites. These fractions express that a state, 1 or 0 in denominators, of each site after one time step is determined by the states of the three sites. Now we consider the state 1 is an empty site or hole, and the state 0 a site where a particle exist, Then the particle is driven left by the evolution rule, whenever the left nearest-neighbor site is empty. The number of the particles is conserved throughout the evolution process. The combination of the binary number in the denominators, 10111000, is 184 in decimal number; That is why this CA is called the rule-184 [103]. It should be noted that the rule-184 is one of the "illegal" rules according to Wolfram, since it lacks the spatial reflection symmetry. This illegality, however, is the source of the asymmetric motion.

The effects of a bottleneck are taken into account by introducing a blockage site. This site has a transmission probability r; If a particle exists on this site and its left nearest-neighbor site is empty, then a particle moves left with probability r and does not move with probability $1-r$. On a blockage site, the evolution rule is modified as

$$\begin{aligned}&\left\{\frac{1101}{01},\frac{1100}{01},\frac{0101}{01},\frac{0100}{01}\right\} &&\text{with probability r,}\\ &\left\{\frac{1101}{10},\frac{1100}{10},\frac{0101}{10},\frac{0100}{10}\right\} &&\text{with probability 1-r.}\end{aligned} \tag{3.2}$$

In each fraction the blockage site is the third digit from left in the numerator, and the denominator expresses the state of the blockage site at the next step. The evolution rule for other states and other sites are the same as that of the pure rule-184 CA. The blockage site will act as a seed of the "traffic jam" for the particles. The model thus constructed evolves mainly with the deterministic rule (3.1); Only at the blockage site, the stochastic rule (3.2) applies.

We study this model by computer simulations of finite lattices with the periodic boundary condition imposed. The present model is expected to have a steady state, because of the periodic boundary condition and the global conservation of the particle. The particle on the blockage site moves with the transmission probability r, so that the "life time" for a particle on the blockage site is $1/r$. If a particle comes to the blockage site, this particle will leave the blockage site after $1+1/r$ time steps on average. Therefore the particles is expected to pile up after the blockage if the particle concentration exceeds $r/(1+r)$; Thus a traffic jam region of finite thickness is expected to form.

Let us define some quantities we observe by the simulations. These quantities are calculated after the system reaches the steady state.

First we define the average speed v as

$$v=\frac{1}{T}\sum_{i=1}^{T}\frac{n_i}{n}\,, \tag{3.3}$$

where T is the total time steps, n_i is the number of particles which move at i-th time step, and n is the total number of particles. Using this average speed, the flow is calculated as

$$v\frac{n}{L}=v\rho, \tag{3.4}$$

where L is the lattice length and ρ is the particle concentration. Next, we define the width of the jam created after the blockage site. The tail of the jam is unambiguously determined as the last site from the blockage where the particle on it is blocked by the particle at the left nearest-neighbor site; In other word, all the particles after the tail can move freely. It is one of the advantage of the present deterministic model over the stochastic TASEP in which the tail position (the shock front in the terminology of TASEP) can be determined only statistically by means of the second-class particle [38]. If the blockage is at I-th site and a tail of the jam is at J_i-th site at i-th time step, the width of jam phase h is defined as

$$h = \frac{1}{T}\sum_i (J_i - I) \ . \tag{3.5}$$

The fluctuations of width Δh^2 of the jam is calculated as

$$\Delta h^2 = \frac{1}{T}\sum_i (J_i - I)^2 - h^2 \ . \tag{3.6}$$

3.3 Results

3.3.1 Simulation

We made computer simulations of the model varying the system size L, the transmission rate r, and the particle concentration ρ. In Figs. 3.3.1(a) and (b), typical results for the average speed and the flow are plotted, respectively, against the concentration for three transmission rates, $r = 0.3, 0.5$, and 1, where the last one corresponds to the pure rule-184. We took $L = 99$ in this figure. Three phases are recognized for $r = 0.3$ and 0.5. On the other hand, only two phases exist for $r = 1$, which we call the free phase (for $\rho < 1/2$) and the fully jam phase (for $\rho > 1/2$). What we call intermediate phase appears for $r = 0.3$ and 0.5 as the flow-constant phase. The plot of the flow is symmetric about $\rho = 1/2$ as expected from the particle-hole symmetry of the model; Thus the two critical points for the blockage model also are at the symmetric positions with respect to $\rho = 1/2$. From the typical flow in Fig. 3.3.1(b), we see that the values of the flow in the flow-constant phase coincide with the values of the lower critical concentration ρ_c, and that the flow is proportional to the concentration in the free phase and in the fully jam phase. These behaviors of the average speed and the flow are quite similar to those found in the two-lane model [68].

Figures 3.2(a) and (b) show the typical plots for the width of the jam region and the fluctuations of the width, respectively, for the three transmission rates. We find that the width of the jam region increases linearly with the concentration in the flow constant phase. In Fig. 3.2(b), the fluctuation of width has a peak at the concentration slightly higher than the critical point.

To see the nature of the flow-constant phase, we show typical snap shots. Figures 3.3(a) and (b) show snap shots for $L = 100$ and $r = 0.5$ at $\rho = 0.5$ and 0.33, respectively. It is clearly seen that the flow-constant phase is a mixture of the free phase before the blockage and the fully jam phase after the blockage, as expected. This mixed phase reminds us of the mixture of the gas phase and the liquid phase in wetting phenomena [19]. The tail of the jam, that is, the interface between the free region and the jam region, shows a "saw tooth" pattern, which means that the tail moves backward gradually and abruptly jumps forward; This behavior coincide with our experience in a real traffic jam caused by a road construction. Figure 3.3 (b) is a snap shot near the critical concentration. In this concentration, jam clusters like droplets appear and disappear from time to time.

The transition to the flow-constant phase is not sharp in the figures we have seen so far, in contrast to the case of the pure rule-184 model, where the sharp transition between the free phase and the fully jam phase is seen even for the finite systems. Origin of such rounding of the phase transition is attributed to the finite-size effects. To study the finite-size effects, we plot v, h/L, and $\Delta h^2/L$ near ρ_c for several system sizes and $r = 0.5$, in Figs. 3.4(a), (b), and (c), respectively. We see the clear trend that the transition becomes sharper with increasing the system size. Such size effects at a glance resemble to that near the phase transition point of equilibrium critical phenomena.

3.3.2 Thermodynamic Limit

In this subsection, we discuss the model in the thermodynamic limit $L \to \infty$ and the long-time limit $T \to \infty$.

First, we deal with the pure rule-184 model, that is, $r = 1.0$. Let ρ_p be the particle concentration and $\rho_h = 1 - \rho_p$ be the hole concentration. For $\rho_p > \rho_h$, we expect that the

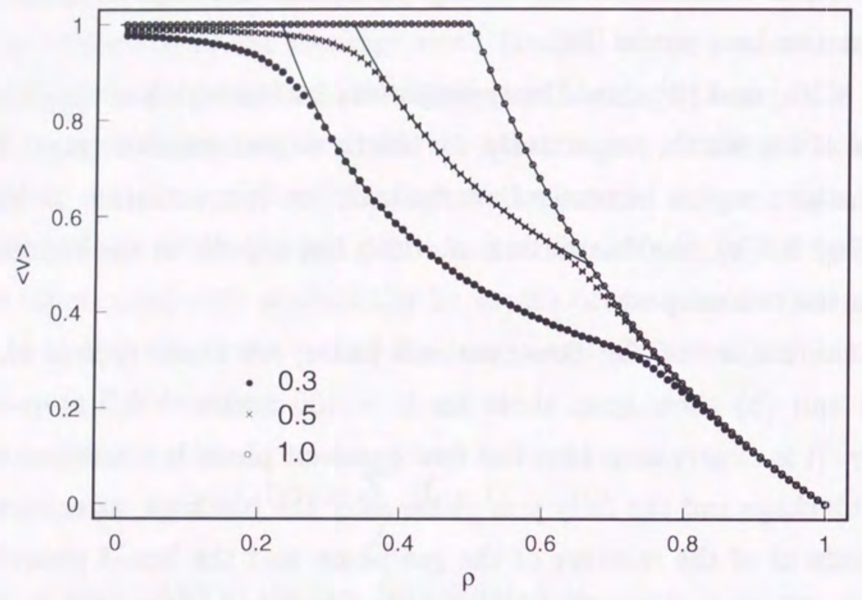

(a) Average Velocity

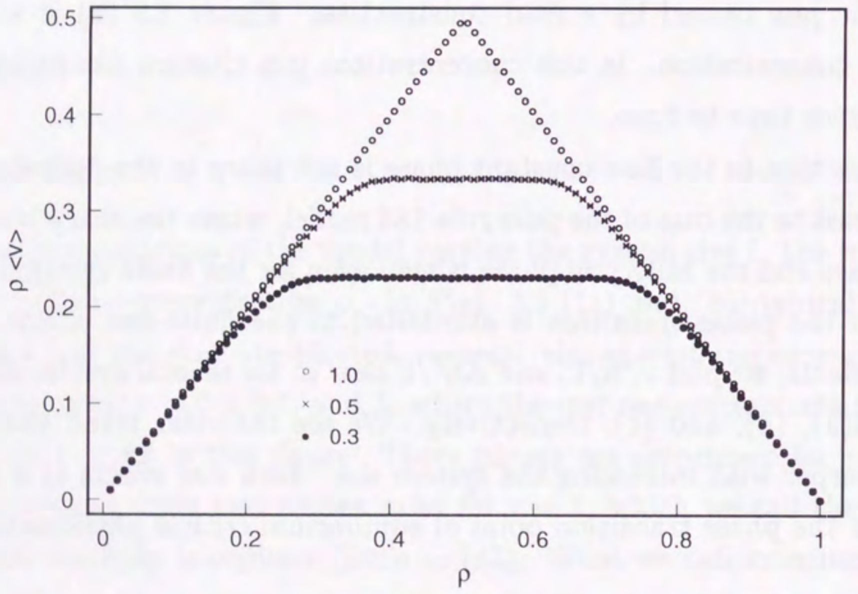

(b) Average Flow

Figure 3.1: (a) Typical results for average speed; Each transmission rate is taken to be $r = 0.3, 0.5, 1.0$ and system size is 99 sites. Solid lines are solutions of mean-field-like analysis. (b) Typical results for flow. Parameters are identical to the same as (a)

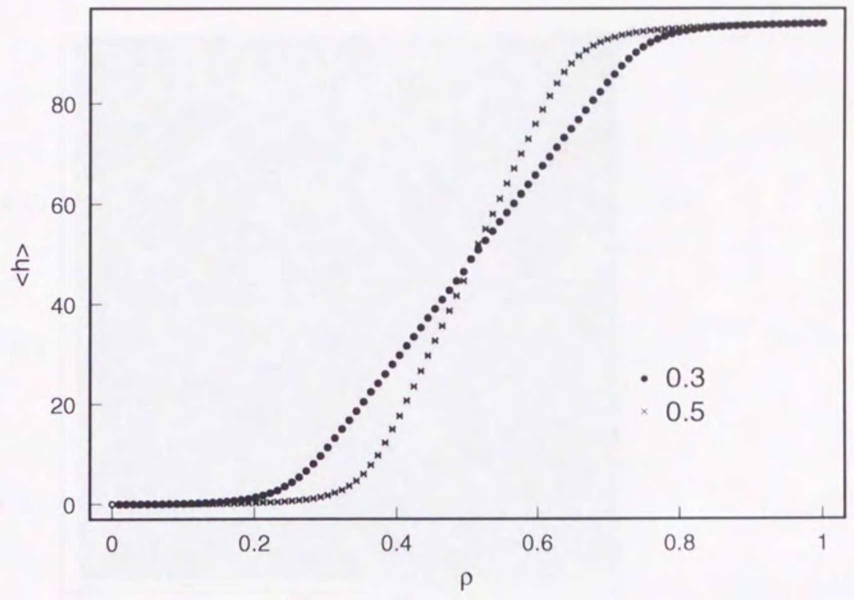

(a) Average Width of Jam Region

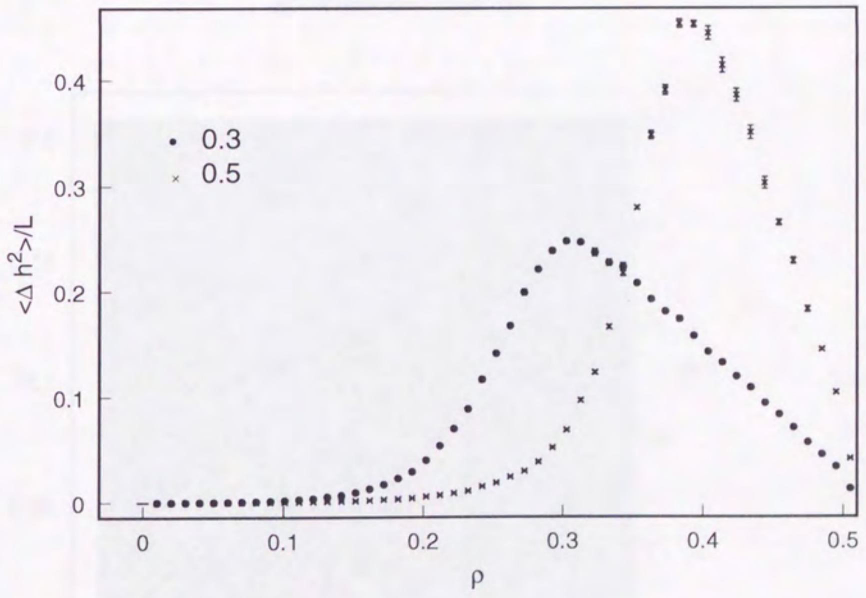

(b) Variance of Fluctuation of Jam Region

Figure 3.2: (a) Typical results for width of the jam region; Each transmission rate is taken to be $r = 0.3, 0.5$ and system size is 99 sites. (b) Typical results for fluctuations of width of the jam region. Parameters are identical to the ones in (a).

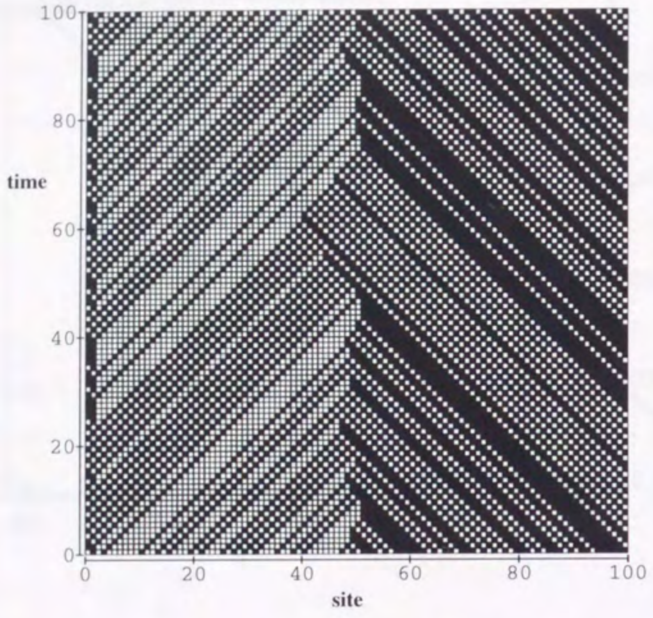

(a) high concentration

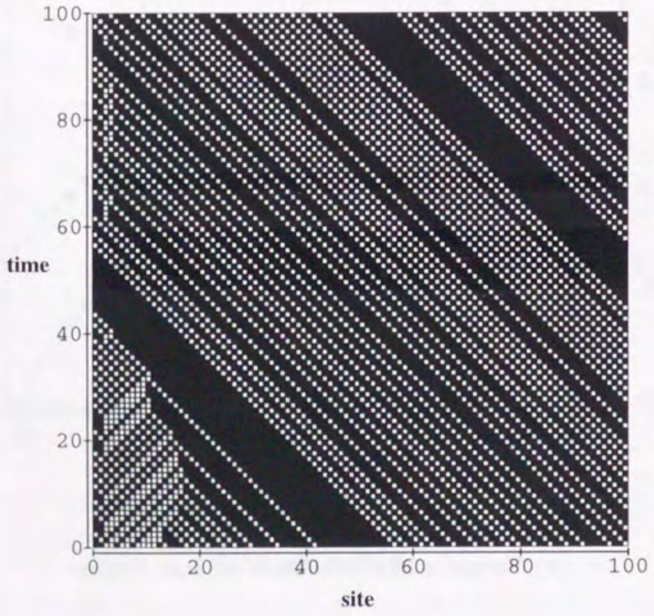

(b) critical concentration

Figure 3.3: (a) Snap shot for 100 sites and transmission rate r = 0.5 at density 0.5. White square is particle and blockage site is 3. (b) Snap shot for 100 sites and transmission rate r = 0.5 at density 0.33, near the critical concentration. White square is particle and blockage site is 3.

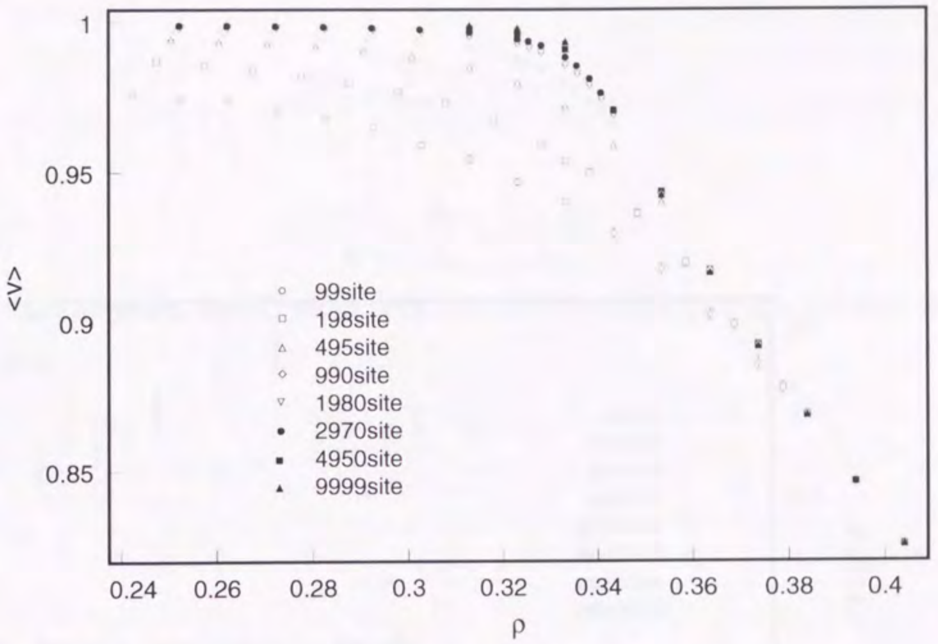

(a) velocity

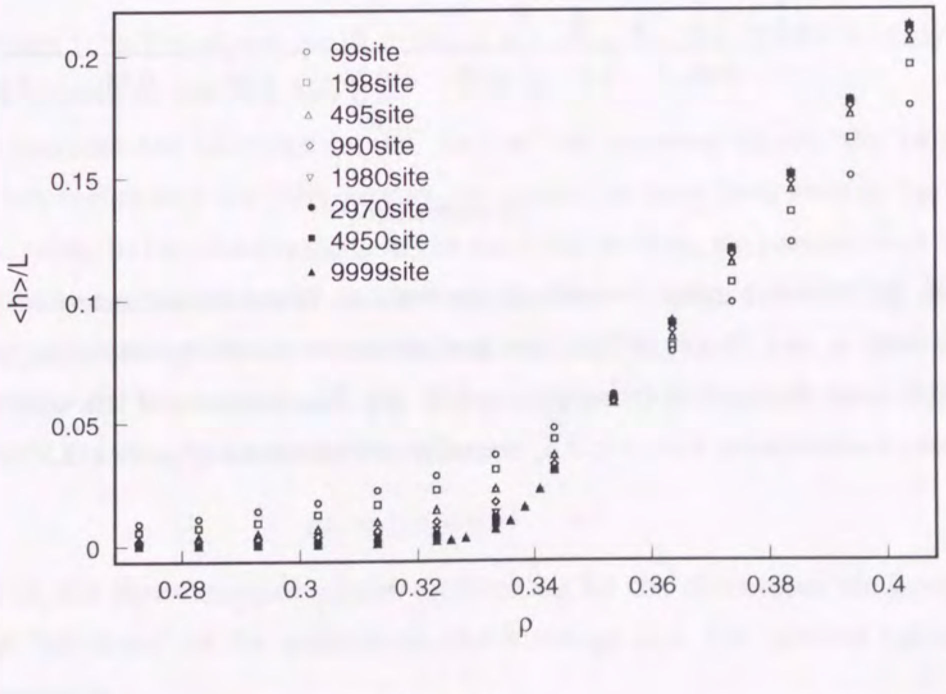

(b) width

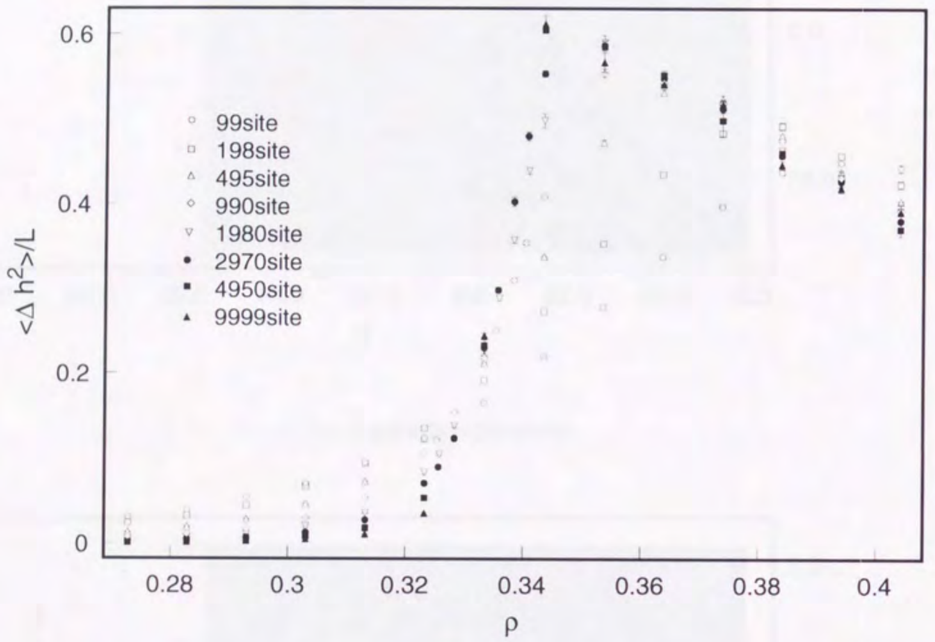

(c) fluctuation

Figure 3.4: (a) Average speed for several system size; transmission rate $r = 0.5$; near the critical density $\rho_c = 1/3$. (b) Width of a jam phase for several system size; transmission rate $r = 0.5$; near the critical density $\rho_c = 1/3$. (c) Fluctuations of the width for several system size; transmission rate $r = 0.5$; near the critical density $\rho_c = 1/3$.

number of movable particles per one step coincides asymptotically with that of movable holes:

$$\lim_{T\to\infty} \frac{1}{T} \sum_i n_i = \rho_h L \ . \tag{3.7}$$

Then

$$\nu = \frac{\rho_h L}{n} = \frac{\rho_h}{\rho_p} = \frac{1-\rho_p}{\rho_p} \ . \tag{3.8}$$

For $\rho_p < \rho_h$, on the other hand, we expect that the movable particle number is just the particle number:

$$\lim_{T\to\infty} \frac{1}{T} \sum_i n_i = \rho_p \ . \tag{3.9}$$

Then

$$\nu = \frac{\rho_p L}{n} = 1. \tag{3.10}$$

Consequently, for the rule-184 CA, we get

$$\nu = \begin{cases} 1 & (0 < \rho < 1/2,) \\ \dfrac{1-\rho}{\rho} & (1/2 < \rho < 1). \end{cases} \tag{3.11}$$

It is well known that the above result is exact not only for the infinite system but also for any finite system of the rule-184 CA.

Next we consider the blockage model. In the flow-constant phase, the two regions, that is, the free region and the fully-jam region coexist as have been seen in the previous section. According to the observations in the previous section, we assume that these two regions are locally equivalent to the corresponding phases in pure rule-184 CA; Especially the particle concentration is assumed uniform in both regions. Let ρ_f and ρ_j be the concentration in the free region and the concentration in the jam region, respectively. For the particle number to conserve, the relation

$$\rho L = \rho_j h + \rho_f (L - h) \tag{3.12}$$

should hold in the flow-constant phase. According to the discussion we have already made on the "life time" of the particle on the blockage site, the particle concentration in the free region is

$$\rho_f = \frac{r}{1+r}. \tag{3.13}$$

Because of the particle-hole symmetry of the model, the transmission of the particle into the free region is equivalent to the transmission of the hole into the jam region. Thus the above discussion also apply to the jam region, and the hole concentration there coincides with ρ_f; The particle-hole symmetry in the jam region is equivalent to

$$\rho_f + \rho_j = 1. \tag{3.14}$$

From Eqs. (3.13) and (3.14), we determine ρ_f and ρ_j as

$$\rho_f = \frac{r}{1+r}, \qquad \rho_j = \frac{1}{1+r}. \tag{3.15}$$

Therefore both the concentration in the free region and the jam region are independent of the total density ρ; Rather, they depend only on the transmission rate r.

From Eq. (3.12), we obtain the width of the jam region as

$$\frac{h}{L} = \frac{\rho - \rho_f}{\rho_j - \rho_f}. \tag{3.16}$$

Combining Eq. (3.15) and Eq. (3.16), we get

$$\frac{h}{L} = \frac{(1+r)\rho - r}{1-r}. \tag{3.17}$$

The critical concentration ρ_c is determined from Eq. (3.17) by putting $h = 0$ and $h = L$; We get $\rho_c = \rho_f$ and ρ_j. Thus by solving Eq. (3.15), the phase boundary in the (ρ, r)-plane in the thermodynamic limit is obtained as

$$r = \frac{\rho}{1-\rho}, \quad \text{and} \quad r = \frac{1-\rho}{\rho}. \tag{3.18}$$

The phase diagram thus obtained is shown in Fig. 3.5.

The average speed in the flow-constant phase can also be calculated. Since the dynamics of the particles is locally rule-184, the particles in the free region move with the speed $v_f = 1$, and the particles in the jam region move with the speed $v_j = (1-\rho_j)/\rho_j$. Thus the average speed of the particles in the flow-constant phase can be written as

$$v = \frac{L}{\dfrac{h}{v_j} + \dfrac{L-h}{v_f}}, \tag{3.19}$$

which gives

$$v = \frac{r}{1+r}\frac{1}{\rho}. \tag{3.20}$$

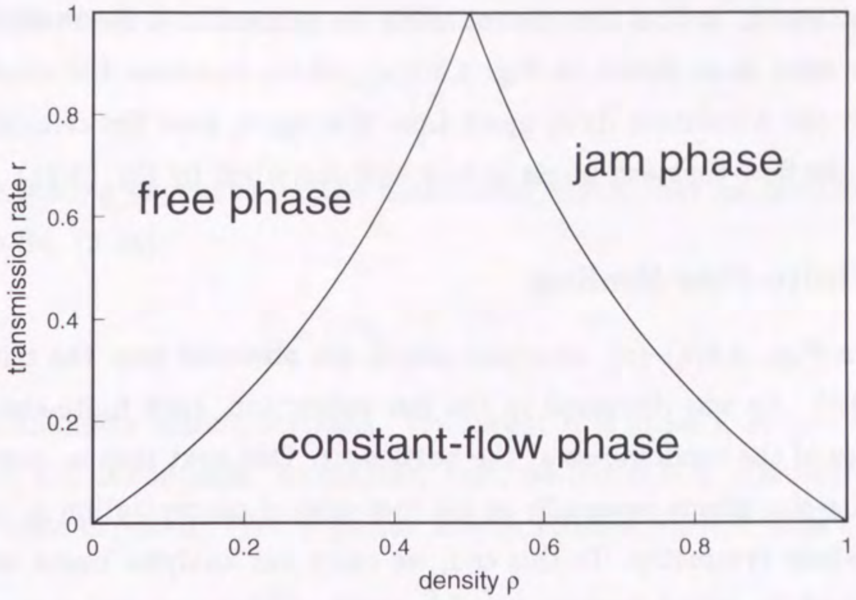

Figure 3.5: Phase diagram for infinite system with blockage; Density ρ vs transmission rate r.

Putting above considerations together, we get the average speed in the thermodynamic limit:

$$v = \begin{cases} 1 & (0 < \rho < \rho_f,) \\ \dfrac{r}{1+r}\dfrac{1}{\rho} & (\rho_f < \rho < \rho_j,) \\ \dfrac{1-\rho}{\rho} & (\rho_j < \rho < 1), \end{cases} \tag{3.21}$$

with $\rho_f = r/(1+r)$ and $\rho_j = 1/(1+r)$. We also get the width of the jam region,

$$h/L = \begin{cases} 0 & (0 < \rho < \rho_f,) \\ \dfrac{\rho - \rho_f}{\rho_j - \rho_f} & (\rho_f < \rho < \rho_j,) \\ 1 & (\rho_j < \rho < 1). \end{cases} \tag{3.22}$$

Since the local motion of the particles in the both regions are treated exactly by applying the results of the rule-184 CA, we expect that the above results are exact in the thermodynamic limit. For finite systems, on the other hand, the effects of randomness at the bottleneck will cause deviations in local motion from the pure rule-184 CA near the bottleneck; Such deviations, however, is expected to remain only in some small region near the bottleneck, so that they do not affect the properties in the thermodynamic limit. In fact, the solid lines shown in Fig. 3.3.1(a), which represent the relation Eq. (3.21), very well to the simulation data, apart from the region near the critical concentration; Especially, the flow-constant phase is very well described by Eq. (3.21).

3.3.3 Finite-Size Scaling

As shown in Figs. 3.4(a)–(c), clear size effects are observed near the critical concentration $\rho_c = 1/3$. As was discussed in the last subsection, such finite-size effects are the consequences of the randomness at the bottleneck. Our next step is to study the nature of these finite-size effects especially at the first critical concentration $\rho_c = \rho_f$, because of the particle-hole symmetry. To this end, we carry out analyses based on the finite-size scaling method [5], which is widely used in the field of the critical phenomena.

First, we consider the finite-size scaling of the average speed. Suppose ν converges to 1 with the system size L at the critical point with a power law:

$$1 - \nu \sim L^{\xi} , \tag{3.23}$$

where we introduced a scaling dimension ξ for the average speed. Following the usual procedure for the finite-size scaling analysis, we assume $1 - \nu$ is expressed in a scaling form

$$1 - \nu = L^{\xi} f_{\nu}\left(\frac{\rho - \rho_c}{\rho_c L^{\zeta}}\right) , \tag{3.24}$$

where f_ν is an unknown scaling function whose argument is the reduced concentration $(\rho - \rho_c)/\rho_c$ scaled by the system size. The exponent ζ is the scaling exponent for the reduced concentration. For the concentration much larger than ρ_c (in the off-critical region), the flow is expected to approach the constant value ρ_c. If we take that into account, we have to assign the same exponent to both the average speed and the reduced concentration, that is, we put $\xi = \zeta$. Thus the expected scaling relation for ν becomes

$$1 - \nu = L^{\xi} f_{\nu}\left(\frac{\rho - \rho_c}{\rho_c L^{\xi}}\right) . \tag{3.25}$$

Next we consider the finite-size scaling for the width of the jam region. The normalized width h/L is also expected to vanish in the thermodynamic limit at ρ_c; Thus we suppose again the power-law dependence of h/L on L:

$$\frac{h}{L} \sim L^{\phi} , \tag{3.26}$$

where ϕ is the scaling exponent for the normalized width. Let us assume the scaling form similar to Eq. (3.25):

$$\frac{h}{L} = L^{\phi} f_h\left(\frac{\rho - \rho_c}{\rho_c L^{\xi}}\right) , \tag{3.27}$$

where f_h is an unknown scaling function. We expect h is order L at $(\rho - \rho_c)/\rho_c \gg 1$, and thus expect h/L is constant. To consider that, we put $\phi = \xi$. Therefore ν and h/L scale with the same exponent. The expected scaling relation for h/L thus becomes

$$\frac{h}{L} = L^{\xi} f_h\left(\frac{\rho - \rho_c}{\rho_c L^{\xi}}\right) . \tag{3.28}$$

Finally, from a simple dimension counting, we expect that the scaling relation for the fluctuation of the width is written as

$$\frac{\Delta h^2}{L} \sim L^{2\xi+1} f_{\Delta h}\left(\frac{\rho - \rho_c}{\rho_c L^{\xi}}\right) \tag{3.29}$$

with an unknown scaling function $f_{\Delta h}$. It should be noted that only a single scaling exponent ξ appears in these scaling relations. If the scaling width h/L at ρ_c is simply a consequence of random fluctuations, it may behaves as $L^{-1/2}$; Therefore, from Eq. (3.26) we expect $\xi = -1/2$ for random fluctuation.

We investigate the validity of the scaling relations derived above with the simulation data. We show results only for the transmission rate $r = 0.5$ in the following. Figure 3.6 shows the scaled average speed $(1 - \nu)L^{1/2}$ against the scaled reduced concentration. We used $(\rho - \rho_c)/\rho$ as the reduced concentration instead of $(\rho - \rho_c)/\rho_c$ used in Eq. (3.25), just because we can get better scaling plot with the former than with the latter. Such change of the definition for the reduced concentration, however, does not affect the leading scaling behavior; It, in fact, only gives an analytic correction-to-scaling term. We see in the scaling plot that all the data for different system sizes indeed collapsed onto a single scaling function. For $\rho - \rho_c > 0$, this scaling function seems to approach a linear function of $(\rho - \rho_c)L^{1/2}/\rho$. This behavior is consistent with the fact that the flow takes the constant value at ρ_c.

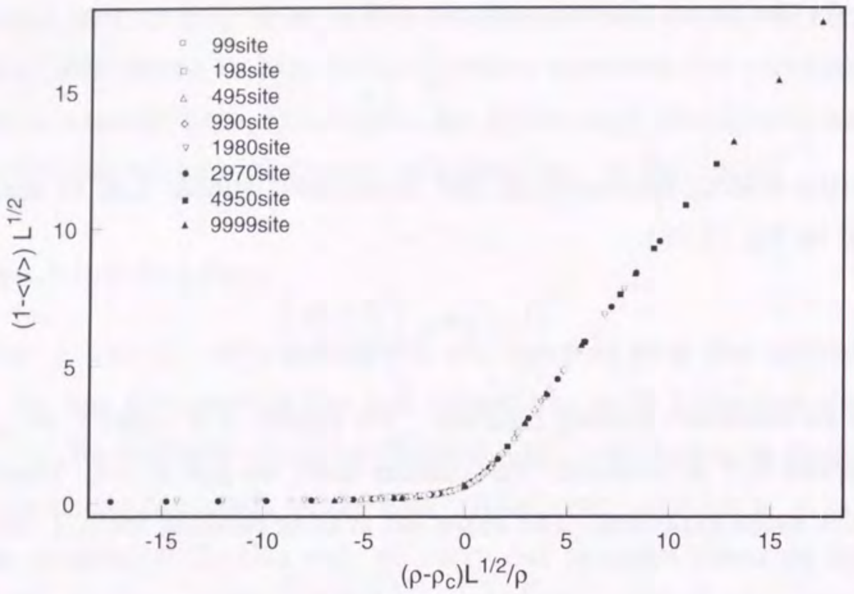

Figure 3.6: Scaled average speed for several system size; transmission rate r=0.5; near the critical density. $\rho_c = 1/3$.

In Fig. 3.7, we plot the scaled width of jam phase $hL^{1/2}$ against the scaled reduced concentration. We took $(\rho - \rho_c)L^{1/2}$ for the horizontal axis. Again we see that all the data fall on a single curve. The scaling function seems to approach the linear function of $(\rho - \rho_c)L^{1/2}$, for $\rho - \rho_c > 0$; That again is consistent with the fact that h/L in the flow-constant phase is proportional to $\rho - \rho_c$.

So far, we have seen that the simulation data are consistent with $\xi = -1/2$. Putting this value into Eq. (3.29), the scaling relation for the fluctuation of width becomes

$$\frac{\Delta h^2}{L} \sim L^0 f_{\Delta h}\left(\frac{\rho - \rho_c}{\rho_c L^{-1/2}}\right) . \tag{3.30}$$

In cases of usual critical phenomena, the power L^0 implies the logarithmic divergence. In the present case, however, where $\xi = -1/2$ is a consequence of the random fluctuation, the power L^0 may simply imply that $\Delta h^2/L$ does not depend on L. In Fig. 3.8, we plot the fluctuation of width $\Delta h^2/L$ without rescaling by L against the scaled reduced concentration. We see a somewhat different scaling behavior from those of v or h/L: While all the data for the concentration lower than the peak collapse into a single curve, the data for higher concentration do not scale. Thus the scaling relation Eq. (3.30) holds

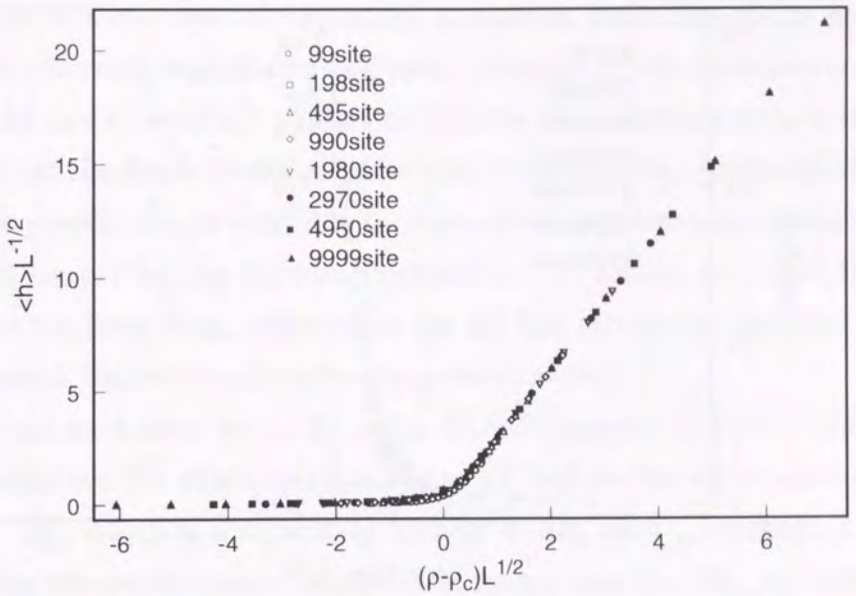

Figure 3.7: Scaled width of jam phase for several system size; transmission rate is 0.5; near the critical density $\rho_c = 1/3$.

only for the concentration lower than the peak, which appears at a small positive value of the reduced concentration. The size dependence of $\Delta h^2/L$ for higher concentration can be deduced from the raw plot in Fig. 3.4(c). We can see that $\Delta h^2/L$ for the concentration higher than the peak is almost independent of the system size without rescaling of the concentration. This behavior in this region coincides with the result for TASEP with blockage, where the unnormalized fluctuation of the shock-front position in the mixed phase behaves as $L^{1/2}$ [38], although the definition of the interface position is different between two models.

3.4 Summary and Discussion

We have examined a one-dimensional cellular automaton model of the traffic flow with a bottleneck, by introducing a blockage into the rule-184 CA. We found the formation of the jam region after the bottleneck when the car concentration exceeds some critical value determined by the transmission rate of the bottleneck. Consequently, in the intermediate range of the concentration between free phase and the fully-jam phase, that is, the

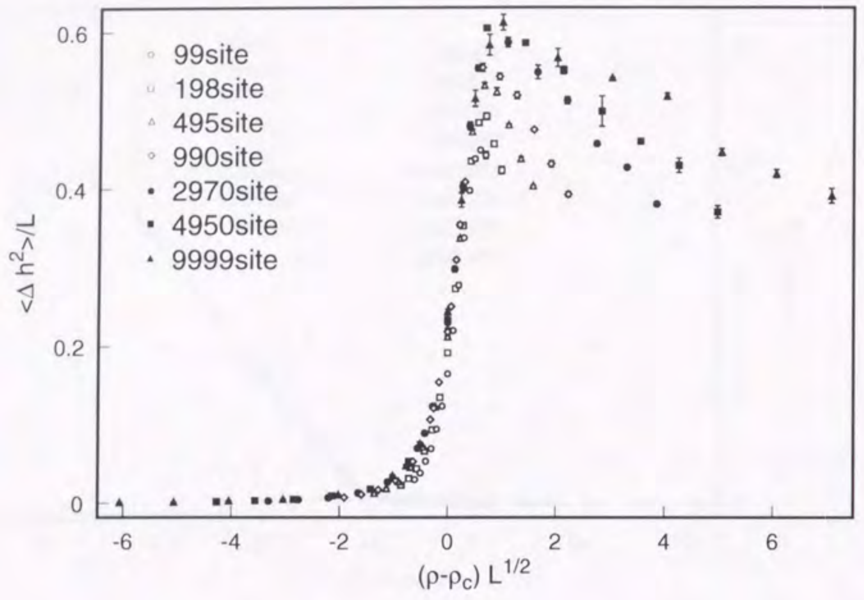

Figure 3.8: Scaled fluctuations for several system size; transmission rate is 0.5; near the critical density $\rho_c = 1/3$.

flow-constant phase, the coexistence of free region and the fully-jam region is observed with well-defined boundary between them. Such behaviors agree with our experience in real traffic ways, when road constructions or tunnels exist. In fact, we sometimes find ourselves trapped in a traffic jam all of a sudden, after having driven freely. In the fully-jam region after the blockage of the present model, a car does not move constantly; Rather it moves and stops alternately. Such intermittent motion also agrees with our real experience. Thus, the model treated in the present study can represent some realities despite its simple structure.

We have discussed the properties of the traffic flow in the thermodynamic limit, where the fluctuations due to the randomness at the blockage can be ignored. The expressions we obtained for the average velocity and the average flow reproduce the simulation results very accurately apart from the concentration near the critical value. Since the local motions of the particles are treated exactly by applying the known results of the rule-184 CA, the above expressions are expected to be exact in the thermodynamic limit. We also obtained the phase diagram of the present model in terms of the concentration and the transmission rate.

By the computer simulation of the model, the strong finite-size effects near the transition point was observed, which were analyzed by means of the finite-size scaling. Since the pure rule-184 model does not exhibit such finite-size effects, they are induced by a randomness only at the single blockage introduced in the system. Although the finite-size behaviors of the present model resemble to those of the equilibrium critical phenomena, they are caused simply by the random fluctuations. It should be noted that no such finite-size behaviors have been reported so far for the stochastic two-lane model [68], although the overall behavior is close to the present model.

Exact solutions have been found for some TASEP-related models [17, 18]; Janowsky and Lebowitz obtained the exact solutions on small lattices for the same model as they treated in Ref. [38], which is a stochastic TASEP model with a blockage, and extrapolated them to the thermodynamic limit by Padé approximation [39]. As another related model in the context of TASEP, Schütz have found the generalized-Bethe-ansatz solution for the two-sublattice deterministic version of the TASEP with a blockage [93], where the system is divided into two sublattices and the particles in the same sublattice move simultaneously. Although these three models including the present CA-based model resemble with each other at a glance, their update dynamics is quite different. Consequently, they behave differently in detail; Especially the phase boundaries do not coincide with each other. Recently analytical and numerical treatments of ASEP have been developed extensively; Some remarkable results are obtained [33, 34, 86].

Chapter 4

Coupled-Map Modeling of Traffic Flow

4.1 Introduction

In order to understand the traffic flow phenomena, many models have been proposed and tested so far. Among them we will concentrate on microscopic models below. In 1950's, for instance, sets of first-order simultaneous differential equations, called car-following model, were used for representing traffic flow. They, however, had a difficulty in describing both the free flow and the congested flow separated by the jamming transition on unified ground [9, 21, 49, 84]. Recently more realistic models have been proposed by physicists, which successfully reproduce several observed traffic phenomena including the jamming transitions. They are classified into three categories according to structure of the space-time used for constructing the models. Cellular automaton (CA) models [6, 66–68, 70–73, 92, 96, 99, 102, 108]are in the first category. They treat both time and space as discrete; Thus states of vehicles are described by discrete variables. Among CA models, certainly the best known and the most successful model is the one proposed by Nagel and Schreckenberg (NS model) [73]. In the second category, both time and space are treated as continuous. Models under this category describe the traffic flow by a set of differential equations using continuous variables for expressing states of vehicles. Conventional car-following models fall within this category. Recently, Bando *et al.* proposed a new model called the optimal velocity model (OV model), which describes the motion of the cars by second-order differential equations [3, 4, 95]. It exhibits the jamming transition in contrast with former car-following models. In the last category, which is the main subject of this article, the space is treated as continuous, but time as discrete. Thus states of vehicles are expressed by continuous variables, but they are updated at discrete time steps. A few models have been constructed in this category [51, 70, 106, 107, 109]. We call models of this type "coupled-map" models. Coupled-map based modeling bas several advantages over others modeling scheme, as will be described in the following sections. The coupled tanh-map (CTM) model proposed by the present author belongs to this category [106, 107]. The aim of this chapter is to give a general concept of the coupled-map type modeling and results obtained by computer simulations of CTM model. Another coupled-map based model is also presented in the proceedings [97].

The organization of this chapter is as follows: In Sec. 4.2.1 after the general concept of the coupled-map modeling is briefly discussed, CTM model proposed by the author is described. Some results obtained by computer simulations are shown in Secs. 4.3–4.5; We focus our attention on the density fluctuations, the shape of fundamental diagrams and the entropy of traffic flow. The last section is devoted to summary and discussions.

4.2 Coupled-Map Traffic Flow Model

4.2.1 Concept

In this subsection, we give a general discussion about bottom-up modeling of the traffic flow using the concept of the coupled map. Modeling procedure will be as follows: First, essentials of a motion of a single vehicle are extracted and they are made into a form of mathematical model. Since time is taken as a discrete variable, the single vehicle motion is described by a map which updates internal variables of the vehicle one time step further. Next, an array of such vehicles are considered. The maps for different vehicles are connected so that they describe essentials of the interactions between the vehicles properly. All these maps are updated simultaneously by parallel discrete-time dynamics.

Here we take the velocity and the position as the internal variables of the vehicles. Then in the coupled-map models in general, these internal variables at t-th time step

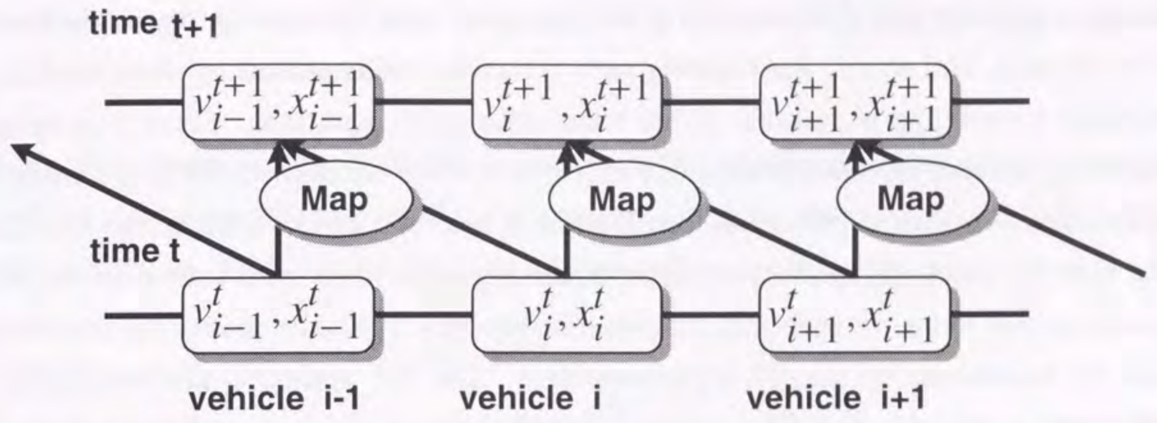

Figure 4.1: Conceptual diagram of coupled-map modeling for one-dimensional traffic flow: An array of vehicles is considered. Each vehicle has the position and velocity as internal variables. These variables are updated by discrete time dynamics according to a map which takes the velocity and headway distance as inputs.

are updated one step further by the following relations:

$$v_i^{t+1} = \mathbf{Map}_i(v_i^t, \Delta x_i^t) \ , \quad (4.1)$$

$$x_i^{t+1} = v_i^t + x_i^t \ , \quad (4.2)$$

where $\mathbf{Map}_i$ expresses a map for updating the velocity of i-th vehicle, which takes the velocity v_i and the headway distance Δx_i to the preceding vehicle at time t as the inputs. The second equation defines a (trivial) map for updating the position x_i. The headway distance is defined as $\Delta x_i^t \equiv x_{i+1}^t - x_i^t + l$, where l is the length of the vehicle. In Fig. 4.1, a conceptual diagram of the coupled-map modeling is shown. This type of dynamics is sometimes called the Coupled Map Lattice (CML) [44], because maps are aligned in an array (one-dimensional, in the present case). In the above equations, effects of interactions with other vehicles enter only through the headway distance to the preceding vehicle. In principle, one can choose more general types of maps for taking other effects into account, *e.g.*, the relative velocity to the preceding vehicle.

One of the advantages of employing coupled-map type modeling is that it can handle rule-based decision-making. Human behavior are not always smooth as what can be described by differential equations. In fact, drivers are sometimes obliged to make decisions in real traffic situations. Sudden braking in case of emergencies is a typical example.

Decision-makings are also required when changing lanes for overtaking, when turning at crossroads, and so on. For treating such behaviors accompanied by decision-making, rule-based modeling is suitable rather than differential equations. Since coupled-map modeling is based on discrete time dynamics, rule-based decision-makings are easily implemented. As a consequence, we can introduce several road conditions into the model like a traffic blockage, multi-lane roads, crossings, open roads with inflow and outflow, junctions and so on. In addition, parallel discrete-time dynamics makes the model suitable for simulation by parallel supercomputers. The CA approach also is suitable for rule-based modeling. But the coupled map approach is much more flexible than CA, because the internal variables describing the state of the vehicle are not restricted to integer values. Coupled-map based models can describe both smooth behaviors and rule-based decision-makings on unified ground. For the above reasons, we believe that the coupled-map type modeling is the most promising modeling scheme for describing traffic flow realistically.

The coupled map modeling has formally the same structure with the first order solver for first-order ordinary differential equations, that is, Euler's method. But here, we by no means intend to solve any differential equations faithfully by time discretization. In fact, the model presented in the next subsection has no corresponding differential equations in continuous time limit.

4.2.2 Model

Let us move on to the CTM model we will actually use in the following sections. What we have to do for making model definite is to give an explicit form of the map $\mathbf{Map}_i$.

According to the plan presented in the preceding subsection, we first consider essentials of a free motion of a single vehicle. The following three are what we consider important for making the models of the free motion:

- **Preferred velocity $v^{\text{pre.}}$ of the driver:** When there is no disturbance by other vehicles or by road conditions, the driver tends to run a car with this preferred velocity. It differs from driver to driver; Some wants to run fast and some slowly.
- **Acceleration and deceleration:** When the velocity is slower (faster) than $v^{\text{pre.}}$, then a vehicle is accelerated (decelerated) until its velocity fits $v^{\text{pre.}}$.

- **Velocity fluctuation:** Even if the velocity is close to $v^{\text{pre.}}$, it is not kept constant. Rather, it fluctuates around $v^{\text{pre.}}$

Taking above essentials into account, we construct the velocity updating map. In general, it will be a function of the velocity, the position and the preferred velocity. But here, for simplicity, we use the following map for describing the free run:

$$\begin{aligned} v^{t+1} &= F(v^t; v^{\text{pre.}}) \\ &\equiv \gamma v^t + \beta \tanh\left(\frac{v^{\text{pre.}} - v^t}{\delta}\right) + \epsilon \ , \end{aligned} \tag{4.3}$$

where v^t and $v^{\text{pre.}}$ are the velocity of the vehicle at time t and its preferred velocity, respectively. β, γ, δ and ϵ are parameters. The return maps of F are presented in Figs. 4.2. Throughout this article, we take parameters $\beta = 0.6$, $\delta = 0.1$, $\epsilon = 0.1$. If $\gamma = 1$, the free motion map expresses constant acceleration and deceleration toward $v^{\text{pre.}}$; Once the velocity becomes close to $v^{\text{pre.}}$, on the other hand, the map describes periodic oscillation of the velocity. Velocity fluctuations made by human drivers, however, are not periodic in reality. For more realistic generation of the fluctuations, we take $\gamma = 1.001$. Then the fluctuation becomes chaotic, while the acceleration and deceleration are still kept approximately constant. This chaotic fluctuation is caused by the overshoot in velocity control; Considering the nature of human responses and mechanical ones as well, the overshoot is indeed one of the natural origins of the velocity fluctuations. But note that we do *not* insist that it is really the most important origin. We introduce it here just for expressing the fluctuations in some sense naturally. From the viewpoint of fast computation, on the other hand, the chaotic fluctuation used here is better than the conventional random numbers generated by pseudo random number generators.

Using this map, we plot a space-time trajectory and time series of velocity in Figs. 4.3: Slight fluctuation originated from chaotic motion of the map F is seen and chaotic fluctuation is clearly observed in the time-series of the velocity.

Next turn to the interactions between vehicles. Following three is what we consider important about the interactions:

- **Free run when the headway distance is large:** When the headway distance is large enough, the vehicle runs freely according to the map (4.3).

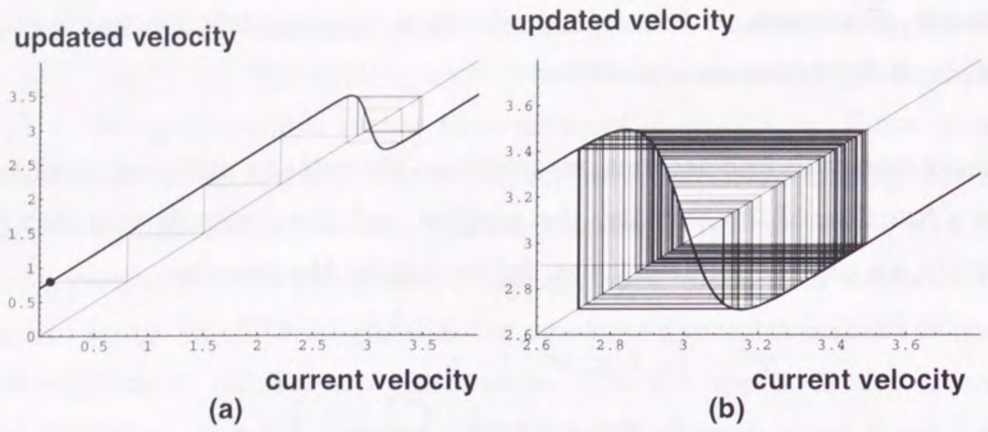

Figure 4.2: The return maps of the free motion map F: Parameters are taken to be $\beta = 0.6$, $\delta = 0.1$, $\epsilon = 0.1$ and $v^{pre.} = 3$. (a) $\gamma = 1$; The map expresses the constant acceleration and deceleration toward $v^{pre.}$. The velocity oscillates periodically near $v^{pre.}$. (b) $\gamma = 1.001$; The acceleration and deceleration are still kept constant approximately. The velocity fluctuation near $v^{pre.}$ becomes chaotic.

- **Sudden braking when the headway distance is small:** When the headway distance becomes too small, the vehicles are forced to stop for avoiding a collision.
- **Smooth speed control between these two situations:** When the headway distance is not sufficiently large for vehicles to run freely, the velocity is kept slower than $v^{pre.}$

For expressing above essentials, we use the following maps:

$$v_i^{t+1} = \begin{cases} G(v_i^t, \Delta x_i^t) & \text{for } v_i^t \leq \Delta x_i^t < \alpha v_i^t \ , \\ B(\Delta x_i^t) & \text{for } \Delta x_i^t \leq v_i^t \ , \end{cases} \tag{4.4}$$

where

$$G(v_i^t, \Delta x_i^t) \equiv \frac{F(v_i^t; v_i^{pre.}) - v_i^t}{(\alpha - 1) v_i^t} (\Delta x_i^t - v_i^t) + v_i^t \ , \tag{4.5}$$

$$B(\Delta x_i^t) \equiv \Delta x_i^t \ . \tag{4.6}$$

α is a constant parameter larger than 1. We call $G(v_i^t, \Delta x_i^t)$ and $B(\Delta x_i^t)$ the deceleration map and the braking map, respectively. The deceleration map seems to be a little

---

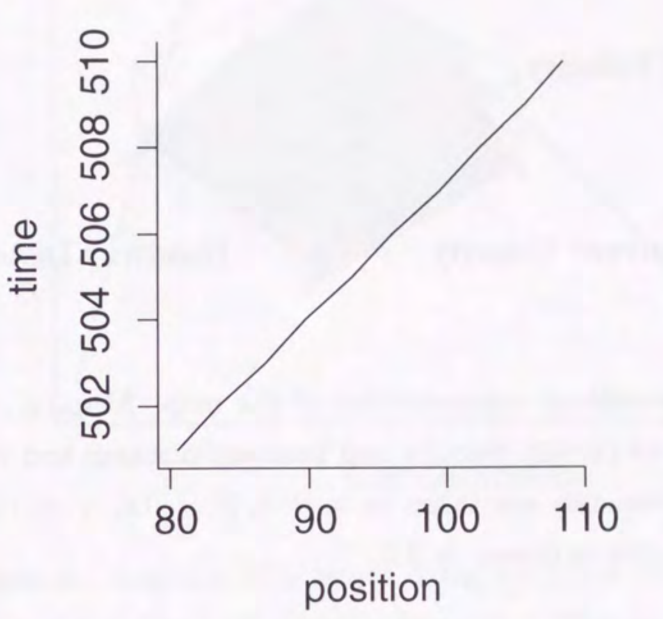

(a) space-time trajectory

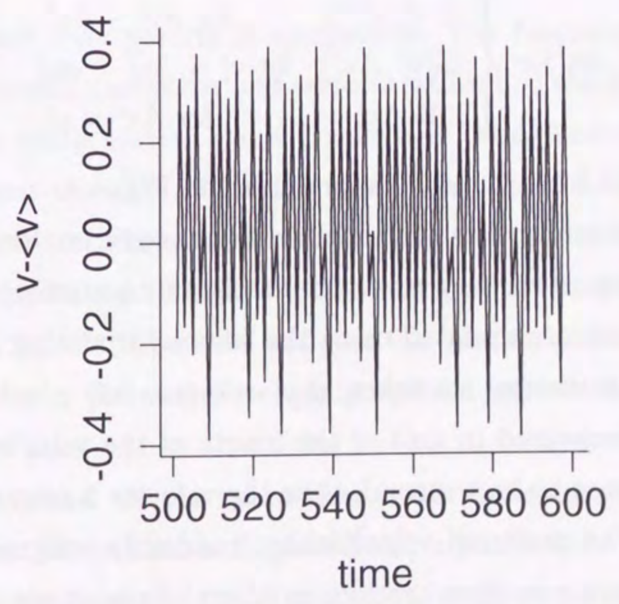

(b) time series of velocity

Figure 4.3: One vehicle motion: (a) Space-time trajectory and (b) time series of velocity. An initial velocity and a preferred velocity are taken to be 3.0 . We show the trajectory of (a) 9 time steps and (b) 100 time steps after discarding 500 steps. Slight fluctuation originated from chaotic motion is seen in (a) and clearly chaotic fluctuation is observed in (b).

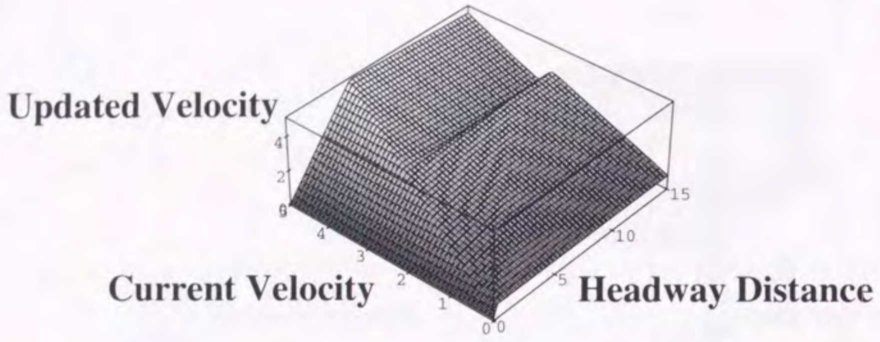

Figure 4.4: Three dimensional representation of the map: $\mathbf{Map}_i(v_i^t, \Delta x_i^t)$. Horizontal two axes represent input current velocity and headway distance and vertical axis shows updated velocity. Parameters are taken as $\alpha = 4$, $\beta = 0.6$, $\gamma = 1.001$, $\delta = 0.1$ and $\epsilon = 0.1$. Preferred velocity is chosen as 3.0.

complicated. But after all it expresses that the velocity is proportional to the headway distance.

Gathering everything up, we define the velocity updating map, $\mathbf{Map}_i(v_i^t, \Delta x_i^t)$, as follows:

$$\mathbf{Map}_i(v_i^t, \Delta x_i^t) = \begin{cases} F(v_i^t; v_i^{pre.}) & \text{for } \alpha v_i^t \le \Delta x_i^t \ , \\ G(v_i^t, \Delta x_i^t) & \text{for } v_i^t \le \Delta x_i^t < \alpha v_i^t \\ B(\Delta x_i^t) & \text{for } \Delta x_i^t \le v_i^t \ . \end{cases} \tag{4.7}$$

Three-dimensional form of $\mathbf{Map}_i(v_i^t, \Delta x_i^t)$ is presented in Fig. 4.4.

One step of the simulation consists of the following procedures: First the headway is measured for all the vehicles. Next they move simultaneously according to the map (4.2). Finally values of the velocity are updated using the velocity updating map (4.7).

In the present study, parameters are taken as $\alpha = 4$, $\beta = 0.6$, $\gamma = 1.001$, $\delta = 0.1$ and $\epsilon = 0.1$. The distance is measured in unit of the length of the vehicle; If we take it to be 5 meters and the time step to be 1 second, then the velocity 3 corresponds to 15 m/s or 54 km/h or 87 mph. The preferred velocities are randomly assigned to the vehicles within the range $[2.0, 4.0]$ using uniform random numbers. Simulations are performed for a single-lane closed circuit with the number of vehicles fixed; No overtaking is allowed then. Initially, the vehicles are put in the circuit randomly.

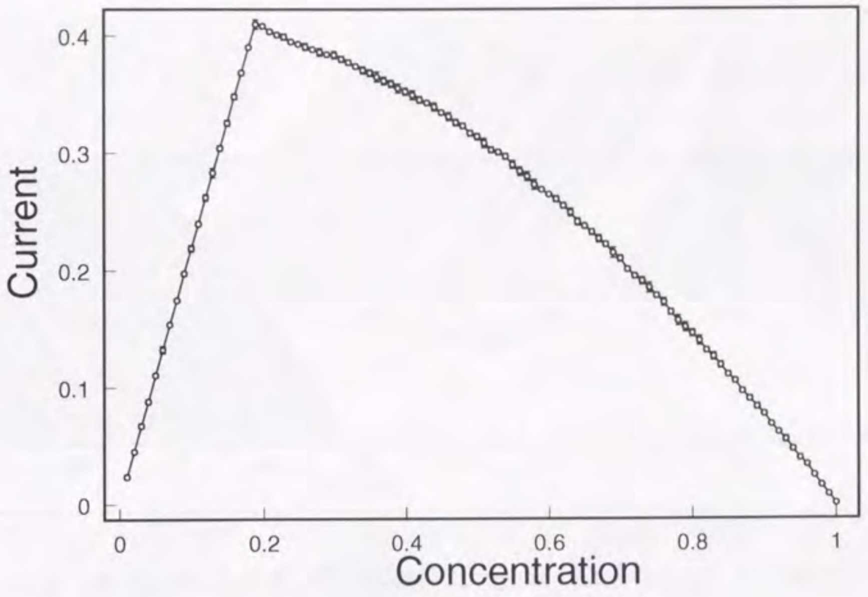

Figure 4.5: Fundamental diagram: The length of the system is 1000. Averages over 1000 steps are taken after discarding 5000 steps for relaxation. The averages are taken further over 10 independent samples.

4.2.3 Basic Results

First, we show some basic results of simulations. The fundamental diagram, that is, the relation between traffic current q and concentration ρ is shown in Fig. 4.5. q and ρ are measured over the whole system and averaged over time. There is a critical concentration ρ_c where the current takes its maximum value. This concentration separates two phases: The free flow phase and the congested flow phase. At concentration lower than ρ_c, the current is proportional to ρ. The above characters of the fundamental diagram is similar to those obtained by the NS model and the OV model, although more or less different in detail; For example, the curve is slightly upward convex in the free flow phase of the OV model.

In Figs. 4.6, 4.7, and 4.8 the space-time trajectories are presented. Figure 4.6 is for the free flow phase. We can see a single cluster, *a platoon*, of vehicles. The formation of the platoon is a consequence of the distribution of the preferred velocity, because all the vehicles are forced to follow the slowest one. In addition, weak density waves propagating downstream are found in the trajectory; They appear and disappear from time to time.

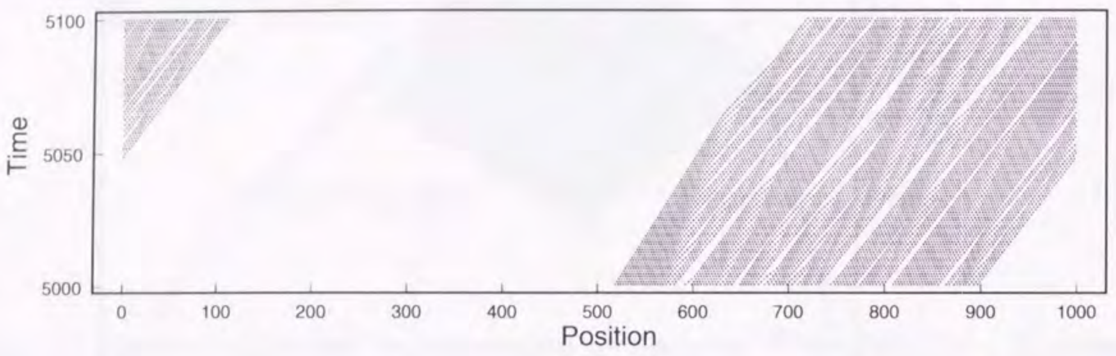

Figure 4.6: Space-time trajectories in the free flow phase: $\rho = 0.1$.

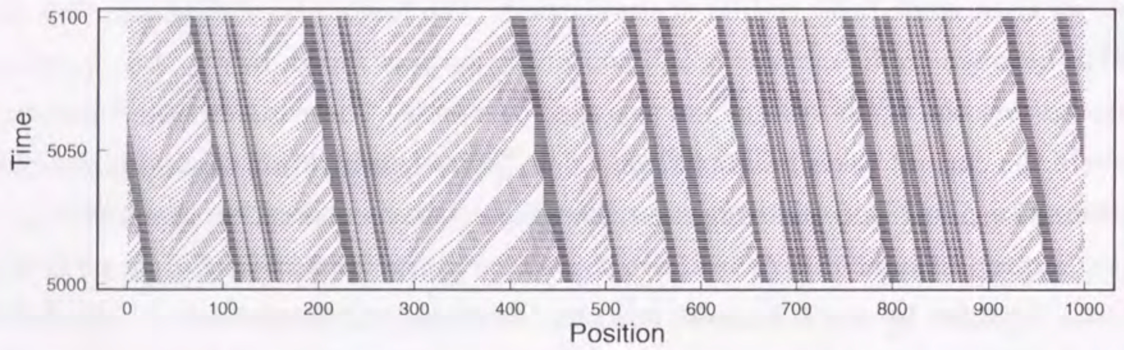

Figure 4.7: Space-time trajectory in the congested flow phase: $\rho = 0.3$. A number of jams are observed, which propagate upstream with the definite velocity $-1/2$.

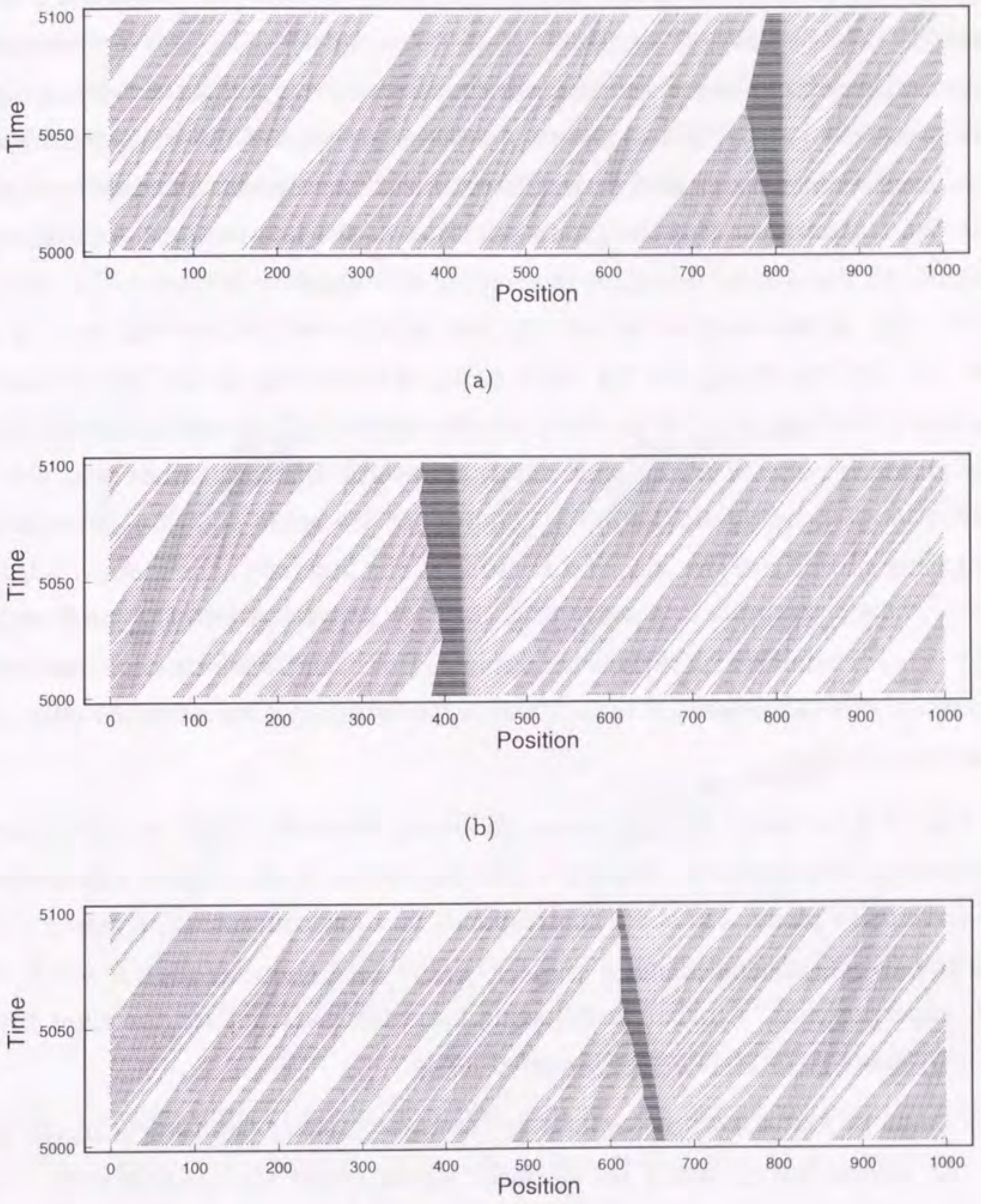

(a)

(b)

(c)

Figure 4.8: Space-time trajectories near the critical concentration: $\rho = 0.193$. They are for different samples. One jam section is seen in all the samples with different group velocities. The group velocity of the jam is (a) ~ 0, (b) ~ -0.1, and (c) exactly $-1/2$, respectively.

Similar density wave is indeed observed in the real traffic flow [50]. Figure. 4.7 is for high concentration. A number of clear traffic jams are recognized; The jam sections propagate upstream with definite *group velocity*, which is exactly $-1/2$. All the vehicles are forced to stop inside the jams. The last three trajectories are taken from the simulations of the same concentration near ρ_c, but with different initial conditions. One jam section is seen each in the trajectories. But the group velocities of the jam sections are different from each other: in Fig. 4.8 (a) it is close to zero, (b) it is negative but not $-1/2$, and (c) it is exactly $-1/2$. In the cases of (a) and (b), the vehicles are still moving even in the jam section. In the case of (c), on the other hand, vehicles stop in the jam section. Thus the nature of the jam in (c) is the same as ones appear in high concentration (Fig. 4.7). So the group velocity of traffic jams can take several different values near the critical concentration depending on the initial conditions. We made additional simulations for investigating stability of the jam, and found that the jams with the group velocity other than $-1/2$ are metastable in a sense that they are converted into the jams with group velocity $-1/2$ if small perturbations are applied. But such transformation does not occur spontaneously in the present model. These metastable jams are observed only near the critical concentration.

In Figs. 4.9, we show the typical car-following behavior, which is a trajectory of a test vehicle with a preferred velocity 3.0 in the actual traffic stream represented in a headway-velocity plane. Fig. 4.9(a) corresponds to a low concentration case $\rho = 0.1$, (b) is near the critical concentration $\rho = 0.2$, (c) is in high concentration $\rho = 0.3$, and (d) is their superposition. All the car-following trajectories except for the right branch in Fig. 4.9(b) make counterclockwise bounded loops.

The loops in Fig. 4.9(a) correspond to the movement of the vehicle in the platoon where the vehicle travels using the deceleration map and the braking map. The left boundary in the same figure is determined by the braking map and the upper one is decided by the feature of the deceleration map. Figure 4.9(b), on the other hand, is near the critical concentration. The trajectory seems to be decomposed into three parts: First is the dense loops same as one at low concentration. Second is triangular loops containing the first loops inside. Its lower right boundary is determined by the properties of acceleration of the deceleration map. The last one is the bunch seen in the right of the triangular loops. It corresponds to the free motion of the test vehicle near the preferred velocity. Fluctuation of velocity near the preferred velocity is seen. Figure 4.9(c) is in a higher concentration than (b). In this case, the upper boundary is not clearly seen, because the vehicle cannot accelerate near the preferred velocity. In contrast with the two trajectories in lower concentration, the loops touch the origin. This result shows that the jam regions where the vehicles stop inside exist in this concentration.

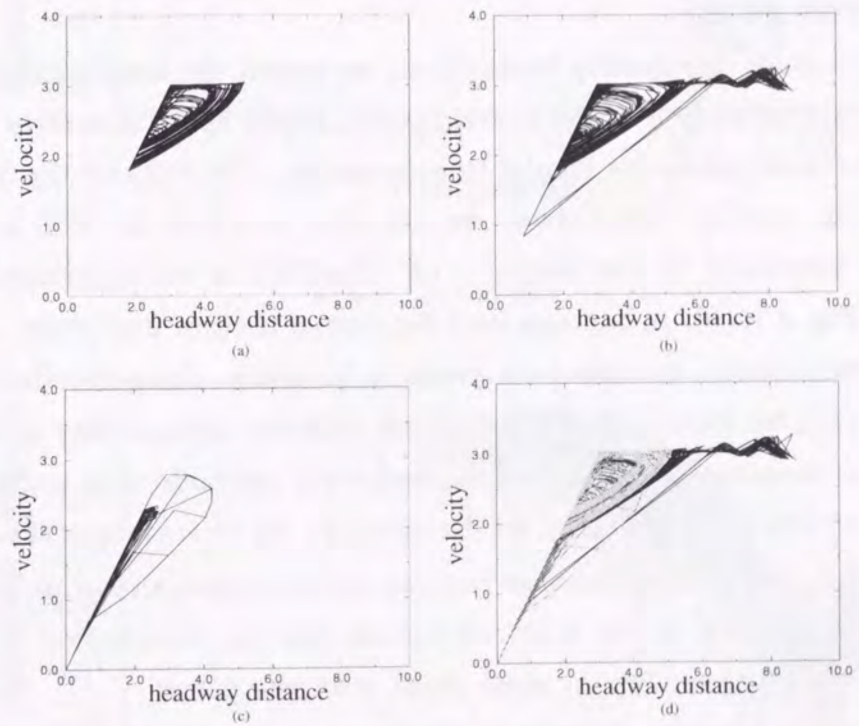

Figure 4.9: Car-following behavior of a test vehicle. An actual trajectory of the test vehicle with a preferred velocity 3.0 in the actual traffic stream is presented in the headway-velocity plane. (a) $\rho = 0.1$: in low concentration, (b) $\rho = 0.2$: near the critical concentration, (c) $\rho = 0.3$: in high concentration, and (d) these superposition. System length and relaxation time are taken to be 500 and 500, respectively. We plot the response for 4000 time.

4.3 Power-Law Density Fluctuations

As was mentioned in the introduction, power-law density fluctuations are observed in the traffic flow [63]. In order to understand the mechanism of such power-law fluctuations, Takayasu and Takayasu made a computer simulation using a simple CA model [99]. Nagel and Rasmussen [72] and Nagel and Paczuski [71] studied several power-law phenomena using the NS model in connection with *the edge of chaos*. The present author also reported the power-law density fluctuations found in the simulation of CTM model, which we discuss below.

In order to study the density fluctuations, we record the time series of the density measured at a local section in the closed circuit. Power spectral density (PSD) of the time series is calculated by the Fourier transformation. The PSD for the free flow phase is shown in Fig. 4.10(a). Clear power-law behavior, in which the PSD is proportional to $1/f^{\alpha}$ (f is frequency), is seen with $\alpha \sim 1.8$. The PSD in the congested flow phase is presented in Fig. 4.10(b). In contrast with the case of the free flow phase, no power-law behavior is seen; rather, the spectrum seems to be white. From detailed investigation of the PSD [107], we found that the power-law behavior appears only at concentration lower than the transition; In other words, long-time correlations of traffic flow persist only in the free flow phase and they are destroyed by the emergence of the traffic jam.

To study the origin of the power-law fluctuations, we make a histogram of the headway distance, which is shown in Fig. 4.12. We can see that the distribution of the headway distance also obeys power law in some range with the power ~ -3. The power-law distribution of the headway distance is considered to be related to the weak density waves in Fig. 4.6. As we have seen, the density waves appear, grow up and disappear from time to time; Such fluctuations remind us of the avalanches of the sand-pile model in the self-organized critical state [1, 2]. The above two power laws, one in space and the other in time, are related to each other[1]; We just observe the same phenomena from two different sides. Thus, the power law in both space and time appear at the same time.

---

[1] In a steady system, we can prove that existence of space-like power law means existence of time-like one and vice versa: M. Takayasu, private communication. In the present case, even though the power -1.8 indicates that the system is not steady in the meaning of existence of correlation functions, the system is steady because of the bounded power-law regime. Thus the argument in steady system could be applied to the present case.

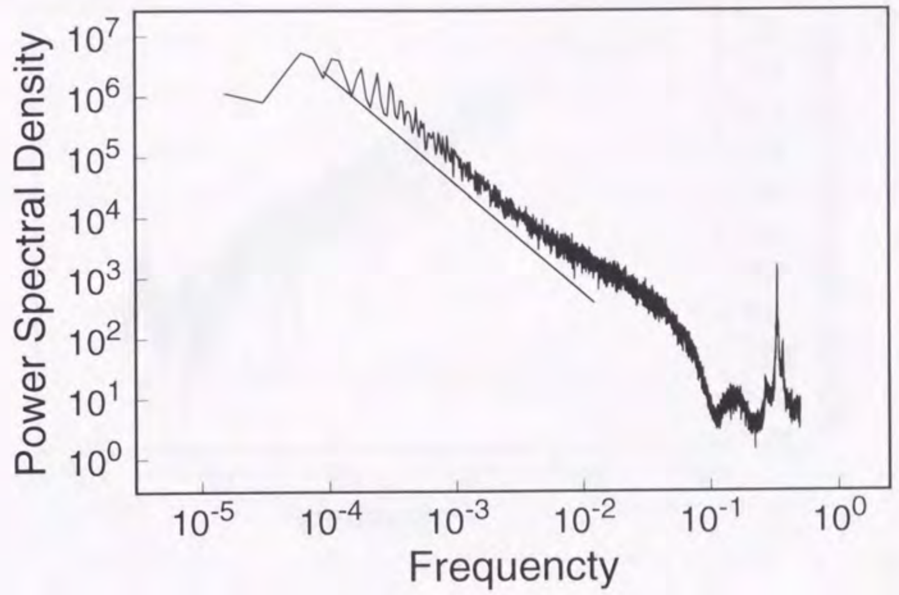

(a) Low concentration

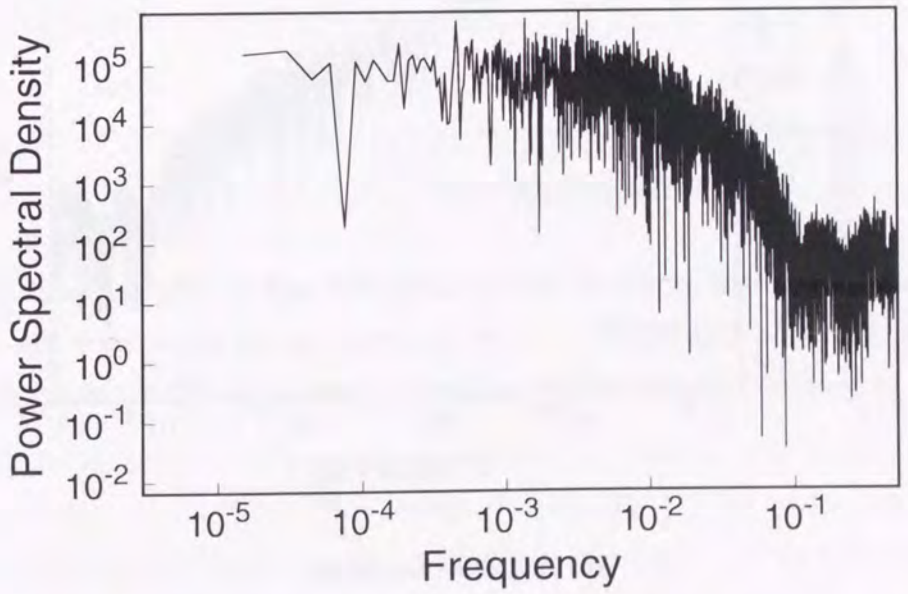

(b) High concentration

Figure 4.10: Power spectral densities of temporal density fluctuations: The log-log plots are shown. Measurements are made in a local section of the length 20 in the system of total length $L = 100000$. We recorded the time series for 65536 steps after discarding 400000 steps. (a) $\rho = 0.19$, in the free flow phase. Averages of 30 samples are shown. The slope of the straight line is -1.8. (b) $\rho = 0.2$, in the congested flow phase. The other conditions are same as in (a). The result for a single sample is shown.

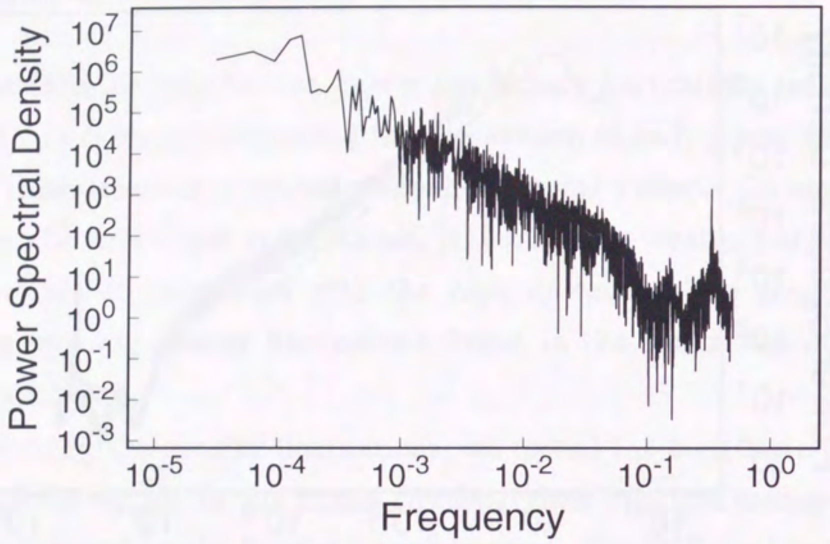

(a) Just below transition

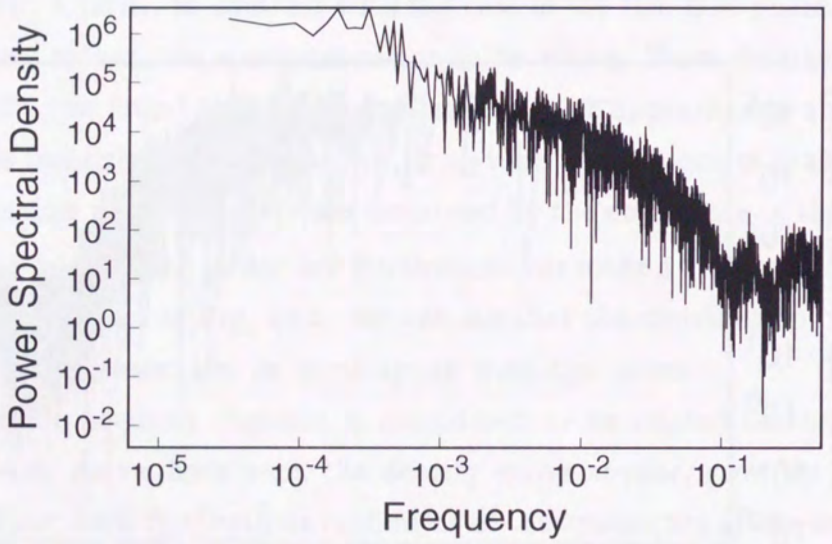

(b) Just above transition

Figure 4.11: Power spectral densities of temporal density fluctuations: The log-log plots are shown. Measurements are made in a local section of the length 20 in the system of total length $L = 200000$. We recorded the time series for 32768 steps after discarding 800000 steps. (a) $\rho = 0.197575$, which is just below the transition. No sample average is taken. (b) $\rho = 0.197576$, which is just above the transition. The other conditions are same as in (a).

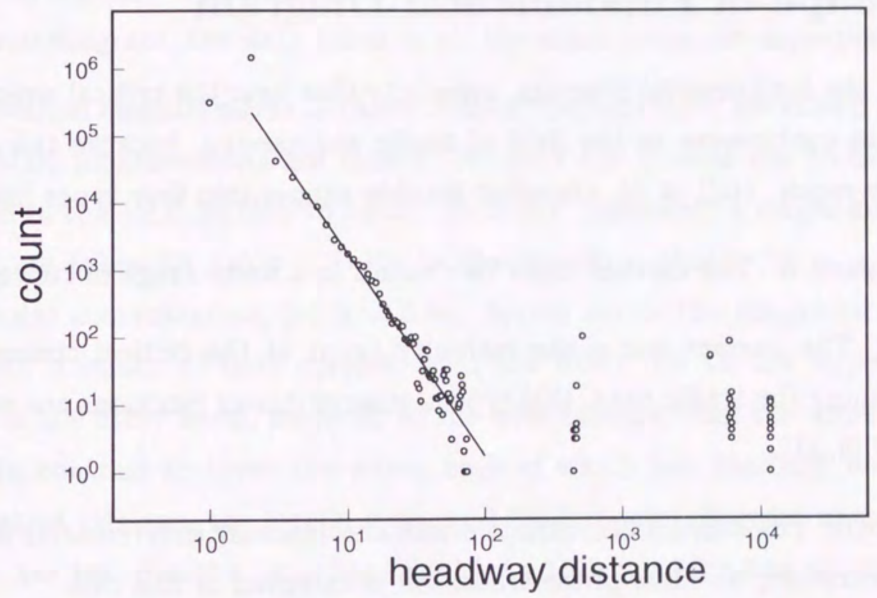

Figure 4.12: Log-log plot of the histogram of the headway distance. The lengths of the system and concentration are taken to be $L = 100000$ and $\rho = 0.19$, respectively. Histogram is made for 100 steps after discarding 500000 steps. The slope of the straight line is -3.

The weak density waves appear in a platoon of the vehicles when there are a sufficient number of vehicles in the free flow phase. So we may say that the cluster flow in the free flow phase is always near the self-organized critical state; The nature of the self-organization is determined not by the concentration but by the number of the vehicles in a platoon. As a consequence, the power-law fluctuations are also found in an open boundary case [97].

4.4 Shape of Fundamental Diagram

A shape of the fundamental diagram, especially that near the critical concentration, has been long in controversy in the field of traffic engineering, because the observed data scatter very much. Hall *et al.* classified feasible shapes into four types [28]:

- **Reversed λ:** The current takes two values in a finite range of concentration [50].
- **Gap:** The current has a discontinuity (gap) at the critical concentration. For explaining the traffic data, this type of discontinuous functions are sometimes preferred [9, 21].
- **Smooth:** The current is continuous and continuously differentiable function of the concentration; No clear phase transition is excepted in this case.
- **Inverted V:** The current is continuous, but not continuously differentiable function at the critical concentration.

Among these possibilities, they concluded that the inverted V shape is suitable for representing the fundamental diagram. Their argument is based on the catastrophe theory [27, 74] and an intuitive view that the traffic current is a one-valued function of the concentration. But it is still not clear whether their conclusion is justified.

Although we obtained the fundamental diagram already in the previous section 4.2.3, Fig. 4.5, it is not appropriate for discussing the shape in detail, because the measurement conditions are quite different from real measurements: Data are usually taken at some *local* segment of an open (that is, not a circular) road for making fundamental diagrams in reality, while the concentration and the current of the whole circuit have been plotted in Fig. 4.5. In other words, the real traffic flow is neither in a closed circuit nor under the condition of the fixed concentration, in contrast with the simulations made in previous sections. Thus we need to get more realistic fundamental diagram using the computer simulations. To this end, we mimic the observation made in the real traffic flow as follows: Simulations are made for the circuit with the *overall* concentration fixed as before. Measurements of the density and the current are made at some *local* segment in the circuit. That is, only a small portion of the circuit is used for measurements. As a consequence, the measured value of the density is not fixed any more. Simulations are made for several different values of the overall concentration independently. For making the fundamental diagram, the data taken in all the simulations are superposed.

Three individual measurements in characteristic concentration are shown in Fig. 4.13: Raw data of 5000 measurements are shown: We took the system size to be $L = 10000$ and the length of the local section to be 20. Each dot represents a single measurement. Three figures are taken for (a) $\rho = 0.10$: in the free flow phase, (b) $\rho = 0.193$: just above the critical concentration, (c) $\rho = 0.40$: deeply inside the congested flow phase. In Fig. 4.13(a), a bunch of dots spreads from the lower left to the upper right. In Fig. 4.13(c), on the other hand, majority of the dots spreads from the upper left to the lower right. In contrast to these two cases, each of which has basically one branch of flow-concentration relation, the locally measured fundamental diagram near the critical concentration has two distinct branches (see Fig. 4.13(b)), which has characters of the congested flow phase and the free flow phase, respectively. It is clearly a consequence of the coexistence of the platoon and the jam section.

The fundamental diagram obtained by superposing the individual results is shown in Figs. 4.14 and 4.15. Raw data are plotted in the diagram (Fig. 4.14), as is frequently done in traffic literatures. The histogram of the same data are also shown in Fig. 4.15. In this figure, the number of data is represented by the brightness of the cell; Bright cell corresponds to one with large number of data. The number distribution clearly shows a shape of the reversed λ, in contrast with Fig. 4.5. Two branches are seen in a finite range of the density near the critical point. Therefore, the local current is bistable there. The free flow phase mainly contributes to the upper branch and the congested flow phase mainly to the lower branch. But from the simulations near the critical concentration, data in both branches are taken. This fundamental diagram made from local measurements resembles nicely with real ones. If we naively average the current for each local density,

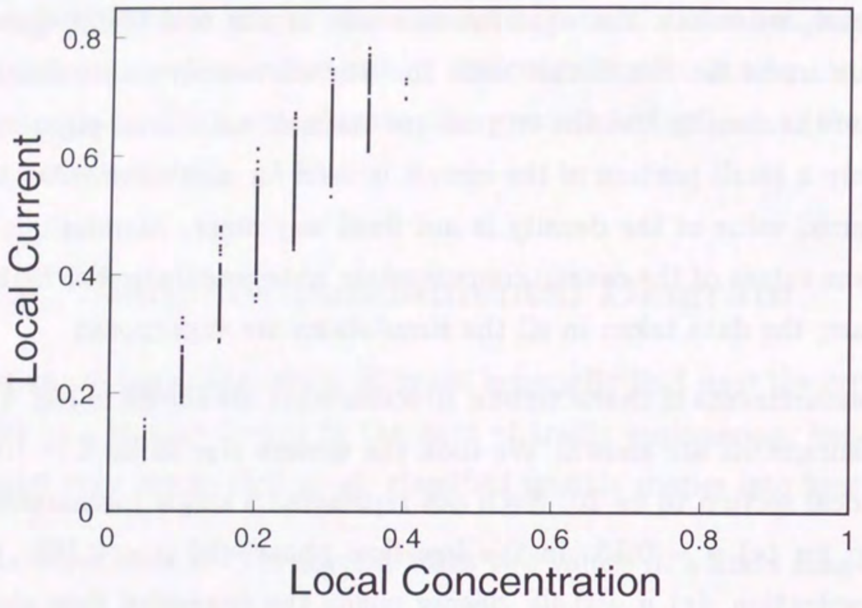

(a) $\rho = 0.100$

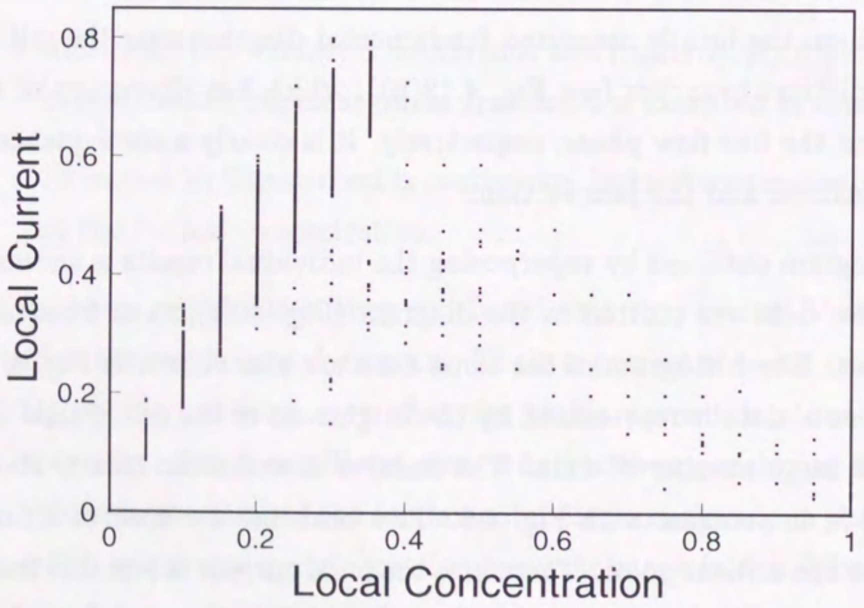

(b) $\rho = 0.193$

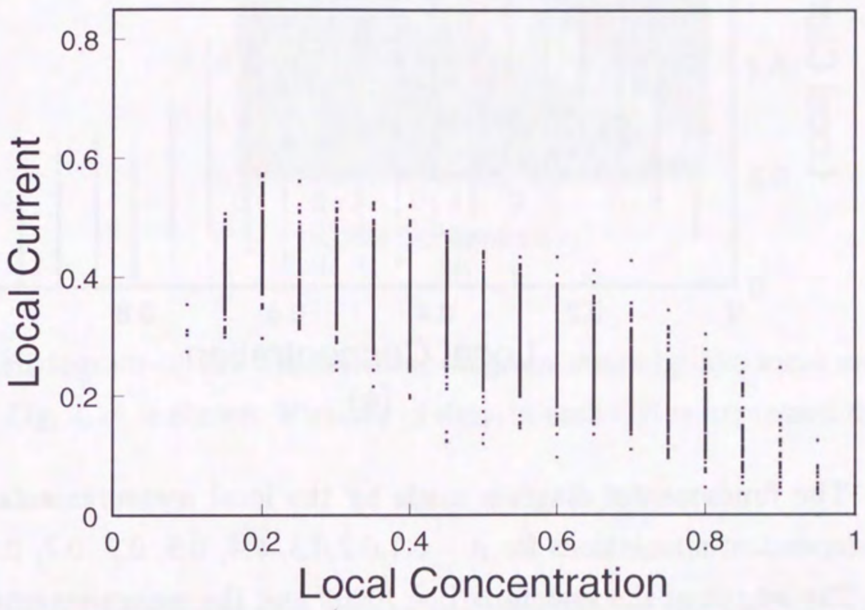

(c) $\rho = 0.500$

Figure 4.13: Individual results of locally measured fundamental diagrams: The system size and the length of the local section are taken to be $L = 10000$ and 20, respectively. Each figure is different in the total concentration: (a) $\rho = 0.100$, (b) $\rho = 0.193$, and (c) $\rho = 0.500$. We calculate the local value of current and concentration for 5000 steps after discarding 50000 steps and we plot raw data on the figures.

we certainly will get the diagram with the inverted V shape. But the averages are not taken usually for presenting fundamental diagrams. Thus we conclude that the reversed λ shape is the appropriate form.

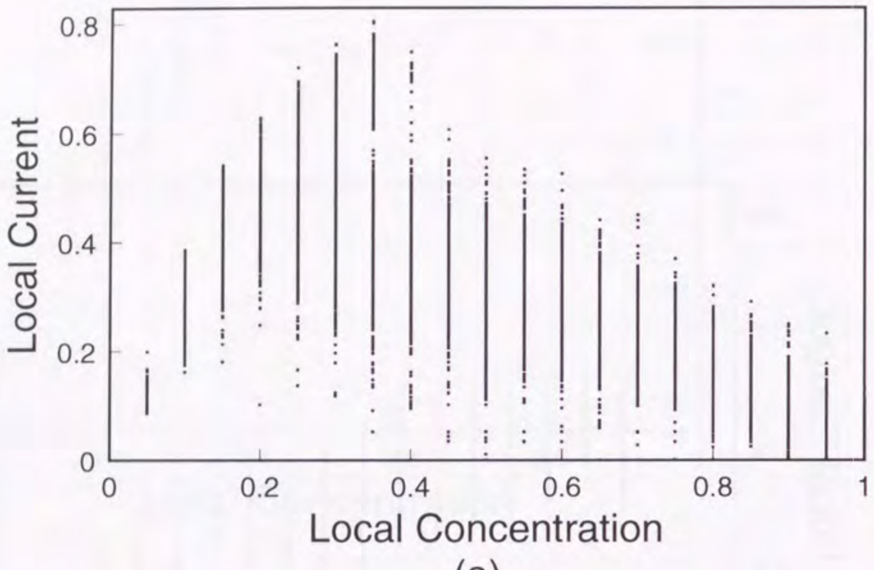

(a)

Figure 4.14: The fundamental diagram made by the local measurements: Data taken from nine independent simulations for $\rho = 0.1, 0.2, 0.3, 0.4, 0.5, 0.6, 0.7, 0.8$ and 0.9 are superposed. The length of the system is $L = 10000$ and the measurements are made at a local segment of the length 20. We measure the local values of the current and density for 5000 steps after discarding 50000 steps. The raw data without taking averages are plotted.

Above results tell us that the shape of fundamental diagrams depends strongly on how the measurements and the analysis are made; If we measure the current in a large scale in space and for very long time, and average the data, then the inverted V shape will result. If, on the other hand, we measure it in a small scale in space and for short time and do not average the data, we will get the reversed λ shape. The latter is the case in usual situations. In many cases of data analysis of real traffic flows, only scattered diagrams are presented when the fundamental diagrams are shown. If the number distributions (histogram) as Fig. 4.15 are made instead of scattered diagrams, we will see the reversed λ feature more clearly. One implication of the present analysis is that the intuitive view where the traffic current is a one-valued function of the concentration is to be reconsidered. The present results also cast a doubt on the argument frequently made that any good model for one-dimensional traffic flow should have a metastability near the jamming transition in the infinite-size limit. Since the real fundamental diagrams reflect only *local* properties of the traffic flow, the reversed λ shape, if seen, does not serve as an evidence for the metastability. We indeed obtained the fundamental diagram which shows clear bistability by the computer simulations. But this bistability by no means imply metastability in the infinite system.

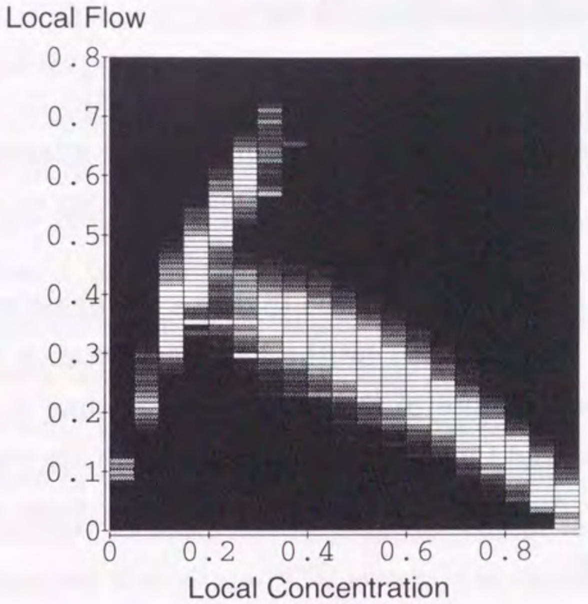

(b)

Figure 4.15: Histogram of the fundamental diagram made by the local measurements: Histogram of Fig. 4.14 is shown. Number of data in each cell is expressed by the brightness.

The observed bistability of the current is simply interpreted. When the jam sections pass the region where the measurement is made, then the observed current falls into the lower branch. Otherwise, the current corresponding to the upper branch is observed. We expect the same scenario for real open traffic flows. So there will be some parameter other than the density which can distinguish these two branches. To specify such parameter for one-dimensional open traffic flow is, however, still an open problem.

4.5 Entropy of Traffic Flow

For representing states of traffic flows, quantities such as the current, the concentration, the average velocity are used. Here we introduce a new quantity for representing the states: the "entropy"[2] of the traffic flow. The entropy gives more detailed information of the traffic flow than the current or the concentration.

Before introducing the entropy, we need to define the phase space of a single vehicle. In the present model, it is spanned by the headway distance Δx and the velocity v. We take $(\Delta x_i^t,\ v_i^{t+1})$ as the state of the i-th vehicle at time t. An alternative choice $(\Delta x_i^t,\ v_i^t)$ also is possible and these two choices give essentially the same results. Using a distribution function $p(\Delta x, v)$ per vehicle per step in the phase space, we can calculate the entropy I as follows:

$$I \equiv -\iint d\Delta x\, dv\ p(\Delta x, v)\ \ln p(\Delta x, v)\ . \tag{4.8}$$

The concentration dependence of the entropy for several system sizes are shown in Fig. 4.16. The entropy has a pronounced maximum at the critical concentration ρ_c. For concentration much lower than ρ_c, it decreases as increasing concentration. It turns to increase rapidly near ρ_c and has a peak. Beyond the peak, it decreases again monotonically and finally becomes zero at $\rho = 1$. Clear size dependence is observed for $\rho < \rho_c$; As the system size becomes larger, the entropy becomes smaller. For $\rho > \rho_c$, on the other hand, no apparent size dependence is seen. Such difference in the size dependence is understood as follows. In the free flow phase, as we already know, the vehicles form a platoon and all the vehicles except for the leading one are forced to run with almost identical velocity and headway distance. In other word, the vehicles run in a highly ordered manner. At concentration just above ρ_c, on the other hand, vehicles behave quite differently because a single jam section is formed. When running into the jam, the vehicles are forced to reduce their velocity; As is seen in the trajectories in Figs. 4.8, they run with the same velocity and headway distance in the jam section. After escaping from the jam, the vehicles separate into a number of small platoons. It is clear that each platoon is headed by the vehicle having the smallest preferred velocity within it. This situation resembles to very early stages of the relaxation toward the stationary state in the free flow phase, where small clusters adjust their mutual distances so that they eventually form a single large platoon. In the present case, however, they do not have time enough to form a single platoon, because vehicles encounter the jam again before they travel around the circuit. Therefore, apart from the jam section, a number of small platoons having different velocities coexist. That is to say, the vehicles runs in less ordered manner just above ρ_c than in the free flow phase, and thus the entropy increases rapidly near ρ_c. For concentration much higher than ρ_c, a number of jams are formed and the intervals between the jams become shorter in average. As a result, durations of the vehicles encountering the adjacent jams become smaller. In such situation, not many platoons are formed in the intervals, because it takes some time for the vehicles to separate into small platoons. In other words, vehicles redress the order, but in a different manner, in the congested flow phase. The system size dependence of the entropy is understood by a similar argument. While the number of vehicles directly contribute to the entropy in $\rho < \rho_c$, the entropy relates to the density of jam sections in $\rho > \rho_c$.

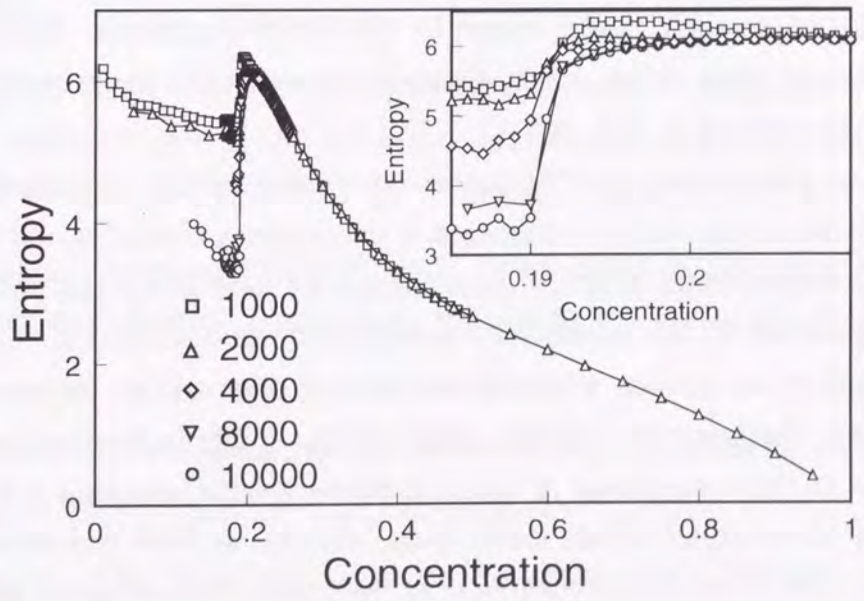

Figure 4.16: The entropy of the traffic flow: Data for the lengths of the system $L = 1000$, 2000, 4000, 8000, and 10000 are shown. Averages over 100 samples are taken. Inset shows the magnified view near the critical concentration.

---

[2] Correctly speaking, the "entropy" introduced here should be called the *informational* entropy. Thus some concepts like H theorem for physical entropy do not hold.

The entropy is, in general, a measure of disorder. But the traffic flow near the critical concentration is by no means randomly disordered; Rather, it is organized in a complicated manner. Large entropy here indicates the coexistence of several platoons of different group velocity. We may say that the traffic flow is *maximally complex* near the critical concentration. Measuring the entropy for real traffic flows will be difficult task. But we expect it behaves similarly to the one observed in the simulations.

4.6 Summary

In this chapter, we have presented the concepts of the coupled-map modeling of one-dimensional traffic flow in general and have described the coupled tanh-map (CTM) model proposed by the author. The coupled-map modeling is highly flexible, so that we can implement CM models easily to several interesting traffic situations. We have followed a bottom-up approach; Thus the choice of the essentials of traffic motions mentioned in Sec. 4.2.2 are crucial. The CTM model presented in this chapter is a totally deterministic microscopic model except for the initial conditions. We can also choose some alternative forms of the maps which also represent the above essentials. Another realization is presented in Ref. [97].

Numerical simulations of CTM model reproduced several phenomena observed in real traffic flows nicely, such as occurrence of the jamming transition and the basic properties of the fundamental diagram. In addition, we have found the power-law density fluctuations caused by the power-law headway distance distribution. By making local measurements of the current, which mimics the real observations, we successfully reproduce a realistic fundamental diagram. Observed bistability in the fundamental diagram is attributed to the consequence of the local measurements, and thus it is also expected to appear in observations of real traffic flows. Finally, we have introduced the entropy of the traffic flow. It exhibits a maximum at the critical concentration; we may say that the traffic flow becomes maximally complex there.

Before closing this chapter, we would like to stress again that the coupled-map type modeling, that is, the modeling scheme treating time as discrete and space as continuous, is a promising approach for modeling the traffic flow realistically, because of its high flexibility. Further investigations in this direction are expected.

Bibliography

[1] P. Bak, C. Tang, and K. Wiesenfeld. "Self-Organized Criticality: An Explanation of 1/f Noise". *Phys. Rev. Lett.*, **59**, (1987), 381.

[2] P. Bak, C. Tang, and K. Wiesenfeld. "Self-organized criticality". *Phys. Rev.* **A**, **38**, (1988), 381.

[3] M. Bando, K. Hasebe, A. Nakayama, A. Shibata, and Y. Sugiyama. "Structure Stability of Congestion in Traffic Dynamics". *Japan J. Indust. Appl. Math.*, **11**, (1994), 203.

[4] M. Bando, K. Hasebe, A. Nakayama, A. Shibata, and Y. Sugiyama. "Dynamical model of traffic congestion and numerical simulation". *Phys. Rev.* **E**, **51**, (1995), 1035.

[5] M. N. Barber. "Finite-size Scaling". In C. Domb and J. L. Lebowitz (eds), *Phase Transition and Critical Phenomena*, volume 8, 145. Academic Press, London, 1983.

[6] O. Biham, A. A. Middleton, and D. Levine. "Self-organization and dynamical transition in traffic-flow models". *Phys. Rev.* **A**, **46**, (1992), 6124.

[7] J. M. Burgers. *The Nonlinear Diffusion Equation.* Riedel, Boston, 1974.

[8] E. Ryerson Case and Kenneth M. Williams. "Queen Elizabeth Way Freeway Surveillance and Control System Demonstration Project". *Transp. Res. Rec.*, **682**, (1978), 84.

[9] Avishai Ceder. "A Deterministic Traffic Flow Model for the Two-regime Approach". *Transp. Res. Rec.*, **567**, (1976), 16.

[10] R. E. Chandler, R. Herman, and E. W. Montroll. "Traffic Dynamics: Studies in Car Following". *Oper. Res.*, **6**, (1958), 163.

[11] Tse-Sun Chow. "Operational Analysis of a Traffic-Dynamics Problem". *Oper. Res.*, **6**, (1958), 827.

[12] J. A. Cuesta, F. C. Martínez, J. M. Molera, and A. Sánchez. "Phase transitions in two-dimensional traffic-flow model". *Phys. Rev.* **E**, **48**, (1993), R4175.

[13] J. O. Cutress and R. F. Pulfer. "X-Ray Investigations of Flowing Powders". *Powder Technol.*, **1**, (1967), 213.

[14] J. M. del Castillo, P. Pintado, and F. G. Benítez. "A Formation for the Reaction Time Traffic Flow Models". In C. F. Daganzo (ed.), *Transportation and Traffic Theory*, 387. Elsevier Science Publishers B. V., Amsterdam, 1993.

[15] Dimitrios S. Dendrinos. "Operating Speeds and Volume to Capacity Ratios: the Observed Relationship and the Fold Catastrophe". *Transpn. Res.*, **12**, (1978), 191.

[16] Dimitrios S. Dendrions. "Urban Traffic Flows and Fourier Transforms". *Geographical Analysis*, **25**, (1994), 261.

[17] B. Derrida, E. Domany, and D. Mukamel. "An Exact Solution of a One-Dimensional Asymmetric Exclustion Model with Open Boundaries". *J. Stat. Phys.*, **69**, (1992), 667.

[18] B. Derrida, M. R. Evans, V. Hakim, and V. Pasquier. "Exact solution of a 1D asymmetric exclusion model using a matrix formulation". *J. Phys. A: Math. Gen.*, **26**, (1993), 1493.

[19] S. Dietrich. "Wetting Phenomena". In C. Domb and J. L. Lebowitz (eds), *Phase Transition and Critical Phenomena*, volume 12, 1. Academic Press, London, 1988.

[20] John E. Disbro and Michael Frame. "Traffic Flow Theory and Chaotic Behavior". *Transpn. Res. Rec.*, **1225**, (1990), 109.

[21] Said M. Easa. "Selecting Two-Regime Traffic-Flow Model". *Transp. Res. Rec.*, **869**, (1983), 25.

[22] L. C. Edie. "Car-Following and Steady-State Theory for Noncongested Traffic". *Oper. Res.*, **9**, (1961), 66.

[23] K. H. Fischer and J. A. Hertz. *Spin Glasses.* Cambridge University Press, Cambridge, 1991.

[24] D. C. Gazis, R. Herman, and R. B. Potts. "Car-following theory of steady-state traffic flow". *Oper. Res.*, **7**, (1959), 499.

[25] D. C. Gazis, R. Herman, and R. W. Rothery. "Nonlinear follow-the-leader models of traffic flow". *Oper. Res.*, **9**, (1961), 545.

[26] H. Greenberg. "An analysis of traffic flow". *Oper. Res.*, **7**, (1959), 79.

[27] Fred L. Hall. "An Interpretation of Speed-Flow-Concentration Relationships Using Catastrophe Theory". *Transpn. Res. A*, **21A**, (1987), 191.

[28] Fred L. Hall, Brian L. Allen, and Margot A. Gunter. "Emprical Analysis of Freeway Flow-Density Relationships". *Transpn. Res. A*, **20A**, (1986), 197.

[29] H. Hayakawa and K. Nakanishi. "Universal Behavior in Granular Flows and Traffic Flows". *Prog. Theor. Phys. Suppl.*, **130**, (1998), 57–75.

[30] D. Helbing. "Traffic Modeling by Means of Physical Concepts". In *Workshop on Traffic and Granular Flow*, 87. World Scientific, Singapore, 1995.

[31] R. R. Herman, E. W. Montroll, R. B. Potts, and R. W. Rothery. "Traffic dynamics: Analysis of stability in car following". *Oper. Res.*, **7**, (1959), 86.

[32] J. Hertz, A. Krogh, and R. G. Palmer. *Introduction to the Theory of Neural Computation.* A Lecture Notes Volume in the Santa Fe Institute Studies in the Science of Complexity. Addison-Wesley, Redwood City, 1991.

[33] Y. Hieida. "Application of the Density Matrix Renormalization Group Method to a Non-Equilibrium Problem". *J. Phys. Soc, Jpn.*, **67**, (1998), 369–372.

[34] H. Hinrichsen and S. Sandow. "Deterministic exclusion process with a stochastic defect: matrix-product ground state". *J. Phys. A: Math. Gen.*, **30**, (1997), 2745–2756.

[35] S. Horikawa, A. Nakahara, T. Nakayama, and M. Matsushita. "Self-Organized Critical Density Waves of Granular Material Flowing through a Pipe". *J. Phys. Soc, Jpn.*, **64**, (1995), 1870.

[36] N. Inui, A. Y. Tretyakov, and H. Takayasu. "Universality of 1-Dimensional Reaction Models". *Fractals*, **1**, (1993), 480.

[37] Y. Ishibashi and M. Fukui. "Temporal Variations of Traffic Flow in the Biham-Middleton-Levine Model". *J. Phys. Soc, Jpn.*, **63**, (1994), 2882–2885.

[38] S. A. Janowsky and J. L. Lebowitz. "Finite-size effects and shock fluctuations in the asymmetric simple-exclustion process". *Phys. Rev.* **A**, **45**, (1992), 618–625.

[39] S. A. Janowsky and J. L. Lebowitz. "Exact Results for the Asymmetric Simple Exclusion Process with Blockage". *J. Stat. Phys.*, **77**, (1994), 35.

[40] D. Jarrett and Z. Xiaoyan. "The Dynamic Behavior of Road Traffic Flow: Stability or Chaos?". In A. J. Crilly, R. A. Earnshow, and H. Jomes (eds), *Applications of Fractals and Chaos*, 237. Springer-Verlag, Berlin, 1993.

[41] K. Kaneko. "Period-Doubling of Kink-Antikink Patterns, Quasiperiodicity in Antiferro-Like Structures and Spatial Intermittency in Coupled Logistic Lattice". *Prog. Theor, Phys.*, **72**, (1984), 480.

[42] K. Kaneko. "Spatiotemporal Intermittency in Coupled Map Lattice". *Prog. Theor, Phys.*, **74**, (1985), 1033.

[43] K. Kaneko. "Overview of coupled map lattices". *CHAOS*, **2**, (1992), 279.

[44] K. Kaneko (ed.). *Theory and Application of Coupled Map Lattices.* Wiley, New York, 1993.

[45] Mehran Karder, Giorgio Parisi, and Yi-Cheng Zhang. "Dynamical Scaling of Growing Interfaces". *Phys. Rev. Lett.*, **56**, (1986), 889.

[46] B. S. Kerner and P. Konhäuser. "Cluster effect in initially homogeneous traffic flow". *Phys. Rev.* **E**, **48**, (1993), R2335.

[47] B. S. Kerner and P. Konhäuser. "Structure and parameters of clusters in traffic flow". *Phys. Rev.* **E**, **50**, (1994), 54.

[48] T. Komatsu and S. Sasa. "Kink soliton characterizing traffic congestion". *Phys. Rev.* **E**, **52**, (1995), 5574–5582.

[49] E. Kometani and T. Sasaki. "A safety index for traffic with liear spacing". *Oper. Res.*, **7**, (1959), 704.

[50] M. Koshi, M. Iwasaki, and I. Ohkura. "Some Findings and Overview on Vehicular Flow Characteristics". In V. F. Hurdle and G. N. Stewart (eds), *Proceedings of the 8th International Symposium on Transportation and Traffic Flow Theory*, 403. University of Toronto Press, Toronto, 1983.

[51] S. Krauß. "Microscopic Traffic Simulation: Robustness of a Simple Approach". In *Workshop on Traffic and Granular Flow*, 269. Springer-Verlag, Singapore, 1998.

[52] J. Krug and H. Spohn. "Universality classes for deterministic surface growth". *Phys. Rev.* **A**, **38**, (1988), 4271.

[53] Reinhart D. Kühne and Richard Beckschulte. "Non-linearity Stochastics of Unstable Traffic Flow". In C. F. Daganzo (ed.), *Trasnportation and Traffic Theory*, 367. Elsevier Science Publishers B.V., Amsterdam, 1993.

[54] Christopher G. Langton. "Life at the Edge of Chaos". In Christopher G. Langton, Charles Taylor, J. Doyne Farmer, and Steen Rasmussen (eds), *Artificial Life II*, A Proceedings Volume in the Santa Fe Institute Studies in the Science of Complexity, 41. Addison-Wesley, 1992.

[55] M. Leibig. "Pattern-formation characteristics of interacting kinematic waves". *Phys. Rev.* **E**, **49**, (1994), 184.

[56] W. Leutzbach. *Introductoin to the theroy of traffic flow.* Springer-Verlag, 1988.

[57] Thomas. M. Liggett. "Ergodic theorems for the asymmetric simple exclusion process". *Trans. Amer. Math. Soc.*, **213**, (1975), 237.

[58] Thomas M. Liggett. "Ergodic theorems for the asymmetric simple exclusion process II". *Ann. Prob.*, **5**, (1977), 795.

[59] Thomas M. Liggett. *Interacting Particle Systems.* Springer-Verlag, New York, 1985.

[60] M. J. Lighthill and G. B. Whitham. "On kinematic waves I. Flood movementin long rivers". *Proc. Roy. Soc.*, **A229**, (1955), 281.

[61] M. J. Lighthill and G. B. Whitham. "On kinematic waves II. A theory of traffic flow on long crowded roads". *Proc. Roy. Soc.*, **A 229**, (1955), 317.

[62] B. B. Mandelbrot. *Fractals and Scaling in Finance.* Springer-Verlag, New York, 1997.

[63] T. Musha and H. Higuchi. "The 1/f Fluctuation of a Traffic Current on an Expressway". *Jpn. J. Appl. Phys.*, **15**, (1976), 1271.

[64] T. Musha and H. Higuchi. "Traffic Current Fluctuation and the Burgers Equation". *Jpn. J. Appl. Phys.*, **17**, (1978), 811.

[65] T. Nagatani. "Jamming transition in the traffic-flow model with two-level crossing". *Phys. Rev.* **E**, **48**, (1993), 3290.

[66] T. Nagatani. "Power-Law Distribution and 1/f Noise of Waiting Time near Traffic-Jam Threshold". *J. Phys. Soc, Jpn.*, **62**, (1993), 2533.

[67] T. Nagatani. "Effect of Jam-Avoiding Turn on Jamming Transition in Two-Dimensional Traffic Flow Model". *J. Phys. Soc, Jpn.*, **63**, (1994), 1228.

[68] T. Nagatani. "Traffic Jam ans Shock Formation in Stochastic Traffic-Flow Model of a Two-Lane Roadway". *J. Phys. Soc, Jpn.*, **63**, (1994), 52.

[69] K. Nagel. "INDIVIDUAL ADAPTATION IN A PATH-BASED SIMULATION OF THE FREEWAY NETWORK OF NORTHRHINE-WESTFALIA". *Int. J. Mod. Phys.*, **C7**, (1996), 883–892.

[70] K. Nagel and H. J. Herrmann. "Deterministic models for traffic jams". *Physica*, **A199**, (1993), 254.

[71] K. Nagel and M. Paczushi. "Emergent traffic jams". *Phys. Rev.* **E**, **51**, (1995), 2909.

[72] K. Nagel and S. Rasmussen. "Traffic at the edge of chaos". In Rodney A. Brooks and Pattie Maes (eds), *Proceedings of Alife 4*, 222. MIT Press, Cambridge, 1994.

[73] K. Nagel and M. Schreckenberg. "A cellular automaton model for freeway traffic". *J. Phys. I France*, **2**, (1992), 2221.

[74] Francis Navin. "Traffic Congestion Catastrophes". *Transportation Planning Technology*, **11**, (1986), 19.

[75] Francis Navin and Fred L. Hall. "Understanding Traffic Flow At and Near Capacity". *ITE journal*, August 1989, 31.

[76] G. F. Newell. "Nonlinear Effects in the Dynamics of Car Following". *Oper. Res.*, **9**, (1961), 209.

[77] G. F. Newell. "Theories of instability in dense highway traffic". *J. Oper. Res. Japan*, **5**, (1963), 9.

[78] K. Nishinari and T. Takahashi. "Private communication".

[79] H. Nozawa. "A neural network model as a globally coupled map and applications based on chaos". *CHAOS*, **2**, (1992), 377.

[80] Harold J. Payne. "Models of Freeway Traffic and Control". *Simulation Council Proceedings*, **1**, (1971), 51.

[81] Harold J. Payne. "Discontinuity in Equilibrium Freeway Traffic Flow". *Transpn. Res. Rec.*, **941**, (1985), 140.

[82] G. Peng and H. J. Herrmann. "Density waves of granular flow in a pipe using lattice-gas automata". *Phys. Rev.* **E**, **49**, (1994), R1796–R1799.

[83] G. Peng and H. J. Herrmann. "Density waves and 1/f density fluctuations in granular flow". *Phys. Rev.* E, **51**, (1995), 1745–1756.

[84] L. A. Pipes. "An Operational Analysis of Traffic Dynamics". *J. Appl. Phys.*, **24**, (1953), 274.

[85] I. Prigogine and F. C. Andrews. "A Boltzmann-like apploach for traffic flow". *Oper. Res.*, **8**, (1960), 789.

[86] N. Rajewsky and M. Schreckenberg. "Exact results for one-dimensional cellular automata with different types of updates". *Physica* **A**, **245**, (1997), 139–144.

[87] A. Reuschel. *Zeits. d. Oestrreich. Ing. u. Arch. Vereines*, **95**, (1950), 59–73.

[88] A. Reuschel. *Oesterreich. Ing. Archiv.*, **4**, (1950), 193.

[89] Paul I. Richards. "Shock Waves on the Highway". *Oper. Res.*, **4**, (1956), 42.

[90] P. Ruján. "Cellular Automata and Statistical Mechanical Model". *J. Stat. Phys.*, **49**, (1987), 139.

[91] K. L. Schick and A. A. Verveen. "1/f noise with a low frequency white noise limit". *Nature*, **251**, (1974), 599–601.

[92] M. Schreckenberg, A. Schadschneider, K. Nagel, and N. Ito. "Discrete stochastic models for traffic flow". *Phys. Rev.* **E**, **51**, (1995), 2939.

[93] G. Schütz. "Generalized Bethe Ansatz Solution of a One-Dimensional Asymmetric Exclusion Process on a Ring with Blockage". *J. Stat. Phys.*, **71**, (1993), 471.

[94] H. P. Simão and W. B. Powell. "Numerical Methods for Simulating Transient, Stochastic Queueing Networks - I: Methodology". *Trans. Sci.*, **26**, (1992), 296.

[95] Y. Sugiyama. "Dynamical Model for Congestion of Freeway Traffic and Its Structural Stability". In *Workshop on Traffic and Granular Flow*, 137. World Scientific, Singapore, 1995.

[96] S. Tadaki and M. Kikuchi. "Jam phases in a two-dimensional cellular-automaton model of traffic flow". *Phys. Rev.* **E**, **50**, (1994), 4564.

[97] S. Tadaki, M. Kikuchi, Y. Sugiyama, and S. Yukawa. "Coupled Map Traffic Flow Simulator Based on Optimal Velocity Functions". In *Workshop on Traffic and Granular Flow*, 373. Springer-Verlag, Singapore, 1998.

[98] S. Tadaki, M. Kikuchi, Y. Sugiyama, and S. Yukawa. "Coupled Map Traffic Flow Simulator Based on Optimal Velocity Functions". *J. Phys. Soc, Jpn.*, **67**, (1998), 2270–2276.

[99] M. Takayasu and H. Takayasu. "1/f noise in a traffic model". *Fractals*, **1**, (1993), 860.

[100] R. Thom. *Structural Stability and Morphogenesis*. W. A. Benjamin, inc., Reading, Massachusetts, 1975.

[101] P. Wagner and J. Peinke. "Scaling Properties of Traffic-flow data". *Z. Naturforsch.*, **52 a**, (1997), 600–604.

[102] D. E. Wolf, M. Schreckenberg, and A. Bachem (eds). *Workshop on Traffic and Granular Flow*. World Scientific, Singapore, 1995.

[103] S. Wolfram. "Statistical Mechanics of Cellular Automata". *Rev. Mod. Phys.*, (1983), 601.

[104] S. Wolfram. *Theory and Applications of Cellular Automata*. World Scientific, Singapore, 1986.

[105] S. Yukawa. "Numerical Study of One-Dimensional Traffic Flow (in Japanese)". Master's thesis, Osaka University, Osaka, 1995.

[106] S. Yukawa and M. Kikuchi. "Coupled-Map Modeling of One-Dimensional Traffic Flow". *J. Phys. Soc, Jpn.*, **64**, (1995), 35.

[107] S. Yukawa and M. Kikuchi. "Density Fluctuations in Traffic Flow". *J. Phys. Soc, Jpn.*, **65**, (1996), 916.

[108] S. Yukawa, M. Kikuchi, and S. Tadaki. "Dynamical Phase Transition in One Dimensional Traffic Flow Model with Blockage". *J. Phys. Soc, Jpn.*, **63**, (1994), 3609.

[109] X. Zhang and G. Hu. "1/f noise in a two-lane highway traffic model". *Phys. Rev.* E, 52, (1995), 4664.

Part II

Quantum Nonequilibrium Flow

Chapter 5

Introduction to Dynamics of Ratchet Systems

5.1 Introduction

A device consisting of an asymmetric wheel and a pawl, in which the wheel is allowed to rotate only in one direction, is called a "ratchet". Unidirectional character ("rectification") of ratchets is utilized widely in industrial tools, such as a ratchet driver. Consider a ratchet fabricated in a microscopic scale. In case that the ratchet is so small that the effect of thermal fluctuations cannot be ignored, the rectification effect will be smeared by the thermal noise, and a motion in the opposite direction which is forbidden in the macroscopic ratchets will take place with certain probability. Feynman examined such situations in his famous lecture [19], connecting them with the second law of thermodynamics. He also discussed if such microscopic ratchets work as thermodynamic engines to produce work from purely thermal noises. Ratchets which are small enough to be regarded in the Brownian regime under influence of the thermal noise are called *thermal* ratchets in general. Feynman's original ratchet as well as other types of thermal ratchets has attracted much attention recently [59, 60].

In theoretical studies of thermal ratchets, a simplified model is frequently used in which a Brownian particle moving in an asymmetric periodic potential is considered instead of the asymmetric wheel and the pawl. Dynamics of such Brownian particles can be treated by the Langevin equation. In such simplified thermal ratchets, what is in question is whether a unidirectional Brownian current appears. This type of thermal ratchets has also been realized experimentally and evidence of the rectification has been observed under certain conditions [17, 58].

For the appearance of a steady current, both the spatial reflection symmetry and the time reversal symmetry need to be lost, unless they break spontaneously, according to Qurie's principle [11]. Let us start from discussing a more or less trivial situation. If the spatial reflection symmetry is globally broken by, for instance, a thermal gradient, an electric field, a gravitational field and so on, the current will appear. The breaking of time reversal symmetry is also needed, however, to maintain the *steady* currents. For example, for a particle under gravitational force to drop down in a constant terminal velocity, the frictional force is required. On the other hand, if the spatial reflection symmetry is broken only locally, while it recovers in large scale, appearance of steady current becomes nontrivial phenomenon. An example is the ratchet with a periodic asymmetric zero-mean potential; There the potential is asymmetric only in a unit cell.

The ratchet systems can be classified into several categories according to the scale in which they are fabricated and the temperature of surrounding environment:

- **Inertia Ratchets:** In the macroscopic world, inertia of particles can not be ignored. In such situation, the ratchet system is called "inertia ratchet" [39]. The inertia ratchet can be used in industrial application such as granular transportation, or size selection [3].

- **Thermal Ratchets:** In the Brownian regime, particles are subject to thermal noise and the inertia can be ignored in the dynamics because of large viscosity. In this situation, the ratchet system is called the thermal ratchet. Detailed features will be mentioned later.

- **Quantum Ratchets:** If the particles are very small and temperature is very low, quantum mechanical effects should also be taken into account. Then the ratchet system is called "quantum ratchet". The concept of the "quantum ratchet" was proposed by the present author and the co-workers [65, 70], and independently by Reimann *et al* [56]. This second part of the thesis is devoted to describe the properties of the quantum ratchets.

Among them, the thermal ratchets have been studied extensively [1–5, 10, 12–14, 16, 17, 32, 35–39, 42, 43, 45–47, 50, 54, 55, 59, 71, 72]. In the thermal ratchet, the time reversal symmetry is broken by a coupling with a thermal heat bath. A steady current of the particle, however, cannot be produced as long as a single heat bath is considered, even though both the spatial reflection symmetry and time inversion symmetry are broken. In that case, the steady state of the system is the thermal equilibrium state and the velocity distribution of the particles is Maxwellian. Thus the current in both direction should be cancelled. In order for the net unidirectional current to appear, an additional mechanism that breaks the thermal equilibrium is required. A possible example for the additional mechanism is a non-thermal stochastic process. In this case, non-thermal *noise* (accompanied by the thermal one) will generate the currents. Thus the thermal ratchet systems of this type are regarded as an example of noise-induced transportation phenomena. Unbiased time-dependent deterministic external force is also a candidate of the additional mechanism. Many other mechanisms have also been introduced so far. In the next section, we briefly review some examples of thermal ratchets.

In the context of biology, the ratchet systems has been discussed in connection with biological motors such as myosin moving on actin filament, or kinesin on microtubule. In 1990, Vale and Oosawa discussed the possibility of the ratchet mechanism of muscle contraction for the first time based on the Feynman ratchet [66]. Essence of their idea is that the anisotropic periodic structure of the filaments on which motor proteins move is regarded as an asymmetric wheel of the ratchet and the motor protein is considered as the pawl. In this model, a chemical energy of ATP hydrolysis is used for producing the temperature difference between the filaments and the motor proteins. In 1993, Magnasco proposed the thermal ratchet model of the Brownian particle as was described above as a more sophisticated model for muscle contraction [46]. In his model, a fluctuating force due to a chemical reaction of ATP hydrolysis is taken as the additional mechanism. Another type of the thermal ratchet has also been proposed as the mechanism of the muscle contraction [4]. Temporally fluctuating asymmetric periodic potential which models the conformational change of proteins caused by the energy of ATP hydrolysis was considered in this case. Experimental evidences, however, imply that a simple thermal ratchet model is not suitable for the model of muscle contraction [64]. Accordingly, more complicated models have also been proposed [5]. Similar conclusion is drawn also from the theoretical study of the energetics of thermal ratchets. Quite recently, Sekimoto proposed a general method to treat energetics of Langevin dynamics and calculated the energetics of the thermal ratchet as well as the Feynman ratchet for the first time [60]. In contrast with the known fact that the efficiency of biological motors is very high, he found that these ratchets show quite low efficiency. Thus more studies are required for determining whether the mechanism of the motor proteins is really explained by some extension of the ratchet mechanism or we should consider a totally different mechanism.

5.2 Classical Ratchets

In this section, we briefly review known properties of classical ratchets, especially of the thermal ratchets. In the thermal ratchets, particles are subject to a thermal noise and the inertia is ignored. Then their dynamics is described by over-damped Langevin equation [22]:

$$\gamma \frac{dx(t)}{dt} = -\frac{\partial U(x)}{\partial x} + \xi(t) + F(t) \ , \tag{5.1}$$

where γ is a friction constant, U is a potential and $\xi(t)$ is a thermal noise satisfying the following relations:

$$\langle \xi(t) \rangle = 0, \ \ \langle \xi(t)\xi(t') \rangle = 2\gamma k_B T \delta(t-t') \ . \tag{5.2}$$

The latter represents the fluctuation-dissipation theorem. k_B and T are Boltzmann constant and temperature of a heat bath, respectively. If the external force $F(t) = 0$, the system will reach thermal equilibrium state eventually and then the distribution function of particles becomes simply a Boltzmann distribution:

$$P(x) \propto \exp(-\beta U(x)) \ , \tag{5.3}$$

where $1/\beta = k_B T$ is the inverse temperature. Clearly, net directional motion of particles does not appear in this case.

In order to generate net drift motion, a finite external force is required : $F(t) \neq 0$. Typical choices of the unbiased external forces are as follows (We are interested only in the unbiased case, since generation of a current under a biased force is more or less trivial):

Fluctuating Force: For example $F(t)$ is chosen as a unbiased sinusoidal force like $a\sin(\omega t)$. This type of forcing was introduced by Magnasco [46].

Fluctuating Potential [17]: In this case potential height fluctuates temporally. In a case of so called "flushing potential", that is, the potential is turned on and of periodically with a period f^{-1}, $F(t)$ is taken to be $(\partial U/\partial x)\Theta(t \bmod f^{-1} - 1/2f)$ where $\Theta(t)$ is Heaviside step function.

Stochastic Processes: There are following two types of choices:

- *Correlated Noise:* In this case $F(t)$ is chosen as a colored noise, in which the autocorrelation of the force is not instantaneous, but has a characteristic correlation time. An additional white noise, which corresponds to the thermal noise of different temperature from T, may also seem to generate the unidirectional Brownian motion. But as long as $F(t)$ is uncorrelated and unbiased, satisfying $\langle F(t)\rangle = 0$ and $\langle F(t)F(t')\rangle = \alpha\delta(t-t')$, the Langevin equation is equivalent to another Langevin equation without the external force at the temperature $T_2 = T + \alpha/2\gamma k_B$. Then the system only approaches the thermal equilibrium at T_2. Accordingly, a stochastic process should be non-white for the present purpose. As a special case of the colored noise, dichotomous noise can be used, in which noise takes only two values which alternate according to a stochastic process. Dichotomous noise is sometimes preferred because it is easy to treat [10, 14, 43, 55].

- *Multi-state Jumping:* Brownian particles are forced to jump between different potential landscapes by a stochastic noise [3, 4, 9, 54, 72]. We call this type of ratchet "multi-state thermal ratchet". In this case the above Langevin equation is slightly modified into simultaneous stochastic differential equations:

$$\gamma_i \frac{dx(t)}{dt} = -\frac{\partial U_i(x)}{\partial x} + \xi_i(t) \ , \tag{5.4}$$

  where γ_i are friction constants, U_i are potentials and $\xi_i(t)$ are thermal noises satisfying the following relations:

$$\langle \xi_i(t)\rangle = 0, \ \ \langle \xi_i(t)\xi_j(t')\rangle = 2\gamma_i k_B T\delta(t-t')\delta_{ij} \ . \tag{5.5}$$

  Here, index i refers to the landscape of potential. The dynamics of the transition between the states is determined by the stochastic process. The dichotomous stochastic process is used when only two different landscapes are considered,

Let us discuss the rectification mechanism of these ratchets. Current is generated in the fluctuating force ratchet essentially due to difference of potential gradient in both directions. Consider a piecewise linear asymmetric periodic potential (see Fig. 5.1):

$$U(x) = \begin{cases} \dfrac{c}{pL}(x \bmod L) & \text{for } 0 < x \bmod L \le pL, \text{ we call region A,} \\[2ex] -\dfrac{c}{(1-p)L}(x \bmod L - L) & \text{for } pL < x \bmod L \le L, \text{ we call region B,} \end{cases} \tag{5.6}$$

where L is the length of unit cell, c gives the maximal potential height and p determines the asymmetry of the potential. We assume $p > 1/2$ without loss of generality. When a

sinusoidally oscillating force $F(t) = a\sin\omega t$ is applied, the forces acting at two regions F_A and F_B become as follows:

$$F_A(t) = -\frac{c}{pL} + a\sin\omega t \ , \tag{5.7}$$

$$F_B(t) = \frac{c}{(1-p)L} + a\sin\omega t \ . \tag{5.8}$$

If we choose $a = \epsilon + c/pL$ with small enough positive constant ϵ, forces vary temporally in the following ranges:

$$-\frac{2c}{pL} - \epsilon \le F_A(t) \le \epsilon \ , \tag{5.9}$$

$$\frac{(2p-1)c}{p(1-p)L} - \epsilon \le F_B(t) \le \frac{c}{p(1-p)L} + \epsilon \ . \tag{5.10}$$

We can choose the value of ϵ so that $F_B(t)$ is always positive and $F_A(t)$ is varying around zero (see Fig. 5.1). Then current flows to positive direction in Fig. 5.1, in other word, the Brownian particle climbs up the less steeper side of the asymmetric potential. According to the nature of the mechanism, the net flow is expected to appear at low but finite frequency. The current vanishes at the zero frequency. We cannot expect the net current also in high frequency regime. Other types of fluctuating force have also been proposed. But the mechanism for the appearance of the current is essentially the same, that is, the difference of the potential gradient in two directions.

Generation mechanism of the current in colored-noise driven ratchets is also similar to that of the fluctuating force thermal ratchet. Comparing the force due to the potential and the amplitude of noise integrated over the correlation time of noise, we can easily confirm that the particle climbs up the less steeper side of the potential.

Situation is different in the fluctuating potential ratchets. For simplicity, we consider the case of the flushing potential. Intuitively the Brownian particle is expected to behave as follows: When the asymmetric periodic potential is "on", the particles tend to relax to thermal equilibrium state under the existence of the potential, that is, particles tend to localize near the bottoms of the potential. When the potential is turned off suddenly, the particle starts to diffuse by the thermal noise. If sufficiently long time is allowed for relaxation, the system reaches thermal equilibrium without the potential, in which particle distribution is spatially homogeneous. Then the centers of these two equilibrium distributions in the unit cell are different. This difference induces the directional motion of particles (see Fig. 5.2). The mechanisms of other fluctuating potential thermal

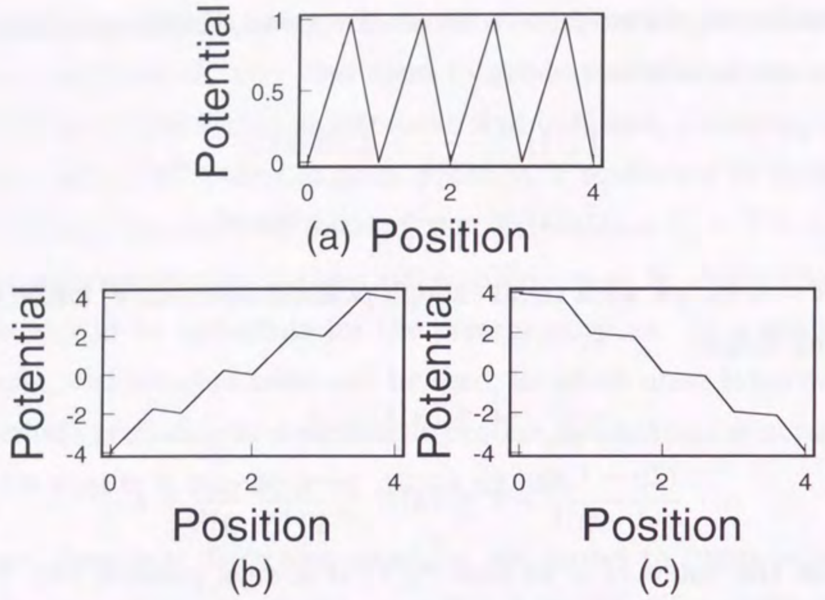

Figure 5.1: Schematic potential shape of a fluctuating force thermal ratchet: (a) asymmetric periodic potential, (b)(c) sinusoidally oscillating force is applied; (b) corresponds to the largest positive gradient. (c) corresponds to the smallest negative gradient.

ratchets are essentially the same. Frequency dependence of the current is quite different from that of fluctuating force thermal ratchets. In low frequency limit, the Brownian particles always achieve thermal equilibrium in which no directional motion appears. Consequently, the net current par unit time becomes smaller as decreasing frequency. In high frequency limit, on the other hand, Brownian particles do not have time enough for relaxation. Thus the form of the distribution becomes steady. Therefore the current does not appear also in high frequency. Only in an intermediate frequency, particles can diffuse sufficiently to generate the currents. The plot of currents against the period has extrema near the characteristic time of diffusion in the unit cell. Thus the direction of the net current is opposite in the fluctuating force ratchet and fluctuating potential ratchet, even if the potential form is same.

Current generating mechanism of multi-state thermal ratchet is also similar to that of the fluctuating potential thermal ratchets; Consider the case of two different potential: one is the flat potential and another the asymmetric periodic potential. Schematic picture is shown in Fig. 5.3. In this case, the centers of the equilibrium distribution in upper and

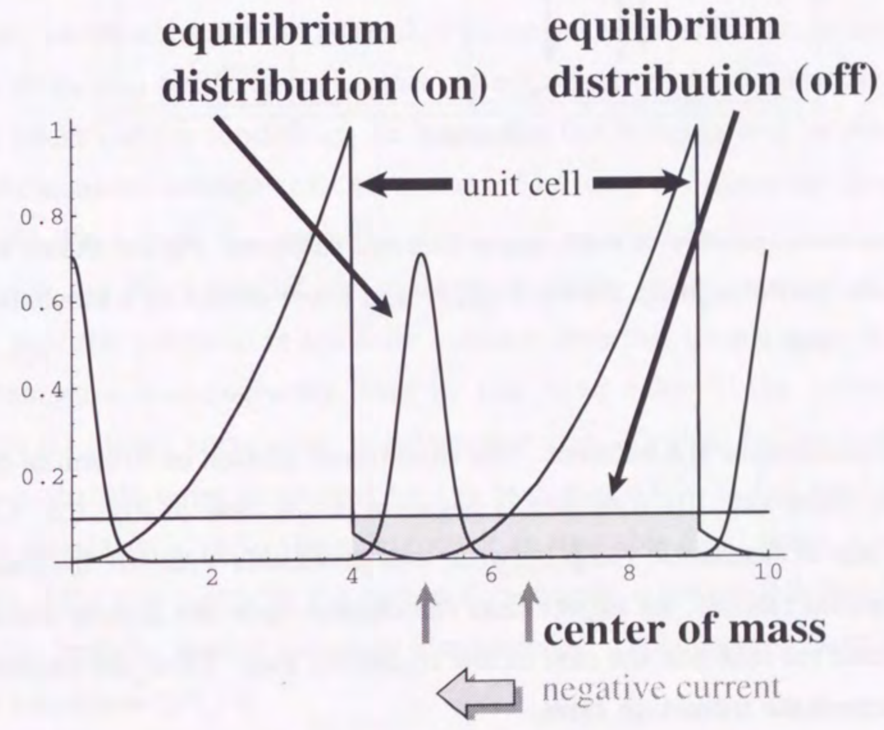

Figure 5.2: Schematic picture of fluctuating potential. Difference of centers of mass causes the directional motion of particles.

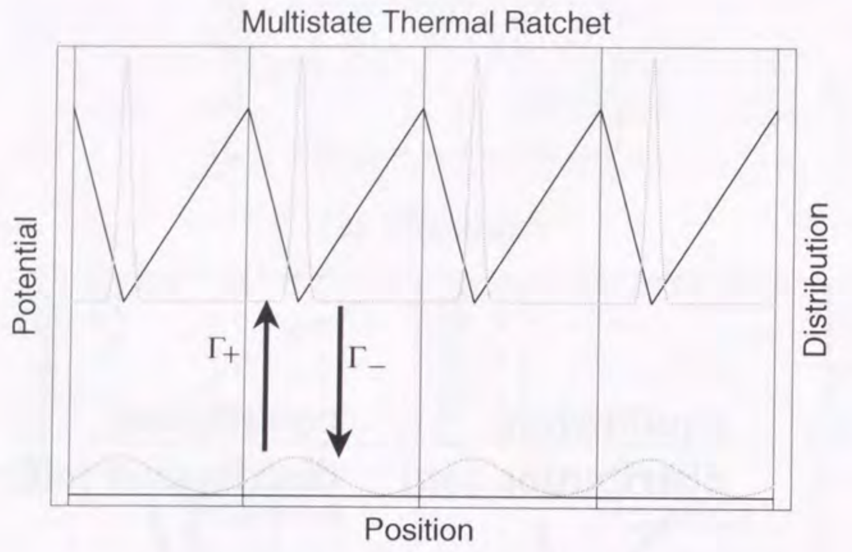

Figure 5.3: Schematic picture of multi-state thermal ratchets. Figure shows a two-state model. Brownian particles jump between upper and lower states by a stochastic process represented as Γ_+ and Γ_-.

lower potential landscapes are different. The directional motion of Brownian particles is induced by this difference. Its direction is negative in the case of Fig. 5.3. Comparing the transition rate of stochastic jump between two potentials with the frequency in the fluctuating potential ratchet, we expect that the current does not appear neither in the case of high transition rate nor the case of low transition rate. Thus the current appears only in an intermediate transition rates.

Many other types of ratchets that are not classified into above categories have also been proposed. An entropic ratchet is one example [52, 63]. This system is realized by the gel electrophoresis of polymers. The polymers are confined in quasi-one-dimensional channel whose inner wall has an asymmetric periodic shape. When symmetric electric pulses are applied to the polymers, they exhibit directional motions under certain conditions. In addition to ordinal ratchet effects, a directional migration is enhanced due to entropic effects, since confined polymers in the narrow asymmetric channel feel effective force by the spatial asymmetry of conformational entropy.

Another example is the cooperative ratchet [13, 37], in which collision of the Brownian particles is introduced, which induces cooperative motion of the Brownian particles.

Remarkable result is that the direction of rectified motion of particle changes as increasing the particle density. The average velocity of particles depends sensitively on the particle size. As a biological model, more realistic interaction has been introduced [36, 37]. Brownian particles in this model represent the myosin heads. In order to take into account the fact that the myosin molecules are attached to each other with their tails, each Brownian particle is connected to the backbone that represents the myosin filament by a spring. Since the spacing of the myosin heads is different from that of the actin monomers, the period of asymmetric periodic potential and spacing of Brownian particles are incommensurate in general. The model is the multi-state thermal ratchet in which the Brownian particles are connected with each other. It shows dynamical phase transition under certain conditions; As increasing the jumping rate between different potentials, the nonzero average current appears. Moreover spontaneous directional motion appears even when both the potential shape and external forcing are symmetric.

There also are other ratchet-like systems in which, in the contrast with ratchet systems, the periodic potential is spatially homogeneous but time-dependent external process has temporal inhomogeneity, that is, the mean value of the external process has no bias but its higher correlation is inhomogeneous. Typical example of such external process is a chaotic noise generated by the tent map [33]. It has zero average but its dynamical correlation due to the existence of an unstable fixed point is inhomogeneous. As a result, Brownian particles subject to this chaotic noise exhibit directional diffusion even though periodic spatial potential is symmetric. Dichotomous noise can also realize the above situations [10, 14].

5.3 Semi-classical Treatment of Quantum Ratchets

If the ratchet is fabricated in smaller scale than the Brownian regime and subject to lower temperature environment, the quantum mechanical effects will become appreciable. The ratchets in this regime are called quantum ratchet [26, 56, 57, 65, 70]. Concept of quantum ratchets were proposed quite recently by the author and the co-workers [65, 70] and independently Reimann *et al* [56]. In the quantum ratchets, quantum tunneling will give appreciable contribution to the current at low temperature. Thus if the system is cooled from high temperature to low temperature, quantum–classical crossover will be observed. In addition, since the quantum tunneling is accompanied by energy dissipation in ratchet systems, the quantum ratchet system gives rise to important issues regarding quantum nonequilibrium steady dynamics caused by interplay of thermal heat bath and external driving. Moreover the quantum ratchets, if fabricated in near future, will be used in new quantum electric devices or quantum energy transducers for industrial purpose. From theoretical point of view, we would be able to explore a new paradigm of quantum thermodynamics such as a quantum engine [24]. Here semi-classical treatment of quantum ratchets is briefly described. A fully quantum treatment will be given in detail in the following chapters.

There are several treatments of dissipative quantum dynamics: Path integral methods [7, 15, 18, 27, 30, 31, 68, 69], projection methods [6, 41, 48, 61], quantum Langevin dynamics [22, 23, 51] and so on. In semi-classical regime, the path integral treatment is widely used. Reimann *et al.* [56] have studied tunneling current for the quantum ratchet system based on the Caldeira-Leggett model of the heat bath [7, 44]. They started with the following Hamiltonian:

$$H_{\mathrm{total}} = \frac{P^2}{2M} + V(Q) + \sum_{\alpha=1}^{N}\left(\frac{p_\alpha^2}{2m_\alpha} + \frac{1}{2}m_\alpha\omega_\alpha^2\left(x_\alpha - \frac{c_\alpha}{m_\alpha\omega_\alpha^2}Q\right)^2\right) , \qquad (5.11)$$

where $\{P, Q\}$ are canonical variables of the ratchet system and M is a particle mass. $V(Q)$ is the asymmetric periodic potential chosen as a combined sinusoidal potential as

$$V(Q) = V_0\left\{\sin\frac{2\pi Q}{L} - 0.22\sin\frac{4\pi Q}{L}\right\} , \qquad (5.12)$$

where L is a period of the potential. $\{p_\alpha, x_\alpha\}$ are canonical variables of the harmonic oscillator with a frequency ω_α and a mass m_α. c_α is a coupling constant between the ratchet system and the heat bath represented by a set of the harmonic oscillators. Assuming the Ohmic dissipation, they obtained the effective action of the ratchet system:

$$S^E_{eff}[Q] = \int_0^{\hbar\beta} d\tau\left(\frac{M}{2}\dot{Q}(\tau)^2 + V(Q(\tau))\right) + \frac{\eta}{4\pi}\int_0^{\hbar\beta} d\tau\int_{-\infty}^{\infty} d\tau'\frac{(Q(\tau) - Q(\tau'))^2}{(\tau - \tau')^2} , \qquad (5.13)$$

where $\hbar, \beta, \eta$ are Planck constant, an inverse temperature of the heat bath, and a viscosity coefficient, respectively, (see Appendix A).

They calculated the currents based on the above effective action and the additional external force. The external force is taken as dichotomous periodic symmetric fluctuating force, whose amplitude is F, with sufficiently large period so that the system can always adiabatically adjust to the instantaneous thermal equilibrium state. Then the potential varies periodically as

$$V(Q) + FQ \leftrightarrows V(Q) - FQ . \qquad (5.14)$$

As a result, the effects of quantum tunneling enhance the directional currents below a classical-quantum crossover temperature and the finite net currents remain in the zero temperature limit. In addition, they reported the direction of currents changes at low temperature.

The above results correspond to dichotomous fluctuating thermal ratchet. Next consider the quantum ratchet system under oscillating force, which has been discussed by Tatara *et al* [65]. An asymmetric periodic potential is simply chosen as a saw-tooth shape with spatial period a. In the unit cell it is written as

$$U(x) = \alpha(a - x) \qquad (0 \le x < a) . \qquad (5.15)$$

A parameter α determines the slope of the potential. External forcing is taken as a sinusoidally fluctuating force with an amplitude ϵ_0 and the frequency ω; Then the total potential is

$$V(x, t) = U(x) + \epsilon_0 x\cos\omega t . \qquad (5.16)$$

The Lagrangian of the ratchet system without an interaction with the heat bath is expressed as

$$\mathcal{L}_s = \frac{m}{2}\left(\frac{dx}{dt}\right) - U(x) + \epsilon_0 x\cos\omega t . \qquad (5.17)$$

Consider the tunneling probability from $x = 0$ to $x = a$ and it is denoted by Γ_R. For weak external forcing, the WKB approximation gives

$$\Gamma_R \sim \omega_0 \exp\left(-\frac{S^R_{\mathrm{eff}}}{\hbar}\right) , \tag{5.18}$$

where ω_0 is a frequency of the zero-point oscillation around $x = 0$. S^R_{eff} is the action along a motion of particle from $x = 0$ to $x = a$ and it can be separated as a non-dissipative part S^0_R and a dissipative part S'_R. The non-dissipative action is expressed as

$$S^0_R = \frac{4}{3}\alpha\tau_0 a - 4\epsilon\tau_0 a\frac{1}{\widetilde{\omega}^3}(\widetilde{\omega}\cosh\widetilde{\omega} - \sinh\widetilde{\omega}) \tag{5.19}$$

with the classical bouncing solution for the Euclidean equation of motion according to a time-dependent WKB approximation [20, 34]. In the above expression we use a half of bouncing time τ_0 without oscillating field under the Euclidean equation of motion, that is, $\tau_0 = \sqrt{2ma}\alpha$, and definitions $\widetilde{\omega} = \omega\tau_0$ and $\epsilon = \epsilon_0 \cos\omega t_0$, in which t_0 is real time of entering a particle into the potential barrier. The dissipative action is

$$\begin{aligned} S'_R = -16\frac{\epsilon}{\alpha}\frac{\eta a^2}{\widetilde{\omega}^2}\bigg[&\frac{4}{3}(4 - 5\ln 2)\widetilde{\omega}\sinh\widetilde{\omega} \\ &+ \int_0^1 dx\int_0^1 dy\frac{x^2+y^2}{x^2-y^2}\left\{\cosh\widetilde{\omega}x + \frac{x+y-2}{x+y}\cosh\widetilde{\omega}(1-x)\right\}\bigg] . \end{aligned} \tag{5.20}$$

Similarly we calculate the tunneling probability from $x = a$ to $x = 0$, which is expressed by Γ_L as

$$\Gamma_L \sim \omega_0 \exp\left(-\frac{S^L_{\mathrm{eff}}}{\hbar}\right) \tag{5.21}$$

and

$$\begin{aligned} S^L_{\mathrm{eff}} = \frac{4}{3}\alpha\tau_0 a - 4|\epsilon|\tau_0 a\frac{1}{\widetilde{\omega}^3}(\sinh\widetilde{\omega} - \widetilde{\omega}) - 16\frac{|\epsilon|}{\alpha}\frac{\eta a^2}{\widetilde{\omega}^2}\bigg[&2(1 - \ln 2)(\cosh\widetilde{\omega} - 1) \\ &+ \int_0^1 dx\int_0^1 dy\frac{x^2+y^2}{x^2-y^2}\left\{\cosh\widetilde{\omega}(1-x) + \frac{x+y-2}{x+y}\cosh\widetilde{\omega}x\right\}\bigg] . \end{aligned} \tag{5.22}$$

Each tunneling probability is obtained by considering only the tunneling of a single potential barrier. If the dissipation of energy and decoherence at the potential bottoms are sufficiently fast, the dynamics can be described by a collection of independent single tunneling. In such situation the currents per unit cell is determined by the difference of single tunneling probability in both directions. This condition restricts the viscosity constant η. Two tunneling probabilities allow us to calculate the current as

$$J \equiv \Gamma_R - \Gamma_L \simeq \omega_0 e^{-4\alpha\tau_0 a/3\hbar} 4|\epsilon|\tau_0 a(I(\widetilde{\omega}) + \eta a^2 K(\widetilde{\omega})) + O(\epsilon^2, \eta^2) , \tag{5.23}$$

where

$$I(\widetilde{\omega}) \equiv \frac{1}{\widetilde{\omega}^3}(\widetilde{\omega}\cosh\widetilde{\omega} - 2\sinh\widetilde{\omega} + \widetilde{\omega}) , \tag{5.24}$$

and

$$\begin{aligned} K(\widetilde{\omega}) \equiv \frac{1}{3}&\left[(51 - 64\ln 2)\frac{\sinh\widetilde{\omega}}{\widetilde{\omega}} + (31 - 36\ln 2)\frac{\cosh\widetilde{\omega} - 1}{\widetilde{\omega}^2}\right] \\ &- \frac{2}{\widetilde{\omega}^2}\int_0^1 dx\int_0^1 dy\frac{(x^2+y^2)(x+y-1)}{(x-y)(x+y)^2} \\ &\times (\cosh\widetilde{\omega}x - \cosh\widetilde{\omega}y + \cosh\widetilde{\omega}(1-x) - \cosh\widetilde{\omega}(1-y)) . \end{aligned} \tag{5.25}$$

This expression shows that the current is actually generated by the oscillating force, since J is proportional to $|\epsilon|$. In addition, because two functions $K(\widetilde{\omega})$ and $I(\widetilde{\omega})$ are positive and monotonically increasing functions of $\widetilde{\omega}$, the dissipation enhances the current.

Experimentally such quantum ratchet systems can be realized in the quantum mechanical devices. For example, superconducting quantum interference devices (SQUID) are one of candidates. Zapata *et al.* [71] have demonstrated that SQUID that contains three Josephson junctions can realize the asymmetric periodic potential. In this case, the phase of the wave function feels the asymmetric periodic potential and exhibits directional motion, although they have only considered thermal noises. Another candidate is a device fabricated by semiconductor superlattices [8]. Capasso *et al.* have experimentally shown that the pulse currents appear in the semiconductor superlattice with asymmetric periodic potential structure by a laser pulse excitation. If the laser pumping is periodically applied, the steady currents will be generated. Its rectification mechanism is also owing to the classical thermal relaxation. Experiments of the ratchet in the quantum regime have not been achieved so far.

Chapter 6

Numerical Treatment of Quantum Driven Dissipative Systems

In this chapter we develop numerical treatment of a quantum driven dissipative systems extending the projection method. In the first section we derive a fundamental equation governing dynamics of the density matrix. In the next section, for a periodic driving, steady periodic state is calculated. The last section is devoted to description of a concrete model of a heat bath and calculation of coefficients appearing in the fundamental equation, for convenience of numerical calculation.

6.1 Projection Method

6.1.1 Quantum Driven Dissipative Liouville Equation

There are many ways to deal with a time-dependent quantum system interacting with a heat bath; For example, the path integral method using the semiclassical expansions are widely used [7, 15, 18, 27, 30, 31, 44, 69]. For deep quantum regime, projection method is sometimes used [6, 23, 41, 48, 61]. In this section we develop the projection method for the system with time-dependent external field, intending to apply to quantum ratchet systems.

Let us derive a fundamental equation governing quantum dynamics of a system. Assume that a total time-dependent system Hamiltonian $\mathsf{H}(t)$ is decomposed into three parts: an subsystem (influenced by the time-dependent field) $\mathsf{H}_{sys}(t)$ whose dynamics is of our main interest, a heat bath H_B, and an interaction between them H_{int}. The total system is isolated. Temporal evolution of a density operator $\sigma(t)$ of the total system is given by the following quantum Liouville equation:

$$\frac{\partial \sigma(t)}{\partial t} = -\frac{i}{\hbar}[H(t), \sigma(t)] \ . \tag{6.1}$$

Denote three Liouville operators as $i\mathcal{L}_{sys}(t) \equiv -(i/\hbar)[H_{sys}(t), \quad]$, $i\mathcal{L}_{int} \equiv -(i/\hbar)[H_{int}, \quad]$, and $i\mathcal{L}_B \equiv -(i/\hbar)[H_B, \quad]$, and define a Liouville operator of the total system as $i\mathcal{L}(t) \equiv i(\mathcal{L}_{sys}(t) + \mathcal{L}_{int} + \mathcal{L}_B)$. Then Equation (6.1) can be rewritten as follows:

$$\frac{\partial \sigma(t)}{\partial t} = i\mathcal{L}(t)\,\sigma(t) = i(\mathcal{L}_{sys}(t) + \mathcal{L}_{int} + \mathcal{L}_B)\sigma(t) \ . \tag{6.2}$$

We define the density operator of the subsystem $\rho(t)$ as:

$$\rho(t) \equiv \mathrm{Tr}_B\,[\sigma(t)] \,,$$

where Tr_B means the trace operation carried out with respect to the Hilbert space of H_B. Assuming that the heat bath is in the thermal equilibrium with inverse temperature β, we can write the density operator of the heat bath ρ_B as

$$\rho_B \equiv \frac{\exp(-\beta H_B)}{\mathrm{Tr}_B \exp(-\beta H_B)} = \frac{1}{Z_B} e^{-\beta H_B} \ ,$$

where Z_B is the partition function of the heat bath, that is, $Z_B = \mathrm{Tr}_B \exp(-\beta H_B)$.

Let us define the projection operators $\mathcal{P}$ and $\mathcal{Q}$ as follows:

$$\mathcal{P}f \equiv \mathrm{Tr}_B\,[f] \otimes \rho_B,$$
$$\mathcal{Q} \equiv 1 - \mathcal{P} \ ,$$

where f is an arbitrary operator acting on the total Hilbert space. $\mathcal{P}$ decomposes an action of the operator on the total Hilbert space into two actions on the each Hilbert space: $\mathrm{Tr}_B\,[f]$ is an operator acting on the Hilbert space of the subsystem and ρ_B is acting on the Hilbert space of the heat bath. The density operator of the subsystem is expressed as

$$\mathcal{P}\sigma(t) = \rho(t) \otimes \rho_B .$$

When the heat bath is in the thermal equilibrium state, these projection operators satisfy the following relations:

$$\begin{aligned}
\mathcal{P}^2 &= \mathcal{P}, & \mathcal{Q}^2 &= \mathcal{Q}, \\
\mathcal{P}\mathcal{Q} &= 0, & \mathcal{Q}\mathcal{P} &= 0, \\
\mathcal{P} + \mathcal{Q} &= 1, & \mathcal{P}\mathcal{L}_{sys}(t) &= \mathcal{L}_{sys}(t)\,\mathcal{P}, \\
\mathcal{P}\mathcal{L}_B &= 0, & \mathcal{L}_B\mathcal{P} &= 0, \\
\mathcal{Q}\mathcal{L}_{sys}(t) &= \mathcal{L}_{sys}(t)\,\mathcal{Q}, & \mathcal{Q}\mathcal{L}_B &= \mathcal{L}_B .
\end{aligned} \tag{6.3}$$

Here, for simplicity, $\mathcal{L}_{int}$ is restricted to satisfy the condition $\mathcal{P}\mathcal{L}_{int}\mathcal{P} = 0$ which means that $\mathrm{Tr}_B[H_{int}\rho_B] = 0$.

Applying these projection operators to Eq. (6.2) gives two equations:

$$\frac{\partial \mathcal{P}\sigma(t)}{\partial t} = \mathcal{P}i\mathcal{L}(t)\,\mathcal{P}\sigma(t) + \mathcal{P}i\mathcal{L}(t)\,\mathcal{Q}\sigma(t),$$
$$\text{and} \quad \frac{\partial \mathcal{Q}\sigma(t)}{\partial t} = \mathcal{Q}i\mathcal{L}(t)\,\mathcal{P}\sigma(t) + \mathcal{Q}i\mathcal{L}(t)\,\mathcal{Q}\sigma(t).$$

A general solution of the second equation is

$$\begin{aligned}
\mathcal{Q}\sigma(t) = \mathcal{T}\exp&\left\{\int_{t_0}^{t} \mathcal{Q}i\mathcal{L}(t')\,dt'\right\}\mathcal{Q}\sigma(t_0) \\
&+ \int_{t_0}^{t} \mathcal{T}\exp\left\{\int_{\tau}^{t} \mathcal{Q}i\mathcal{L}(t')\,dt'\right\}\mathcal{Q}i\mathcal{L}(\tau)\,\mathcal{P}\sigma(\tau)d\tau,
\end{aligned}$$

where t_0 is an initial time and $\mathcal{T}$ indicates that a time-ordered product is taken. If the initial condition is selected as $\sigma(t_0) = \rho(t_0) \otimes \rho_B$, the first term of the solution is zero. Substituting the solution to the first equation, we get

$$\frac{\partial \mathcal{P}\sigma(t)}{\partial t} = \mathcal{P}i\mathcal{L}(t)\,\mathcal{P}\sigma(t) + \mathcal{P}i\mathcal{L}(t)\int_{t_0}^{t} \mathcal{T}\exp\left\{\int_{\tau}^{t} \mathcal{Q}i\mathcal{L}(t')\,dt'\right\}\mathcal{Q}i\mathcal{L}(\tau)\,\mathcal{P}\sigma(\tau)d\tau.$$

Expanding the action of $\mathcal{P}$ by using the relations (6.3),

$$\begin{aligned}
\frac{\partial \rho(t)}{\partial t} &= i\mathcal{L}_{sys}(t)\,\rho(t) \\
&+ \mathrm{Tr}_B\left(i\mathcal{L}_{int}\int_{t_0}^{t} d\tau\,\mathcal{T}\exp\left\{\int_{\tau}^{t} (i\mathcal{L}_{sys}(t') + i\mathcal{L}_B + i\mathcal{Q}\mathcal{L}_{int})\,dt'\right\}\mathcal{Q}i\mathcal{L}_{int}\rho(\tau)\rho_B\right)
\end{aligned} \tag{6.4}$$

is obtained. Hereafter we call the second term of r.h.s of Eq. (6.4) as a dissipation term (DT).

In order to consider weak coupling case of the interaction, we parametrize $i\mathcal{L}_{\mathrm{int}}$ to $i\epsilon\mathcal{L}_{\mathrm{int}}$ by introducing a small parameter ϵ. Then

$$(\mathrm{DT}) = \mathrm{Tr}_{\mathrm{B}}\left(i\epsilon^2\mathcal{L}_{\mathrm{int}}\int_{t_0}^{t} d\tau\mathcal{T}\exp\left\{\int_{\tau}^{t}\left(i\mathcal{L}_{\mathrm{sys}}(t') + i\mathcal{L}_{\mathrm{B}} + i\epsilon\mathcal{Q}\mathcal{L}_{\mathrm{int}}\right)dt'\right\}\mathcal{Q}i\mathcal{L}_{\mathrm{int}}\rho(\tau)\rho_{\mathrm{B}}\right).$$

We set $t_0 = 0$ and assume that $H_{\mathrm{int}} = \sum_j H_I^j \otimes \xi^j$, where H_I^j acts on the Hilbert space of the system and ξ^j acts on the Hilbert space of the heat bath. Let us define the following time-ordered product operators:

$$\overleftarrow{\mathcal{T}}(t,\tau) \equiv \overleftarrow{\mathcal{T}}\exp\left\{-\frac{i}{\hbar}\int_{\tau}^{t} H_{\mathrm{sys}}(t')\,dt'\right\},$$
$$\overrightarrow{\mathcal{T}}^{\dagger}(t,\tau) \equiv \overrightarrow{\mathcal{T}}\exp\left\{\frac{i}{\hbar}\int_{\tau}^{t} H_{\mathrm{sys}}(t')\,dt'\right\},$$

where $\overleftarrow{\mathcal{T}}$ (resp. $\overrightarrow{\mathcal{T}}^{\dagger}$) indicates increasing time ordering from the right to the left (resp. from the left to the right). Heisenberg representation of ξ^j is defined as

$$\xi^j(t) \equiv \exp\left(\frac{i}{\hbar}H_{\mathrm{B}}t\right)\xi^j\exp\left(-\frac{i}{\hbar}H_{\mathrm{B}}t\right). \tag{6.5}$$

We define the notation

$$A^{:t,\tau} \equiv \overleftarrow{\mathcal{T}}(t,\tau)A\overrightarrow{\mathcal{T}}^{\dagger}(t,\tau) \tag{6.6}$$

for arbitrary operator A. Using these definitions, we can approximate DT as

$$(\mathrm{DT}) \sim -\frac{\epsilon^2}{\hbar^2}\mathrm{Tr}_{\mathrm{B}}\left([\sum_j H_I^j\xi^j, \int_0^t d\tau[\sum_l H_I^{l:t,\tau}\xi^l(-(t-\tau)), \rho(\tau)^{:t,\tau}\rho_{\mathrm{B}}]]\right),$$

up to order ϵ^2. Variable transformation $\tau \to t - s$ gives

$$(\mathrm{DT}) \sim -\frac{\epsilon^2}{\hbar^2}\mathrm{Tr}_{\mathrm{B}}\left([\sum_j H_I^j\xi^j, \int_0^t ds[\sum_l H_I^{l:t,t-s}\xi^l(-s), \rho(t-s)^{:t,t-s}\rho_{\mathrm{B}}]]\right).$$

After carrying out the trace-operation, we get

$$(\mathrm{DT}) \sim -\frac{\epsilon^2}{\hbar^2}\int_0^t ds\sum_{j,l}\Big([H_I^j, H_I^{l:t,t-s}\rho(t-s)^{:t,t-s}]\Phi_{jl}(s)$$
$$- [H_I^j, \rho(t-s)^{:t,t-s}H_I^{l:t,t-s}]\Phi_{lj}(-s)\Big),$$

where $\Phi_{jl}(s)$ is the correlation function of the operator $\xi^j(s)$ and $\xi^l(0)$:

$$\begin{aligned}\Phi_{jl}(s) &\equiv \mathrm{Tr}_{\mathrm{B}}\left(\rho_{\mathrm{B}}e^{\frac{iH_{\mathrm{B}}s}{\hbar}}\xi^j e^{-\frac{iH_{\mathrm{B}}s}{\hbar}}\xi^l\right)\\ &\equiv \langle\xi^j(s)\xi^l(0)\rangle\\ &= \langle\xi^j(0)\xi^l(-s)\rangle\ .\end{aligned}$$

Now the equation, we call *a dissipative Liouville equation*, becomes

$$\begin{aligned}\frac{\partial\rho(t)}{\partial t} &= -\frac{i}{\hbar}[H_{\mathrm{sys}}(t), \rho(t)]\\ &\quad -\frac{\epsilon^2}{\hbar^2}\int_0^t ds\sum_{j,l}\Big([H_I^j, H_I^{l:t,t-s}\rho(t-s)^{:t,t-s}]\Phi_{jl}(s)\\ &\quad - [H_I^j, \rho(t-s)^{:t,t-s}H_I^{l:t,t-s}]\Phi_{lj}(-s)\Big)\ ,\end{aligned} \tag{6.7}$$

which is exact up to order ϵ^2.

The dissipation term is written in convolution form, which makes the equation difficult to handle. Let us consider an approximation scheme without convolution. Since we have assumed the parameter ϵ to be small, the characteristic time of the temporal change of $\rho(t)$ caused by the heat bath is very long. Moreover, if the heat bath is sufficiently large, the function $\Phi_{jl}(s)$ vanishes quickly as increasing time. In such situation only the integrand near $s \sim 0$ contributes to the integral. In addition, assuming that the external field is slowly varying, we can justify the following approximation:

1. $\overleftarrow{\mathcal{T}}(t,t-s)\rho(t-s)\overrightarrow{\mathcal{T}}^{\dagger}(t,t-s) \to \rho(t)$
2. $\overleftarrow{\mathcal{T}}\exp\left\{-\frac{i}{\hbar}\int_t^{t-s} H_{\mathrm{sys}}(t')\,dt'\right\} \to \exp\left\{-\frac{i}{\hbar}H_{\mathrm{sys}}(t)\,s\right\}$
3. $\overrightarrow{\mathcal{T}}\exp\left\{\frac{i}{\hbar}\int_t^{t-s} H_{\mathrm{sys}}(t')\,dt'\right\} \to \exp\left\{\frac{i}{\hbar}H_{\mathrm{sys}}(t)\,s\right\}$
4. $\int_0^t ds \to \int_0^{\infty} ds$

Therefore we can approximate DT as

$$\begin{aligned}(\mathrm{DT}) = -\frac{\epsilon^2}{\hbar^2}\int_0^{\infty} ds\sum_{j,l}\Big(&[H_I^j, \exp\left\{-\frac{i}{\hbar}H_{\mathrm{sys}}(t)\,s\right\}H_I^l\exp\left\{\frac{i}{\hbar}H_{\mathrm{sys}}(t)\,s\right\}\rho(t)]\Phi_{jl}(s)\\ &- [H_I^j, \rho(t)\exp\left\{-\frac{i}{\hbar}H_{\mathrm{sys}}(t)\,s\right\}H_I^l\exp\left\{\frac{i}{\hbar}H_{\mathrm{sys}}(t)\,s\right\}]\Phi_{lj}(-s)\Big)\ .\end{aligned}$$

Using the property of the correlation functions $\Phi^*_{jl}(s) = \Phi_{lj}(-s)$, which is proven by Hermitian property of $\xi_j(s)$,$\xi_l(s)$ and ρ_B, we get

$$(DT) = -\frac{\epsilon^2}{\hbar^2}\int_0^\infty ds \sum_{j,l}\Big([H_I^j, [\exp\left\{-\frac{i}{\hbar}H_{sys}(t)\,s\right\} H_I^l \exp\left\{\frac{i}{\hbar}H_{sys}(t)\,s\right\}, \rho(t)]]\,\mathrm{Re}\,\Phi_{jl}(s)$$
$$+ [H_I^j, [\exp\left\{-\frac{i}{\hbar}H_{sys}(t)\,s\right\} H_I^l \exp\left\{\frac{i}{\hbar}H_{sys}(t)\,s\right\}, \rho(t)]_+]\,i\,\mathrm{Im}\,\Phi_{lj}(s)\Big) \ .$$

Now we introduce the following new operators $\mathcal{K}(t)_{jl}, \mathcal{H}(t)_{jl}$:

$$\mathcal{K}(t)_{jl} = \int_0^\infty ds \exp\left\{-\frac{i}{\hbar}H_{sys}(t)\,s\right\} H_I^l \exp\left\{\frac{i}{\hbar}H_{sys}(t)\,s\right\} \mathrm{Re}\,\Phi_{jl}(s),$$
$$\mathcal{H}(t)_{jl} = \int_0^\infty ds \exp\left\{-\frac{i}{\hbar}H_{sys}(t)\,s\right\} H_I^l \exp\left\{\frac{i}{\hbar}H_{sys}(t)\,s\right\} \mathrm{Im}\,\Phi_{jl}(s).$$

Finally the equation of motion of the density operator $\rho(t)$ of the subsystem becomes

$$\frac{\partial\rho(t)}{\partial t} = -\frac{i}{\hbar}[H_{sys}(t), \rho(t)] - \frac{\epsilon^2}{\hbar^2}\sum_{jl}\left([H_I^j, [\mathcal{K}(t)_{jl}, \rho(t)]] + i[H_I^j, [\mathcal{H}(t)_{jl}, \rho(t)]_+]\right) \ , \quad (6.8)$$

for the weak coupling case. This expression is valid when the following condition is satisfied:

$$\tau_{bath} \ll \tau_{system} \ll \frac{1}{\epsilon},$$

where $\tau_{bath}, \tau_{system}$ are the characteristic times of the heat bath and the system, respectively. The above approximations including weak coupling expansion are not appropriate in the case where long-time correlation in the heat bath exists. If we are interested in short time dynamics corresponding to the scale of the correlation time of the heat bath, we should use time-convolution-less (TCL) equations for describing dynamics [61, 67] instead of Eq. (6.8). In the present study, however, we do not discuss such case.

When the interaction Hamiltonian is factorized as $H_{int} = H_I\xi$, the dissipation term becomes simple. Taking the indices j, l as 1 and omitting them, we get

$$\frac{\partial\rho(t)}{\partial t} = -\frac{i}{\hbar}[H_{sys}(t), \rho(t)] - \frac{\epsilon^2}{\hbar^2}\left([H_I, [\mathcal{K}(t), \rho(t)]] + i[H_I, [\mathcal{H}(t), \rho(t)]_+]\right) \ , \quad (6.9)$$

where two kernels are defined as follows:

$$\mathcal{K}(t) = \int_0^\infty ds \exp\left\{-\frac{i}{\hbar}H_{sys}(t)\,s\right\} H_I \exp\left\{\frac{i}{\hbar}H_{sys}(t)\,s\right\} \mathrm{Re}\,\phi(s) \ ,$$
$$\mathcal{H}(t) = \int_0^\infty ds \exp\left\{-\frac{i}{\hbar}H_{sys}(t)\,s\right\} H_I \exp\left\{\frac{i}{\hbar}H_{sys}(t)\,s\right\} \mathrm{Im}\,\phi(s) \ .$$

6.1.2 Physical Interpretation

Time-independent Case

Here we discuss the physical meanings of the dissipative Liouville equation. Let us consider first the time-independent case. We write the dissipation term (DT) in a matrix representation with the matrix elements using eigenstates $\{|n\rangle\}$ of the system Hamiltonian and corresponding eigenvalues $\{E_n\}$;

$$\langle n|(DT)|m\rangle = -\frac{\epsilon^2}{\hbar^2}\sum_{j,l}\sum_{p,q}\Big(\int_0^\infty ds\Phi_{jl}(s)\left\{M^{j,l}_{nppq}\rho_{pm}e^{-i\omega_{pq}s} - M^{j,l}_{pmnq}\rho_{qp}e^{-i\omega_{nq}s}\right\}$$
$$-\int_0^\infty ds\Phi_{lj}(-s)\left\{M^{j,l}_{npqm}\rho_{pq}e^{-i\omega_{qm}s} - M^{j,l}_{pmqp}\rho_{nq}e^{-i\omega_{qp}s}\right\}\Big) \ ,$$

where

$$M^{j,l}_{nlpq} \equiv \langle n|H_I^j|l\rangle\langle p|H_I^l|q\rangle = M^{l,j}_{pqnl} \ ,$$
$$\omega_{pq} \equiv \frac{1}{\hbar}(E_p - E_q) = -\omega_{qp} \ ,$$
$$\rho_{qm} \equiv \langle q|\rho(t)|m\rangle \ .$$

Two coefficients are defined as follows:

$$\Gamma^+_{kmnl} \equiv \frac{1}{\hbar^2}\sum_{j,l} M^{j,l}_{kmnl}\int_0^\infty ds\Phi_{jl}(s)e^{-i\omega_{nl}s}$$
$$= \frac{1}{\hbar^2}\sum_{j,l} M^{j,l}_{kmnl}\left\{\frac{1}{2}\tilde{\Phi}_{jl}(-\omega_{nl}) - i\mathbf{P}\int_{-\infty}^\infty \frac{d\omega}{2\pi}\tilde{\Phi}_{jl}(\omega)\frac{1}{\omega + \omega_{nl}}\right\} \ ,$$
$$\Gamma^-_{kmnl} \equiv \frac{1}{\hbar^2}\sum_{j,l} M^{j,l}_{nlkm}\int_0^\infty ds\Phi_{lj}(-s)e^{-i\omega_{km}s}$$
$$= \frac{1}{\hbar^2}\sum_{j,l} M^{j,l}_{nlkm}\left\{\frac{1}{2}\tilde{\Phi}_{lj}(\omega_{km}) + i\mathbf{P}\int_{-\infty}^\infty \frac{d\omega}{2\pi}\tilde{\Phi}_{lj}(\omega)\frac{1}{\omega - \omega_{km}}\right\} \ ,$$

where $\tilde{\Phi}_{jl}(\omega)$ is the Fourier transformation of the correlation function $\Phi_{jl}(t)$ (see, Sec. 6.3.1). These definitions allow us to express DT as

$$\langle n|(DT)|m\rangle = -\epsilon^2\sum_{p,q}\left\{\rho_{qm}\Gamma^+_{nppq} - \rho_{qp}\Gamma^+_{pmnq} - \rho_{pq}\Gamma^-_{qmnp} - \rho_{nq}\Gamma^-_{qppm}\right\}$$
$$= \epsilon^2\sum_{p,q}\rho_{pq}\left\{\Gamma^+_{qmnp} + \Gamma^-_{qmnp} - \delta_{qm}\sum_r\Gamma^+_{nrrp} - \delta_{pn}\sum_r\Gamma^-_{qrrm}\right\} \ .$$

Defining a dissipative superoperator by matrix elements as

$$R_{nmpq} \equiv \Gamma^{+}_{qmnp} + \Gamma^{-}_{qmnp} - \delta_{qm}\sum_{r}\Gamma^{+}_{nrrp} - \delta_{pn}\sum_{r}\Gamma^{-}_{qrrm} ,$$

we can write DT as

$$\langle n|(DT)|m\rangle = \epsilon^{2}\sum_{p,q} R_{nmpq}\rho_{pq} .$$

Now the dissipative Liouville equation is expressed by the matrix elements as

$$\frac{\partial\rho_{nm}(t)}{\partial t} = -i\omega_{nm}\rho_{nm}(t) + \epsilon^{2}\sum_{p,q} R_{nmpq}\rho_{pq}(t) .$$

Consider the equation of motion for the diagonal elements of $\rho(t)$ Substituting $m = n$ gives

$$\frac{\partial\rho_{nn}(t)}{\partial t} = \epsilon^{2}\sum_{p,q} R_{nnpq}\rho_{pq}(t) .$$

We decompose the right-hand side into two parts; one expresses the temporal change caused by the diagonal elements of $\rho(t)$, so-called *a diagonal-to-diagonal part*, and another is the remaining *a off-diagonal-to-diagonal part*, and obtain

$$\begin{aligned}\frac{\partial\rho_{nn}(t)}{\partial t} &= \epsilon^{2}\left\{\sum_{p} W_{np}\rho_{pp}(t) - \sum_{p} W_{pn}\rho_{nn}(t)\right\}\\ &\quad + \epsilon^{2}\sum_{\substack{p,q\\ p\neq q}}\left\{\Gamma^{+}_{qnnp} + \Gamma^{-}_{qnnp} - \sum_{r}\left(\Gamma^{+}_{qrrp}\delta_{qn} + \Gamma^{-}_{qrrp}\delta_{pn}\right)\right\}\rho_{pq}(t) . \qquad (6.10)\end{aligned}$$

The first term is the diagonal-to-diagonal part and the second term is the off-diagonal-to-diagonal part. Here we have introduced coefficients, which can be interpreted as a transition probability from the state p to the state n, as follows:

$$W_{np} = \Gamma^{+}_{pnnp} + \Gamma^{-}_{pnnp}. \qquad (6.11)$$

It is rewritten further as

$$\begin{aligned}W_{np} &= \Gamma^{+}_{pnnp} + \Gamma^{-}_{pnnp}\\ &= \Gamma^{+}_{pnnp} + (\Gamma^{+}_{pnnp})^{*}\\ &= 2\,\mathrm{Re}\,\Gamma^{+}_{pnnp}\\ &= \frac{2}{\hbar^{2}}\,\mathrm{Re}\sum_{j,l} M^{j,l}_{pnnp}\int_{0}^{\infty} e^{-i\omega_{np}(t)s}\Phi_{jl}(s)ds\\ &= \sum_{j,l}\int_{-\infty}^{\infty}\frac{d\omega}{\hbar^{2}}\tilde{\Phi}_{jl}(\omega)M^{j,l}_{pnnp}\delta(\omega+\omega_{np})\\ &= \sum_{j,l}\frac{1}{\hbar^{2}}\tilde{\Phi}_{jl}(\omega_{pn})M^{j,l}_{pnnp} ,\end{aligned}$$

where $\tilde{\Phi}_{jl}(\omega)$ is the Fourier transformation of the correlation function $\Phi_{jl}(t)$ (see Sec. 6.3.1). Substituting the explicit form of the Fourier transformation into the above expression, we get

$$\begin{aligned}W_{np} &= \frac{2\pi}{\hbar}\int_{-\infty}^{\infty}\int_{-\infty}^{\infty} dEdE'g(E)g(E')\frac{e^{-\beta E}}{Z_{B}}\delta(E'-E-\hbar\omega_{pn}) \qquad (6.12)\\ &\qquad \sum_{j,l}\langle p,E|H^{j}_{I}\otimes\xi^{j}|n,E'\rangle\langle n,E'|H^{l}_{I}\otimes\xi^{l}|p,E\rangle\\ &= \frac{2\pi}{\hbar}\int_{-\infty}^{\infty}\int_{-\infty}^{\infty} dEdE'g(E)g(E')\frac{e^{-\beta E}}{Z_{B}}\delta(E'-E-\hbar\omega_{pn})\,|\langle n,E'|H_{int}|p,E\rangle|^{2} .\end{aligned}$$

Integrand is understood as the transition probability from the initial state $|p,E\rangle$ (states of the heat bath $\{|E\rangle\}$ are in thermal equilibrium) to the final state $|n,E'\rangle$ by Fermi's golden rule. Thus the coefficient W_{np} represents the process that the system is excited by the boson in the heat bath or the system emits the boson which is absorbed into the heat bath (see Fig. 6.1).

Since $\Phi_{jl}(t)$ is the thermal correlation function, the Kubo-Martin-Schwinger (KMS) relation [40, 49], $\tilde{\Phi}_{jl}(\omega) = e^{\hbar\omega\beta}\tilde{\Phi}_{lj}(-\omega)$, should be satisfied. It provides

$$\begin{aligned}W_{np} &= \sum_{j,p}\frac{1}{\hbar^{2}}\tilde{\Phi}_{jl}(\omega_{pn})M^{j,l}_{pnnp}\\ &= \sum_{j,l}\frac{1}{\hbar^{2}}\tilde{\Phi}_{lj}(\omega_{np})M^{l,j}_{nppn}e^{\hbar\omega_{pn}\beta}\\ &= W_{pn}e^{-\hbar\omega_{np}\beta} .\end{aligned}$$

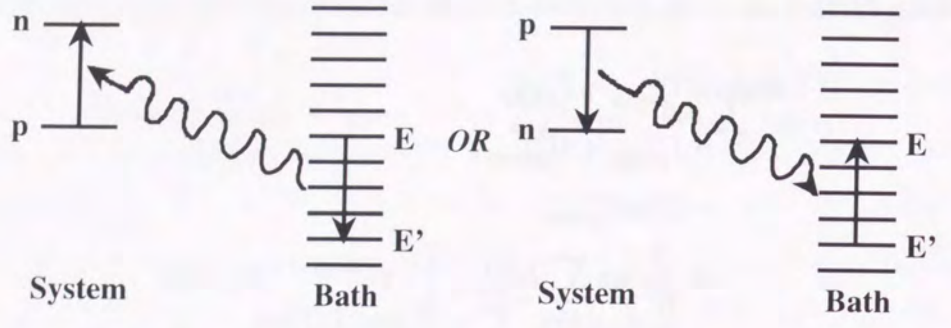

Figure 6.1: Schematic diagram of the process W_{np}.

Thus the KMS relation ensures that the system relaxes to the thermal equilibrium and supports the detailed balance. As a result, the diagonal-to-diagonal term is interpreted as the classical Master equation.

The off-diagonal-to-diagonal term of Eq. (6.10):

$$\epsilon^2 \sum_{\substack{p,q \\ p\neq q}} \left\{ \Gamma^+_{qnnp} + \Gamma^-_{qnnp} - \sum_r \left(\Gamma^+_{qrrp}\delta_{qn} + \Gamma^-_{qrrp}\delta_{pn} \right) \right\} \rho_{pq}(t)$$

manages the phase relaxation. It forces an initial pure state to be a mixed state and, finally, to be a classical state.

Let us consider the equation of motion for the off-diagonal elements $\rho_{nm}(t) \quad (n \neq m)$. The equation is

$$\begin{aligned} \frac{\partial \rho_{nm}(t)}{\partial t} &= -i\omega_{nm}\rho_{nm}(t) + \epsilon^2 \sum_{p,q} R_{nmpq}\rho_{pq}(t) \\ &= -i\omega_{nm}\rho_{nm}(t) + \epsilon^2 R_{nmnm}\rho_{nm}(t) + \epsilon^2 \sum_{\substack{p,q \\ p\neq n\ q\neq m}} R_{nmpq}\rho_{pq}(t) \ . \end{aligned} \tag{6.13}$$

First term in the last expression expresses the purely quantum dynamics. The second term represents the relaxation effects and the corrections of purely quantum dynamics, because it is proportional to the off-diagonal elements ρ_{nm} and R_{nmnm} is a complex coefficient. This coefficient is written as

$$R_{nmnm} = -\tilde{\gamma}_{nm} - \gamma_{nm} \ ,$$

where

$$\tilde{\gamma}_{nm} \equiv -\Gamma^+_{mmnn} - \Gamma^-_{mmnn} \ , \quad \gamma_{nm} = \sum_r \Gamma^+_{nrrn} + \Gamma^-_{mrrm} \ ,$$

and they satisfy

$$\gamma_{nm} = \gamma^*_{mn} \ , \qquad \tilde{\gamma}_{nm} = \tilde{\gamma}^*_{mn} \ .$$

We express R_{nmnm} another way:

$$R_{nmnm} = -\gamma^{(n,m)} - i\Delta\omega_{nm} \ ,$$

where $\gamma^{(n,m)}$ and $\Delta\omega_{nm}$ are real parameters defined as:

$$\gamma^{(n,m)} \equiv \mathrm{Re}\,\tilde{\gamma}_{nm} + \mathrm{Re}\,\gamma_{nm} \ , \quad \Delta\omega_{nm} \equiv \mathrm{Im}\,\tilde{\gamma}_{nm} + \mathrm{Im}\,\gamma_{nm} \ .$$

The last part of Eq. (6.13) contains the transition from the diagonal elements to the off-diagonal elements and from the off-diagonal elements to the off-diagonal elements. Thus this part also contributes to the phase relaxation.

Consider the second term; Here we calculate two coefficients, γ_{nm} and $\tilde{\gamma}_{nm}$. The former is decomposed as

$$\begin{aligned} \gamma_{nm} &\equiv \sum_r \{\Gamma^+_{nrrn} + \Gamma^-_{mrrm}\} \\ &= \frac{1}{2}\sum_r \{W_{rn} + W_{rm}\} - i\left(\Delta E_n - \Delta E_m\right) \ , \end{aligned}$$

where W_{rn} is the transition probability defined by Eq. (6.12) and ΔE_n is defined by

$$\begin{aligned} \Delta E_n &\equiv \frac{1}{\hbar^2} \sum_{j,l} \sum_r M^{j,l}_{nrrn} \mathbf{P} \int_{-\infty}^{\infty} \frac{d\omega}{2\pi} \tilde{\Phi}_{jl}(\omega) \frac{1}{\omega + \omega_{rn}} \\ &= \mathbf{P} \int_{-\infty}^{\infty} g(E)dE \frac{e^{-\beta E}}{Z_B} \int_{-\infty}^{\infty} g(E')dE' \sum_r \frac{|\langle r, E'|H_{int}|n, E\rangle|^2}{E' - E + \hbar\omega_{rn}} \ . \end{aligned}$$

which is interpreted as the energy shift of the eigenstate with label n caused by the second-order perturbation of the interaction Hamiltonian H_{int}. For the coefficient $\tilde{\gamma}_{nm}$, on the other hand, we obtain

$$\begin{aligned}\tilde{\gamma}_{nm} &\equiv -\left(\Gamma^{+}_{mmnn} + \Gamma^{-}_{mmnn}\right)\\ &= -\frac{1}{\hbar^2}\sum_{j,l}\left(M^{j,l}_{mmnn}\int_0^\infty ds\Phi_{jl}(s) + M^{j,l}_{nnmm}\int_0^\infty ds\Phi_{lj}(-s)\right)\\ &= -\frac{1}{\hbar^2}\sum_{j,l} M^{j,l}_{mmnn}\tilde{\Phi}_{jl}(0)\\ &= -\frac{2\pi}{\hbar}\int_{-\infty}^{\infty} dEg(E)^2\frac{e^{-\beta E}}{Z_B}\langle m, E|H_{int}|m, E\rangle\langle n, E|H_{int}|n, E\rangle \ .\end{aligned}$$

Defining $W^{ad}_{nm} \equiv (2\pi/\hbar)\int_{-\infty}^{\infty} dEg(E)^2(e^{-\beta E}/Z_B)\langle m, E|H_{int}|m, E\rangle\langle n, E|H_{int}|n, E\rangle$, we get

$$\begin{aligned}\gamma^{(n,m)} &= \frac{1}{2}\sum_r\{W_{rn} + W_{rm}\} - W^{ad}_{nm} \ ,\\ \Delta\omega_{nm} &= -\left(\Delta E_n - \Delta E_m\right) \ .\end{aligned}$$

Then the complex coefficient R_{nmnm} is

$$\begin{aligned}R_{nmnm} &= -\gamma^{(n,m)} - i\Delta\omega_{nm}\\ &= -\frac{1}{2}\sum_r\{W_{rn} + W_{rm}\} + W^{ad}_{nm} - i\left(\Delta E_m - \Delta E_n\right) \ .\end{aligned}$$

Therefore the relaxation effects caused by the second term is represented by the transition probabilities W_{rn} and the real coefficients W^{ad}_{nm}. The corrections to the purely quantum dynamics is described by the energy shift calculated by the second-order perturbation.

In the special case that $H_{int} = H_I\xi$ and $H_I = H_{sys}$, the equation of motion becomes very simple:

$$\frac{\partial\rho_{nm}}{\partial t} = -i\omega_{nm}\left(1 + \epsilon^2\frac{E_n + E_m}{\hbar}\,\mathrm{Im}\int_0^\infty ds\Phi(s)\right)\rho_{nm} - \epsilon^2\omega_{nm}^2\left(\mathrm{Re}\int_0^\infty ds\Phi(s)\right)\rho_{nm} \ .$$

The first term represents the purely quantum dynamics including a correction term of energy shift. The second term expresses the phase relaxation. In this case, however, the thermal equilibrium is not ensured, since energy does not dissipate, even though the entropy is generated.

Time-dependent case

When the system Hamiltonian depends on time explicitly, the above discussion should slightly be modified. There are two cases of the dependence on time of the eigensystem in the present situation; one is that only the eigenvalues depend on time and another is that both the eigenvalues and the eigenstates depends on time. In the first case, the eigenstates $\{|n\rangle\}$ and eigenvalues $\{E_n(t)\}$ satisfy the following eigenvalue equation:

$$H_{sys}\,(t)\,|n\rangle = E_n(t)|n\rangle \ ,$$

where $|n\rangle$ does *not* depend on time. For instance, two-level systems with time-varying energy level, and harmonic oscillators having time-dependent frequency correspond to this case. Then the dissipative Liouville equation expressed by the matrix elements,

$$\frac{\partial\rho_{nm}(t)}{\partial t} = -i\omega_{nm}\rho_{nm}(t) + \epsilon^2\sum_{p,q} R_{nmpq}\rho_{pq}(t) \ ,$$

does not change. Only the frequency ω_{nm} becomes dependent on time. Thus all ω_{nm} in the equation must be replaced by $\omega_{nm}(t)$.

In the second case, the fundamental equation is a little complicated. Consider the eigenvalues $\{E_n(t)\}$ and the eigenstates $\{|n\rangle\}$ satisfying

$$H_{sys}\,(t)\,|n\rangle = E_n(t)|n\rangle \ .$$

The eigenstates depend on time implicitly. Let the basis $\{|\mu\rangle\}$ (indicated by Greek letter) be independent of time. Using these bases we can write the dissipative Liouville equation as

$$\begin{aligned}\frac{\partial\langle\mu|\rho(t)|\nu\rangle}{\partial t} &= \sum_{n,m}\langle\mu|n\rangle\langle n|\left\{-\frac{i}{\hbar}[H_{sys}\,(t)\,,\rho(t)]\right.\\ &\qquad\left.-\frac{\epsilon^2}{\hbar^2}\sum_{jl}\left([H^j_I,[\mathcal{K}(t)_{jl},\rho(t)]] + i[H^j_I,[\mathcal{H}(t)_{jl},\rho(t)]_+]\right)\right\}|m\rangle\langle m|\nu\rangle\\ &= \sum_{n,m}\langle\mu|n\rangle\left(-i\omega_{nm}\rho_{nm}(t) + \epsilon^2\sum_{p,q} R_{nmpq}\rho_{pq}(t)\right)\langle m|\nu\rangle\\ &= -i\sum_{n,m,\lambda,\kappa}\omega_{nm}\langle\mu|n\rangle\langle m|\nu\rangle\langle n|\lambda\rangle\langle\kappa|m\rangle\rho_{\lambda\kappa}(t)\\ &\qquad+\epsilon^2\sum_{p,q,n,m,\lambda,\kappa} R_{nmpq}\langle\mu|n\rangle\langle m|\nu\rangle\langle p|\lambda\rangle\langle\kappa|q\rangle\rho_{\lambda\kappa}(t) \ .\end{aligned}$$

In the final expression all the frequencies ω_{nm} depend on time t. Besides them, the coefficients $\langle\mu|n\rangle, \langle m|\nu\rangle, \ldots$ depend on time. In the next chapter numerical calculation will be done based on the above equation.

6.2 Steady Periodic States in Quantum Driven Dissipative Systems

In this section we consider a steady state of the systems whose temporal evolution is described by the time-dependent dissipative Liouville equation. In Sec. 6.1 we have already obtained the equation of motion for the density operator $\rho(t)$ as follows:

$$\frac{\partial\rho(t)}{\partial t} = -\frac{i}{\hbar}[H_{sys}(t), \rho(t)] - \frac{\epsilon^2}{\hbar^2}\sum_{j,l}\Big([H_I^j, [\mathcal{K}(t)_{jl}, \rho(t)]] + i[H_I^j, [\mathcal{H}(t)_{jl}, \rho(t)]_+]\Big). \quad (6.14)$$

This is a linear equation for the matrix elements of the density operator. Thus we can rewrite the equation as follows:

$$\frac{\partial\vec{\rho}(t)}{\partial t} = \mathcal{M}(t)\vec{\rho}(t), \quad (6.15)$$

where $\vec{\rho}(t) \in \mathbf{C}^{N^2}$ (N is a dimension of Hamiltonian) is vector representation of the density matrix and $\mathcal{M}(t) \in \mathbf{C}^{N^2 \otimes N^2}$ is matrix representation of the dissipative Liouville superoperator. In general $\mathcal{M}(t)$ is a complex asymmetric matrix. Formal solution of Eq. (6.15) can be obtained as follows:

$$\vec{\rho}(t) = \mathcal{D}(t, t_0)\vec{\rho}(t_0), \quad (6.16)$$

where $\mathcal{D}(t, t_0)$ is a time-evolution operator:

$$\mathcal{D}(t, t_0) \equiv \overleftarrow{\mathcal{T}} \exp\int_{t_0}^{t} \mathcal{M}(t')dt'. \quad (6.17)$$

If the Hamiltonian of the system is independent of time and the matrix $\mathcal{M}$ is symmetric, the steady state is given by the linear combination of the eigenstates corresponding to largest eigenvalue 0 of the matrix $\mathcal{M}$. But in the present case $\mathcal{M}$ is asymmetric and the naive diagonalization fails to give steady states.

What we are interested in is the "steady state" of the time-dependent systems, especially periodically driven systems. When an external forcing is periodic with period T, $\mathcal{M}(t) = \mathcal{M}(t+T)$. Then we expect that the dynamics of the system also becomes eventually periodic with the same period and periodically steady $\vec{\rho}(t) = \vec{\rho}(t+T)$ by analogy to classical forced damping oscillators. Let us introduce the time-evolution operator $\mathcal{D}$ for one period:

$$\mathcal{D} \equiv \mathcal{D}(t_0, t_0+T) \quad (6.18)$$

$$= \overleftarrow{\mathcal{T}} \exp\int_T \mathcal{M}(t')dt' . \quad (6.19)$$

The steady periodic state $\vec{\rho}_s(t)$ then should be in right invariant subspace of $\mathcal{D}$ corresponding to the largest weight 1, that is, $\vec{\rho}_s = \mathcal{D}\vec{\rho}_s$.

Let us construct the steady periodic state: Consider Schur decomposition of $\mathcal{D}$,

$$\mathcal{D}U = UT , \quad (6.20)$$

where matrix $U \in \mathbf{C}^{N^2 \otimes N^2}$ is a unitary matrix and $T \in \mathbf{C}^{N^2 \otimes N^2}$ is a complex upper triangular matrix whose diagonal elements are the eigenvalues of $\mathcal{D}$. If $U = [u_1, \ldots, u_{N^2}]$ is a column partitioning of the unitary matrix U and

$$\operatorname{diag} T = (\lambda_1, \cdots, \lambda_{N^2}) , \quad (6.21)$$

then the u_i are referred to as Schur vectors corresponding to the eigenvalues λ_i. When the steady periodic state exists, the matrix T can be written in the following form:

$$T = \begin{pmatrix} I_M & A \\ 0 & T^{(1)} \end{pmatrix},$$

where M represents multiplicity of the largest eigenvalues, I_M is a $M \times M$ identity matrix, A is a $M \times (N^2 - M)$ complex matrix and $T^{(1)}$ is a $(N^2 - M) \times (N^2 - M)$ complex upper-triangular matrix corresponding to the rest subspace with smaller eigenvalues. In this representation indexes of Schur vectors from 1 to M correspond to the subspace of the largest eigenvalues. The multiplicity M reflects the symmetry of the system.

Since Schur vectors $\{u_i\}$ are orthogonal and can be normalized, an initial state vector $\vec{\rho}(0)$ can be decomposed as follows:

$$\vec{\rho}(0) = \sum_{i=1}^{N^2} a_i u_i . \quad (6.22)$$

Consider a following matrix Z:

$$Z = \begin{pmatrix} I_M & -X \\ 0 & I_{N^2-M} \end{pmatrix} , \tag{6.23}$$

where I_M and I_{N^2-M} are $M \times M$ and $(N^2-M) \times (N^2-M)$ identity matrices, respectively. X is a $M \times (N^2-M)$ complex matrix determined later. Then the inverse matrix of Z is

$$Z^{-1} = \begin{pmatrix} I_M & X \\ 0 & I_{N^2-M} \end{pmatrix} . \tag{6.24}$$

The matrix T can be decomposed into a block diagonal form using Z, Z^{-1}:

$$Z^{-1}TZ = \begin{pmatrix} I_M & -X + A + XT^{(1)} \\ 0 & T^{(1)} \end{pmatrix} = \begin{pmatrix} I_M & 0 \\ 0 & T^{(1)} \end{pmatrix} , \tag{6.25}$$

if the matrix X satisfies the following matrix equation:

$$-X + A + XT^{(1)} = 0 , \tag{6.26}$$

which is a kind of Sylvester equation. A Sylvester equation can be solved by a standard way [25], so that the matrix X is easily obtained.

Using $\mathcal{D} = UTU^\dagger$, the solution X of Eq. (6.26), and $T = Z[I_M \oplus T^{(1)}]Z^{-1}$, we obtain

$$\mathcal{D} = UZ[I_M \oplus T^{(1)}]Z^{-1}U^\dagger . \tag{6.27}$$

Defining a matrix Q as $Q = UZ$, we get

$$\mathcal{D} = Q[I_M \oplus T^{(1)}]Q^{-1}, \tag{6.28}$$

thus

$$\mathcal{D}^n = Q[I_M \oplus (T^{(1)})^n]Q^{-1} . \tag{6.29}$$

Since the absolute values of the diagonal elements of the upper-triangular matrix $T^{(1)}$ are smaller than 1, $(T^{(1)})^n$ vanishes for $n \to \infty$. Thus in the long time limit

$$\begin{aligned} \vec{\rho}_s &= \lim_{n\to\infty} \mathcal{D}^n \vec{\rho}(0) = \lim_{n\to\infty} Q[I_M \oplus (T^{(1)})^n]Q^{-1}\vec{\rho}(0) \\ &= Q[I_M \oplus 0]Q^{-1}\vec{\rho}(0) = UZ \begin{pmatrix} I_M & 0 \\ 0 & 0 \end{pmatrix} Z^{-1}U^\dagger(\sum_i a_i u_i) \\ &= U \begin{pmatrix} I_M & X \\ 0 & 0 \end{pmatrix} \begin{pmatrix} {}^t u_1 \\ {}^t u_2 \\ \vdots \end{pmatrix} (\sum_i a_i u_i) = U \begin{pmatrix} I_M & X \\ 0 & 0 \end{pmatrix} \begin{pmatrix} a_1 \\ \vdots \\ a_{N^2} \end{pmatrix} . \end{aligned}$$

Writing a row partitioning of the matrix X is $X = {}^t({}^t\vec{X}_1, {}^t\vec{X}_2, \dots, {}^t\vec{X}_M)$ and defining a vector $\vec{a_{N^2-M}}$ as $\vec{a_{N^2-M}} = {}^t(a_{M+1}, a_{M+2}, \dots, a_{N^2})$, we obtain

$$\vec{\rho}_s = U \begin{pmatrix} a_1 + \vec{X}_1 \cdot \vec{a_{N^2-M}} \\ a_2 + \vec{X}_2 \cdot \vec{a_{N^2-M}} \\ \vdots \\ a_M + \vec{X}_M \cdot \vec{a_{N^2-M}} \\ 0 \\ \vdots \\ 0 \end{pmatrix} = \sum_{j=1}^{M} (a_j + \vec{X}_j \cdot \vec{a_{N^2-M}})\vec{u}_j . \tag{6.30}$$

If the matrix $\mathcal{M}$ is symmetric, the matrix $\mathcal{D}$ also is symmetric, and the solution of Sylvester equation (6.26) is zero. In that case the steady state becomes well-known form $\sum_{j=1}^{M} a_j \vec{u}_j$ where $\{\vec{u}_j\}_{j=1}^{M}$ span an invariant subspace corresponding to the largest weight 1. But, in the asymmetric case, the steady state depends on all the coefficients appearing in the decomposition by Schur vectors through the solution of the Sylvester equation (6.26).

6.3 Thermal Correlation Function, Model of Heat Bath, and Dissipation Kernels

6.3.1 Thermal Correlation Function and Model of Heat Bath

In this section we consider general features of the thermal correlation function and a model of heat bath which are convenient for numerical computation. In addition, assuming the factorized interaction Hamiltonian, we will calculate explicit form of the thermal correlation function. First general features of a Fourier transformation of the thermal correlation function are briefly reviewed. Consider the Fourier transformation of the correlation function $\Phi_{jl}(t)$ given as follows:

$$\tilde{\Phi}_{jl}(\omega) = \int_{-\infty}^{\infty} dt e^{i\omega t} \Phi_{jl}(t) , \qquad \Phi_{jl}(t) = \int_{-\infty}^{\infty} \frac{d\omega}{2\pi} e^{-i\omega t} \tilde{\Phi}_{jl}(\omega) . \tag{6.31}$$

Substituting the explicit form of the thermal correlation function, we obtain

$$\begin{aligned}
\tilde{\Phi}_{jl}(\omega) &= \int_{-\infty}^{\infty} dt e^{i\omega t}\,\mathrm{Tr}_B\{\rho_B \xi^j(t)\xi^l(0)\} \\
&= \int_{-\infty}^{\infty} dt e^{i\omega t} \int_{-\infty}^{\infty} g(E)dE \int_{-\infty}^{\infty} g(E')dE' \langle E|\rho_B|E\rangle\langle E|\xi^j(t)|E'\rangle\langle E'|\xi^l(0)|E\rangle \\
&= \int_{-\infty}^{\infty} dt e^{i\omega t} \int_{-\infty}^{\infty} g(E)dE \int_{-\infty}^{\infty} g(E')dE' \frac{e^{-\beta E}}{Z_B} e^{\frac{iEt}{\hbar}} e^{\frac{-iE't}{\hbar}} \langle E|\xi^j|E'\rangle\langle E'|\xi^l|E\rangle \\
&= \int_{-\infty}^{\infty} g(E)dE \int_{-\infty}^{\infty} g(E')dE' \frac{e^{-\beta E}}{Z_B} 2\pi\hbar\delta(E+\hbar\omega-E')\langle E|\xi^j|E'\rangle\langle E'|\xi^l|E\rangle \ ,
\end{aligned}$$

where $|E\rangle$ and $g(E)$ are the energy eigenstates and the density of states, respectively. Introducing the function $j_{\xi^j,\xi^l}(E,E') \equiv \mathrm{Tr}_B\left\{\delta(E-H_B)\xi^j\delta(E'-H_B)\xi^l\right\}$, we can rewrite the above equation as

$$\begin{aligned}
\tilde{\Phi}_{jl}(\omega) &= \int_{-\infty}^{\infty} dt e^{i\omega t} \int_{-\infty}^{\infty} dE \int_{-\infty}^{\infty} dE' \frac{e^{-\beta E}}{Z_B} e^{\frac{i(E-E')t}{\hbar}} j_{\xi^j,\xi^l}(E,E') \\
&= \int_{-\infty}^{\infty} dE \int_{-\infty}^{\infty} dE' \frac{e^{-\beta E}}{Z_B} 2\pi\hbar\delta(E+\hbar\omega-E') j_{\xi^j,\xi^l}(E,E') \ .
\end{aligned}$$

By exchanging E and E' in the final expression of above equation, we obtain the Kubo-Martin-Schwinger (KMS) relation:

$$\tilde{\Phi}_{jl}(\omega) = e^{\hbar\omega\beta}\tilde{\Phi}_{lj}(-\omega) \ . \tag{6.32}$$

Since $\Phi^*_{jl}(t) = \Phi_{lj}(-t)$, $\tilde{\Phi}_{jl}(\omega)$ should also satisfy the following relation:

$$\tilde{\Phi}^*_{jl}(\omega) = \tilde{\Phi}_{lj}(\omega) \ . \tag{6.33}$$

For $j = l$, explicit calculation of a trace operation gives

$$j_{\xi^j,\xi^j}(E,E') = g(E)g(E')|\langle E'|\xi^j|E\rangle|^2 \ . \tag{6.34}$$

Using this, we can further rewrite $\tilde{\Phi}_{jj}(\omega)$ as

$$\begin{aligned}
\tilde{\Phi}_{jj}(\omega) &= \int_{-\infty}^{\infty} g(E)dE \int_{-\infty}^{\infty} g(E')dE' \frac{e^{-\beta E}}{Z_B} 2\pi\hbar\delta(E+\hbar\omega-E')|\langle E'|\xi^j|E\rangle|^2 \\
&= \int_{-\infty}^{\infty} g(E)dE \frac{e^{-\beta E}}{Z_B} 2\pi\hbar g(E+\hbar\omega)|\langle E+\hbar\omega|\xi^j|E\rangle|^2 \ .
\end{aligned}$$

Integrand is interpreted as the transition probability from the initial state with energy E to the final state with energy $E' = E + \hbar\omega$ except for multiplicative factors, in terms

of Fermi's golden rule. Therefore the Fourier transformation of the correlation function $\Phi_{jj}(t)$ is proportional to the transition probability from the initial thermal equilibrium state to the thermal equilibrium state absorbing (or emitting) the boson with energy $\hbar\omega$.

Next let us fix a model of heat bath and an interaction between the subsystem and the heat bath. We assume that the heat bath is represented by a set of harmonic oscillators:

$$H_B = \sum_\alpha \hbar\omega_\alpha \left(a^\dagger_\alpha a_\alpha + \frac{1}{2}\right) \ .$$

For simplicity we consider the case where the interaction Hamiltonian is able to be factorized, $H_{int} = H_I\xi$. We suppose that the part acting on the Hilbert space of the heat bath of the interaction Hamiltonian is taken to be

$$\xi = \sum_\alpha \left(a_\alpha + a^\dagger_\alpha\right) \ .$$

This form satisfies the requirement of $\mathcal{P}\mathcal{L}_{int}\mathcal{P} = 0$ or $\mathrm{Tr}_B[H_{int}\rho_B] = 0$. When the heat bath is large enough, modes α is continuously distributed. Thus we replace the summation for the modes by the integration with respect to the frequency. Here we assume the functional form of the spectral density of the heat bath as $J(\omega) = \eta\omega\exp(-\lambda\omega)$, in which λ is inverse cut-off frequency of the heat bath. η is a coefficient which has dimension of $[\text{time}]^2$. [1] Then the heat bath Hamiltonian becomes

$$H_B = \int_0^\infty d\omega J(\omega)\hbar\omega\left(a^\dagger(\omega)a(\omega) + \frac{1}{2}\right) \ ,$$

and ξ becomes

$$\xi = \int_0^\infty d\omega J(\omega)\left(a(\omega) + a^\dagger(\omega)\right) \ .$$

---

[1] In the special case where H_{int} is proportional to the coordinate operator, it is related with a viscosity coefficient.

Then the thermal correlation function $\Phi(t)$ is calculated as follows:

$$
\begin{aligned}
\Phi(\tau) &= \frac{1}{\mathrm{Tr}_B\left(e^{-\beta H_B}\right)} \sum_{\alpha,\alpha'} \mathrm{Tr}_B \left\{ e^{-\beta H_B} e^{i\tau H_B/\hbar} (a_\alpha + a_\alpha^\dagger) e^{-i\tau H_B/\hbar} (a_{\alpha'} + a_{\alpha'}^\dagger) \right\} \\
&= \sum_\alpha \frac{\cosh\left(\frac{\hbar\omega_\alpha\beta}{2} - i\omega_\alpha\tau\right)}{\sinh\left(\frac{\hbar\omega_\alpha\beta}{2}\right)} \\
&= \int_0^\infty d\omega J(\omega) \frac{\cosh\left(\frac{\hbar\omega\beta}{2} - i\omega\tau\right)}{\sinh\left(\frac{\hbar\omega\beta}{2}\right)}, \\
&\quad \text{where} \quad J(\omega) = \eta\omega\exp(-\lambda\omega) \ ,
\end{aligned}
$$

and its Fourier transformation

$$
\begin{aligned}
\tilde{\Phi}(\omega) &= \sum_\alpha \frac{\pi}{\sinh\frac{\hbar\omega_\alpha\beta}{2}} \left\{ e^{\frac{\hbar\omega_\alpha\beta}{2}} \delta(\omega_\alpha - \omega) + e^{-\frac{\hbar\omega_\alpha\beta}{2}} \delta(\omega_\alpha + \omega) \right\} \\
&= \begin{cases} \eta\pi\omega e^{-\lambda\omega} \dfrac{e^{\frac{\hbar\omega\beta}{2}}}{\sinh\frac{\hbar\omega\beta}{2}} & \omega \geq 0 \\ \eta\pi\omega e^{\lambda\omega} \dfrac{e^{\frac{\hbar\omega\beta}{2}}}{\sinh\frac{\hbar\omega\beta}{2}} & \omega \leq 0 \\ \dfrac{2\pi\eta}{\hbar\beta} & \omega = 0 \end{cases} \\
&= \eta\pi\omega \frac{\exp\left\{\frac{\hbar\omega\beta}{2} - \lambda|\omega|\right\}}{\sinh\frac{\hbar\omega\beta}{2}} \ .
\end{aligned}
$$

Integrating the above, we get the real part of the thermal correlation function as follows:

$$
\begin{aligned}
\mathrm{Re}\,\Phi(\tau) &= \int_0^\infty d\omega J(\omega) \coth\left(\frac{\hbar\omega\beta}{2}\right) \cos\omega\tau \\
&= \eta \frac{\lambda^2 - \tau^2}{(\lambda^2 + \tau^2)^2} - 2\eta \sum_{n=1}^{\infty} \frac{\tau^2 - (\lambda + \hbar\beta n)^2}{(\tau^2 + (\lambda + \hbar\beta n)^2)^2} \qquad (6.35) \\
&\approx \eta \frac{\lambda^2 - \tau^2}{(\lambda^2 + \tau^2)^2} + \eta\frac{1}{\tau^2} - \eta\frac{\pi^2}{\hbar^2\beta^2} \mathrm{cosech}^2\left(\frac{\tau\pi}{\hbar\beta}\right), \\
&\quad \text{in the case of low temperature or sufficiently large heat bath, that is, } \frac{\lambda}{\hbar\beta} \ll 1 \ , \\
&\approx \eta \frac{\lambda^2 - \tau^2}{(\lambda^2 + \tau^2)^2} \ , \\
&\quad \text{in zero temperature limit} \ , \qquad (6.36)
\end{aligned}
$$

and imaginary part:

$$
\mathrm{Im}\,\Phi(\tau) = -\int_0^\infty d\omega J(\omega) \sin\omega\tau = \eta \frac{\partial}{\partial\lambda} \frac{\tau}{\lambda^2 + \tau^2} = \eta \frac{-2\lambda\tau}{(\lambda^2 + \tau^2)^2} \ . \qquad (6.37)
$$

6.3.2 Dissipation Kernels for Factorized Interaction

Consider dissipation kernels in the simple case of interaction. When the interaction Hamiltonian is factorized, only two kernels $\mathcal{K}(t)$ and $\mathcal{H}(t)$ are required. They are explicitly calculated in this section. First we calculate two coefficients for later convenience:

$$
\int_0^\infty ds \exp\{-i\Omega s\} \,\mathrm{Re}\,\Phi(s) \qquad \text{and} \qquad \int_0^\infty ds \exp\{-i\Omega s\} \,\mathrm{Im}\,\Phi(s) \ .
$$

The former is

$$
\begin{aligned}
\int_0^\infty ds \exp\{-i\Omega s\} \,\mathrm{Re}\,\Phi(s) &= \eta \left\{ \frac{\pi}{2}\Omega e^{-\lambda|\Omega|} \coth\frac{\hbar\beta\Omega}{2} \right. \\
&\qquad \left. - i\frac{\Omega}{2}\mathcal{A}_p(\lambda|\Omega|) - i\Omega \sum_{n=1}^{\infty} \mathcal{A}_p((\lambda + n\hbar\beta)|\Omega|) \right\} \\
&= \eta \left\{ \frac{\pi}{2}\Omega e^{-\lambda|\Omega|} \coth\frac{\hbar\beta\Omega}{2} - i\frac{\Omega}{2}\mathcal{A}_p(\lambda|\Omega|) \right. \\
&\qquad \left. - i\frac{\Omega}{2} \int_0^\infty dx e^{-|\Omega|(\lambda + \hbar\beta/2)x} \,\mathrm{sech}\,\frac{\beta x\hbar|\Omega|}{2} \left(\mathbf{P}\frac{1}{1-x} - \frac{1}{1+x} \right) \right\}
\end{aligned}
$$

and the latter is

$$
\int_0^\infty ds \exp\{-i\Omega s\} \,\mathrm{Im}\,\Phi(s) = \eta \left\{ -\frac{1}{\lambda} - \frac{|\Omega|}{2}\mathcal{A}_m(\lambda|\Omega|) + i\frac{\pi}{2}\Omega e^{-\lambda|\Omega|} \right\}
$$

with the explicit form of the thermal correlation functions (6.35) and (6.37). For computational convenience, we decompose them into real parts and imaginary parts as follows:

$$\mathrm{Re}\int_0^\infty ds \exp\{-i\Omega s\}\, \mathrm{Re}\,\Phi(s) = \eta\frac{\pi}{2}\Omega e^{-\lambda|\Omega|}\coth\frac{\hbar\beta\Omega}{2} \quad , \tag{6.38}$$

$$\mathrm{Im}\int_0^\infty ds \exp\{-i\Omega s\}\, \mathrm{Re}\,\Phi(s) = -\eta\frac{\Omega}{2}\mathcal{A}_p(\lambda|\Omega|) - \eta\Omega\sum_{n=1}^{\infty}\mathcal{A}_p((\lambda+n\hbar\beta)|\Omega|) \quad , \tag{6.39}$$

$$\mathrm{Re}\int_0^\infty ds \exp\{-i\Omega s\}\, \mathrm{Im}\,\Phi(s) = -\frac{\eta}{\lambda} - \frac{\eta|\Omega|}{2}\mathcal{A}_m(\lambda|\Omega|) \quad , \tag{6.40}$$

$$\mathrm{Im}\int_0^\infty ds \exp\{-i\Omega s\}\, \mathrm{Im}\,\Phi(s) = +\eta\frac{\pi}{2}\Omega e^{-\lambda|\Omega|} \quad . \tag{6.41}$$

The functions $\mathcal{A}_p(x)$ and $\mathcal{A}_m(x)$ $(x > 0)$ are defined as follows:

$$\mathcal{A}_p(x) = e^x\,\mathrm{Ei}(-x) + e^{-x}\overline{\mathrm{Ei}}(x) \quad ,$$
$$\mathcal{A}_m(x) = e^x\,\mathrm{Ei}(-x) - e^{-x}\overline{\mathrm{Ei}}(x) \quad .$$

$\mathrm{Ei}(-x), \overline{\mathrm{Ei}}(x), (x > 0)$ are the exponential integral functions:

$$\begin{aligned}\mathrm{Ei}(-x) &= \int_{-\infty}^{-x} dt\frac{e^t}{t} && \text{for } x > 0\\ &= \gamma + \ln x + \sum_{n=1}^{\infty}\frac{(-1)^n x^n}{n!n}, && \text{Taylor expansion,}\\ &\sim -\frac{e^{-x}}{x}\sum_{n=0}^{\infty}(-1)^n\frac{n!}{x^n} && \text{asymptotic expansion,}\end{aligned}$$

and

$$\begin{aligned}\overline{\mathrm{Ei}}(x) &= \mathbf{P}\int_{\infty}^{-x} dt\frac{e^{-t}}{t} && \text{for } x > 0\\ &= \gamma + \ln x + \sum_{n=1}^{\infty}\frac{x^n}{n!n} && \text{Taylor expansion,}\\ &\sim \frac{e^x}{x}\sum_{n=0}^{\infty}\frac{n!}{x^n} && \text{asymptotic expansion,}\end{aligned}$$

where γ is Euler constant and $\mathbf{P}$ represents the principal value. In the special case, $\Omega = 0$, we obtain

$$\int_0^\infty ds\Phi(s) = \eta\frac{\pi}{\hbar\beta} - i\frac{\eta}{\lambda}$$

In the actual numerical calculation, the functions

$$\mathcal{A}_p(x) = e^x\,\mathrm{Ei}(-x) + e^{-x}\overline{\mathrm{Ei}}(x)\,,$$
$$\mathcal{A}_m(x) = e^x\,\mathrm{Ei}(-x) - e^{-x}\overline{\mathrm{Ei}}(x)\,,$$

are calculated using routine C.1.

Now we can calculate two dissipation kernels, $\mathcal{K}(t)$ and $\mathcal{H}(t)$:

$$\mathcal{K}(t) = \int_0^\infty ds \exp\left\{-\frac{i}{\hbar}H_{sys}(t)\,s\right\} H_I \exp\left\{\frac{i}{\hbar}H_{sys}(t)\,s\right\}\mathrm{Re}\,\Phi(s) \quad ,$$
$$\mathcal{H}(t) = \int_0^\infty ds \exp\left\{-\frac{i}{\hbar}H_{sys}(t)\,s\right\} H_I \exp\left\{\frac{i}{\hbar}H_{sys}(t)\,s\right\}\mathrm{Im}\,\Phi(s) \quad .$$

Using the eigenstates $\{|n\rangle\}$ and the eigenvalues $\{E_n(t)\}$ of $H_{sys}(t)$, we obtain

$$\begin{aligned}\langle n|\mathcal{K}(t)|m\rangle &= \langle n|H_I|m\rangle\int_0^\infty ds\exp(-i\omega_{nm}s)\,\mathrm{Re}\,\Phi(s)\\ &= \langle n|H_I|m\rangle\eta\left\{\frac{\pi}{2}\omega_{nm}e^{-\lambda|\omega_{nm}|}\coth\frac{\hbar\beta\omega_{nm}}{2}\right.\\ &\qquad\left. -i\frac{\omega_{nm}}{2}\mathcal{A}_p(\lambda|\omega_{nm}|) - i\omega_{nm}\sum_{n=1}^{\infty}\mathcal{A}_p((\lambda+n\hbar\beta)|\omega_{nm}|)\right\}\end{aligned}$$

and

$$\begin{aligned}\langle n|\mathcal{H}(t)|m\rangle &= \langle n|H_I|m\rangle\int_0^\infty ds\exp(-i\omega_{nm}s)\,\mathrm{Im}\,\Phi(s)\\ &= \langle n|H_I|m\rangle\eta\left\{-\frac{1}{\lambda} - \frac{|\omega_{nm}|}{2}\mathcal{A}_m(\lambda|\omega_{nm}|) + i\frac{\pi}{2}\omega_{nm}e^{-\lambda|\omega_{nm}|}\right\} \quad ,\end{aligned}$$

where $\omega_{nm} = (E_n(t) - E_m(t))/\hbar$. In the next chapter we use these two kernels for numerical calculation.

Chapter 7

Resonance Current in Quantum Ratchet Systems

In this chapter we describe one possible realization of quantum ratchets. In Sec. 7.1 we construct a model based on a tight-binding model. In the next section, before presenting numerical results, we demonstrate that the linear response theory is not suitable for calculating the current in the present situation. Sec. 7.3 gives Numerical results obtained by means of the treatment developed in the previous chapters. In Secs. 7.4 and 7.5 we discuss detailed features of the quantum ratchet system. Simpler minimal model, in which only the essentials of quantum ratchet are taken into account, is also given in Sec. 7.5. The last section 7.6 is devoted to the summary.

7.1 Model

The model studied in this chapter is based on the tight-binding model. The Hamiltonian is as follows:

$$\begin{aligned} H(t) &= H_{sys}(t) + \epsilon H_{int} + H_B, \\ H_{sys}(t) &= \sum_n (|n\rangle\langle n+1| + |n\rangle\langle n-1|) + \sum_n V_{n \bmod N}|n\rangle\langle n| - \sum_n F_n(t)|n\rangle\langle n|, \\ H_{int} &= \epsilon H_I \otimes \xi, \\ H_B &= \sum_\alpha \hbar\omega_\alpha \left(a_\alpha^\dagger a_\alpha + \frac{1}{2}\right), \end{aligned}$$

where $H(t)$ is a Hamiltonian of the total system with a dimensionless coupling constant ϵ, $H_{sys}(t)$ is a tight-binding Hamiltonian including a spatially asymmetric periodic potential $V_{n \bmod N}$, whose period is N. An external oscillating field is represented by $F_n(t)$. We measure energy in unit of the hopping coefficient from now on. The localized state at site n is denoted by the ket state $|n\rangle$. H_{int} is the interaction Hamiltonian which is a direct product of two parts, H_I and ξ:

$$H_I = \sum_n \left(|n\rangle\langle n+1| + |n\rangle\langle n-1|\right), \tag{7.1}$$

$$\xi = \sum_\alpha \left(a_\alpha + a_\alpha^\dagger\right) . \tag{7.2}$$

This interaction expresses that the particle hopping is influenced by the thermal fluctuations. Applying the treatment developed in Sec. 6.1, we get an equation of motion for a density matrix of the ratchet system $\rho(t)$ as

$$\frac{\partial \rho(t)}{\partial t} = -\frac{i}{\hbar}[H_{sys}(t), \rho(t)] - \frac{\epsilon^2}{\hbar^2}\Big([H_I, [\mathcal{K}(t), \rho(t)]] + i[H_I, [\mathcal{H}(t), \rho(t)]_+]\Big) . \tag{7.3}$$

Since we are interested in whether or not the net currents appear, we first define a current operator. A local current is defined through the conservation of probability; Taking the diagonal elements of Eq. (7.3), we obtain

$$\begin{aligned}\langle n|\frac{\partial \rho(t)}{\partial t}|n\rangle &= -\frac{i}{\hbar}\langle n|[H_{sys}(t), \rho(t)]|n\rangle - \frac{\epsilon^2}{\hbar^2}\langle n|[H_I, W(t)]|n\rangle \\ &= \frac{2}{\hbar}\,\mathrm{Im}\langle n+1|\rho(t)|n\rangle - \frac{2}{\hbar}\,\mathrm{Im}\langle n|\rho(t)|n-1\rangle \\ &\quad - \frac{2\epsilon^2}{\hbar^2}\,\mathrm{Re}\langle n+1|W(t)|n\rangle + \frac{2\epsilon^2}{\hbar^2}\,\mathrm{Re}\langle n|W(t)|n-1\rangle ,\end{aligned}$$

where

$$W(t) = [\mathcal{K}(t), \rho(t)] + i[\mathcal{H}(t), \rho(t)]_+ . \tag{7.4}$$

Since the local current J_n satisfies the conservation of probability, $\langle n|\partial\rho(t)/\partial t|n\rangle + J_{n+1} - J_n = 0$, we get

$$J_n = -\frac{2}{\hbar}\,\mathrm{Im}\langle n|\rho(t)|n-1\rangle + \frac{2\epsilon^2}{\hbar^2}\,\mathrm{Re}\langle n|W(t)|n-1\rangle , \tag{7.5}$$

This definition is equivalent to the expectation value of a local current operator $\hat{J}_n(t)$ defined as

$$\hat{J}_n(t) \equiv \hat{J}_n^0 + \frac{\epsilon^2}{\hbar}\Big(-i[\hat{J}_n^0, \mathcal{K}(t)] + [\hat{J}_n^0, \mathcal{H}(t)]_+\Big), \tag{7.6}$$

where $\hat{J}_n^0$ is an ordinary current operator of the tight-binding model defined by $\hat{J}_n^0 \equiv (i/\hbar)(|n-1\rangle\langle n| - |n\rangle\langle n-1|)$. The second term expresses a correction by the interaction with the heat bath. For the weak coupling case, contribution of this correction term is small.

In the present study, we adopt the on-off type external forcing, i.e.,

$$F_n(t) = V_{n \bmod N}\Theta(t \bmod(\tau_1 + \tau_2) - \tau_1) ,$$

where $\Theta(t)$ is the Heaviside step function. Then the potential exists in the first duration τ_1 and in the next duration τ_2 the potential vanishes. We call the first duration as "on-potential" period and next one as "off-potential" period for convenience. This type of forcing is sometimes called as "flushing" potential. Thus, hereafter, we call the model as a flushing quantum ratchet.

Next we determine a specific form for the asymmetric periodic potential. Simple choice like a piecewise linear potential is not appropriate in the present case. For this purpose, we consider dynamics of energy of the system. The expectation value of energy is defined as follows:

$$\langle E(t)\rangle = \mathrm{Tr}\{(H_{sys}(t) + \epsilon H_I)\rho(t)\}. \tag{7.7}$$

Let us take its time derivative. For both durations, on-potential and off-potential, we obtain

$$\begin{aligned}\frac{d\langle E(t)\rangle}{dt} &= \mathrm{Tr}\{(H_{sys}(t) + \epsilon H_I)\frac{\partial \rho(t)}{\partial t}\} \\ &= -\frac{i\epsilon}{\hbar}\,\mathrm{Tr}\left(H_I[H_{sys}(t), \rho(t)]\right) \\ &\quad - \frac{\epsilon^2}{\hbar}\,\mathrm{Tr}\left(H_{sys}(t)\,[H_I, [\mathcal{K}(t), \rho(t)]] + iH_{sys}(t)\,[H_I, [\mathcal{H}(t), \rho(t)]_+]\right) .\end{aligned}$$

If the system Hamiltonian and the interaction Hamiltonian commute with each other, both $\mathcal{K}(t)$ and $\mathcal{H}(t)$ are proportional to the interaction Hamiltonian H_I. Then $H_{sys}(t)$, $\mathcal{K}(t)$, $\mathcal{H}(t)$, and H_I all commute with one another. In this case, energy does not dissipate to nor transfer from the heat bath apart from the instant of the switching. Thus H_I must not commute with $H_{sys}(t)$.

The commutation relation between the tight-binding type Hamiltonian $H_{tb} = \sum_n(|n\rangle\langle n-1| + |n\rangle\langle n+1|)$ and the diagonal Hamiltonian $V = \sum_n V_n|n\rangle\langle n|$ is calculated as follows:

$$[H_{tb}, V] = \sum_n \{(V_{n-1} - V_n)\,|n\rangle\langle n-1| + (V_{n+1} - V_n)\,|n\rangle\langle n+1|\} . \tag{7.8}$$

If we set $V_n = c$ (constant), H_{tb} and V are commutable. On the other hand, if we choose V_n proportional to the coordinate n, $[H_{tb}, V] \propto H_{tb}$. In these cases it is shown that $\mathcal{K}(t)$ and $\mathcal{H}(t)$ also are proportional to the tight-binding Hamiltonian. Therefore, when the potential is a constant or a linear function of the coordinate, the energy dose not dissipate. Thus for energy to dissipate, a nonlinear part in terms of the coordinate is required for the potential.

For the sake of simplicity, we choose the interaction Hamiltonian proportional to the tight-binding Hamiltonian and the asymmetric periodic potential as shifted harmonic potential, which is defined later. Therefore energy dissipates only during the on-potential period and not during the off-potential period. Only the relaxation of entropy takes place in the off-potential period. Since we consider only the weak coupling case, such details of dissipation will not affect the qualitative results.

7.2 Linear Response Theory

Before presenting numerical results, we analyze the ratchet system in the framework of the linear response theory [41]. Let us take the tight-binding Hamiltonian as the unperturbed Hamiltonian H_0:

$$H_0 = \sum_n \{|n\rangle\langle n+1| + |n\rangle\langle n-1|\} \quad ,$$

and regard asymmetric periodic potential as the perturbation. For that purpose, the potential V_n is multiplied by the small parameter γ. The linear response theory gives the expectation value of the lowest correction to the current operator, which is denoted as $\Delta\langle\hat{J}_0\rangle$, as

$$\Delta\langle\hat{J}_0\rangle \equiv \langle\hat{J}_0\rangle_t - \langle\hat{J}_0\rangle_\beta = \int_{-\infty}^{t} ds f(s)\Phi_{JA}(t-s) \quad ,$$

where $\langle\ldots\rangle_t$ and $\langle\ldots\rangle_\beta$ represent expectation value at time t and the thermal average with the inverse temperature β, respectively. $\hat{J}_0$ is the ordinary current operator defined as follows:

$$\hat{J}_0 = \frac{i}{\hbar}\sum_n (|n-1\rangle\langle n| - |n\rangle\langle n-1|) \quad .$$

In the above integral, $f(s)$ is the time-dependent part of the external force, which is taken $f(t)$ as $\Theta(\tau_1 - t \bmod(\tau_1+\tau_2))$ in the present case. $\Phi_{JA}(t)$ is the response function defined as follows:

$$\Phi_{JA}(t) \equiv -\frac{1}{i\hbar}\langle[A, \hat{J}_0(t)]\rangle_\beta \quad , \text{ where } \qquad A = -\sum_n \gamma V_n|n\rangle\langle n| \ .$$

$\hat{J}_0(t)$ is the current operator in Heisenberg picture, that is, $\exp(itH_0/\hbar)\hat{J}_0\exp(-itH_0/\hbar)$.

The response function can also be expressed as

$$-\frac{1}{i\hbar}\langle[A, \hat{J}_0(t)]\rangle_\beta = \frac{1}{i\hbar}\frac{\mathrm{Tr}\left\{A[\hat{J}_0(t), e^{-\beta H_0}]\right\}}{\mathrm{Tr}\, e^{-\beta H_0}} \quad .$$

In the present case the total current operator $\hat{J}_0$ commutes with the Hamiltonian H_0, that is, the total current is a conserved quantity of the unperturbed system. Thus the response function vanishes exactly and, as a result, net current cannot be expected. Therefore, the net current does not appear in the linear order of small asymmetric periodic potential. If the current appears in the numerical calculation, it is caused by the *nonlinear* and *nonequilibrium* effects.

7.3 Numerical Calculation and Results

In the actual calculation, we take values of the parameters as follows:

$N = 5$	number of sites in an unit cell,
$L = 10$	number of sites in a whole system,
$\hbar = 1$	Planck constant,
$\lambda = 0.01$	inverse cut-off frequency of a heat bath,
$\eta = 1$	"viscosity" coefficient.

The asymmetric periodic potential is taken to be a shifted harmonic shape (see Fig. 7.1):

$$V_{0\bmod 5} = 0, V_{1\bmod 5} = \frac{1}{9}, V_{2\bmod 5} = \frac{4}{9}, V_{3\bmod 5} = 1, \text{and} V_{4\bmod 5} = \frac{1}{9} \ . \qquad (7.9)$$

The time dependence of external forcing is simply chosen as "symmetric", that is, $\tau_1 = \tau_2 = T/2$ with a period T. Two dissipation kernels are calculated according to Sec. 6.3.2.

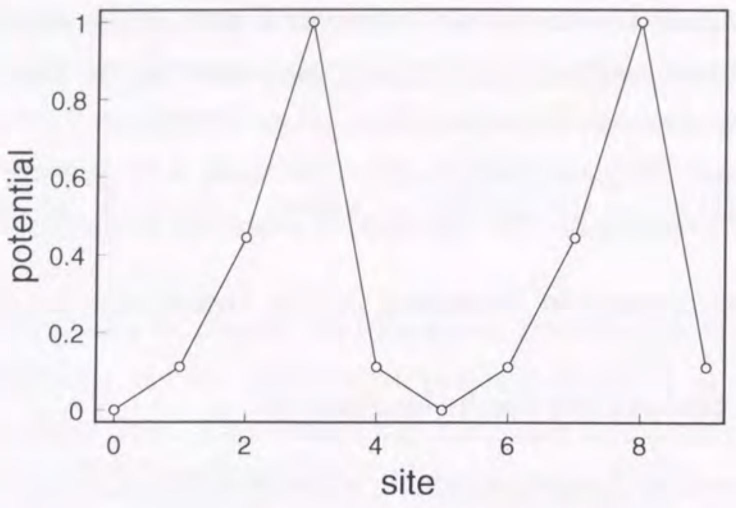

Figure 7.1: Asymmetric periodic potential

Inserting the eigenstates $\{|E_n\rangle\}$ of $H_{sys}(t)$, we obtain

$$\begin{aligned}\mathcal{K}(t)(\text{or}\mathcal{H}(t)) &= \int_0^\infty ds e^{-iH_{sys}(t)s/\hbar} H_I e^{iH_{sys}(t)s/\hbar}\,\text{Re}(\text{or Im})\Phi(s) \\ &= \int_0^\infty ds \sum_{E_n,E_m} |E_n\rangle\langle E_n| e^{-iH_{sys}(t)s/\hbar} |E_n\rangle\langle E_n|H_I|E_m\rangle\langle E_m| e^{iH_{sys}(t)s/\hbar} |E_m\rangle\langle E_m| \\ &\qquad \text{Re}(\text{or Im})\Phi(s) \\ &= \sum_{E_n,E_m} |E_n\rangle\langle E_n|H_I|E_m\rangle\langle E_m| \int_0^\infty ds \exp\left\{-\frac{i(E_n - E_m)s}{\hbar}\right\} \text{Re}(\text{or Im})\Phi(s) \ .\end{aligned}$$

The integral in the final line can be calculated numerically using the routine presented in Appendix 6.3.2. Note that the eigenstates inserted here depend on time. Thus, in the actual calculation, we must convert the basis $\{|E_n\rangle\}$ to the time-independent basis such as the site representation $|n\rangle$.

We suppose that the system is initially in thermal equilibrium state of the ratchet Hamiltonian under the existence of the asymmetric periodic potential at inverse temperature β, that is,

$$\rho(0) = \frac{e^{-\beta H_{sys}}}{\text{Tr}\, e^{-\beta H_{sys}}}.$$

Using this initial distribution and above-mentioned parameters, we integrate the density matrix by means of 4th order Runge-Kutta method [53]. A typical result of the time series of the expectation value of total current is shown in Fig. 7.2. For this calculation, we take the period as $T = 1000$, the inverse temperature of the heat bath as $\beta = 0.8$, and the coupling constant as $\epsilon = 1.5 \times 10^{-2}$. We see that the current oscillates rapidly in the on-potential period. This oscillation is induced by the asymmetric periodic potential, because the total current operator does not commute with the asymmetric periodic potential. In the off-potential period, on the other hand, the current is kept constant. In this case the total current is conserved. In addition, it is found that the time series supports the existence of the steady periodic state with period T. After some relaxation time is passed, the current seems to repeat the same dynamical behavior with period T. For other T and β, we also find the steady periodic states. Therefore the physical quantities can also be calculated by the method described in Sec. 6.2 without explicit integration of the differential equation. We found that if we take different state from the thermal equilibrium as the initial state, slightly different periodic states is produced. That implies the lack of ergodicity. In high temperature, $\beta \lesssim 1$, the difference is invisibly small. Even in low temperature, where the difference is recognizable, we found that it is still quite small. Thus we use the thermal equilibrium state as the initial state of the computation. Qualitative features are unchanged by choosing other initial conditions.

The periodic behavior of the density matrix is caused by the dissipation of energy, that is, the existence of the heat bath, and the periodic driving. That is confirmed by a calculation for the "pure" system, i.e., $\epsilon = 0$, which is presented in Fig. 7.3. In this calculation, the ratchet system does not interact with the heat bath, and thus obeys pure quantum dynamics. We choose the same initial condition as Fig. 7.2 apart from ϵ. Characteristic behavior is similar to Fig. 7.2. Current oscillates in the on-potential period and is kept constant in the off-potential period. Different feature is seen in the value of the conserved currents in the off-potential period. In the present case the current does not reach the steady periodic state, because of the absence of the dissipation. As a result, the value of the conserved current varies randomly in each off-potential period. Therefore the interaction with the heat bath is necessary for maintaining the periodically steady state and generating net currents.

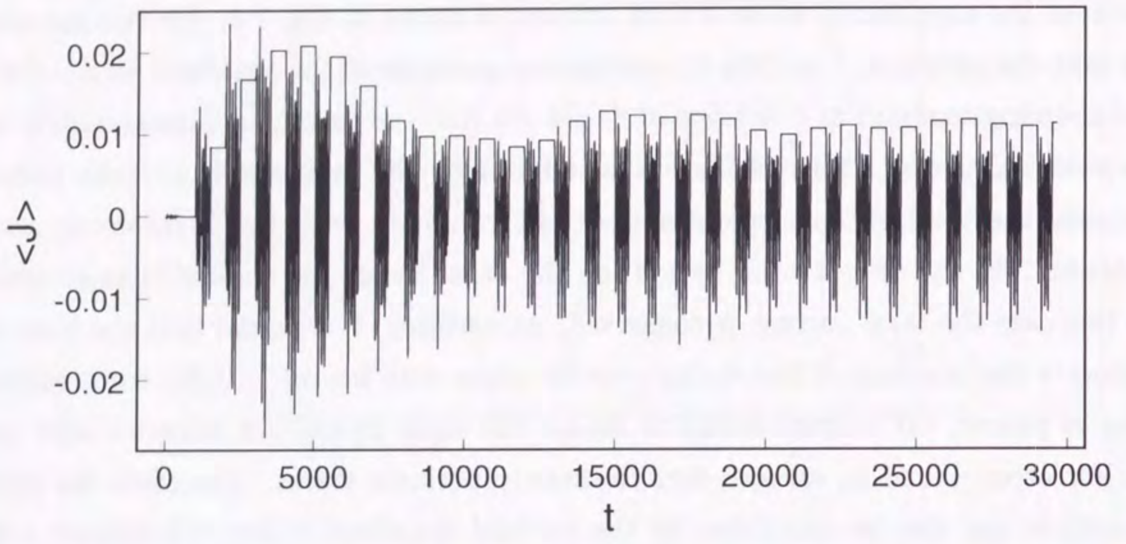

Figure 7.2: Time series of current. The period of external forcing, the inverse temperature of the heat bath, and the coupling constant are $T = 1000$, $\beta = 0.8$, and $\epsilon = 1.5\times10^{-2}$, respectively. At time $t = 0$, the system is in thermal equilibrium state of the ratchet Hamiltonian with the asymmetric periodic potential at the inverse temperature $\beta = 0.8$.

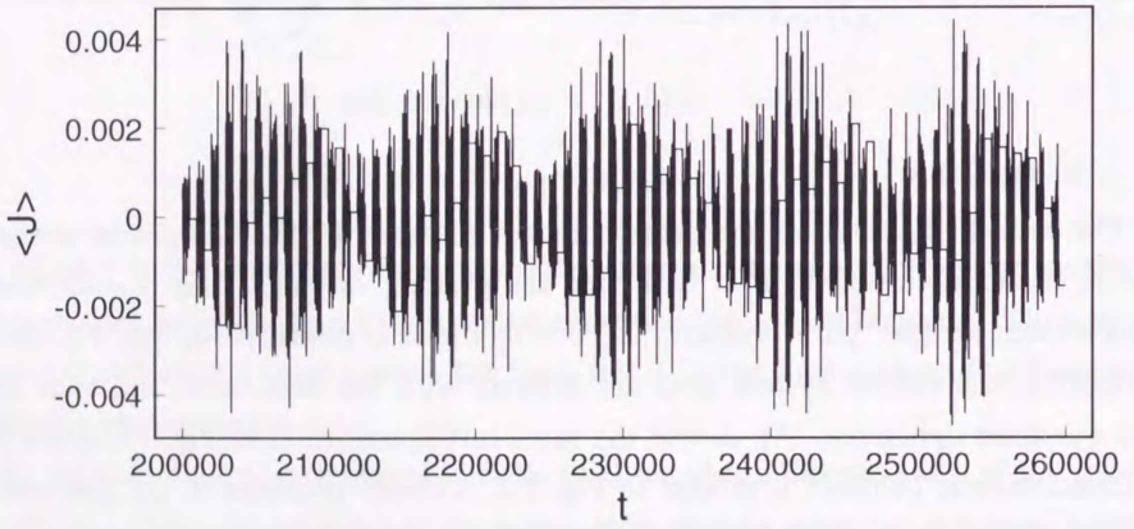

Figure 7.3: Time series of the current. The period of external forcing and the coupling constant are $T = 1000$ and $\epsilon = 0$, respectively. At time $t = 0$, the state of the system is same as thermal equilibrium state with the inverse temperature $\beta = 0.8$. The dynamics of current obeys pure quantum mechanics.

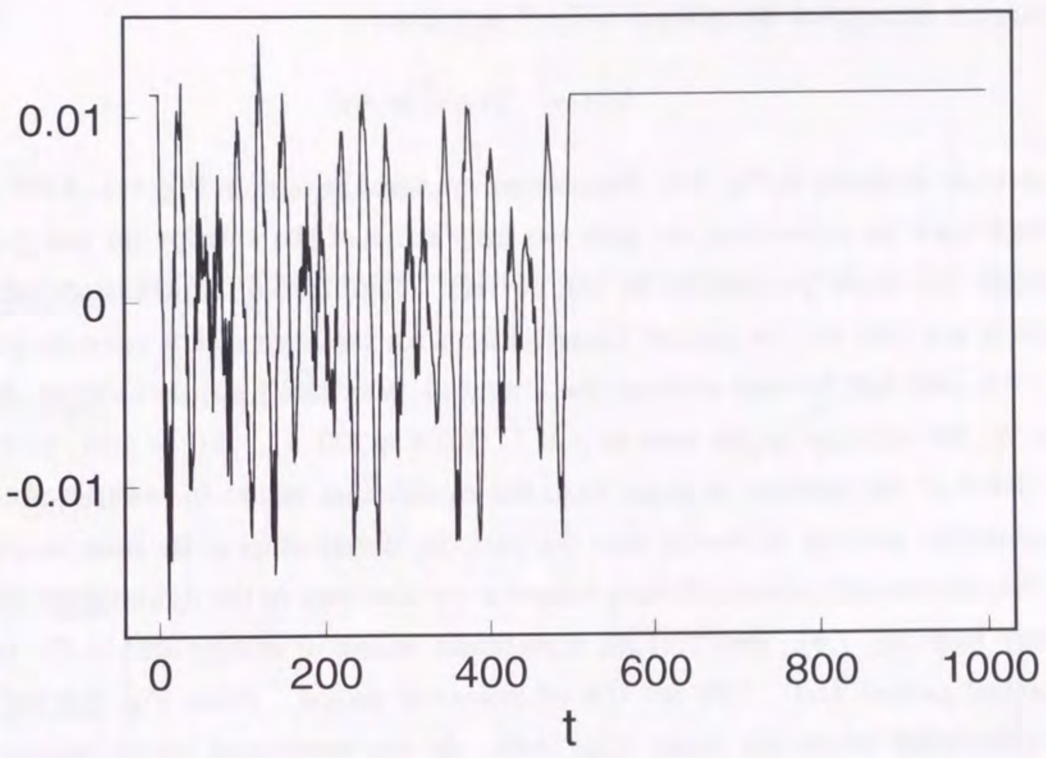

Figure 7.4: Dynamics of the current for one period corresponding to the periodically steady states. We plot the current for one period after discarding 500000 time for relaxation. Parameters are same as ones in Fig. 7.2. At time $t = 0$, the system is in thermal equilibrium state of the ratchet Hamiltonian with the asymmetric periodic potential at the inverse temperature $\beta = 0.8$.

7.3.1 Dynamics in Steady Periodic State

Dynamics of the current for one period is shown in Fig. 7.4. Parameters are same as ones in Fig. 7.2. After discarding 500000 time for relaxation, we plot the time series of the current for one period. The figure shows the steady periodic dynamics of the density matrix. In the first 500 time, i.e., the on-potential period, the current oscillates with several frequencies. These frequencies are related with the eigenvalue differences of the ratchet Hamiltonian with the asymmetric periodic potential. Moreover the oscillations seems to resonate with half the period of the external forcing. More detailed studies are left for Sec. 7.4.

Other physical quantities also have same periodicity. For example, we calculate von

Neumann entropy of the system defined as follows:

$$I(t) = -\operatorname{Tr} \rho(t) \ln \rho(t) \ .$$

The result is shown in Fig. 7.5. Parameters are same as ones in Fig. 7.2. After discarding 500000 time for relaxation, we plot the time series of the entropy for one period. The entropy has same periodicity as the current. Equilibrium expectation values of the entropy are 1.84 for the ratchet Hamiltonian with the asymmetric periodic potential at $\beta = 0.8$, and 1.87 for one without the potential. Maximal possible value of the entropy, that is, the entropy in the case of $\rho = (1/10)\,\mathrm{diag}(1, 1, 1, \ldots 1)$, is 2.30. In this figure, the value of the entropy is larger than the equilibrium values in both on-potential and off-potential periods. It means that the periodic steady state is far from equilibrium.

Periodicity and nonequilibrium behavior are also seen in the dynamics of the internal energy (see Fig. 7.6). Equilibrium expectation values of energy are -0.977 for the on-potential period and -1.24 for the off-potential period. From Fig. 7.6 we find that the calculated values are larger than both. As was mentioned above, energy does not dissipate in the off-potential period, so that the expectation value is conserved. In this case, all the energy which is injected by the external forcing should be wasted in the on-potential period.

7.3.2 Parameter Dependence

Numerical integration has shown the existence of the steady periodic state for the density matrix. Therefore we can apply the method developed in Sec 6.2 for studying the properties of the steady periodic state in detail. In Figs. 7.7 and 7.8 we plot typical temperature dependence of the currents. By a technical reason, we do not plot the time-averaged current $\langle J \rangle$ but the conserved current J in the off-potential period. Thus, for the purpose of getting time-averaged current, we should multiply some period-dependent factor. Qualitative results is, however, independent of this choice.

We discuss characteristic behavior of the current based on these figures: First, the current vanishes in the high temperature limit and remain finite in the zero temperature limit. At low temperature the current is proportional to the temperature (see Fig. 7.8) $\sim -0.0016 + 0.061(1/\beta)$. In the intermediate regime, the value of the current takes maximal at some temperature, which is close to the characteristic energy scale of the

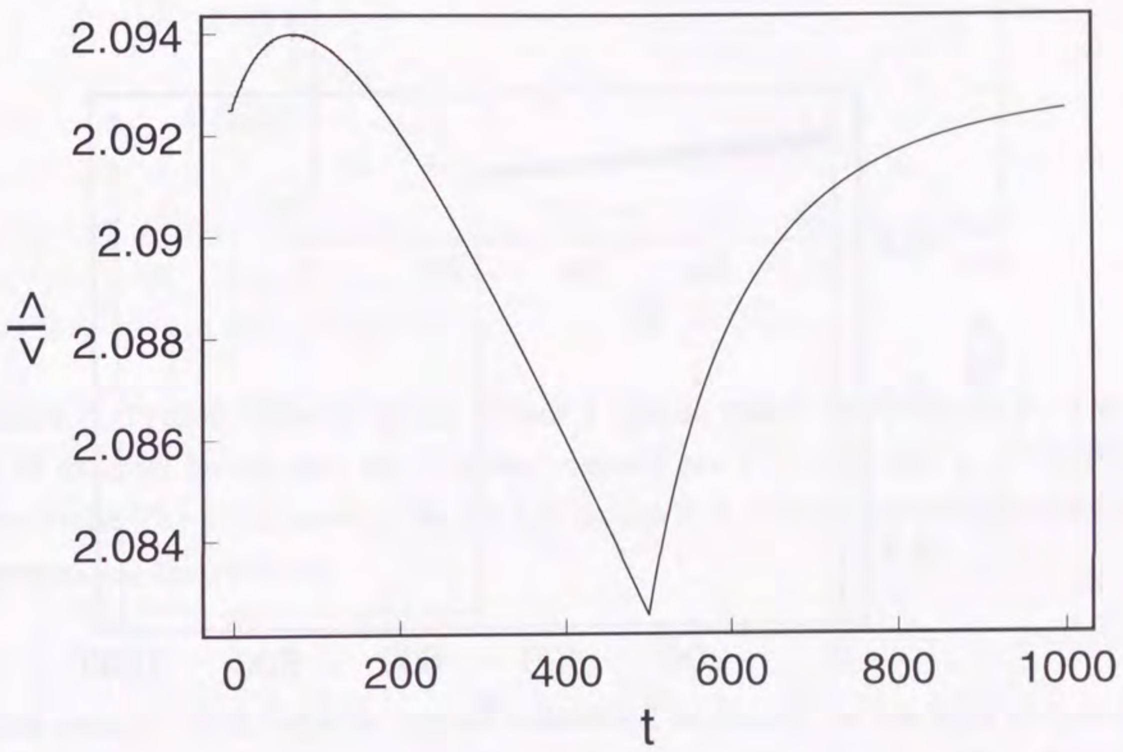

Figure 7.5: Dynamics of the entropy for one period. It also has same period as the one of external forcing. Parameters are same as ones in Fig. 7.2. At time $t = 0$, the system is in thermal equilibrium state with the inverse temperature $\beta = 0.8$. After discarding 500000 time for relaxation, we plot one-period time series. Equilibrium expectation values of entropy are 1.84 in the on-potential case, 1.87 in the off-potential case at $\beta = 0.8$. Maximal allowed value of entropy is 2.30.

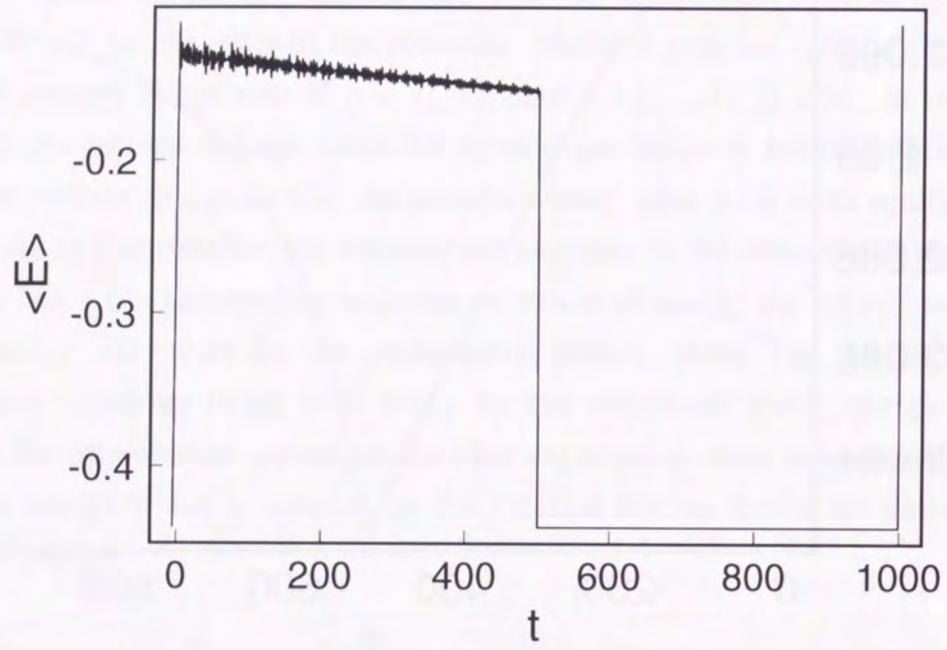

Figure 7.6: Dynamical behavior of the expectation value of internal energy in the ratchet system for one period. Parameters are same as ones in Fig. 7.2. At time $t = 0$, the system is in thermal equilibrium state with the inverse temperature $\beta = 0.8$. Equilibrium expectation values of energy are -0.977 in the on-potential case, -1.24 in the off-potential case.

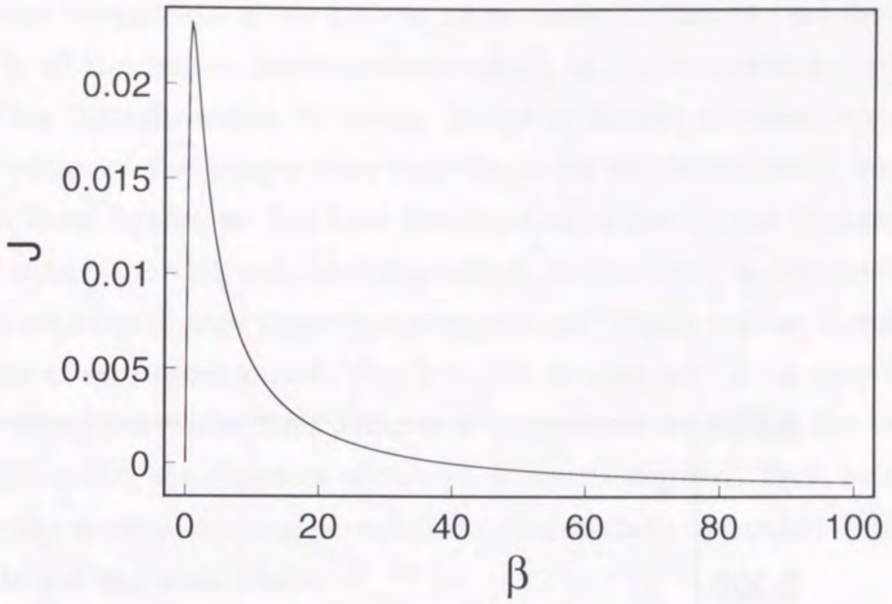

Figure 7.7: Typical behavior of the current J against inverse temperature β. The period of external forcing and the coupling constant are $T = 1000$ and $\epsilon = 1.5 \times 10^{-2}$, respectively. The initial state of the ratchet system is in thermal equilibrium state with corresponding temperature.

ratchet system. Such behavior can be understood as follows: In the high temperature limit $\beta \to 0$, it is natural to expect that current vanishes, because the influence of potential becomes negligible as increasing the temperature. This situation is similar to the case of the classical fluctuating potential ratchet. In the low temperature limit $\beta \to \infty$, the thermal fluctuation, which causes the thermal diffusion, can be ignored and the particle diffusion is governed by the quantum diffusion. In addition entropy is generated even at zero temperature. This is the reason why the net current remains finite at zero temperature. In the intermediate temperature range, the current becomes maximal near the temperature close to the scale of the characteristic energy of the ratchet system. Such behavior reminds us of the similarity to the stochastic resonance (SR) [21]. In SR, the thermal noise acting on a nonlinear oscillator amplifies the response to a weak coherent signal. It happens most efficiently for some finite optimal intensity of the noise. Thus the present behavior may be concerned with the quantum stochastic resonance [28, 29].

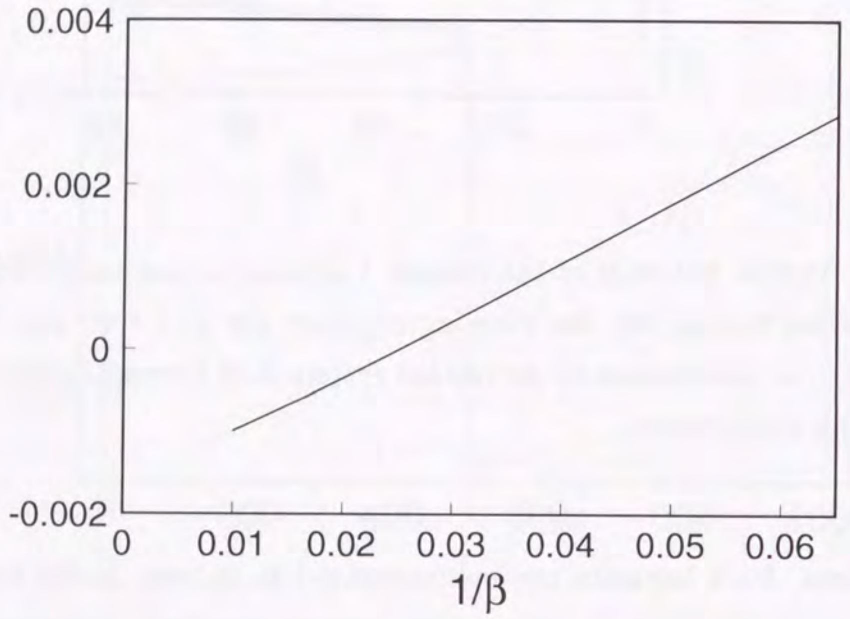

Figure 7.8: Low temperature behavior of the current. Extrapolation of the current to lower temperature is shown. Parameters are same as Fig. 7.7. The current J behaves like $J \sim -0.0016 + 0.061(1/\beta)$ near $1/\beta \sim 0$.

Temperature dependence of the current under several different periods T is plotted in Fig. 7.9. In all the figures, finite currents remain at low temperature, while at high temperature the currents vanish as before. Single or double extremes are seen in the intermediate range of the temperature near the scale of characteristic energy of the system. From these figures, we find that the direction of the current changes both with the period of external forcing and the temperature. For instance, in the case of $T = 110$, the current is negative in high temperature regime and crosses zero as increasing β and finally positive at zero temperature. For $T = 310$, in contrast to the case of $T = 110$, the direction of current varies from positive to negative as decreasing the temperature. In the case of $T = 210$, the direction of current is always negative. Such behavior is not recognized in the classical flushing potential thermal ratchets. Therefore it is not due to thermal effects but quantum effects.

Next three figures show other dependence of currents: First we plot a typical behavior of currents against the coupling constant in Fig. 7.10. Inverse temperature and period of external forcing are taken to be $\beta = 0.8$ and $T = 1000$, respectively. $\epsilon = 0$ corresponds to the pure quantum dynamics, where the current does not appear. Figure 7.11 presents the dependence of the current on the asymmetry of the potential shape. the horizontal axis represents the degree of asymmetry, which we take as the height of on-site potential, $V_{2\,\mathrm{mod}\,5}$. If $V_{2\,\mathrm{mod}\,5} = 1$, spatial reflection symmetry is not broken and no finite net current is expected. Actually we observe that the current is zero at $V_{2\,\mathrm{mod}\,5} = 1$. In the intermediate range, the current violently oscillates with varying potential height. Last Figure 7.12 shows dependence on the amplitude of forcing. So far we take the time dependent part of the forcing as $\Theta(T/2 - t \bmod T)$. Here and only here we multiply it by a factor P. Varying P in the range $[0, 1]$, we calculate the current and the results are presented in Fig. 7.12. Remember that the linear response theory did not result in a finite net current. The plot for small P confirms the conclusion of the linear response theory. For large P, on the other hand, the current oscillation is observed again.

The above results imply that generation of the currents strongly depends on the eigenset, i.e., eigenvalues and corresponding eigenstates, of the ratchet Hamiltonian. Changing a parameter which is accompanied by modification of the eigenset induces violent change of the behavior. For example, changing $V_{2\,\mathrm{mod}\,N}$ (Fig. 7.11) or P (Fig. 7.12) induces discontinuous change of the current. Changing a parameter not accompanied by

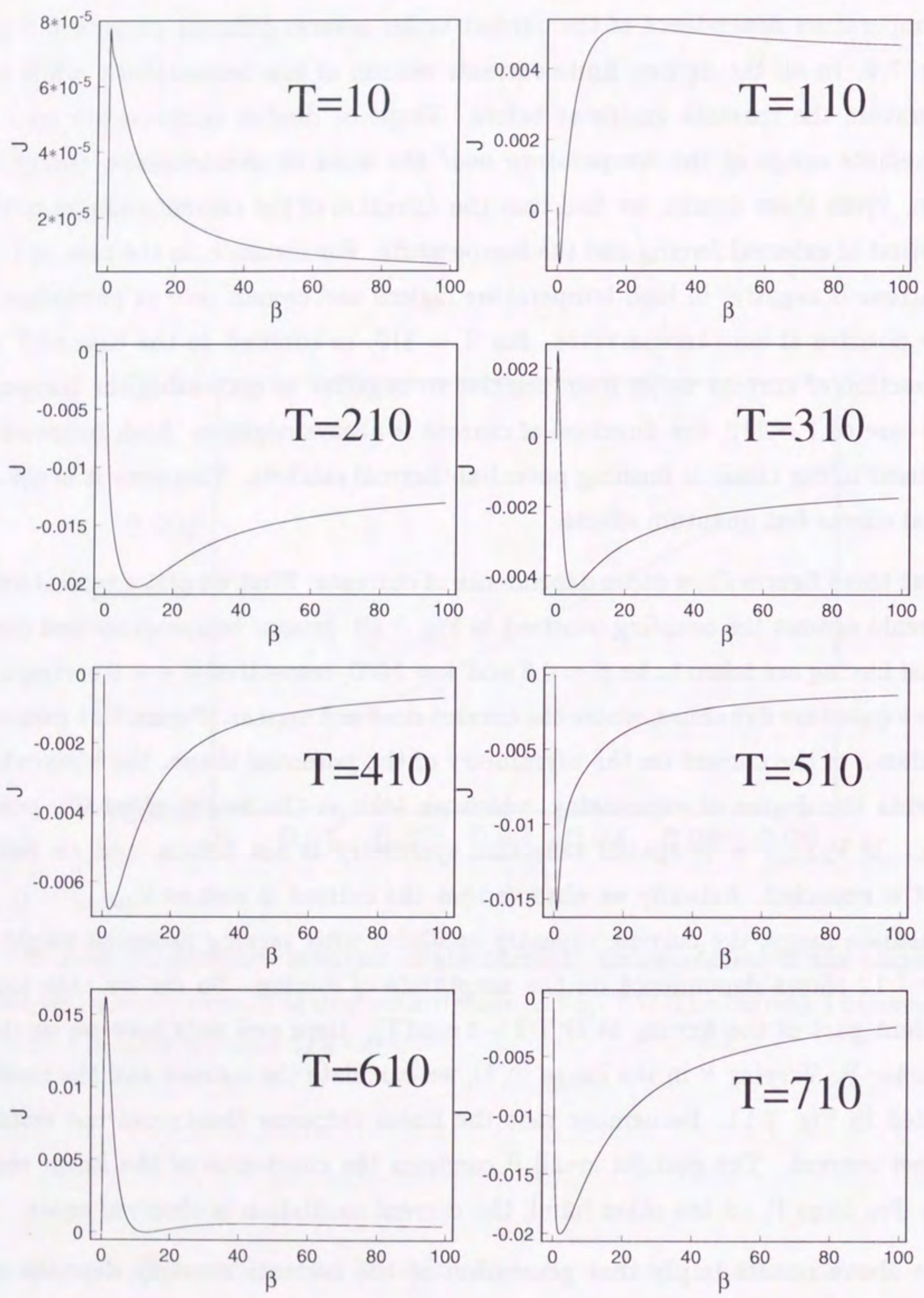

Figure 7.9: Many sample of current-temperature plot. Each figure is different in the period of external forcing, which is shown inside the plot. Coupling constant is $\epsilon = 1.5 \times 10^{-2}$. Initial state of the ratchet system is in thermal equilibrium state with corresponding temperature.

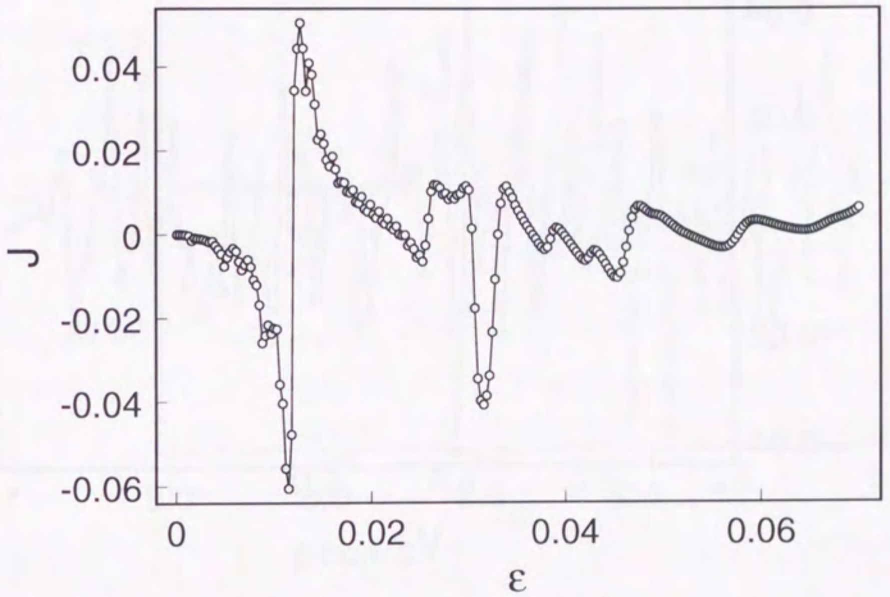

Figure 7.10: Current against coupling constant: We plot behavior of dependence of currents on the coupling constant. Inverse temperature and period of external forcing are taken to be $\beta = 0.8, T = 1000$, respectively. $\epsilon = 0$ is corresponding to pure quantum dynamics.

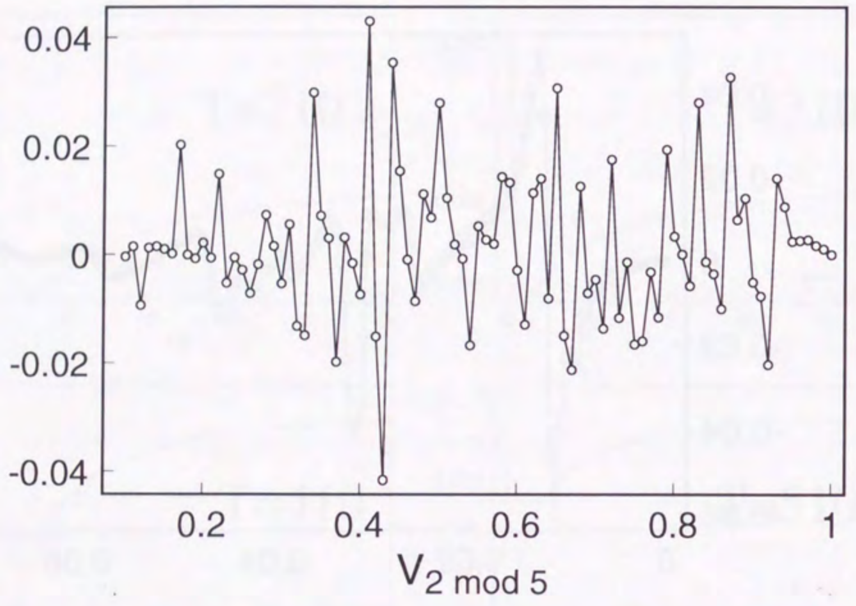

Figure 7.11: Dependence on asymmetry of the potential shape: Horizontal axis represents the asymmetry; Height of $V_{2\,\mathrm{mod}\,5}$ is varying in the range $[0.1, 1]$. When $V_{2\,\mathrm{mod}\,5} = 1$, then the potential is symmetric, no one breaks spatial inversion symmetry. Inverse temperature, coupling constant, and period of the external forcing are taken to be $\beta = 0.8, \epsilon = 1.5 \times 10^{-2}$, and $T = 1000$, respectively.

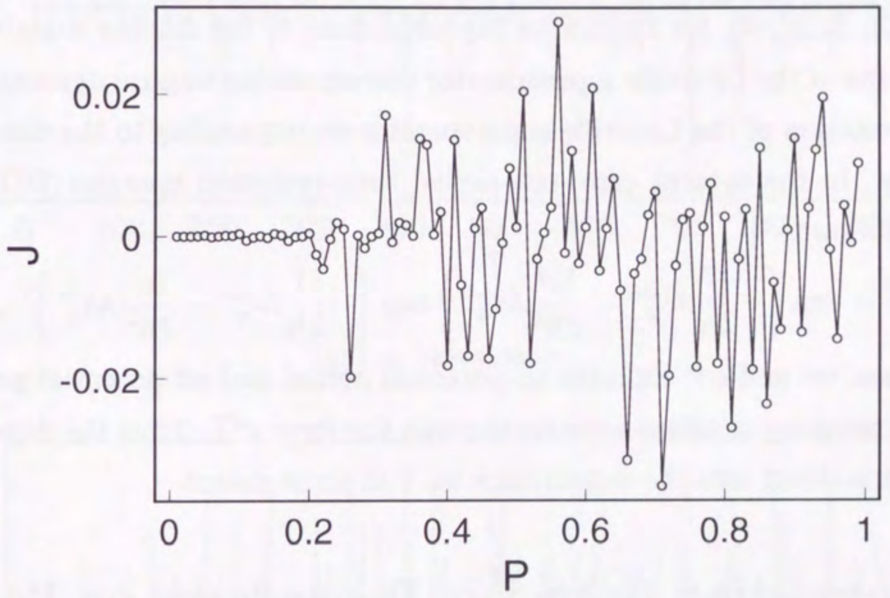

Figure 7.12: Dependence on amplitude of the forcing. P represents amplitude of the forcing. If $P = 1$, the forcing is same as one used in the calculations so far. $P = 0$ means that the forcing no longer exist. Thus, near $P \sim 0$, the linear response theory is valid. As was mentioned in the previous section, no finite net currents appear near $P \sim 0$. Inverse temperature, coupling constant, and period of the external forcing are taken to be $\beta = 0.8$, $\epsilon = 1.5 \times 10^{-2}$, and $T = 1000$, respectively.

the modification of the eigenset, on the other hand, makes smooth change of the current as is seen in Fig. 7.7.

Let us see that the dependence on the coupling constant and the dependence on the period of the external forcing is related to each other. Since equation (7.3) is a linear equation for the matrix elements of the density matrix, it is formally rewritten as follows:

$$\frac{\partial \vec{\rho}(t)}{\partial t} = -\frac{i}{\hbar}\mathcal{M}_{p}(t)\vec{\rho}(t) - \frac{\epsilon^2}{\hbar^2}\mathcal{M}_{d}(t)\vec{\rho}(t) \ ,$$

where $\vec{\rho}$, $\mathcal{M}_p$ and $\mathcal{M}_d$ are the vector representation of the density matrix, the matrix representation of the Liouville superoperator corresponding to pure dynamics, and a matrix representation of the Liouville superoperator corresponding to the dissipative term, respectively. In the present case, one-period time-evolution operator $\mathcal{D}(T)$ is formally written as follows:

$$\mathcal{D}(T) = \exp\left\{-\frac{iT}{2\hbar}\mathcal{M}_{p}^{off} - \frac{T\epsilon^2}{2\hbar^2}\mathcal{M}_{d}^{off}\right\} \exp\left\{-\frac{iT}{2\hbar}\mathcal{M}_{p}^{on} - \frac{T\epsilon^2}{2\hbar^2}\mathcal{M}_{d}^{on}\right\} \ ,$$

where suffixes on and off indicate on-potential period and off-potential period, respectively. The coupling constant appears through the form $\epsilon^2 T$. Thus the dependence on ϵ can be renormalized into the dependence on T to some extent.

7.4 Resonating Behavior: Dependence on Period

In this section, we study the dependence on the period of the external forcing in detail. We show the behavior of the current in a wide range of the period in Figs 7.13(a) and (b). Parameters are taken to be (a) $\beta = 51$ and (b)$\beta = 1$, and $\epsilon = 1.5 \times 10^{-2}$. Direction of the current varies with the period in both low and high temperature case. In the low temperature case, many sharp peaks are seen. In the high temperature, on the other hand, many resonance-like peaks with large width are seen. In both cases, the current is zero at $T = 0$. Also in the limit of $T \to \infty$ the current is expected to vanishes. Since the current is finite at $T = 1000$, the relaxation time of the ratchet system is larger than 1000, which is consistent with the order of the inverse square coupling constant. Both positive and negative current appear, so that neither of the directions seem to be preferred.

We investigate dependence on the period and the temperature in detail. The results are shown in Fig. 7.14. The inverse temperature varies in the range $[1, 100]$, from high

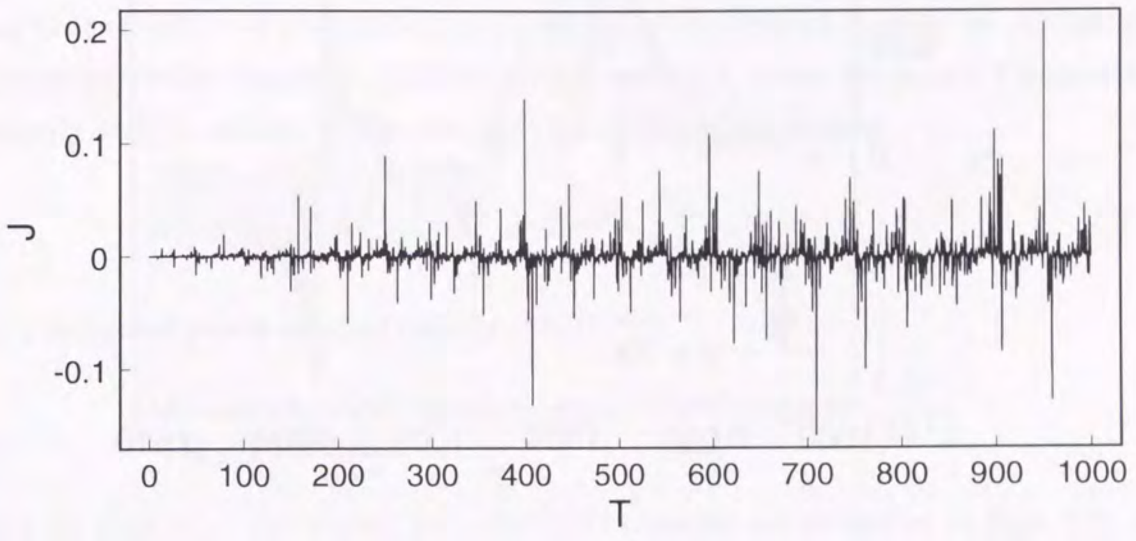

(a) Low Temperature

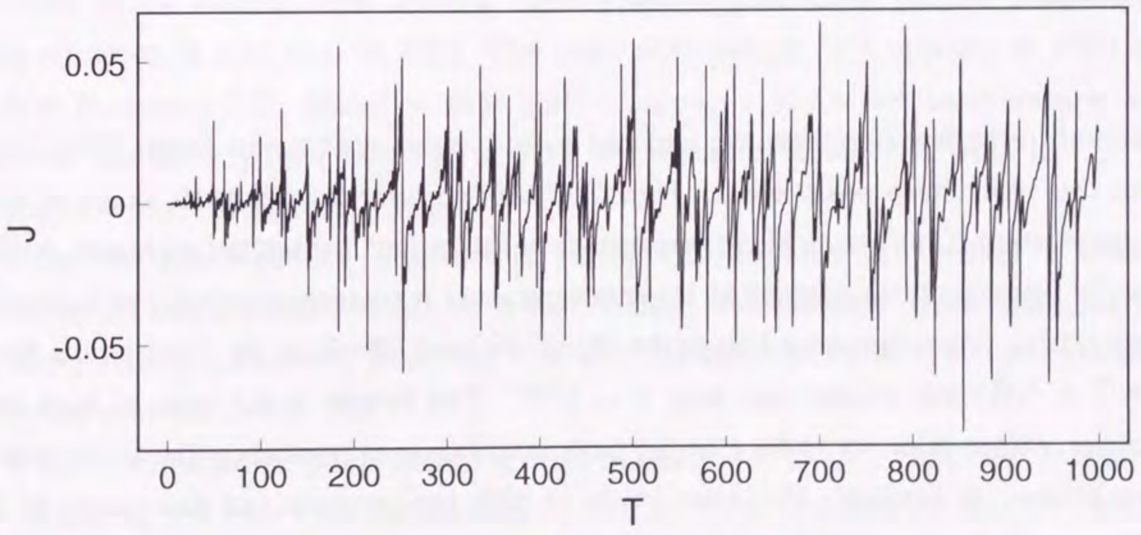

(b) High Temperature

Figure 7.13: Dependence of the current on the period of external forcing. Parameters are taken to be (a) $\beta = 51$ (b) and $\beta = 1$; $\epsilon = 1.5 \times 10^{-2}$. The period is varying in the range $[0, 1000]$.

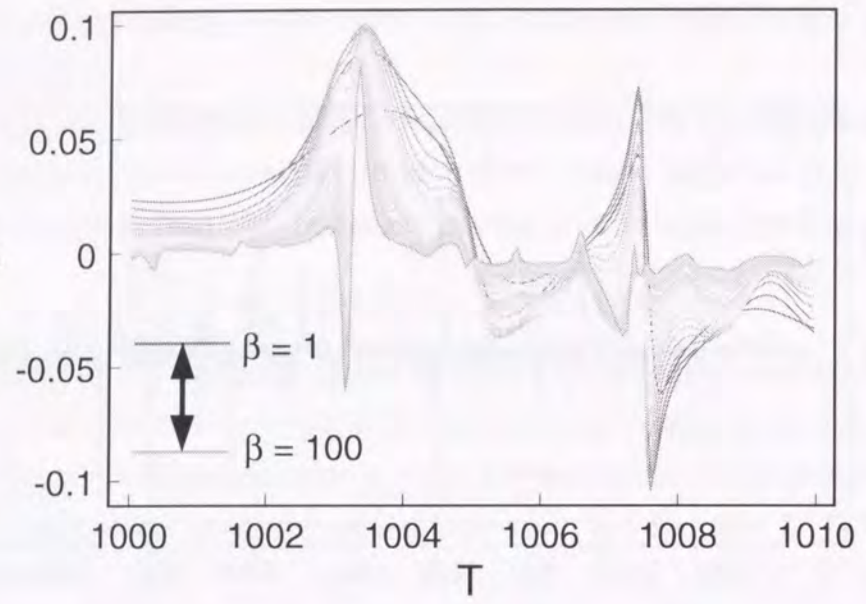

Figure 7.14: Dependence on the period and the temperature. The coupling constant ϵ is taken to be 1.5×10^{-2}. The inverse temperature is varying in the range $[1, 100]$ and the period is varying in the range $[1000, 1010]$.

temperature to low temperature, and the period varies within the range $[1000, 1010]$. From this plot, sharp peaks seen in Figs. 7.13 continuously changes their shape as varying parameters. Comparing high temperature behavior and low temperature one, we find that the fine structures existing at lower temperature is smeared gradually as increasing temperature. Two resonance-like peaks should be paid attention to: First one is found near $T = 1003$ and second one near $T = 1007$. The former is not seen at high temperature, rather it seems to be a broad peak, and becomes resonance-like as decreasing temperature. In contrast, the latter exists at high temperature and disappears at low temperature. It is natural that the peak becomes narrower as decreasing the temperature, so that the broadening behavior of the former peak is caused by high temperature effects. But the behavior that the peak disappears at low temperature seems to be strange at first sight. Amplitude of the currents near two points $T = 1003$ and $T = 1007$ depends on the inverse temperature. But the positions of the peaks hardly depend on the temperature.

To study the dependence on the period, especially of the resonance-like behavior,

we focus the pseudo-periodicity seen in Figs. 7.13. It is seen in high temperature case (Fig. 7.13(b)), while it is hardly recognized in low temperature case(Fig. 7.13(a)). Identifying the periodicity of the currents as the period of the external forcing, we can calculate the autocorrelation function $\langle\langle J[0]J[T]\rangle\rangle$ of the current J, where we denote T dependence explicitly as $J[T]$, defined by the discrete Fourier transformation as:

$$\langle\langle J[0]J[n\Delta T]\rangle\rangle \equiv \frac{1}{N_s}\sum_{k=0}^{N_s-1} e^{-2\pi i n k/N_s}\left|\sum_{l=0}^{N_s-1} e^{2\pi i l k/N_s} J[l\Delta T]\right|^2 , \qquad (7.10)$$

and a one-sided power spectral density (PSD) $P(f)$:

$$P\left(\frac{k}{N_s\Delta T}\right) \equiv \left|\sum_{l=0}^{N_s-1} e^{2\pi i l k/N_s} J[l\Delta T]\right|^2 + \left|\sum_{l=0}^{N_s-1} e^{-2\pi i l k/N_s} J[l\Delta T]\right|^2 , \qquad (7.11)$$

where we take $N_s = 65536$ and $\Delta T = 0.01$. The results are presented in Figs. 7.15 and 7.16. In the plot of the autocorrelation function, clear periodicity is seen in both high and low temperature cases with period 50.4. The peak with period 59.5, on the other hand, vanishes at low temperature. Several other peaks also disappear at low temperature. Such situation is also seen in PSD. The peak with period 50.4 appears in PSD as a peak at frequency 0.02. Many peaks in PSD disappear again at low temperature. Such behavior has already been seen in Fig. 7.14; For example, the second peak in Fig. 7.14 belongs to these disappearing peaks.

From the above results, existence of periodic behavior in the current is evident, although the origin of the periodicity is still unclear. For the later convenience, we pick up characteristic periods T_k^F from Fig. 7.16 and list them in Table 7.1. Corresponding peaks are marked in Fig. 7.16.

If the resonance-like behavior in Fig. 7.14 is really due to the resonance, it is probably caused by the resonance between the quantum oscillation and the periodic forcing. When the frequencies determined by the eigenvalue differences, namely eigenfrequencies, is close to the inverse of half the period of the external forcing, the resonance is expected. In addition the current in Fig. 7.4 seems to be consistent with the resonance mechanism between the oscillations with the eigenfrequencies and the periodical driving. In order to confirm above argument, we have to identify the resonance-like peak as the eigenfrequencies. But this process has a little difficulty, because there are many frequencies which distribute almost continuously. Since the present system has ten energy

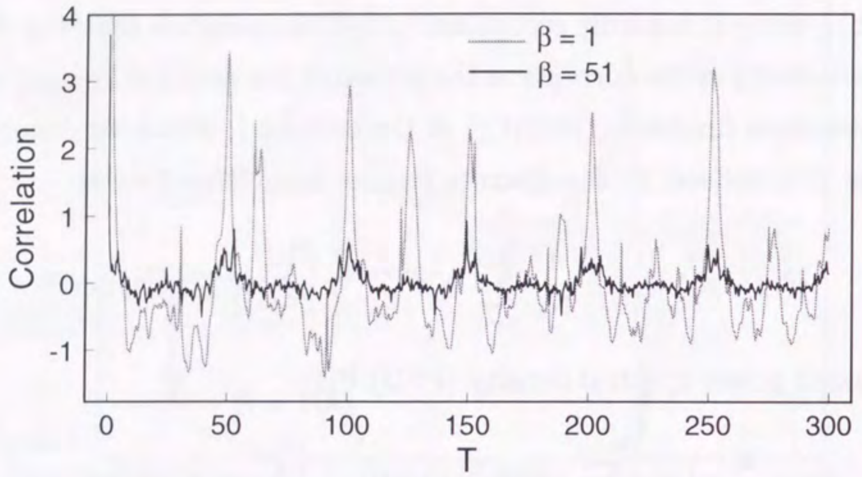

Figure 7.15: Autocorrelation of the current J. Parameters are taken to be $\beta = 1$, high temperature, $\beta = 51$, low temperature, and $\epsilon = 1.5 \times 10^{-2}$.

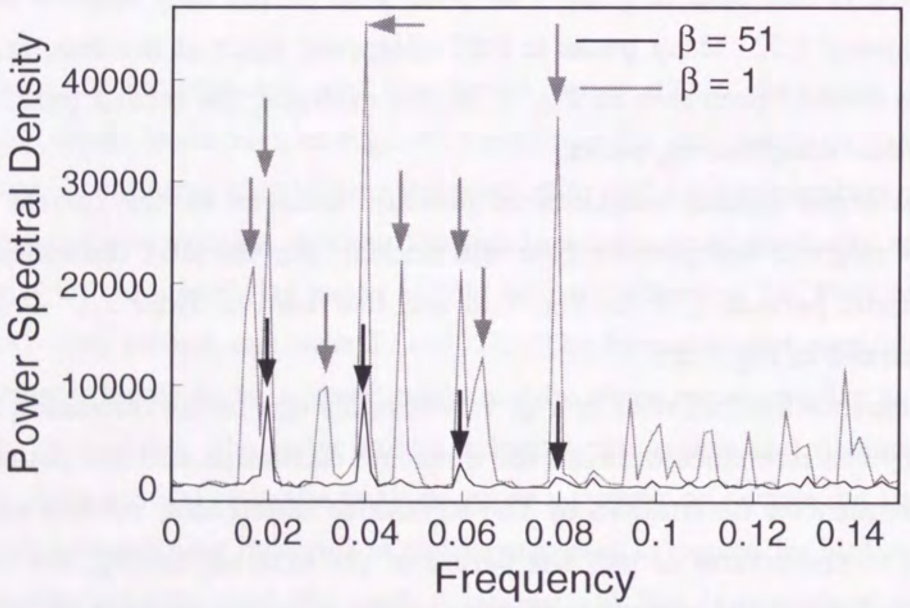

Figure 7.16: One-sided power spectral density of the current J. Parameters are same as ones in Fig. 7.15. Marked peaks are corresponding to periods listed in Table 7.1.

characteristic period of PSD	
high temperature case	low temperature case
59.5	50.4
50.4	25.2
31.2	21.1
25.2	12.6
21.1	
16.8	
15.6	
12.6	

Table 7.1: Characteristic periods T_R^F picked up from Fig. 7.16. Corresponding peaks are marked in Fig. 7.16.

levels without degeneracy, we should treat forty five different eigenfrequencies. Moreover higher harmonics should also be taken into account. Thus we wonder which frequency causes resonance. For making clear which frequency resonates and understanding the mechanism of the resonating behavior, we consider further simplified models in the next section.

7.5 Simplified Ratchet Models

In this section we consider two simplified models for understanding resonating behavior. First is a three-level model which has a linearly increasing potential and second is a "delta-kicked" ratchet, in which the duration of the off-potential period is fixed to a small value instead of the symmetric forcing.

7.5.1 Ratchet-like Three-Level Model

The first model is basically the same as the flushing ratchet model, but for the system size and the potential shape. We consider only one unit cell which consists of only three sites with the following potential:

$$V_{0\,\mathrm{mod}\,3} = 0, \quad V_{1\,\mathrm{mod}\,3} = \frac{1}{2}, \quad V_{2\,\mathrm{mod}\,3} = 1 \ .$$

The periodic boundary condition is imposed, so that the linearly increasing potential becomes an asymmetric periodic potential. Note that such potential does not cause the energy dissipation in the unit cell as was mentioned in the previous section and the energy dissipates only at the boundary of the unit cell. In the present model, however, only three bonds are in the unit cell and thus such localized dissipation is not expected to arise serious influence.

This system has a periodically steady state too, so that the state can be calculated directory. Dependence of the current on the period of flushing potential is plotted in Figs. 7.17 and 7.18 for both low and high temperature cases. Global tendency is similar to the case of the flushing ratchet discussed in the previous section: Direction of the current varies with the period. Many peaks are seen both at high and low temperature and, in the high temperature case, they seem the resonance-like peak with large width. The current behaves systematically in both cases, and the periodicity of the current is clearly recognized, in contrast to the flushing ratchet. Periodic feature of the current can be seen also in the autocorrelation function and its power spectral density, which are calculated using Eqs. 7.10 and 7.11. The results are presented in Figs. 7.19 and 7.20. Clearly we find one period $T_R^T = 21.8$ in both figures.

In the present case, we can identify T_R^T as the characteristic time of the three-level model. Taking account only of the oscillating current in the on-potential period, we calculate the characteristic periods T_D^T as $2\pi\hbar/|E_n - E_m|$ by the numerical diagonalization of the Hamiltonian in the on-potential period. The result are listed in Table 7.2.

In the actual situation, energy levels are modified by the correction from the interaction with the heat bath. The shift of the energy by this correction is given as follows:

$$\Delta E_n \equiv \frac{\epsilon^2}{\hbar^2} \sum_r |\langle n|H_I|r\rangle|^2 \mathbf{P} \int_{-\infty}^{\infty} \frac{d\omega}{2\pi} \tilde{\Phi}(\omega) \frac{1}{\omega + \omega_{rn}} \ ,$$

where $\tilde{\Phi}(\omega)$ is the Fourier transformation of the bath correlation function and $\omega_{rn} = (E_r - E_n)/\hbar$. Remember that the current oscillates in the on-potential period. Then the quantum oscillation resonates with half the period $T/2$ instead of the period T. Thus we must compare $T_R^T/2$ with the characteristic times T_D^T. W e find that $T_R^T = 21.8$ corresponds

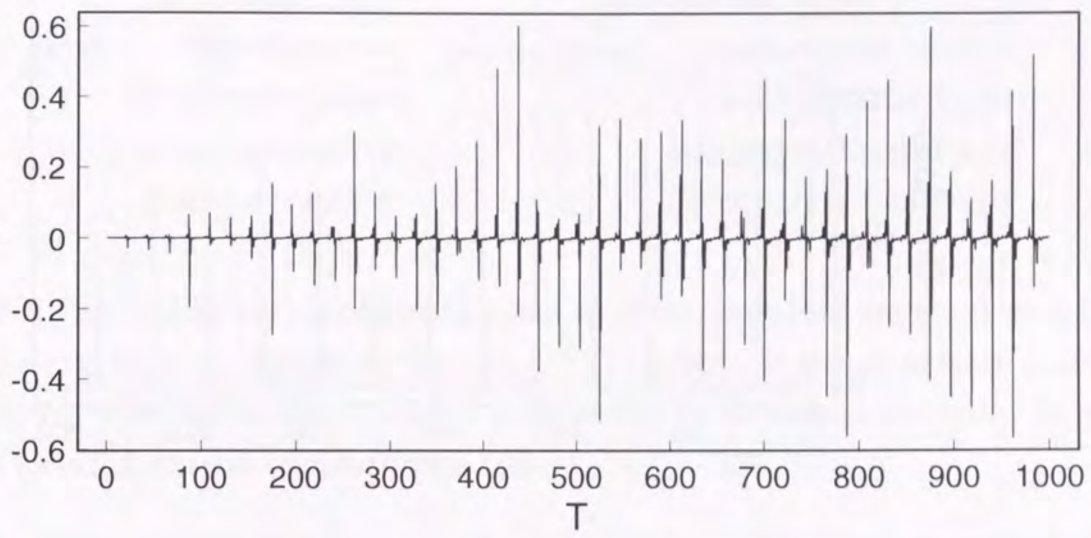

Figure 7.17: Dependence of the current on the period of flushing potential for the three-level system. Low temperature behavior is presented; We take $\beta = 100$. The coupling constant is taken to be $\epsilon = 1.5 \times 10^{-2}$.

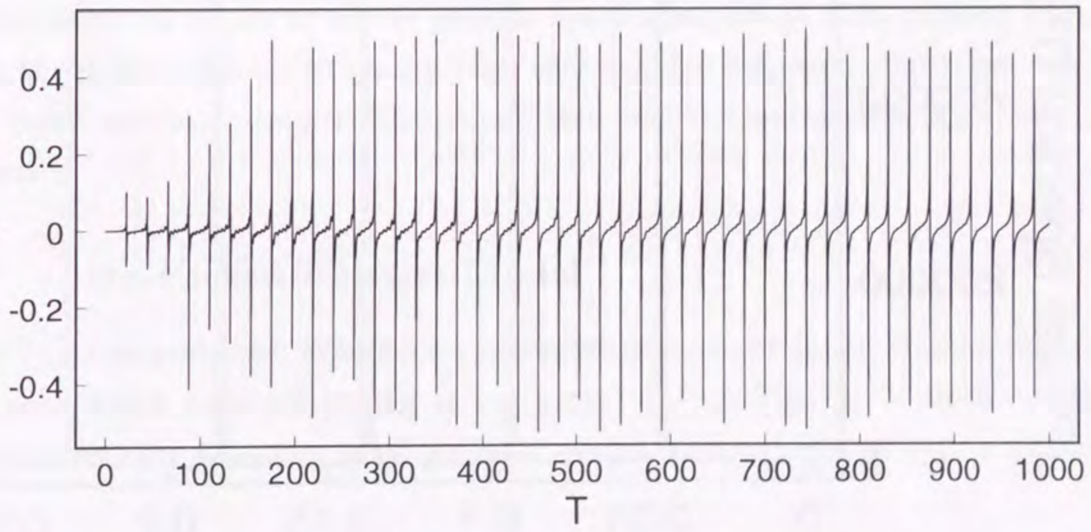

Figure 7.18: Dependence of the current on the period for the three-level system. Inverse temperature is taken to be $\beta = 1$, high temperature. Other parameters are equivalent to ones in Fig. 7.17.

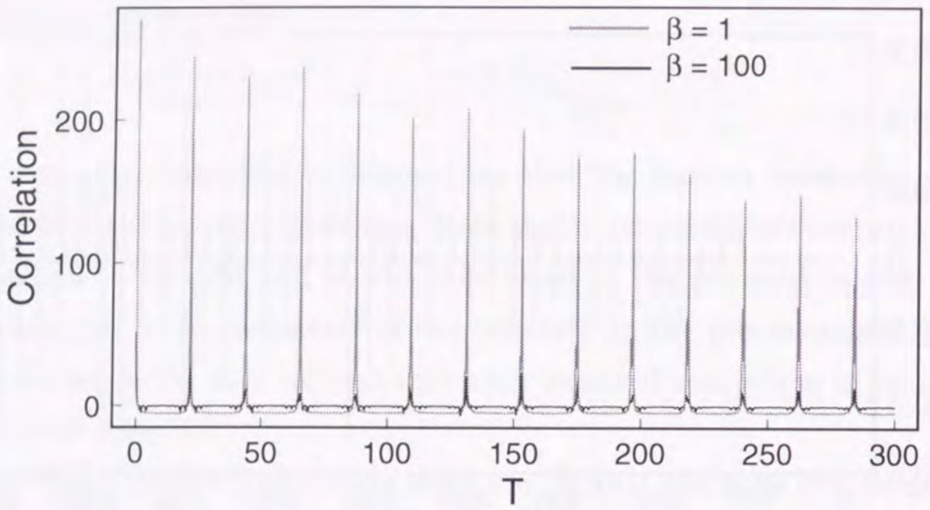

Figure 7.19: Autocorrelation of dependence of the current on the period. We plot the autocorrelation function of Figs. 7.17 and 7.18.

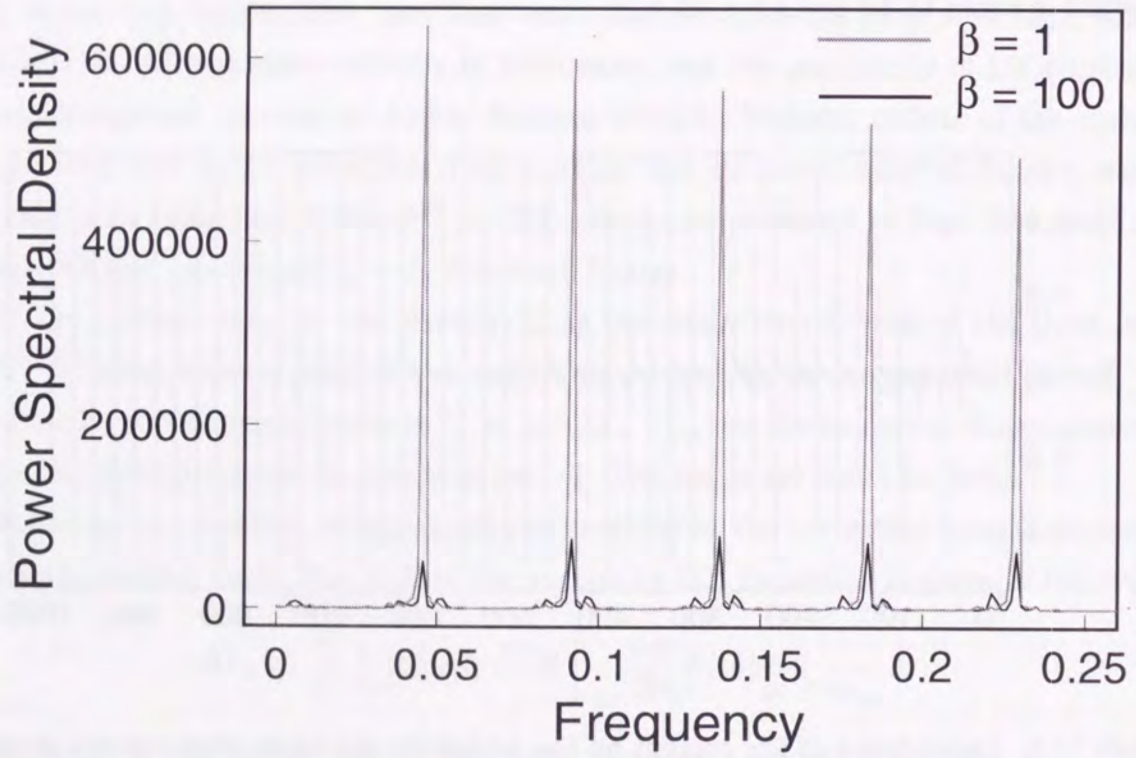

Figure 7.20: Power spectral density of dependence of the current on the period. We plot the one-sided power spectral density of Figs. 7.17 and 7.18.

eigenvalue		characteristic times		
label	eigenvalue	related states		characteristic time
1	-0.792016575144414	1	2	0.109297232727052E+02
2	-0.217145160264573	1	3	0.182855283862893E+01
3	2.64413541854713	2	3	0.219593476031441E+01

Table 7.2: Eigenvalues and characteristic times T_D^T of the three-level system at on potential duration; They are defined by $2\pi\hbar/|E_n - E_m|$ where E_n is energy of state n of the Hamiltonian with the potential. Energy shift caused by the interaction with the heat bath is included. Inverse temperature is taken to be $\beta = 100$.

to twice of $T_D^T = 10.930$. That is, we confirm that this period is really generated by the resonance between the quantum oscillation and the periodically driving. Other two possible periods $T_D^T \times 2 = 2.1959 \times 2$ and 1.8286×2 observed neither in Figs. 7.19 nor in 7.20. That implies some selection mechanism, which is unclear at present.

To summarize in short, we have found that the quantum stochastic current is generated by the resonance between the quantum oscillation and the periodic driving. The resonance does not appear at all the possible frequencies, but at some selected frequencies. In the present three-level system case, only minimal frequency, which corresponds to the lowest excitation between the ground state and the first excited state, seems to be selected.

7.5.2 Delta-Kicked Ratchet Model

Now we face new problems: Where have unselected frequencies gone? What is the origin of the peak which does not belong to the period 21.8 in Fig. 7.17? Both questions are related with the dynamics in off-potential period, although the current is conserved there.

In the off-potential period, relaxation of the off-diagonal elements of the density matrix takes place, even though the current is conserved. In the present case, the density matrix obeys the following equation in the off-potential period:

$$\frac{\partial \rho(t)_{pq}}{\partial t} = \left\{ -i\omega_{pq} \left(1 - \epsilon^2 \frac{E_p + E_q}{\hbar} \frac{\eta}{\lambda} \right) - \epsilon^2 \omega_{pq}^2 \pi \frac{\eta}{\hbar\beta} \right\} \rho(t)_{pq} ,$$

where $\omega_{pq} = (E_p - E_q)/\hbar$ and E_p are eigenvalues of the tight-binding Hamiltonian. If $p = q$, then

$$\frac{\partial \rho(t)_{pp}}{\partial t} = 0 \ ;$$

The diagonal element is thus conserved. In addition, if the states q and p degenerate with each other, $\omega_{pq} = 0$, so that

$$\frac{\partial \rho(t)_{pq}}{\partial t} = 0, \quad \text{if } q, p \text{ are degenerated}$$

If p and q are not degenerate, on the other hand, the off-diagonal elements decay in a similar manner as damping oscillation with the frequency $\omega_{pq}(1 - \epsilon^2\eta(E_p + E_q)/(\hbar\lambda))$ and a inverse time constant $\epsilon^2\omega_{pq}^2\pi\eta/(\hbar\beta)$.

To remove the relaxation effects, we introduce a time-asymmetric forcing, while so far we have used symmetric forcing. Here we set the period of the off-potential period as a small interval $T_{off} = 1 \times 10^{-5}$ (we call "delta-kicked" ratchet for convenience, although it is not truly the delta-function). For the three-level model, we show the dependence of current on the length of the on-potential period T_{on} in Figs. 7.21 and 7.22. Note that the time-averaged net current becomes smaller when T_{off} is short, because it is the conserved current which contributes mainly to the net current. The plots of the conserved current is still useful to understand the mechanism of the generation of the net currents. Using the delta-kicked ratchet, we see that the behavior of the current becomes more systematic than the case of the symmetric forcing. In fact, the envelope of the peaks behaves in highly organized manner, in contrast to the case of the symmetric forcing. In the both figures, peaks corresponding to almost the same values of the listed values of T_D^T in Table 7.2 are recognized. In addition, short characteristic times T_D^T disappear for large T_{on}. The direction of the currents is always the same for same frequency, in contrast to the case of symmetric forcing.

Based on the results for the short off-potential period, we can identify all the eigenfrequencies for the three-level ratchet system. Next we apply the time-asymmetric forcing to the flushing ratchet model. We set $T_{off} = 1 \times 10^{-5}$ and investigate the dependence on T_{on}. The results are plotted in Figs. 7.23 (global behavior) and 7.24 (magnification). We can easily identify the period T_R^D appearing the figures as eigenfrequencies of the flushing ratchet as in the case of the three-level ratchet. For later convenience, we calculate the

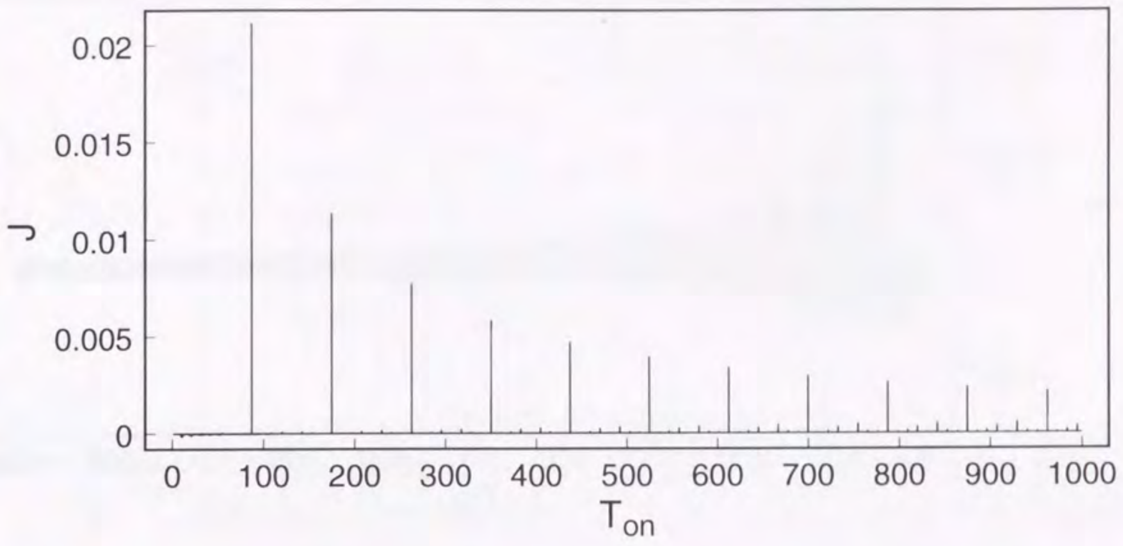

Figure 7.21: Dependence on the period of on-potential duration. We plot the result of the delta-kicked three-level system in low temperature $\beta = 100$. The period of the off-potential duration is taken to be 1×10^{-5}. Interval between each large peak is 87.47 . Thins time is near $87.44 = 8 \times 10.930$: 10.930 is characteristic time which appears in Figs. 7.17, 7.18, 7.19 and 7.20. The envelope of large peaks behaves like $\sim 1/T_{on}$.

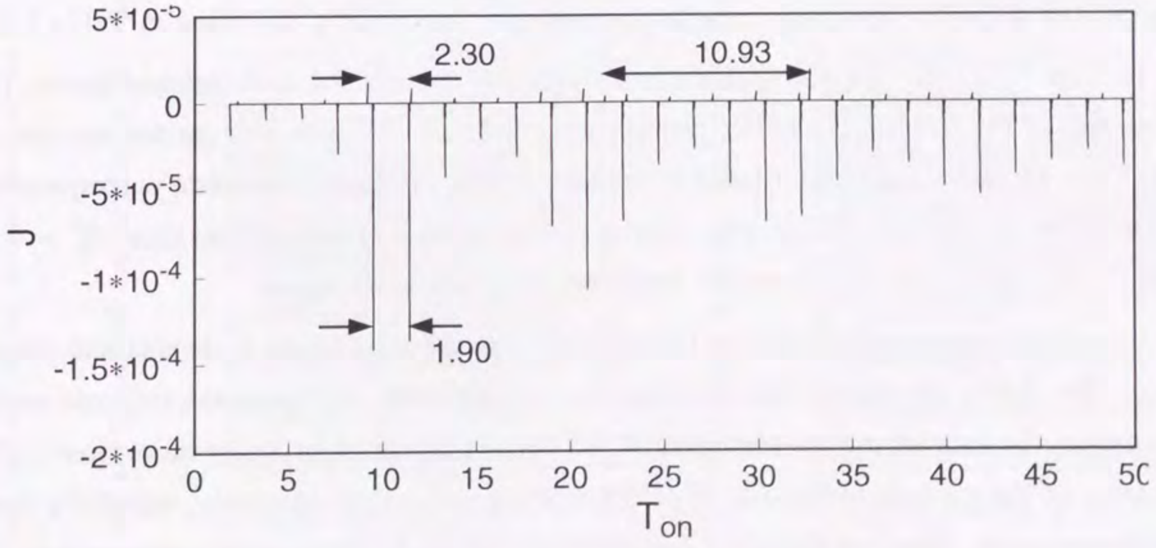

Figure 7.22: Magnification of Fig. 7.21. We zoom in the behavior at short T_{on} period. Interval time between the peaks is presented in the figure.

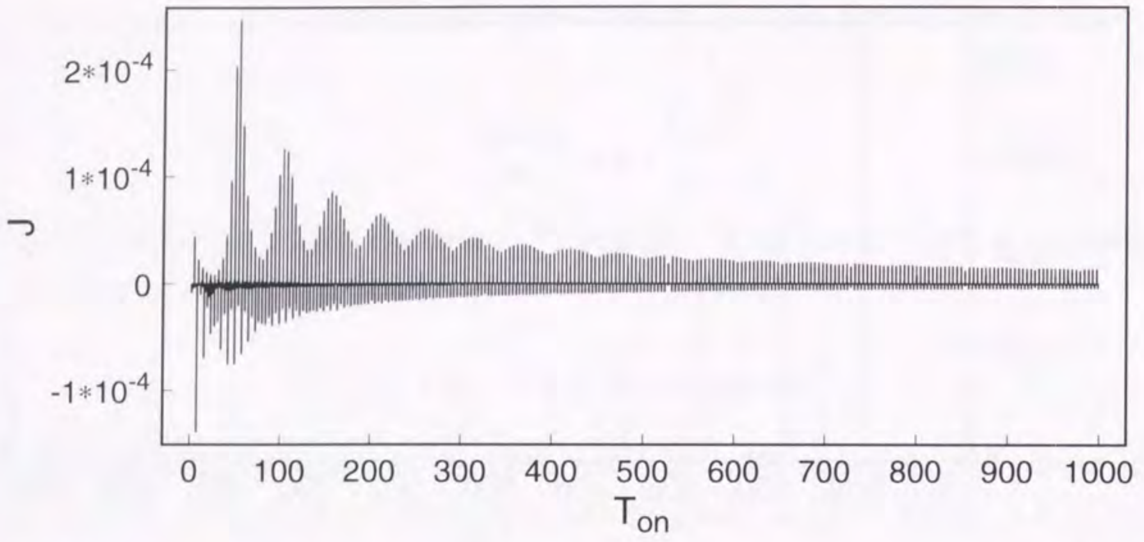

Figure 7.23: Dependence on the on-potential period. We plot the result for the delta-kicked flushing ratchet model in low temperature $\beta = 51$. The period of off-potential duration is taken to be $T_{off} = 1 \times 10^{-5}$.

characteristic times T^{Γ}_{D} determined by the eigenfrequencies at the on-potential period. We take the correction of energy into account, because energy levels are modified by the interaction with the heat bath in actual situations. The results are listed in Table 7.3.

In Figs. 7.23 and 7.24, the systematic behavior of the current is recognized again; The envelopes of the peaks behave like damping oscillations. At least four modes are seen in Fig. 7.23. In each mode, one period is concerned; For instance, the mode corresponding to the positive current seen in Fig. 7.23 is identified as a characteristic time $T^{D}_{R} = 4.47$ (Fig. 7.24). Other T^{D}_{R} of each mode is presented in the same figure.

Numerical comparison between T^{D}_{R} and the characteristic times T^{Γ}_{D} is still not clearly done. To clarify the resonance, we consider another way. If the peaks indicate really resonance, the related matrix elements of the density operator becomes large there. The behavior of the currents reflects that of the off-diagonal matrix elements, especially their imaginary parts. Thus we calculate dynamics of the off-diagonal matrix elements of the density operator directly.

We calculate the dependence of imaginary parts of the off-diagonal elements on the period T_{on}. The results are shown in Figs. 7.25 and 7.26. Corresponding T_{on} dependence

eigenvalue

label	eigenvalue	label	eigenvalue
1	-1.65098840215929	6	0.844696352513499
2	-1.46390826051103	7	1.05351661983403
3	-1.05457167685571	8	1.79164542372574
4	-0.401063986891026	9	2.29590644792017
5	-0.143856290629779	10	2.51190998207248

characteristic times

related states		characteristic time	related states		characteristic time
1	2	0.335855287828377E+02	3	10	0.176173217274119E+01
1	3	0.105348914868659E+02	4	5	0.244284505221154E+02
1	4	0.502685234824908E+01	4	6	0.504365509422825E+01
1	5	0.416896795838864E+01	4	7	0.431958562693308E+01
1	6	0.251761985173041E+01	4	8	0.286548935832670E+01
1	7	0.232322936394261E+01	4	9	0.232971982225864E+01
1	8	0.182511001744714E+01	4	10	0.215696588742976E+01
1	9	0.159193130820261E+01	5	6	0.635594424394703E+01
1	10	0.150932953487998E+01	5	7	0.524747589252819E+01
2	3	0.153496797816535E+02	5	8	0.324628257129564E+01
2	4	0.591167082325700E+01	5	9	0.257532643758610E+01
2	5	0.475980160280385E+01	5	10	0.236586538002532E+01
2	6	0.272163775753419E+01	6	7	0.300889638857743E+02
2	7	0.249587804231280E+01	6	8	0.663518838872899E+01
2	8	0.192998982398848E+01	6	9	0.432961809038713E+01
2	9	0.167114232197013E+01	6	10	0.376867449415419E+01
2	10	0.158035028229618E+01	7	8	0.851231580301119E+01
3	4	0.961455477649342E+01	7	9	0.505733815585418E+01
3	5	0.689917572169623E+01	7	10	0.430829270395283E+01
3	6	0.330821420929827E+01	8	9	0.124601846673808E+02
3	7	0.298051343100354E+01	8	10	0.872344114285904E+01
3	8	0.220755664799483E+01	9	10	0.290883457378743E+02
3	9	0.187531010441844E+01			

Table 7.3: Eigenvalues and characteristic times of the ratchet system at on-potential duration T^{Γ}_{D}; They are defined by $2\pi\hbar/|E_n - E_m|$ where E_n is energy of state n for on-potential duration. Energy shift caused by the interaction with the heat bath is taken into account. Inverse temperature is taken to be $\beta = 51$. Pairs of energy levels, 2-3, 4-5,

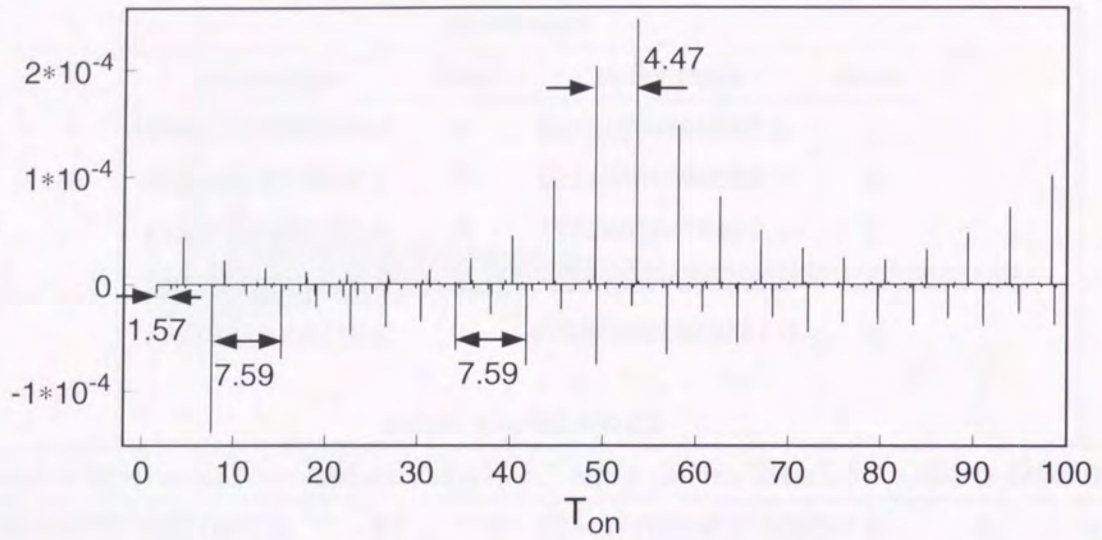

Figure 7.24: Magnification plot of Fig. 7.23 at small T_{on} period. Interval time between the peaks are presented in the figure.

of the current is also shown in Fig. 7.27. We plot only the values of the off-diagonal matrix elements which exhibit nontrivial behavior. The other values do not vary largely with the period. In addition we give two separate figures, for the matrix elements connected to the ground state and the ones disconnected from the ground state.

Figure 7.25 shows that the imaginary parts of the matrix elements $\mathrm{Im}\langle 1|\rho(t)|4\rangle$, $\mathrm{Im}\langle 1|\rho(t)|5\rangle$, $\mathrm{Im}\langle 1|\rho(t)|8\rangle$, and $\mathrm{Im}\langle 1|\rho(t)|9\rangle$ (labels of the states are explained in Table. 7.3) vary periodically. In contrast to Fig. 7.25, Figure 7.26 shows a little complicated behavior, which is understood as higher order effects of the dynamics shown in Fig. 7.25. The behavior of the matrix elements $\mathrm{Im}\langle 4|\rho|5\rangle$, for example, can be regarded as the superposition of the dynamics of $\mathrm{Im}\langle 1|\rho(t)|4\rangle$ and $\mathrm{Im}\langle 1|\rho(t)|5\rangle$. In addition, order of magnitude of the current are all less than ones in Fig. 7.25. The reason why only the matrix elements connected among the states 1, 4, 5, 8, and 9 show nontrivial behavior is concerned with the translational symmetry of the Hamiltonian, especially the invariance in the unit-cell-translation. The eigenstates of the Hamiltonian in both on-potential and off-potential periods are classified into two subspaces by the operation of the unit cell translation, one changing the sign of the eigenstate and one not changing the sign. In this sense, the ground state and the excited states 4, 5, 8, and 9 belong to same subspace

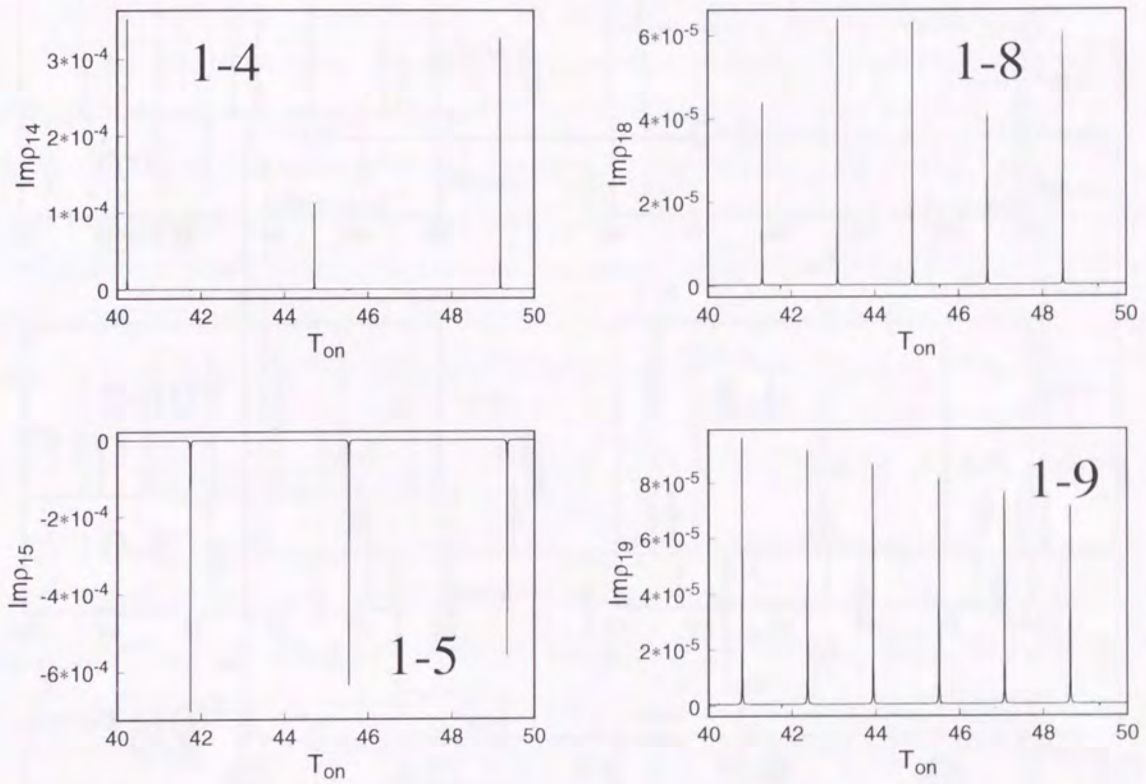

Figure 7.25: Dependence of the off-diagonal matrix elements on the period of the on-potential duration. Imaginary parts of the off-diagonal elements of the density matrix are plotted. Basis is taken to be the eigenstate of the on-potential Hamiltonian. Corresponding two states are presented inset of the figure. This index is same as one in Table 7.3. Here only the results of the matrix elements connected between the ground state 1 and higher excited state are plotted; Period-independent matrix elements are discarded. Parameters are equivalent to ones in Fig. 7.23.

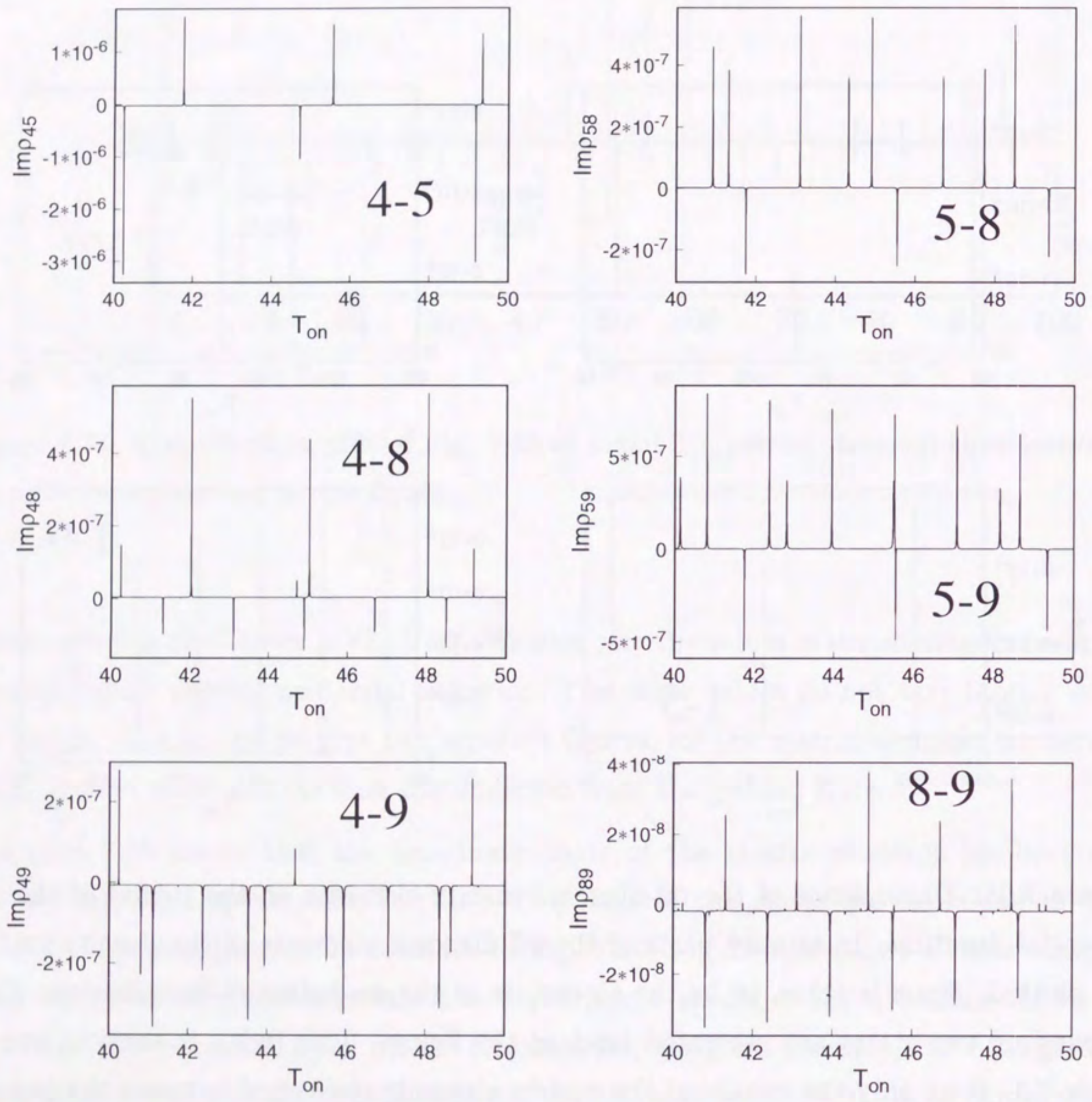

Figure 7.26: Dependence of the off-diagonal matrix elements on the period of the on-potential duration. Remaining results which show nontrivial behavior is plotted. Period-independent matrix elements are discarded. Other conditions are equivalent to Fig. 7.25.

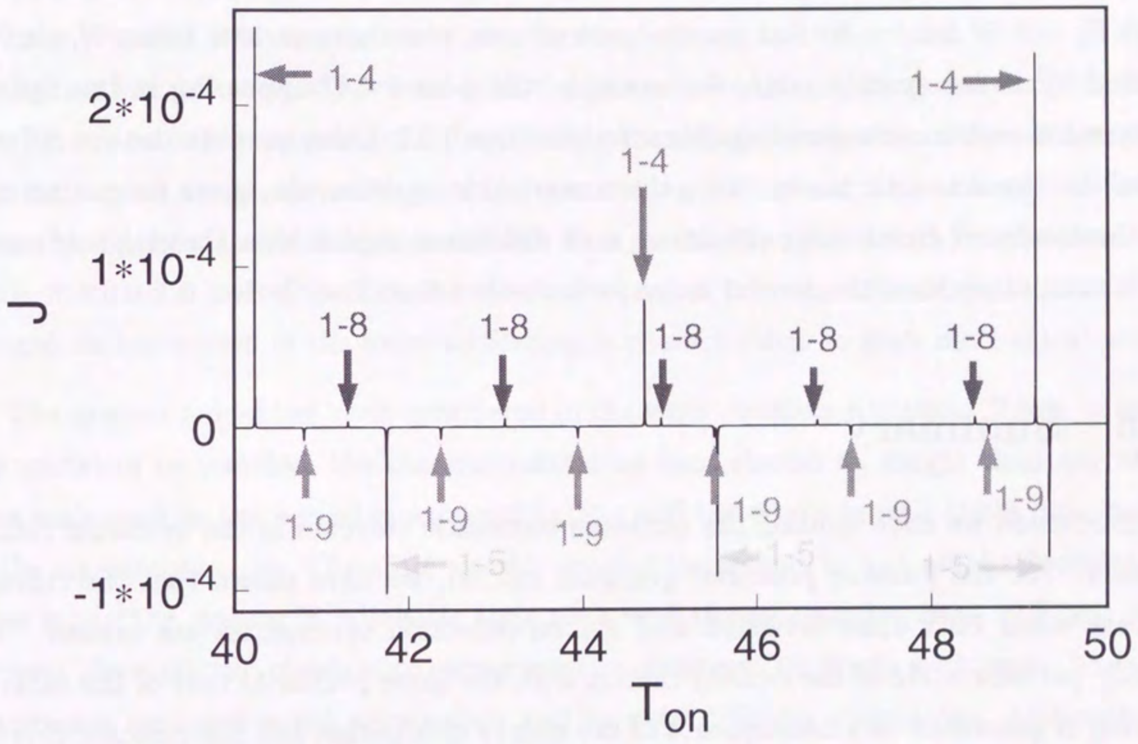

Figure 7.27: Identification of peaks in period vs current plot with eigenstates; We plot the current corresponding to the range of Figs. 7.25 and 7.26. The arrows and labels in the plot show related eigenstates which is determined by comparing with Fig. 7.25.

both in the on-potential and off-potential period. In low temperature case, majority of the population of particles gather in the ground state. Therefore the states connecting among the states 1, 4, 5, 8, and 9 is selected. Comparing with Fig. 7.27, we conclude that the dynamics of the above four matrix elements determine the behavior of the current.

Now we can identify the period T_R^D which is taken from Fig. 7.24 with the characteristic times T_D^F calculated by the diagonalization. We know only four characteristic times appear; They are $T_D^F = 5.03$ for the states $1-4$, $T_D^F = 4.17$ for $1-5$, $T_D^F = 1.83$ for $1-8$, and $T_D^F = 1.59$ for $1-9$. But, in the present case, the characteristic times T_D^F and the period T_R^D is not exactly same; For example, the period 4.47 appearing in the figure is different from the corresponding characteristic time 5.03. Other periods also are different from the characteristic times. Since the numerical integration also gives the period close to the results of direct diagonalization, such difference implies that the origin of energy shift exist other than the second order perturbation described in Sec. 6.1.

7.6 Summary

In conclusion we have studied the quantum stochastic currents in the quantum ratchet system. For the flushing potential quantum ratchet, we have shown that the currents appear when both time inversion and spatial reflection symmetries are broken. The steady periodic state of the density matrix with the same period as that of the external forcing is generated as a consequence of the energy dissipation and the periodic driving. By the direct diagonalization of the dissipative Liouville superoperator, we have investigated in detail how the current depends on the temperature and the period of external forcing. The current depends linearly on temperature at low temperature and the net current remains finite even in the zero temperature limit. In the high temperature limit, on the other hand, the currents vanish. In the intermediate range of temperature, the currents have a single extremum or multiple ones near the characteristic energy scale of the flushing ratchet system. Such behavior reminds us of similarity with the (quantum) stochastic resonance (e.g. [21, 28, 29]). Relation between the quantum ratchet and the quantum SR, however, is not clear yet, and will be left to a future problem.

The current depends on the period of external forcing in a singular manner; As increasing the period, the direction of the current changes violently around zero. Generation of the finite currents is essentially due to a quantum resonance; Temporal oscillation of the currents with an eigenfrequency resonates with the periodical flushing of the external potential. For simplified ratchet models, namely, the three-level ratchet-like model and the delta-kicked ratchet model, we can identify the period of the external forcing at which a finite net current appears as the eigenfrequencies of the Hamiltonian. All the eigenfrequencies, however, does not resonate, but some eigenfrequencies are selected by the symmetry of the system. This conclusion is for the simplest models of the ratchet; But the essential features are same also for the flushing ratchet model. In the flushing ratchet system, other effects related with the relaxation of the off-diagonal element of the density matrix is also important for explaining the detailed behavior of the currents. As was mentioned above, the mechanism for generating the net currents is totally different from that of the classical flushing ratchets. It is essentially a (quantum) mechanical one, while mechanics is irrelevant in the classical thermal ratchets. The dependence of the current on the period of the external forcing is characteristic to such mechanical origin.

The present model has been considered in the weak coupling situation. Thus, in order the model to be justified, the thermal relaxation time should be longer than any other time scale such as the period of external forcing and the characteristic times determined by the eigenfrequencies. Therefore we only studied the system in non-adiabatic situation. If we study the system in adiabatic time scale and strong coupling case, different phenomena like quantum-classical crossover may be observed. To study such cases, however, the present approach is not appropriate and we need different approaches. Although the present study is only on some specific models and the details of the results depends on the detail of the model, we believe that the essential mechanism of generating currents applies widely to other models of this type. Especially there is a possibility of producing the currents more effectively by tuning the details of the model.

Finally let us consider possible experimental realizations. The present model may be fabricated in the quantum dots array. Order of typical hopping energy and length of interval between quantum dots are $\sim 10\,\mathrm{meV}, 100\,\mathrm{nm}$, respectively [62]. If we take the unit of energy and length in the present model as these values, the order of the unit of time and total stochastic currents become $\sim 1\,\mathrm{psec}, \sim 1 \times 10^7\,\mathrm{m/sec}$, respectively. In case that the population of electrons is 2 per one quantum dot, the concentration is about $\sim 10^{21}\,\mathrm{m}^{-3}$. Then the unit of current corresponds to $\sim 1\,\mathrm{mA}$. The current is generated most efficiently in the regime about $\beta = 1 \sim 10$ and $T \sim 1000$, which corresponds to the real scale of the temperature 10 K ~ 100 K and 1 GHz switching of the potential. These conditions are certainly realistic for experimental setup.

Appendix A

Path-Integral Treatment of Quantum Dissipative Systems

Here we briefly review the method based on path integral treatment according to Caldeira and Leggett [7, 68]: Let us start with a following Hamiltonian:

$$H_{total} = H_s + H_R + H_I \ , \tag{A.1}$$

$$\text{where} \quad H_s = \frac{P^2}{2M} + V(Q) \ , \tag{A.2}$$

$$H_R = \sum_{\alpha=1}^{N} \left(\frac{p_\alpha^2}{2m_\alpha} + \frac{1}{2} m_\alpha \omega_\alpha^2 x_\alpha^2 \right) \ , \tag{A.3}$$

$$H_I = -\sum_{\alpha=1}^{N} F_\alpha(Q) x_\alpha + \Delta V(Q) \ . \tag{A.4}$$

H_s represents a Hamiltonian of one-dimensional system and P, Q are its canonical variables. H_R denotes a thermal heat bath system represented by a set of harmonic oscillators, and H_I is an interaction part between the isolated system and the heat bath described by linear coupling term $F_\alpha(Q)$ and a counter term $\Delta V(Q)$. If we choose $\Delta V(Q) = 0$, then the potential of the system is represented as follows:

$$V_{eff}(Q) = V(Q) - \sum_{\alpha=1}^{N} \frac{F_\alpha^2(Q)}{2m_\alpha \omega_\alpha^2} \ . \tag{A.5}$$

This expression shows that the energy spectrum of the system is renormalized by the second term which comes form the interaction part. To remove such renormalization effects we take $\Delta V(Q)$ as

$$\Delta V(Q) = \sum_{\alpha=1}^{N} \frac{F_\alpha^2(Q)}{2m_\alpha \omega_\alpha^2} \ . \tag{A.6}$$

Supposing the interaction is separable and linear, that is, $F_\alpha(Q) = c_\alpha Q$, we get the Hamiltonian of total system as

$$H_{total} = \frac{P^2}{2M} + V(Q) + \sum_{\alpha=1}^{N} \left(\frac{p_\alpha^2}{2m_\alpha} + \frac{1}{2} m_\alpha \omega_\alpha^2 \left(x_\alpha - \frac{c_\alpha}{m_\alpha \omega_\alpha^2} Q \right)^2 \right) \ . \tag{A.7}$$

This model is called Caldeira-Leggett model. Path integral treatment allows us to calculate a Green function for real time or a density matrix for imaginary time. Here we are interested in calculating a density matrix, because the statistical nature such as tunneling probability is given by the density matrix. In order to calculate the density matrix, Euclidean Lagrangian must be required; First we calculate the corresponding Lagrangian (not Euclidean) to each Hamiltonian as follows:

$$\mathcal{L}_s = \frac{1}{2} M \dot{Q}^2 - V(Q) \ , \tag{A.8}$$

$$\mathcal{L}_R = \sum_{\alpha=1}^{N} \left(\frac{1}{2} m_\alpha \dot{x}_\alpha^2 - \frac{1}{2} m_\alpha \omega_\alpha^2 x_\alpha^2 \right) \ , \tag{A.9}$$

$$\mathcal{L}_I = -\sum_{\alpha=1}^{N} \left(-c_\alpha x_\alpha Q + \frac{c_\alpha^2 Q^2}{2m_\alpha \omega_\alpha^2} \right) \ , \tag{A.10}$$

by the standard way $\mathcal{L} = \sum \dot{q} p - H$. A Green function $\mathcal{K}(Q'', \vec{x}''; Q', \vec{x}')$, we express the heat bath coordinates by the vector form, $\vec{x} = \{x_\alpha\}$, is given by the path integral as

$$\mathcal{K}(Q'', \vec{x}''; Q', \vec{x}') = \int_{\substack{Q(t')=Q', \\ \vec{x}(t')=\vec{x}'}}^{\substack{Q(t'')=Q'', \\ \vec{x}(t'')=\vec{x}''}} \mathcal{D}Q \, \mathcal{D}\vec{x} \exp\left(\frac{i}{\hbar} S[Q, \vec{x}] \right) \ , \tag{A.11}$$

where $S[Q, \vec{x}]$ is an action defined by

$$S[Q, \vec{x}] = \int_{t'}^{t''} dt \left(\mathcal{L}_s[Q] + \mathcal{L}_R[\vec{x}] + \mathcal{L}_I[Q, \vec{x}] \right) \ . \tag{A.12}$$

Wick rotation $t = -i\tau$ and appropriate boundary conditions give the density matrix $W_\beta(Q'', \vec{x}''; Q', \vec{x}')$ for the inverse temperature β as

$$W_\beta(Q'', \vec{x}''; Q', \vec{x}') = Z^{-1} \int_{Q(0)=Q'}^{Q(\hbar\beta)=Q''} \mathcal{D}Q \int_{\vec{x}(0)=\vec{x}'}^{\vec{x}(\hbar\beta)=\vec{x}''} \mathcal{D}\vec{x} \exp\left(-\frac{1}{\hbar} S^E[Q, \vec{x}] \right) \ , \tag{A.13}$$

where suffix E represents the Euclidean action defined as

$$S^E[Q, \vec{x}] = \int_0^{\hbar\beta} d\tau \left(\mathcal{L}_s^E[Q] + \mathcal{L}_R^E[\vec{x}] + \mathcal{L}_I^E[Q, \vec{x}] \right) \ , \tag{A.14}$$

and Euclidean Lagrangian: $\mathcal{L}_s^E[Q] = \frac{1}{2} M \dot{Q}^2 + V(Q)$, (A.15)

$$\mathcal{L}_R^E[\vec{x}] = \sum_{\alpha=1}^{N} \left(\frac{1}{2} m_\alpha \dot{x}_\alpha^2 + \frac{1}{2} m_\alpha \omega_\alpha^2 x_\alpha^2 \right) \ , \tag{A.16}$$

$$\mathcal{L}_I^E[Q, \vec{x}] = \sum_{\alpha=1}^{N} \left(-c_\alpha x_\alpha Q + \frac{c_\alpha^2 Q^2}{2m_\alpha \omega_\alpha^2} \right) \ , \tag{A.17}$$

and Z is partition function defined as

$$Z = \oint \mathcal{D}Q \oint \mathcal{D}\vec{x} \exp\left(-\frac{1}{\hbar} S^E[Q, \vec{x}] \right) \ , \tag{A.18}$$

where $\oint \mathcal{D}Q$ means path integrating for the all periodic path with period $\hbar\beta$.

The reduced density matrix of the system $\rho_\beta(Q'', Q')$ is calculated by taking trace for heat bath variables and we obtain it as

$$\rho_\beta(Q'', Q') = \int_{-\infty}^{\infty} d\vec{x}' W_\beta(Q'', \vec{x}'; Q', \vec{x}') \ . \tag{A.19}$$

Defining the reduced partition function Z_d as $Z_d = Z/Z_R$, where Z_R is the thermal equilibrium partition function of heat bath Hamiltonian not including interaction part:

$$Z_R = \prod_{\alpha=1}^{N} Z_R^{(\alpha)} = \prod_{\alpha=1}^{N} \frac{1}{2\sinh(\omega_\alpha \hbar\beta/2)} \ , \tag{A.20}$$

we get

$$\rho_\beta(Q'', Q') = Z_d^{-1} \int_{Q(0)=Q'}^{Q(\hbar\beta)=Q''} \mathcal{D}Q \exp\left(-\frac{1}{\hbar} S_s^E[Q] \right) \mathcal{F}^E[Q] \ , \tag{A.21}$$

where $S_s^E[Q]$ is the Euclidean action of the system:

$$S_s^E[Q] = \int_0^{\hbar\beta} d\tau \mathcal{L}_s^E[Q] \tag{A.22}$$

and $\mathcal{F}^E[Q] = Z_R^{-1} \oint \mathcal{D}\vec{x} \exp\left(-\frac{1}{\hbar} (S_R^E[\vec{x}] + S_I^E[Q, \vec{x}]) \right)$. (A.23)

The functional $\mathcal{F}^{E}[Q]$ represents the interaction effects with the heat bath and it is called an influence functional.

For the Caldeira-Leggett model we can evaluate the influence functional. By the periodicity with period $\hbar\beta$, we expand the variables Q and x_α as Fourier series

$$Q(\tau) = \frac{1}{\hbar\beta} \sum_{n=-\infty}^{\infty} Q_n e^{i\nu_n \tau} \tag{A.24}$$

$$x_\alpha(\tau) = \frac{1}{\hbar\beta} \sum_{n=-\infty}^{\infty} x_{\alpha,n} e^{i\nu_n \tau} \ , \tag{A.25}$$

where $\nu_n = 2\pi n/\hbar\beta$. Using the properties $Q_n = Q^*_{-n}, x_{\alpha,n} = x^*_{\alpha,-n}$, we obtain

$$S^E_R[\vec{x}] + S^E_I[Q,\vec{x}] = \sum_{\alpha=1}^{N} \frac{1}{\hbar\beta} \sum_{n=-\infty}^{\infty} \frac{1}{2} m_\alpha \left(\nu_n^2 |x_{\alpha,n}|^2 + \omega_\alpha \left| x_{\alpha,n} - c_\alpha \frac{Q_n}{m_\alpha \omega_\alpha^2} \right|^2 \right) \ . \tag{A.26}$$

Classical Euclidean equations of motion give us the classical solution of dynamics: Denoting the classical solution by suffix (cl), we obtain the equations of motion as follows:

$$M\ddot{Q}^{(cl)}(\tau) - \frac{\partial V(Q^{(cl)}(\tau))}{\partial Q^{(cl)}(\tau)} + \sum_{\alpha=1}^{N} \left(c_\alpha x_\alpha^{(cl)}(\tau) - \frac{c_\alpha^2 Q^{(cl)}(\tau)}{m_\alpha \omega_\alpha^2} \right) = 0 \tag{A.27}$$

$$m_\alpha \ddot{x}_\alpha^{(cl)}(\tau) - m_\alpha \omega_\alpha^2 x_\alpha^{(cl)}(\tau) - c_\alpha Q^{(cl)}(\tau) = 0 \ . \tag{A.28}$$

Substituting the Fourier series of the variable $x_\alpha^{(cl)}$, we get the classical solution for x_α as

$$x_{\alpha,n}^{(cl)} = \frac{c_\alpha^2}{m_\alpha(\nu_n^2 + \omega_\alpha^2)} Q_n^{(cl)} \ . \tag{A.29}$$

We define the fluctuation $y_{\alpha,n}$ for $x_{\alpha,n}$ as

$$y_{\alpha,n} \equiv x_{\alpha,n} - \frac{c_\alpha^2}{m_\alpha(\nu_n^2 + \omega_\alpha^2)} Q_n \ . \tag{A.30}$$

Note that this fluctuation includes the effects of the fluctuation of Q_n, so that we use Q_n instead of $Q_n^{(cl)}$. Using the fluctuation $y_{\alpha,n}$, we rewrite the action corresponding to the influence functional as

$$S^E_R[\vec{x}] + S^E_I[Q,\vec{x}] = S^E_R[\vec{y}] + S^E_{infl}[Q] \ , \tag{A.31}$$

and

$$S^E_R[\vec{y}] = \sum_{\alpha=1}^{N} \int_0^{\hbar\beta} d\tau \frac{m_\alpha}{2} (\dot{y}_\alpha^2 + \omega_\alpha^2 y_\alpha^2) \tag{A.32}$$

$$S^E_{infl}[Q] = \sum_{\alpha=1}^{N} \frac{c_\alpha^2}{2m_\alpha} \frac{1}{\hbar\beta} \sum_{n=-\infty}^{\infty} \frac{1}{\nu_n^2 + \omega_\alpha^2} \frac{\nu_n^2}{\omega_\alpha^2} |Q_n|^2 \ . \tag{A.33}$$

The first action is identical to the action of the harmonic oscillators. Then the path integral for $y_{\alpha,n}$ gives the partition function Z_R. Finally we obtain

$$\mathcal{F}^E[Q] = \exp\left(-\frac{1}{\hbar} S^E_{infl}[Q] \right) \ . \tag{A.34}$$

The action corresponding to the influence functional can be rewritten as

$$S^E_{infl}[Q] = \frac{1}{2}\mu \int_0^{\hbar\beta} d\tau Q(\tau)^2 - \int_0^{\hbar\beta} d\tau \int_0^{\tau} d\tau' K(\tau-\tau') Q(\tau) Q(\tau') \ , \tag{A.35}$$

where

$$\mu = \sum_{\alpha=1}^{N} \frac{c_\alpha^2}{m_\alpha \omega_\alpha^2} \tag{A.36}$$

$$K(\tau) = \sum_{\alpha=1}^{N} \frac{c_\alpha^2}{m_\alpha} \frac{1}{\hbar\beta} \sum_{n=-\infty}^{\infty} \frac{e^{i\nu_n \tau}}{\nu_n^2 + \omega_\alpha^2} = \sum_{\alpha=1}^{N} \frac{c_\alpha^2}{2m_\alpha \omega_\alpha} \frac{\cosh(\omega_\alpha(\hbar\beta/2 - |\tau|))}{\sinh(\hbar\beta\omega_a lpha/2)} \ . \tag{A.37}$$

or

$$S^E_{infl}[Q] = \frac{1}{2} \int_0^{\hbar\beta} d\tau \int_0^{\tau} d\tau' K(\tau-\tau') (Q(\tau) - Q(\tau'))^2 \ . \tag{A.38}$$

Introducing continuous spectral density $J(\omega)$, we can replace the summation with the integration, then

$$K(\tau) = \frac{1}{\pi} \int_0^{\infty} d\omega J(\omega) D_\omega(\tau) \ , \tag{A.39}$$

where the spectral density

$$J(\omega) = \frac{\pi}{2} \sum_{\alpha=1}^{N} \frac{c_\alpha^2}{m_\alpha \omega_\alpha} \delta(\omega_\alpha - \omega) \tag{A.40}$$

and

$$D_\omega(\tau) = \frac{\cosh(\omega(\hbar\beta/2 - |\tau|))}{\sinh(\hbar\beta\omega/2)} \ . \tag{A.41}$$

To summarize above arguments, we obtain the reduced density matrix $\rho_\beta(Q'', Q')$ as

$$\rho_\beta(Q'', Q') = Z_d^{-1} \int_{Q(0)=Q'}^{Q(\hbar\beta)=Q''} \mathcal{D}Q(\tau) \exp\left(-\frac{1}{\hbar} (S^E_s[Q] + S^E_{infl}[Q]) \right) \ . \tag{A.42}$$

The second action $S^E_{infl}[Q]$ represents the influence of the thermal heat bath. The effective action $S^E_{eff}[Q] \equiv S^E_s[Q] + S^E_{infl}[Q]$ is as follows:

$$S^E_{eff}[Q] = \int_0^{\hbar\beta} d\tau \left(\frac{M}{2}\dot{Q}(\tau)^2 + V(Q(\tau)) + \frac{1}{2}\int_0^{\tau} d\tau' K(\tau-\tau')(Q(\tau)-Q(\tau'))^2\right) . \quad (A.43)$$

The variable $Q(\tau)$ is defined in $0 \le \tau < \hbar\beta$ and $K(\tau)$ holds the periodicity $K(\tau + \hbar\beta) = K(\tau)$. Extending the variable $Q(\tau)$ to outside the range $0 \le \tau < \hbar\beta$ by the prescription $Q(\tau + n\hbar\beta) = Q(\tau)$, we can rewrite the influence action

$$S^E_{infl}[Q] = \frac{1}{2}\int_0^{\hbar\beta} d\tau \int_0^{\tau} d\tau' K(\tau-\tau')(Q(\tau)-Q(\tau'))^2 \quad (A.44)$$

$$= \int_0^{\hbar\beta} d\tau \int_0^{\hbar\beta} d\tau' K(\tau-\tau')(Q(\tau)-Q(\tau'))^2 \quad (A.45)$$

$$= \frac{1}{2}\int_0^{\hbar\beta} d\tau \int_{-\infty}^{\infty} d\tau' K_0(\tau-\tau')(Q(\tau)-Q(\tau'))^2 , \quad (A.46)$$

where

$$K_0(\tau) = \sum_\alpha \frac{c_\alpha^2}{4m_\alpha\omega_\alpha} \exp(-\omega_\alpha|\tau|) = \frac{1}{2\pi}\int_0^{\infty} d\omega J(\omega) \exp(-\omega|\tau|) . \quad (A.47)$$

For realizing the Ohmic dissipation, the spectral density $J(\omega)$ is chosen as $\eta\omega$. In this case the kernel is $K_0(\tau) = \eta/(2\pi\tau^2)$. Then the effective action is as follows:

$$S^E_{eff}[Q] = \int_0^{\hbar\beta} d\tau \left(\frac{M}{2}\dot{Q}(\tau)^2 + V(Q(\tau))\right) + \frac{\eta}{4\pi}\int_0^{\hbar\beta} d\tau \int_{-\infty}^{\infty} d\tau' \frac{(Q(\tau)-Q(\tau'))^2}{(\tau-\tau')^2} . \quad (A.48)$$

This is the exact expression for the linear coupling and Ohmic dissipation. For the actual application this effective action is calculated by several ways.

Appendix B

Time-Convolution and Time-Convolutionless Equations

In this chapter, we consider the two equations obtained by the weak-coupling expansion in the projection method; There are a time-convolution (TC) equation and a time-convolutionless (TCL) equation.

Consider the following linear differential equation:

$$\frac{\partial\sigma(t)}{\partial t} = L\sigma(t) , \quad (B.1)$$

where L is an arbitrary linear operator and $\sigma(t)$ is an arbitrary variable describing the state of the whole system. In the present case, we assume that the linear operator L can be decomposed into two parts, L_0 and L_1; L_0 describes the time evolution of the subsystem A that we are interested in and L_1 is the time-evolution operator of the remaining part B of the system. We express such decomposition as $L = L_0 + \gamma L_1$ with a coupling constant γ.

When we are interested in the dynamics of the subsystem A, the effects of the remaining system B can be projected to the dynamics of A by the projection method. Before carrying out the process of the projection, we describe the equation in the interaction representation. Expressing the variable in the interaction picture as $\widehat{\sigma}(t) = \exp(-L_0 t)\sigma(t)$, we get

$$\frac{\partial\widehat{\sigma}(t)}{\partial t} = e^{-L_0 t}\gamma L_1 e^{L_0 t}\widehat{\sigma}(t) \quad (B.2)$$

with the commutation relation $[L_0, \exp(-L_0 t)] = 0$. Defining the operator as $\widehat{L_1}(t) =$

$e^{-L_0 t} L_1 e^{L_0 t}$, we obtain

$$\frac{\partial \widehat{\sigma}(t)}{\partial t} = \gamma \widehat{L_1}(t) \widehat{\sigma}(t) \ . \tag{B.3}$$

Hereafter we deal with the above equation for the renormalizing the effects of the system B according to the projection method.

We define the projector that projects the variable belonging to the subsystem B to the subsystem A as $\mathcal{P}$ and the conjugate projector $\mathcal{Q}$ is defined through the identity decomposition $1 = \mathcal{P} + \mathcal{Q}$.

Using them, we obtain the following two equations:

$$\frac{\partial \mathcal{P}\widehat{\sigma}(t)}{\partial t} = \gamma \mathcal{P}\widehat{L_1}(t)\mathcal{P}\widehat{\sigma}(t) + \gamma \mathcal{P}\widehat{L_1}(t)\mathcal{Q}\widehat{\sigma}(t) \ , \tag{B.4}$$

$$\frac{\partial \mathcal{Q}\widehat{\sigma}(t)}{\partial t} = \gamma \mathcal{Q}\widehat{L_1}(t)\mathcal{P}\widehat{\sigma}(t) + \gamma \mathcal{Q}\widehat{L_1}(t)\mathcal{Q}\widehat{\sigma}(t) \ . \tag{B.5}$$

The solution of the second equation can be described as

$$\mathcal{Q}\widehat{\sigma}(t) = \mathcal{G}_+(t, t_0)\mathcal{Q}\widehat{\sigma}(t_0) + \int_{t_0}^{t} ds \mathcal{G}_+(t, s)\gamma \mathcal{Q}\widehat{L_1}(s)\mathcal{P}\widehat{\sigma}(s) \tag{B.6}$$

formally. Here we define the operator $\mathcal{G}_+(t, s)$ as

$$\mathcal{G}_+(t, s) = \overleftarrow{\mathcal{T}} \exp\left(\gamma \int_s^t dt_1 \mathcal{Q}\widehat{L_1}(t_1)\right) \ , \tag{B.7}$$

where $\overleftarrow{\mathcal{T}}$ represents the chronological ordered product.

When the formal solution is substituted into the Equation (B.4), we obtain a TC equation. Actually we get

$$\begin{aligned}\frac{\partial \mathcal{P}\widehat{\sigma}(t)}{\partial t} = {} & \gamma \mathcal{P}\widehat{L_1}(t)\mathcal{P}\widehat{\sigma}(t) + \gamma \mathcal{P}\widehat{L_1}(t)\mathcal{G}_+(t, t_0)\mathcal{Q}\widehat{\sigma}(t_0) \\ & + \gamma \mathcal{P}\widehat{L_1}(t) \int_{t_0}^{t} ds \mathcal{G}_+(t, s)\gamma \mathcal{Q}\widehat{L_1}(s)\mathcal{P}\widehat{\sigma}(s) \ . \end{aligned} \tag{B.8}$$

This is a time-convolution equation that is same as one obtained in Sec. 6.1.

From the original equation (B.3), the formal solution of $\widehat{\sigma}(t)$ is described as

$$\widehat{\sigma}(t) = \overleftarrow{\mathcal{T}} \exp\left(\gamma \int_{t_0}^{t} dt_1 \widehat{L_1}(t_1)\right) \widehat{\sigma}(t_0) \ . \tag{B.9}$$

Defining the time-evolution operator $\mathcal{G}_-(t, s)$ as

$$\mathcal{G}_-(t, s) = \overrightarrow{\mathcal{T}} \exp\left(-\gamma \int_s^t dt_1 \widehat{L_1}(t_1)\right) \ , \tag{B.10}$$

we can write $\widehat{\sigma}(s) \quad (s < t)$ as

$$\widehat{\sigma}(s) = \mathcal{G}_-(t, s)\widehat{\sigma}(t) \ . \tag{B.11}$$

Substituting this into the formal solution (B.6), we get

$$\mathcal{Q}\widehat{\sigma}(t) = \mathcal{G}_+(t, t_0)\mathcal{Q}\widehat{\sigma}(t_0) + \int_{t_0}^{t} ds \mathcal{G}_+(t, s)\gamma \mathcal{Q}\widehat{L_1}(s)\mathcal{P}\mathcal{G}_-(t, s)\widehat{\sigma}(t) \ . \tag{B.12}$$

Thus we get the explicit description of $\mathcal{Q}\widehat{\sigma}(t)$ as

$$\mathcal{Q}\widehat{\sigma}(t) = (1 - \Sigma(t))^{-1} \left(\mathcal{G}_+(t, t_0)\mathcal{Q}\widehat{\sigma}(t_0) + \Sigma(t)\mathcal{P}\widehat{\sigma}(t)\right) \ , \tag{B.13}$$

where

$$\Sigma(t) = \gamma \int_{t_0}^{t} ds \mathcal{G}_+(t, s)\mathcal{Q}\widehat{L_1}(s)\mathcal{P}\mathcal{G}_-(t, s) \ . \tag{B.14}$$

Substituting this into the equation (B.4), we obtain a time-convolutionless equation:

$$\frac{\partial \mathcal{P}\widehat{\sigma}(t)}{\partial t} = K(t)\mathcal{P}\widehat{\sigma}(t) + K(t)\mathcal{G}_+(t, t_0)\mathcal{Q}\widehat{\sigma}(t_0) \ , \tag{B.15}$$

where

$$K(t) = \gamma \mathcal{P}\widehat{L_1}(t)(1 - \Sigma(t))^{-1} \ . \tag{B.16}$$

The TC and TCL equations obtained above are exact equations. Thus, we can study the dynamics of the subsystem A, solving these equations. But, in practical studies, it is difficult to solve them analytically or numerically. Therefore some approximation is sometimes preferred. Here consider the weak-coupling expansion for two equations.

First we expand two chronological ordered time evolution operators by γ up to sufficient order; We obtain

$$\begin{aligned}\mathcal{G}_+(t, s) = {} & 1 + \gamma \int_s^t \mathcal{Q}\widehat{L_1}(t_1)dt_1 + \gamma^2 \int_s^t dt_1 \int_s^{t_1} dt_2 \mathcal{Q}\widehat{L_1}(t_1)\mathcal{Q}\widehat{L_1}(t_2) \\ & + \gamma^3 \int_s^t dt_1 \int_s^{t_1} dt_2 \int_s^{t_2} dt_3 \mathcal{Q}\widehat{L_1}(t_1)\mathcal{Q}\widehat{L_1}(t_2)\mathcal{Q}\widehat{L_1}(t_3) + O(\gamma^4) \end{aligned} \tag{B.17}$$

$$\mathcal{G}_-(t, s) = 1 - \gamma \int_s^t \widehat{L_1}(t_1)dt_1 + \gamma^2 \int_s^t dt_1 \int_s^{t_1} dt_2 \widehat{L_1}(t_2)\widehat{L_1}(t_1) + O(\gamma^3) \ . \tag{B.18}$$

With these series, we expand the TC equation by γ. Then

$$\begin{aligned}\frac{\partial\mathcal{P}\hat{\sigma}(t)}{\partial t} &= \gamma\mathcal{P}\widehat{L_1}(t)\left(\mathcal{P}\hat{\sigma}(t)+\mathcal{Q}\hat{\sigma}(t_0)\right)\\ &+\gamma^2\int_{t_0}^{t}dt_1\mathcal{P}\widehat{L_1}(t)\mathcal{Q}\widehat{L_1}(t_1)\left(\mathcal{P}\hat{\sigma}(t_1)+\mathcal{Q}\hat{\sigma}(t_0)\right)\\ &+\gamma^3\int_{t_0}^{t}dt_1\int_{t_0}^{t_1}dt_2\mathcal{P}\widehat{L_1}(t)\mathcal{Q}\widehat{L_1}(t_1)\mathcal{Q}\widehat{L_1}(t_2)\left(\mathcal{P}\hat{\sigma}(t_2)+\mathcal{Q}\hat{\sigma}(t_0)\right)\\ &+\gamma^4\int_{t_0}^{t}dt_1\int_{t_0}^{t_1}dt_2\int_{t_0}^{t_2}dt_3\mathcal{P}\widehat{L_1}(t)\mathcal{Q}\widehat{L_1}(t_1)\mathcal{Q}\widehat{L_1}(t_2)\mathcal{Q}\widehat{L_1}(t_3)\left(\mathcal{P}\hat{\sigma}(t_3)+\mathcal{Q}\hat{\sigma}(t_0)\right)\\ &+O(\gamma^5)\end{aligned}\tag{B.19}$$

is obtained. If the initial condition is taken to be $\mathcal{Q}\hat{\sigma}(t_0)=0$, the equation becomes

$$\begin{aligned}\frac{\partial\mathcal{P}\hat{\sigma}(t)}{\partial t} &= \gamma\mathcal{P}\widehat{L_1}(t)\mathcal{P}\hat{\sigma}(t)\\ &+\gamma^2\int_{t_0}^{t}dt_1\mathcal{P}\widehat{L_1}(t)\mathcal{Q}\widehat{L_1}(t_1)\mathcal{P}\hat{\sigma}(t_1)\\ &+\gamma^3\int_{t_0}^{t}dt_1\int_{t_0}^{t_1}dt_2\mathcal{P}\widehat{L_1}(t)\mathcal{Q}\widehat{L_1}(t_1)\mathcal{Q}\widehat{L_1}(t_2)\mathcal{P}\hat{\sigma}(t_2)\\ &+\gamma^4\int_{t_0}^{t}dt_1\int_{t_0}^{t_1}dt_2\int_{t_0}^{t_2}dt_3\mathcal{P}\widehat{L_1}(t)\mathcal{Q}\widehat{L_1}(t_1)\mathcal{Q}\widehat{L_1}(t_2)\mathcal{Q}\widehat{L_1}(t_3)\mathcal{P}\hat{\sigma}(t_3)\\ &+O(\gamma^5)\ .\end{aligned}\tag{B.20}$$

Similarly the expansion of the TCL equation is obtained as

$$\begin{aligned}\frac{\partial\mathcal{P}\hat{\sigma}(t)}{\partial t} &= \gamma\mathcal{P}\widehat{L_1}(t)\left(\mathcal{P}\hat{\sigma}(t)+\mathcal{Q}\hat{\sigma}(t_0)\right)\\ &+\gamma^2\int_{t_0}^{t}dt_1\mathcal{P}\widehat{L_1}(t)\mathcal{Q}\widehat{L_1}(t_1)\left(\mathcal{P}\hat{\sigma}(t)+\mathcal{Q}\hat{\sigma}(t_0)\right)\\ &+\gamma^3\int_{t_0}^{t}dt_1\int_{t_0}^{t_1}dt_2\left(\mathcal{P}\widehat{L_1}(t)\mathcal{Q}\widehat{L_1}(t_1)\mathcal{Q}\widehat{L_1}(t_2)-\mathcal{P}\widehat{L_1}(t)\mathcal{Q}\widehat{L_1}(t_2)\mathcal{P}\widehat{L_1}(t_1)\right)\\ &\qquad\left(\mathcal{P}\hat{\sigma}(t)+\mathcal{Q}\hat{\sigma}(t_0)\right)\\ &+\gamma^4\int_{t_0}^{t}dt_1\int_{t_0}^{t_1}dt_2\int_{t_0}^{t_2}dt_3\Big(\mathcal{P}\widehat{L_1}(t)\mathcal{Q}\widehat{L_1}(t_1)\mathcal{Q}\widehat{L_1}(t_2)\mathcal{Q}\widehat{L_1}(t_3)\\ &\qquad+\mathcal{P}\widehat{L_1}(t)\mathcal{Q}\widehat{L_1}(t_3)\mathcal{P}\widehat{L_1}(t_2)\mathcal{P}\widehat{L_1}(t_1)\\ &\qquad-\mathcal{P}\widehat{L_1}(t)\mathcal{Q}\widehat{L_1}(t_1)\mathcal{Q}\widehat{L_1}(t_3)\mathcal{P}\widehat{L_1}(t_2)\\ &\qquad-\mathcal{P}\widehat{L_1}(t)\mathcal{Q}\widehat{L_1}(t_2)\mathcal{Q}\widehat{L_1}(t_3)\mathcal{P}\widehat{L_1}(t_1)\\ &\qquad-\mathcal{P}\widehat{L_1}(t)\mathcal{Q}\widehat{L_1}(t_2)\mathcal{P}\widehat{L_1}(t_1)\mathcal{Q}\widehat{L_1}(t_3)\\ &\qquad-\mathcal{P}\widehat{L_1}(t)\mathcal{Q}\widehat{L_1}(t_3)\mathcal{P}\widehat{L_1}(t_1)\mathcal{Q}\widehat{L_1}(t_2)\Big)\left(\mathcal{P}\hat{\sigma}(t)+\mathcal{Q}\hat{\sigma}(t_0)\right)+O(\gamma^5)\ .\end{aligned}\tag{B.21}$$

If the initial state satisfies $\mathcal{Q}\hat{\sigma}(t_0)=0$, the part $(\mathcal{P}\hat{\sigma}(t)+\mathcal{Q}\hat{\sigma}(t_0))$ is replaced by $\mathcal{P}\hat{\sigma}(t)$.

In the expansion of the TC equation, to avoid a memory integral, the Markovian approximation is sometimes adopted; That is, the part of the integrand $\mathcal{P}\hat{\sigma}(s)\quad(s<t)$ is replaced by the $\mathcal{P}\hat{\sigma}(t)$. Then the both expansions of TC and TCL equations are identical up to the order γ^2; Difference appears in higher order than γ^2.

To clear the difference between the expansion of TCL equation and one of the TC equation with the Markovian approximation, we choose the projection operator $\mathcal{P}$ as taking the avarage for the subsystem B, which operation expresses as, for instance, $\mathcal{P}\widehat{L_1}(t)=\langle\widehat{L_1}(t)\rangle$. Then the expansion of TC equation with the initial state satisfying the condition $\mathcal{Q}\widehat{\sigma}(t_0) = 0$ becomes

$$\begin{aligned}
\frac{\partial\langle\widehat{\sigma}(t)\rangle}{\partial t} &= \gamma\langle\widehat{L_1}(t)\rangle\langle\widehat{\sigma}(t)\rangle \\
&+\gamma^2\int_{t_0}^{t} dt_1\left(\langle\widehat{L_1}(t)\widehat{L_1}(t_1)\rangle - \langle\widehat{L_1}(t)\rangle\langle\widehat{L_1}(t_1)\rangle\right)\langle\widehat{\sigma}(t_1)\rangle \\
&+\gamma^3\int_{t_0}^{t} dt_1\int_{t_0}^{t_1} dt_2\{\langle\widehat{L_1}(t)\widehat{L_1}(t_1)\widehat{L_1}(t_2)\rangle - \langle\widehat{L_1}(t)\widehat{L_1}(t_1)\rangle\langle\widehat{L_1}(t_2)\rangle \\
&\qquad - \langle\widehat{L_1}(t)\rangle\langle\widehat{L_1}(t_1)\widehat{L_1}(t_2)\rangle + \langle\widehat{L_1}(t)\rangle\langle\widehat{L_1}(t_1)\rangle\langle\widehat{L_1}(t_2)\rangle\}\langle\widehat{\sigma}(t_2)\rangle \\
&+\gamma^4\int_{t_0}^{t} dt_1\int_{t_0}^{t_1} dt_2\int_{t_0}^{t_2} dt_3\left(\langle\widehat{L_1}(t)\widehat{L_1}(t_1)\widehat{L_1}(t_2)\widehat{L_1}(t_3)\rangle\right. \\
&\quad - \langle\widehat{L_1}(t)\rangle\langle\widehat{L_1}(t_1)\widehat{L_1}(t_2)\widehat{L_1}(t_3)\rangle - \langle\widehat{L_1}(t)\widehat{L_1}(t_1)\rangle\langle\widehat{L_1}(t_2)\widehat{L_1}(t_3)\rangle \\
&\quad - \langle\widehat{L_1}(t)\widehat{L_1}(t_1)\widehat{L_1}(t_2)\rangle\langle\widehat{L_1}(t_3)\rangle + \langle\widehat{L_1}(t)\widehat{L_1}(t_1)\rangle\langle\widehat{L_1}(t_2)\rangle\langle\widehat{L_1}(t_3)\rangle \\
&\quad + \langle\widehat{L_1}(t)\rangle\langle\widehat{L_1}(t_1)\widehat{L_1}(t_2)\rangle\langle\widehat{L_1}(t_3)\rangle + \langle\widehat{L_1}(t)\rangle\langle\widehat{L_1}(t_1)\rangle\langle\widehat{L_1}(t_2)\widehat{L_1}(t_3)\rangle \\
&\quad \left. - \langle\widehat{L_1}(t)\rangle\langle\widehat{L_1}(t_1)\rangle\langle\widehat{L_1}(t_2)\rangle\langle\widehat{L_1}(t_3)\rangle\right)\langle\widehat{\sigma}(t_3)\rangle + O(\gamma^5) \\
&= \gamma\langle\widehat{L_1}(t)\rangle_{pc}\langle\widehat{\sigma}(t)\rangle \\
&+\gamma^2\int_{t_0}^{t} dt_1\langle\widehat{L_1}(t)\widehat{L_1}(t_1)\rangle_{pc}\langle\widehat{\sigma}(t_1)\rangle \\
&+\gamma^3\int_{t_0}^{t} dt_1\int_{t_0}^{t_1} dt_2\langle\widehat{L_1}(t)\widehat{L_1}(t_1)\widehat{L_1}(t_2)\rangle_{pc}\langle\widehat{\sigma}(t_2)\rangle \\
&+\gamma^4\int_{t_0}^{t} dt_1\int_{t_0}^{t_1} dt_2\int_{t_0}^{t_2} dt_3\langle\widehat{L_1}(t)\widehat{L_1}(t_1)\widehat{L_1}(t_2)\widehat{L_1}(t_3)\rangle_{pc}\langle\widehat{\sigma}(t_3)\rangle + O(\gamma^5) \ , \qquad \text{(B.22)}
\end{aligned}$$

where $\langle A(t_1)...B(t_n)\rangle_{pc}$ is a partial cumulant defined by

$$\langle A(t_1)...B(t_n)\rangle_{pc} = \sum_{\text{all partitions}}{}^{\prime}(-1)^{(\text{number of partition})-1}\prod_{\text{keep the order of } t_i}\langle A(t_1)...\rangle\langle...\rangle\ldots\langle..B(t_n)\rangle \ , \tag{B.23}$$

that is, the summation of the product of the averaged operators with corresponding sign for all partitions keeping the order of the operator.

In the same way, we average the TCL equation:

$$\begin{aligned}
\frac{\partial\langle\widehat{\sigma}(t)\rangle}{\partial t} &= \gamma\langle\widehat{L_1}(t)\rangle\langle\widehat{\sigma}(t)\rangle \\
&+\gamma^2\int_{t_0}^{t} dt_1\left(\langle\widehat{L_1}(t)\widehat{L_1}(t_1)\rangle - \langle\widehat{L_1}(t)\rangle\langle\widehat{L_1}(t_1)\rangle\right)\langle\widehat{\sigma}(t)\rangle \\
&+\gamma^3\int_{t_0}^{t} dt_1\int_{t_0}^{t_1} dt_2\left(\langle\widehat{L_1}(t)\widehat{L_1}(t_1)\widehat{L_1}(t_2)\rangle - \langle\widehat{L_1}(t)\widehat{L_1}(t_1)\rangle\langle\widehat{L_1}(t_2)\rangle\right. \\
&\quad - \langle\widehat{L_1}(t)\rangle\langle\widehat{L_1}(t_1)\widehat{L_1}(t_2)\rangle - \langle\widehat{L_1}(t)\widehat{L_1}(t_2)\rangle\langle\widehat{L_1}(t_1)\rangle \\
&\quad \left. + \langle\widehat{L_1}(t)\rangle\langle\widehat{L_1}(t_1)\rangle\langle\widehat{L_1}(t_2)\rangle + \langle\widehat{L_1}(t)\rangle\langle\widehat{L_1}(t_2)\rangle\langle\widehat{L_1}(t_1)\rangle\right)\langle\widehat{\sigma}(t)\rangle \\
&+\gamma^4\int_{t_0}^{t} dt_1\int_{t_0}^{t_1} dt_2\int_{t_0}^{t_2} dt_3\left(\langle\widehat{L_1}(t)\widehat{L_1}(t_1)\widehat{L_1}(t_2)\widehat{L_1}(t_3)\rangle\right. \\
&\quad - \langle\widehat{L_1}(t)\widehat{L_1}(t_1)\widehat{L_1}(t_2)\rangle\langle\widehat{L_1}(t_3)\rangle - \langle\widehat{L_1}(t)\widehat{L_1}(t_2)\widehat{L_1}(t_3)\rangle\langle\widehat{L_1}(t_1)\rangle \\
&\quad - \langle\widehat{L_1}(t)\widehat{L_1}(t_1)\widehat{L_1}(t_3)\rangle\langle\widehat{L_1}(t_2)\rangle - \langle\widehat{L_1}(t)\rangle\langle\widehat{L_1}(t_1)\widehat{L_1}(t_2)\widehat{L_1}(t_3)\rangle \\
&\quad - \langle\widehat{L_1}(t)\widehat{L_1}(t_1)\rangle\langle\widehat{L_1}(t_2)\widehat{L_1}(t_3)\rangle - \langle\widehat{L_1}(t)\widehat{L_1}(t_2)\rangle\langle\widehat{L_1}(t_1)\widehat{L_1}(t_3)\rangle \\
&\quad - \langle\widehat{L_1}(t)\widehat{L_1}(t_3)\rangle\langle\widehat{L_1}(t_1)\widehat{L_1}(t_2)\rangle + \langle\widehat{L_1}(t)\widehat{L_1}(t_1)\rangle\langle\widehat{L_1}(t_2)\rangle\langle\widehat{L_1}(t_3)\rangle \\
&\quad + \langle\widehat{L_1}(t)\widehat{L_1}(t_1)\rangle\langle\widehat{L_1}(t_3)\rangle\langle\widehat{L_1}(t_2)\rangle + \langle\widehat{L_1}(t)\widehat{L_1}(t_2)\rangle\langle\widehat{L_1}(t_3)\rangle\langle\widehat{L_1}(t_1)\rangle \\
&\quad + \langle\widehat{L_1}(t)\widehat{L_1}(t_2)\rangle\langle\widehat{L_1}(t_1)\rangle\langle\widehat{L_1}(t_3)\rangle + \langle\widehat{L_1}(t)\widehat{L_1}(t_3)\rangle\langle\widehat{L_1}(t_1)\rangle\langle\widehat{L_1}(t_2)\rangle \\
&\quad + \langle\widehat{L_1}(t)\widehat{L_1}(t_3)\rangle\langle\widehat{L_1}(t_2)\rangle\langle\widehat{L_1}(t_1)\rangle + \langle\widehat{L_1}(t)\rangle\langle\widehat{L_1}(t_1)\widehat{L_1}(t_2)\rangle\langle\widehat{L_1}(t_3)\rangle \\
&\quad + \langle\widehat{L_1}(t)\rangle\langle\widehat{L_1}(t_1)\widehat{L_1}(t_3)\rangle\langle\widehat{L_1}(t_2)\rangle + \langle\widehat{L_1}(t)\rangle\langle\widehat{L_1}(t_2)\widehat{L_1}(t_3)\rangle\langle\widehat{L_1}(t_1)\rangle \\
&\quad + \langle\widehat{L_1}(t)\rangle\langle\widehat{L_1}(t_3)\rangle\langle\widehat{L_1}(t_1)\widehat{L_1}(t_2)\rangle + \langle\widehat{L_1}(t)\rangle\langle\widehat{L_1}(t_1)\rangle\langle\widehat{L_1}(t_2)\widehat{L_1}(t_3)\rangle \\
&\quad + \langle\widehat{L_1}(t)\rangle\langle\widehat{L_1}(t_2)\rangle\langle\widehat{L_1}(t_1)\widehat{L_1}(t_3)\rangle - \langle\widehat{L_1}(t)\rangle\langle\widehat{L_1}(t_1)\rangle\langle\widehat{L_1}(t_2)\rangle\langle\widehat{L_1}(t_3)\rangle \\
&\quad - \langle\widehat{L_1}(t)\rangle\langle\widehat{L_1}(t_1)\rangle\langle\widehat{L_1}(t_3)\rangle\langle\widehat{L_1}(t_2)\rangle - \langle\widehat{L_1}(t)\rangle\langle\widehat{L_1}(t_2)\rangle\langle\widehat{L_1}(t_3)\rangle\langle\widehat{L_1}(t_1)\rangle \\
&\quad - \langle\widehat{L_1}(t)\rangle\langle\widehat{L_1}(t_2)\rangle\langle\widehat{L_1}(t_1)\rangle\langle\widehat{L_1}(t_3)\rangle - \langle\widehat{L_1}(t)\rangle\langle\widehat{L_1}(t_3)\rangle\langle\widehat{L_1}(t_2)\rangle\langle\widehat{L_1}(t_1)\rangle \\
&\quad \left. - \langle\widehat{L_1}(t)\rangle\langle\widehat{L_1}(t_3)\rangle\langle\widehat{L_1}(t_1)\rangle\langle\widehat{L_1}(t_2)\rangle\right)\langle\widehat{\sigma}(t)\rangle + O(\gamma^5) \ . \qquad \text{(B.24)}
\end{aligned}$$

Using a definition of the ordered cumulant, we can express the above one as

$$\begin{aligned}\frac{\partial\langle\widehat{\sigma}(t)\rangle}{\partial t} &= \gamma\langle\widehat{L_1}(t)\rangle_{oc}\langle\widehat{\sigma}(t)\rangle \\ &+\gamma^2\int_{t_0}^{t} dt_1\langle\widehat{L_1}(t)\widehat{L_1}(t_1)\rangle_{oc}\langle\widehat{\sigma}(t)\rangle \\ &+\gamma^3\int_{t_0}^{t} dt_1\int_{t_0}^{t_1} dt_2\langle\widehat{L_1}(t)\widehat{L_1}(t_1)\widehat{L_1}(t_2)\rangle_{oc}\langle\widehat{\sigma}(t)\rangle \\ &+\gamma^4\int_{t_0}^{t} dt_1\int_{t_0}^{t_1} dt_2\int_{t_0}^{t_2} dt_3\langle\widehat{L_1}(t)\widehat{L_1}(t_1)\widehat{L_1}(t_2)\widehat{L_1}(t_3)\rangle_{oc}\langle\widehat{\sigma}(t)\rangle + O(\gamma^5)\ ,\end{aligned} \tag{B.25}$$

where $\langle A(t_1)...B(t_n)\rangle_{oc}$ is the ordered cumulant, which is an ordinal cumulant but keeping the chronological order and one of operator products.

Clearly we can find that the cumulant appearing in series of the TC equation with Markovian approximation and one in TCL equation are different for the higher order than three but the structure of both series expantions are identical for all orders. In the case of TCL equation, only the weak coupling expansion is applied. Thus the higher-order term of the series expansion is significant for appropriate situations. In the case of TC equation, on the other hand, the higher-order term of the series expansion is hardly justifiable. Therefore, in the actual situation, we should use the series expansion of TCL equation for the study of dynamics.

Appendix C

Numerical Routines

C.1 Exponential Integrals

The functions $\mathcal{A}_p(x)$ and $\mathcal{A}_m(x)$ are calculated with the following FORTRAN subroutines. For small argument, Taylor expansion is used for the calculation. In contrast, for large argument, asymptotic expansion is used. In the intermediate range, we use numerical integration for getting numerical accuracy. This routine requires several routines in "Numerical Recipes in FORTRAN 2nd ed." [53]: qromo, polint, midpnt and midinf routines.

```
cccccccccccccccccccccccccccccccccccccccccccccccccccccccc
      real*8 function ei(x)
      real*8 x
      ei = -exp(-x)/x
      return
      end
cccccccccccccccccccccccccccccccccccccccccccccccccccccccc
      real*8 function eibb(x)
      real*8 x
      if(x.eq.0d0) then
        eibb = 1d0
        return
      endif
```

```
      eibb = (exp(x)-1d0)/x
      return
      end
cccccccccccccccccccccccccccccccccccccccccccccccccccccccccc
      real*8 function eeibx(x)
c
c      this function calculates
c      exp(-x) \bar{Ei}(x), where x must be positive,
c      with Taylor expansion, numerical integration,
c      and asymptotic expansion,
c      calling numerical integration subroutines,
c      qromo, polint, midpnt and midinf, which can be
c      obtained from Numerical Recipes in FORTRAN 2nd ed.
c
c
      implicit none
      integer maxit
      real*8 x,eps,euler,fpmin
      parameter (euler=.57721566490153)
      parameter (eps=1.0d-15)
      parameter (maxit=300000,fpmin=1.d-30)
      integer k
      real*8 fact,prev,sum,term,rx,zero
      parameter (zero = 0d0)
      real*8 eibb,res2
      external eibb,midpnt

      if(x.le.0d0) stop 'bad argument in eibar'
      if(x.lt.fpmin) then
        eeibx = (log(x)+euler)*exp(-x)
      else if(x.le.3)then
        sum = 0d0
```

```
        fact = 1d0
        do k = 1,maxit
          fact = fact*x/k
          term = fact/k
          sum = sum+term
          if(term.lt.eps*sum) goto 1
        end do
        stop 'series failed in eeibx'
1       eeibx = (sum+log(x)+euler)*exp(-x)
      else if(x.gt.30) then
        sum = 0d0
        term = 1d0
        rx = 1d0/x
        do k = 1,maxit
          prev = term
          term = term*k*rx
          if(term.lt.eps) goto 2
          if(term.lt.prev) then
            sum = sum+term
          else
            sum = sum-prev
            goto 2
          endif
        end do
2       eeibx = (1d0+sum)*rx
      else
        call qromo(eibb,zero,x,res2,midpnt)
        eeibx = (res2+log(x)+euler)*exp(-x)
      end if
      return
      end
cccccccccccccccccccccccccccccccccccccccccccccccccccccccccc
```

```
      real*8 function eeix(x)
c
c      this function calculates
c      exp(x) Ei(-x), where x must be positive,
c      with Taylor expansion, numerical integration,
c      and asymptotic expansion
c      calling numerical integration subroutines,
c      qromo, polint, midpnt and midinf, which can be
c      obtained from Numerical Recipes in FORTRAN 2nd ed.
c
      implicit none
      integer maxit
      real*8 x,eps,euler,fpmin
      parameter (euler=.57721566490153)
      parameter (eps=1.0d-15)
      parameter (maxit=300000,fpmin=1.d-30)
      integer k
      real*8 fact,prev,sum,term,tmp,rx,infty,res,ei
      external midinf,ei
      parameter (infty = 1d30)

      if(x.le.0d0) stop 'bad argument in ei'
      if(x.lt.fpmin) then
        eeix = (log(x)+euler)*exp(x)
      else if(x.le.3)then
        sum = 0d0
        fact = x
        do k = 1,maxit
          tmp = 2*k*(x-2*k) - x
          tmp = tmp/(4*k*k*(2*k-1))
          term = fact*tmp
          sum = sum+term
```

```
          fact = fact*x*x/(2*k*(2*k+1))
          if(abs(term).lt.eps*abs(sum)) goto 1
        end do
        stop 'series failed in eebx'
 1      eeix = (sum+log(x)+euler)*exp(x)
      else if(x.gt.30) then
        sum = 0d0
        term = 1d0
        rx = 1d0/x
        do k = 1,maxit
          prev = term
          term = -term*k*rx
          if(abs(term).lt.eps) goto 2
          if(abs(term).lt.abs(prev)) then
            sum = sum+term
          else
            sum = sum-prev
            goto 2
          endif
        end do
 2      eeix = -(1d0+sum)*rx
      else
        call qromo(ei,x,infty,res,midinf)
        eeix = res*exp(x)
      end if
      return
      end
```

Bibliography

[1] A. Ajdari and J. Prost. *C. R. Acad. Sci. Paris*, **315**, (1992), 1635.

[2] C. M. Arizmendi and F. Family. "Approach to steady-state current in ratchets". *Physica*, **A232**, (1996), 119–133.

[3] R. D. Astumian. "Thermodynamics and Kinetics of a Brownian Motor". *SCIENCE*, **276**, (1997), 917–922.

[4] R. D. Astumian and M. Bier. "Fluctuation Driven Ratchets: Molecular Motors". *Phys. Rev. Lett.*, **72**, (1994), 1766.

[5] R. D. Astumian and M. Bier. "Mechanochemical Coupling of the Motion of Molecular Motors to ATP Hydrolysis". *Biophys. J.*, **70**, (1996), 637–653.

[6] K. Blum. *Density Matrix Theory and Applications.* Plenum Press, New York, 1981.

[7] A. O. Caldeira and A. J. Leggett. "Quantum Tunneling in a Dissipative System". *Ann. Phys.*, **149**, (1983), 374.

[8] F. Capasso, S. Luryi, W. T. Tsang, C. G. Bethea, and B. F. Levine. "New Transient Electrical Polarization Phenomenon in Sawtooth Superlattices". *Phys. Rev. Lett.*, **51**, (1983), 2318–2321.

[9] J.-F. Chauwin, A. Ajdari, and J. Prost. "Force-Free Motion in Asymmetric Structures: a Mechanism without Diffusive Step". *Europhys. Lett.*, **27**, (1994), 421–426.

[10] D. R. Chialvo and M. M. Millonas. "Asymmetric unbiased fluctuations are sufficient for the operation of a correlation ratchet". *Phys. Lett.* **A**, **209**, (1995), 26.

[11] P. M. P. Curie. "SUR LA SYMÉTRIE DANS LES PHÉNOMENES PHYSIQUES, SYMÉTRIE D'UN CHAMP ÉLECTRIQUE ET D'UN CHAMP HAGNÉTIQUE". *J. de Phys. III.*, **3**, (1894), 393.

[12] I. Derényi and T. Vicsek. "Realistic models of biological motion". *Physica* **A**, **249**, (1988), 397–406.

[13] I. Derényi and T. Vicsek. "Cooperative Transport of Brownian Particles". *Phys. Rev. Lett.*, (1995), 374–377.

[14] C. R. Doering, W. Horsthemke, and J. Riordan. "Nonequilibrium Fluctuation-Induced Transport". *Phys. Rev. Lett.*, **72**, (1994), 2984.

[15] R. Egger, C. H. Mak, and U. Weiss. "Rate concept and retarded master equations for dissipative tight-binding models". *Phys. Rev.* **E**, **50**, (1994), R655–R658.

[16] T. C. Elston and C. R. Doering. "Numerical and Analytical Studies of Nonequilibrium Fluctuation-Induced Transport Processes". *J. Stat. Phys.*, **83**, (1996), 359.

[17] L. P. Faucheux, L. S. Bourdieu, P. D. Kaplan, and A. J. Libchaber. "Optical Thermal Ratchet". *Phys. Rev. Lett.*, **74**, (1995), 1504.

[18] R. P. Feynman and Jr. F. L. Vernon. "The Theory of a General Quantum System Interacting with a Linear Dissipative System". *Ann. Phys.*, **24**, (1963), 118–173.

[19] R. P. Feynman, R. B. Leighton, and M. Sands. *The Feynman Lectures on Physics Vol. I.* Addison-Wesley, Reading, Massachusetts, 1996.

[20] M. P. A. Fisher. "Resonantly enhanced quantum decay: A time-dependent Wentzel-Kramers-Brillouin approach". *Phys. Rev.* **B**, **37**, (1988).

[21] L. Gammaitoni, P. Hänggi, P. Jung, and F. Marchesoni. "Stochastic resonance". *Rev. Mod. Phys.*, **70**, (1998), 223–287.

[22] C. W. Gardiner. *Handbook of Stochastic Methods: for Physics, Chemistry and the Natural Sciences.* Springer-Verlag, Berlin, second edition, 1985.

[23] C. W. Gardiner. *Quantum Noise.* Springer-Verlag, Berlin, 1991.

[24] E. Geva and R. Kosloff. "Three-level quantum amplifier as a heat engine: A study in finite-time thermodynamics". *Phys. Rev.* **E**, **49**, (1994), 3903–3918.

[25] G. H. Golub and C. F. Van Loan. *Matrix Computations, 3rd ed.* The Johns Hopkins University Press, London, 1996.

[26] I. Goychuk, M. Grifoni, and P. Hänggi. "Nonadiabatic Quantum Brownian Rectifiers". *Phys. Rev. Lett.*, **81**, (1998), 649–652.

[27] M. Grifoni. "Dynamics of the dissipative two-state system under ac modulation of bias and coupling energy". *Phys. Rev.* **E**, **54**, (1996), R3086–R3089.

[28] M. Grifoni and P. Hänggi. "Nonlinear quantum stochastic resonance". *Phys. Rev.* **E**, **54**, (1996), 1390.

[29] M. Grifoni, L. Hartmann, S. Berchtold, and P. Hänggi. "Quantum tunneling and stochastic resonance". *Phys. Rev.* **E**, **53**, (1996), 5890.

[30] M. Grifoni, M. Sassetti, J. Stockburger, and U. Weiss. "Nonlinear respose of a periodically driven damped two-state system". *Phys. Rev.* **E**, **48**, (1993), 3497–3509.

[31] M. Grifoni, M. Sassetti, and U. Weiss. "Exact master equations for driven dissipative tight-binding models". *Phys. Rev.* **E**, **53**, (1996), R2033–R2036.

[32] T. Harms and R. Lipowsky. "Driven Ratchets with Disordered Tracks". *Phys. Rev. Lett.*, (1997), 2895–2898.

[33] T. Hondou and Y. Sawada. "Dynamical Behavior of a Dissipative Particle in a Periodic Potential Subject to Chaotic Noise: Retrieval of Chaotic Determinism with Broken Parity". *Phys. Rev. Lett.*, **75**, (1995), 3269–3272.

[34] B. I. Ivlev and V. I. Mel'nikov. "Alternating-current-induced decay of zero-voltage states of Josephson junctions". *Sov. Phys. JETP*, **62**, (1985), 1298–1302.

[35] A. M. Jayannavar. "Simple model for Maxwell's-demon-type information engine". *Phys. Rev.* **E**, **53**, (1996), 2957.

[36] F. Jülicher, A. Ajdari, and J. Prost. "Modeling molecular motors". *Rev. Mod. Phys.*, **69**, (1997), 1269–1281.

[37] F. Jülicher and J. Prost. "Cooperative Molecular Motors". *Phys. Rev. Lett.*, **75**, (1995), 2618.

[38] F. Jülicher and J. Prost. "Spontaneous Oscillations of Collective Molecular Motors". *Phys. Rev. Lett.*, **78**, (1997), 4510.

[39] P. Jung, J. G. Kissner, and P. Hänggi. "Regular and Chaotic Transport in Asymmetric Periodic Potentials: Inertia Ratchets". *Phys. Rev. Lett.*, **76**, (1996), 3436–3439.

[40] R. Kubo. "Statistical-Mechanical Theory of Irreversible Processes. I.". *J. Phys. Soc. Jpn*, **12**, (1957), 570–586.

[41] R. Kubo, M. Toda, and N. Hashitsume. *Statistical Physics II*. Springer-Verlag, Berlin, 1991.

[42] J. Kula, T. Czernik, and J. Łuczka. "Transport generated by dichotomous fluctuations". *Phys. Lett.* **A**, **214**, (1996), 14.

[43] J. Kula, T. Czernik, and J. Łuczka. "Brownian Ratchets: Transport Controlled by Thermal Noise". *Phys. Rev. Lett.*, **80**, (1998), 1377–1380.

[44] A. J. Leggett, S. Chakravarty, A. T. Dorsey, M. P. A. Fisher, A. Garg, and W. Zwerger. "Dynamics of the dissipative two-state system". *Rev. Mod. Phys.*, **59**, (1987), 1–85.

[45] Y.-X. Li. "Transport generated by fluctuating temperatuer". *Physica*, **A238**, (1997), 245–251.

[46] M. O. Magnasco. "Forced Thermal Ratchets". *Phys. Rev. Lett.*, **71**, (1993), 1477.

[47] M. O. Magnasco. "Molecular combustion Motors". *Phys. Rev. Lett.*, **72**, (1994), 2656.

[48] G. Mahler and V. A. Weberruß. *Quantum Networks*. Springer-Verlag, Berlin, 1995.

[49] P. C. Martin and J. Schwinger. "Theory of Many-Particle Systems. I". *Phys. Rev.*, **115**, (1959), 1342–1373.

[50] M. M. Millonas. "Self-Consistent Microscopic Theory of Flucutation-Induced Trasnport". *Phys. Rev. Lett.*, **74**, (1995), 10.

[51] K. Nemoto and F. Shibata. "A Projection Operator Method in the Heisenberg Picture". *J. Phys. Soc. Jpn*, **65**, (1996), 3492–3499.

[52] G. I. Nixon and G. W. Slater. "Entropic trapping and electrophoretic drift of a polyelectrolyte down a channel with a periodically oscillating width". *Phys. Rev.* **E**, **53**, (1996), 4969–4980.

[53] W. Press, S. A. Teukolsky, W.T.Vetterling, and B.P. Flannery. *Numerical recipes in FORTRAN 2nd ed.* Cambridge University Press, Cambridge, 1992.

[54] J. Prost, J.-F. Chauwin, L. Peliti, and A. Ajdari. "Asymmetric Pumping of Particles". *Phys. Rev. Lett.*, **72**, (1994), 2652–2655.

[55] P. Reimann and T. C. Elston. "Kramers Rate for Thermal Plus Dichotomous Noise Applied to Ratchets". *Phys. Rev. Lett.*, **77**, (1996), 5328–5331.

[56] P. Reimann, M. Grifoni, and P. Hänggi. "Quantum Ratchets". *Phys. Rev. Lett.*, **79**, (1997), 10.

[57] R. Roncaglia and G. P. Tsironis. "Discrete Quantum Motors". *Phys. Rev. Lett.*, **81**, (1998), 10–13.

[58] J. Rousselet, L. Salome, A. Ajdari, and J. Prost. "Directional motion of brownian particles induced by a periodic asymmetric potential". *Nature*, **370**, (1994), 446.

[59] H. Sagakuchi. "A Langevin Simulation for the Feynman Ratchet Model". *J. Phys. Soc. Jpn*, **67**, (1998), 709.

[60] K. Sekimoto. "Energetics of thermal ratchet models". *J. Phys. Soc. Jpn*, **66**, (1997), 1234.

[61] F. Shibata and T. Arimitsu. "Expansion Formulas in Nonequilibrium Statistical Mechanics". *J. Phys. Soc. Jpn*, **49**, (1980), 891–897.

[62] C. Sikorski and U. Merkt. "Spectroscopy of Electronic States in InSb Quantum Dots". *Phys. Rev. Lett.*, **62**, (1989), 2164–2167.

[63] G. W. Slater, H. L. Guo, and G. I. Nixon. "Bidirectional Transport of Polyelectrolytes Using Self-Modulating Entropic Ratchets". *Phys. Rev. Lett.*, **78**, (1997), 1170.

[64] K. Svoboda, P. P. Mitra, and S. M. Block. "Fluctuation analysis of motor protein movement and single enzyme kinetics". *Proc. Natl. Acad. Sci. USA*, **91**, (1994), 11782.

[65] G. Tatara, M. Kikuchi, S. Yukawa, and H. Matsukawa. "Dissipation Enhanced Asymmetric Transport in Quantum Ratchets". *J. Phys. Soc. Jpn*, **67**, (1998), 1090–1093.

[66] R. D. Vale and F. Oosawa. "PROTEIN MOTORS AND MAXWELL'S DEMONS: DOES MECHANOCHEMICAL TRANSDUCTION INVOLVE A THERMAL RATCHET?". *Adv. Biophys.*, **26**, (1990), 97.

[67] V. Čápek. "Carrier transfoer in inhomogeneous media". *Z. Phys.* **B**, **99**, (1996), 261–267.

[68] U. Weiss. *Quantum Dissipative Systems*. World Scientific, Singapore, 1993.

[69] U. Weiss and M. Wollensak. "Dynamics of the Biased Two-Level System in Metals". *Phys. Rev. Lett.*, **62**, (1989), 1663–1666.

[70] S. Yukawa, M. Kikuchi, G. Tatara, and H. Matsukawa. "Quantum Ratchets". *J. Phys. Soc. Jpn*, **66**, (1997), 2953–2956.

[71] I. Zapata, R. Bartussek, F. Sols, and P. Hänggi. "Voltage Rectification by a SQUID Ratchet". *Phys. Rev. Lett.*, **77**, (1996), 2292.

[72] H.-X. Zhou and Y. d. Chen. "Chemically Driven Motility of Brownian Particles". *Phys. Rev. Lett.*, **77**, (1996), 194–197.